

AD-A044 800

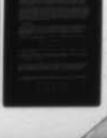
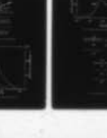
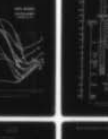
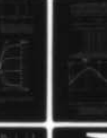
ADVISORY GROUP FOR AEROSPACE RESEARCH AND DEVELOPMENT--ETC F/G 20/14
EM PROPAGATION CHARACTERISTICS OF SURFACE MATERIALS AND INTERFA--ETC(U)
JUN 77 H J ALBRECHT

UNCLASSIFIED

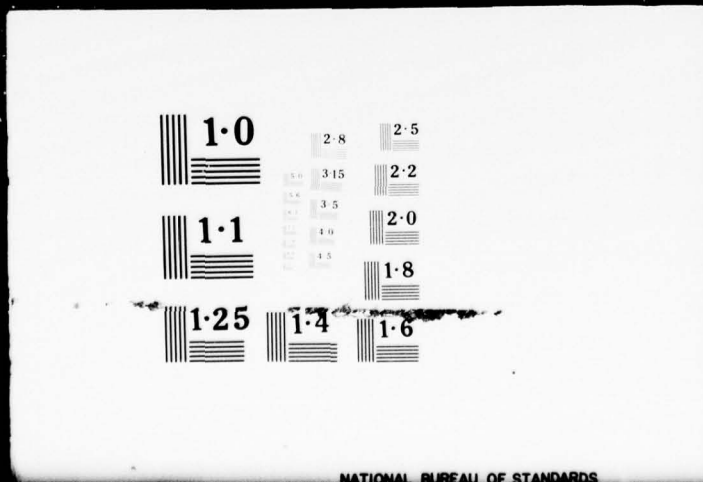
AGARD-CP-208

NL

1 OF 3
ADA
044800



1 OF 3
 ADA
 044800



NATIONAL BUREAU OF STANDARDS

$$\rho = (X^2 + Y^2 + Z^2)^{\frac{1}{2}}$$

AGARD

ADVISORY GROUP FOR AEROSPACE RESEARCH & DEVELOPMENT

7 RUE ANCELLE 92200 NEUILLY SUR SEINE FRANCE

AGARD CONFERENCE PROCEEDINGS No. 208

EM Propagation Characteristics of Surface Materials and Interface Aspects

Edited by
H.J. Albrecht



NORTH ATLANTIC TREATY ORGANIZATION



DISTRIBUTION AND AVAILABILITY
ON BACK COVER

DISTRIBUTION STATEMENT A
Approved for public release
Distribution Unlimited

NORTH ATLANTIC TREATY ORGANIZATION
ADVISORY GROUP FOR AEROSPACE RESEARCH AND DEVELOPMENT
(ORGANISATION DU TRAITE DE L'ATLANTIQUE NORD)

9
AGARD Conference Proceedings No. 208
6 EM PROPAGATION CHARACTERISTICS OF SURFACE
MATERIALS AND INTERFACE ASPECTS

10 H. J. Albrecht

11 Jun 77

12 246p.

DDC
RECEIVED
OCT 3 1977
C

Papers presented at the Electromagnetic Wave Propagation Panel
Specialists' Meeting held in Istanbul, 18-19 October 1976.

400 043

LB

THE MISSION OF AGARD

The mission of AGARD is to bring together the leading personalities of the NATO nations in the fields of science and technology relating to aerospace for the following purposes:

- Exchanging of scientific and technical information;
- Continuously stimulating advances in the aerospace sciences relevant to strengthening the common defence posture;
- Improving the co-operation among member nations in aerospace research and development;
- Providing scientific and technical advice and assistance to the North Atlantic Military Committee in the field of aerospace research and development;
- Rendering scientific and technical assistance, as requested, to other NATO bodies and to member nations in connection with research and development problems in the aerospace field;
- Providing assistance to member nations for the purpose of increasing their scientific and technical potential;
- Recommending effective ways for the member nations to use their research and development capabilities for the common benefit of the NATO community.

The highest authority within AGARD is the National Delegates Board consisting of officially appointed senior representatives from each member nation. The mission of AGARD is carried out through the Panels which are composed of experts appointed by the National Delegates, the Consultant and Exchange Program and the Aerospace Applications Studies Program. The results of AGARD work are reported to the member nations and the NATO Authorities through the AGARD series of publications of which this is one.

Participation in AGARD activities is by invitation only and is normally limited to citizens of the NATO nations.

A large part of the content of this publication has been reproduced directly from material supplied by AGARD or the authors; the remainder has been set by Technical Editing and Reproduction Ltd.

Published June 1977

Copyright © AGARD 1977
All Rights Reserved

ISBN 92-835-0196-9



*Printed by Technical Editing and Reproduction Ltd
Harford House, 7-9 Charlotte St, London, W1P 1HD*

PREFACE

"Electromagnetic Propagation Characteristics of Surface Materials and Interface Aspects" was the topic of a Specialists' Meeting conducted by the Electromagnetic Wave Propagation Panel of AGARD in autumn 1976. It took place at the Technical University of Istanbul, Turkey, on 18th and 19th October 1976. These Conference Proceedings contain papers and contributions to discussions, as well as an account of the round-table discussion covering the entire subject of the meeting.

In the field of electromagnetic wave propagation, essential limiting conditions may be represented by characteristics and behaviour of upper and lower boundaries of the propagation environment. The performance of propagation paths may depend significantly upon variations in such surface properties; optimum predictability is one of the desired features.

The subject of surface characteristics is usually addressed in connection with or as part of meetings concerning other main topics. The more direct approach undertaken in this meeting has allowed to account for the increasing importance of appropriate parameters for a number of modern fields of research and engineering applications such as remote sensing and surveillance, target recognition, sub-surface propagation, etc. In addition to a general evaluation of recent data, papers and discussions at the meeting covered the variability of parameters, their geographical distribution, and limitations to their validity.

The entire subject of the meeting was dealt with in three sessions, concerning EM surface characteristics, propagation in interface media, and global distribution of EM surface characteristics. A round-table discussion at the conclusion of the meeting assisted in clarifying the present state of the art, engineering aspects, and promising areas of research. Two review papers at the beginning of the first session concerned the present state of the art with regard to electromagnetic properties of water, and methods of measuring ground resistivity. Other contributions in this session presented recent results in this general field. The second session commenced with papers on theoretical work and analytical methods with emphasis on interface media and modern communication requirements; other papers included experimental data obtained under special surface-dependent propagation conditions. Following a review paper in the third session on the possibilities of monitoring atmospheric and surface propagation characteristics from space, other contributions reported results related to global distribution in general.

In summary, this Specialists' Meeting provided the intended review of the state of the art in this field of research, discussed theoretical and partial aspects, and indicated promising areas of research. These Conference Proceedings give a full account of papers and discussions.

Appreciation is expressed to all who assisted in the organization of the Specialists' Meeting as well as in the compilation of these Proceedings, to members of the programme committee, authors and contributors to discussions, session chairmen, to the host coordinator, to AGARD-staff and other collaborators.

H.J. ALBRECHT
Editor

ACCESSION FOR	FILED ON	✓
NTIS	B. H. S. 100	□
DOC		□
UNANNOUNCED		
JUSTIFICATION		
BY	DISTRIBUTION/AVAILABILITY NOTES	
	SPECIAL	
A		

**AGARD ELECTROMAGNETIC WAVE
PROPAGATION PANEL**

CHAIRMAN: Mr P.Halley
Ingenieur en Chef au CNET France

DEPUTY CHAIRMAN: Dr H.J.Albrecht
FGAN Germany

PROGRAM COMMITTEE MEMBERS

Dr H.J.Albrecht (Chairman)
Forschungsgesellschaft für
Angewandte Naturwissenschaften E.V.
5307 Wachtberg-Werthhoven
Königstrasse 2
Germany

Mr P.Halley
France

Professor A.M.Biggs
USA

Professor A. Van der Vorst
Belgium

Dr G.P. de Loor
Netherlands

PANEL EXECUTIVE

CDR. D.G.Carruthers, US Navy

HOST COORDINATOR

Prof.A.Ataman
Istanbul Teknik Universitesi
Istanbul, Turkey

SESSION CHAIRMEN

Prof.A.Ataman (I)
Istanbul Teknik Universitesi
Istanbul, Turkey

Prof.A.W.Biggs (II)
University of Kansas
Kansas, USA

Mr L.Boithias (III)
CNET
Paris, France

THEME

Although the material characteristics of one or both of upper and lower boundaries of propagation environments have been touched upon during the last few years, the subject has gained in interest and has become important for a number of modern fields of research and engineering applications, such as remote sensing and surveillance, target recognition, sub-surface propagation, etc. Consequently, essential progress is being made in the general field of surface characteristics and with regard to some special aspects, as, for instance, the variability of parameters, their geographical distribution, and limitations to their validity. The topic proposed promises to be relevant to military applications as well as to projects in space research.

CONTENTS

	Page
PREFACE	iii
PROGRAM AND MEETING OFFICIALS – THEME	iv
	Reference
<u>SESSION I – ELECTROMAGNETIC SURFACE CHARACTERISTICS</u>	
ELECTROMAGNETIC PROPERTIES OF WATER, AT FREQUENCIES BELOW 1000 GHZ, AS MET IN ITS VARIOUS FORMS FOUND AT THE SURFACE OF THE EARTH (Review Paper)	
LES PROPRIETES ELECTROMAGNETIQUES DE L'EAU AUX FREQUENCES INFERIEURES A 1000 GHZ, SOUS LES DIVERSES FORMES RENCONTREES A LA SURFACE DE LA TERRE (Rapport de Synthese)	
par P.M. Halley	1
DETERMINATION OF THE EARTH'S RESISTIVITY BY SURFACE MEASUREMENTS (Review Paper)	
by H.Flathe	2
ELECTROMAGNETIC WAVE PROPAGATION FROM SOURCES IN COMPOSITE MEDIA	
by A.W.Biggs	3
RECENTS PROGRES DANS QUELQUES PROCEDES ELECTROMAGNETIQUES DE DETECTION D'HETEROGENEITES	
par M.Cauterman, P.Degauque, B.Demoulin, et R.Gabillard	4
VARIATIONS OF TEMPORAL, SPECTRAL AND ANGULAR RADAR BACKSCATTERING COEFFICIENT OF VEGETATION	
by F.T.Ulaby	5
AN EMPIRICAL MODEL FOR AVERAGE SCATTERING CROSS SECTION COMPUTATIONS FOR LAND AND SEA SURFACES	
by W.Keydel	6
<u>SESSION II – PROPAGATION IN INTERFACE MEDIA</u>	
GROUND WAVE PROPAGATION IN THE PRESENCE OF SMOOTH HILLS AND DEPRESSIONS	
by L.B.Felsen and A.Green	7
THE TRANSIENT RESPONSE OF A SLIGHTLY ROUGH DIELECTRIC SURFACE	
by K.J.Langenberg, K.-D.Becker, and G.Dobmann	8
EFFECTS OF NOCTURNAL GROUND-BASED TEMPERATURE INVERSION LAYERS ON LINE-OF-SIGHT RADIO LINKS	
by L.Fehlhaber and H.G.Giloi	9
EXPERIMENTAL RESULTS CONCERNING THE INFLUENCE OF WAVE PROPAGATION ON TELEMETRY DATA TRANSMISSIONS AT 230 MHZ COMPARED WITH 2, 3 GHZ	
by G.V.Mayer	10
SPECULATIONS ON MEDIA INTERFACES WITH INTERESTING ELF COMMUNICATIONS	
by G.Tacconi	11
<u>SESSION III – GLOBAL DISTRIBUTION OF EM SURFACE CHARACTERISTICS</u>	
SATELLITE-BORNE MONITORING OF ATMOSPHERIC AND SURFACE CHARACTERISTICS AFFECTING THE PROPAGATION OF MICROWAVES IN THE TROPOSPHERE (Review Paper)	
by E.Raschke	12

DISTRIBUTION OF ELECTRICAL RESISTIVITY ON CONTINENTAL AREAS

by V.Haak, M.Beblo, and A.BerktoId

13

CONSEQUENCES DE LA DIFFUSION ET DE LA DEPOLARISATION DES ONDES
ELECTROMAGNETIQUES PAR LE SOL DANS LES PROBLEMES DE RETRODIFFUSION

par C.Goutelard et J.L.Coatanhay

14

ROUND-TABLE DISCUSSION

RTD

ELECTROMAGNETIC PROPERTIES OF WATER,
AT FREQUENCIES BELOW 1 000 GHZ, AS
MET IN ITS VARIOUS FORMS FOUND AT THE
SURFACE OF THE EARTH

by

P.M. HALLEY

Centre National d'Etudes des Télécommunications
38-40, rue du Général Leclerc - 92131 Issy-les-Moulineaux

Contents of exposé

1. The three fundamental e.m. characteristics of physical media
2. The scale of values of conductivity and the major rôle of water on these values at the surface of the Earth
3. Distribution of water at the surface of the Earth
4. The electrical moments and molecular polarizability
 - 4.1. The potential of a charge distribution
 - 4.2. Polarizability of molecules
 - 4.3. Polarization
5. The water molecule
 - 5.1. The electrical properties of free water molecules
 - 5.2. Water molecule configurations
 - 5.3. Isotopes
6. The Clausius Mossotti formula
 - 6.1. The static condition
 - 6.2. The harmonic condition and the Debye equation
7. The ionic composition of sea-water
8. The ionic conductivity of soft water and sea-water :
 - 8.1. The principle of current flow in the electrolyte
 - 8.2. Measurement procedures and experimental results
 - 8.3. The conductivity of pure water
 - 8.4. Conductivity of sea-water
9. Liquid state water in harmonic condition :
 - 9.1. Experimental measurement procedure to determine e.m. characteristics of water
 - 9.2. Using experimental results associated with the Debye equations
 - 9.3. Water at frequencies below 1 000 GHz
 - 9.4. Water at frequencies above 1 000 GHz
10. Dielectric characteristics of ice :
 - 10.1. Ice at frequencies below 1 GHz
 - 10.2. Ice and snow at 10 GHz

Notations

α	Molecular polarizability
σ	Conductivity in mho/m
σ'	Ionic conductivity
σ''	Dipolar conductivity
ϵ	Permittivity (dielectric constant)
ϵ_0	Permittivity of free space
ϵ_r	Relative permittivity $\epsilon_r = \epsilon/\epsilon_0$
$\bar{\epsilon}_r$	Complex relative permittivity

$$\bar{\epsilon}_r = \epsilon_r - j \frac{\sigma}{\omega \epsilon_0}$$

$$\bar{\epsilon}_r = \epsilon' - j\epsilon'' - j \frac{\sigma'}{\omega \epsilon_0} \equiv \epsilon' - j \frac{\sigma' + \sigma''}{\omega \epsilon_0}$$

ϵ'	Real part of $\bar{\epsilon}_r$
ϵ''	Imaginary part of $\bar{\epsilon}_r$, due to polarization
ϵ_S	$\epsilon'(0)$ real part of $\bar{\epsilon}_r$ in static condition
ϵ_∞	$\epsilon'(\infty)$ real theoretical part of $\bar{\epsilon}_r$ for an infinitely high frequency
μ_0	Magnetic permeability of free space

$$\mu_0 = 4\pi \cdot 10^{-7} \text{ (Hm}^{-1}\text{)}$$

μ	Magnetic permeability or dipolar electric moment
β	Absorption coefficient $A = A_0 e^{-\beta z}$
n	Refractive index
\vec{P}	Electric polarization
T	Absolute temperature ($^{\circ}\text{K}$)
t	Celsius temperature ($^{\circ}\text{C}$) or time
ω	Angular wave frequency
τ	Relaxation time

Electromagnetic properties of water,
at frequencies below 1 000 GHz, as
met in its various forms found at the
surface of the Earth

by

P.M. HALLEY *

ABSTRACT

Water is the most commonly found form of matter on the Earth's surface and it is practically present everywhere.

In the static condition, the dielectric properties of water and the conductivity of aqueous electrolytes, such as sea-water, are very well known. Recent theories in the field are undergoing development (Kirkwood - Fröhlich).

In the harmonic condition, the application of a relatively simple theory (Debye, Onsager) provides perfectly satisfactory results.

These theories are closely linked to a water molecule model which is folded, strongly polar and to mutual inter-molecular action.

The most widespread natural body and the most homogeneous on the Earth's surface is the Ocean. Its characteristics are quite well known up to 10^{12} Hz. It is very opaque to e.m. waves.

The polar ice-caps are less homogeneous, with less well known characteristics up to 10^{11} Hz only. Ice, at low temperatures is less opaque to e.m. waves than the Ocean.

1. - THE THREE FUNDAMENTAL e.m. CHARACTERISTICS OF PHYSICAL MEDIA (1) :

Most problems in macroscopic electromagnetism - where non-linear effects are not considered - can be solved by supposing that certain linear equations hold in the vicinity of the point under consideration for field vectors. These equations are :

$$(1) \quad \vec{D} = \epsilon \vec{E} \qquad (2) \quad \vec{H} = \frac{1}{\mu} \vec{B} \qquad (3) \quad \vec{J} = \sigma \vec{E}$$

The coefficients are labelled

ϵ : the electric permittivity or specific induction power or dielectric constant

μ : the magnetic permeability

σ : the conductivity

These coefficients have to be evaluated in the vicinity of the point, and at the frequency, under consideration solely from the physical properties of the medium, using both theory and experimentation.

Obviously, from the three fundamental characteristics ϵ , μ , σ one can elaborate others better suited to certain problems.

* Captain, Marine Nationale - FRANCE

Graduate Ecole Supérieure d'Electricité

Senior Executive Engineer at the Centre National d'Etudes des Télécommunications

Within the scope of the present study we shall first briefly examine the relative importance of the characteristics and the order of magnitude of the known values. We shall then proceed with an in-depth study of the main characteristics of water and ice forms.

1.1. Magnetic permeability μ

On the Earth's surface, exceptional cases being neglected, and if one leaves out ferromagnetic materials, we need not concern ourselves with magnetic permeability, to all intents and purposes, and we can take it that the magnetic permeability μ is the same everywhere and equal to that in free space or in a vacuum i.e., μ_0 .

In the MKS (A) system, which we shall be using (except where noted otherwise in the text)

$$(4) \quad \mu_0 = 4\pi \cdot 10^{-7} \text{ (H m}^{-1}\text{)}$$

1.2. Electric permittivity ϵ

This characteristic varies on the Earth's surface, not only from one body to another, but also varies as a function of frequency.

$$\text{The electric permittivity of a vacuum is (5) } \epsilon_0 = \frac{1}{c^2 \mu_0} \text{ (F m}^{-1}\text{)}$$

where c is the speed of light.

For each material body we can define the electric permittivity relative to that in a vacuum, as per :

$$(6) \quad \epsilon_r = \frac{\epsilon}{\epsilon_0}$$

Moreover, Maxwell's equations lead to the equation (7) $\epsilon_r = n^2$, where n is the refractive index of the medium, valid for the harmonic condition.

It proves convenient to introduce a vector for induced electrical polarization, defined by the equation

$$(8) \quad \vec{P} = \vec{D} - \epsilon_0 \vec{E}$$

The vector \vec{P} is self-cancelling in a vacuum and likewise where there is no field present. This vector, therefore, represents presence of matter.

1.3. Electric conductivity σ

This is the most variable e.m. characteristic by far, and hence the most important.

Free space or a vacuum is the only physical medium which presents an identically nil conductivity. For this reason, space is perfectly transparent to electromagnetic waves. Other physical media, called materials, all present a certain degree of opacity, i.e., they have a finite, non-nil, equivalent conductivity σ . It is for this reason that the most important e.m. characteristic of a propagation medium is its conductivity ! It is measured in siemens per meter or mho per meter. Naturally σ is a function of frequency.

1.4. Complex electric permittivity

Maxwell's equations lead to a combinatory formulation with both characteristics ϵ and σ for a non-ferromagnetic body, in the space where the field is to be considered and in the harmonic condition defined by the operator

$$(9) \quad \frac{\partial}{\partial t} = j\omega,$$

into a single characteristic called the complex electric permittivity

$$(10) \quad \overline{\epsilon}_r = \frac{\epsilon}{\epsilon_0} - j \frac{\sigma}{\omega \epsilon_0} = \epsilon_r (1 - jp)$$

Using this formulation, one need only refer to a single characteristic, although distinguishing the real and the imaginary parts, or taking the relative permittivity ϵ_r , on one hand, and the tangent of the loss angle p on the other hand.

The electric permittivity of a body is related directly to its molecular structure. The dipolar electric moment is one of the most important molecular constants. Polarizability is another major characteristic. These values can both be obtained from dielectric measurements.

Recently an effort has been made into a theoretical analysis of dielectrics has led to improved interpretation of the properties of condensed media and to a utilization of measurements made with vapours and diluted solutions.

The complex electric permittivity depends on frequency ; it is also highly interesting as regards the orientation of the molecule and regarding our knowledge of relaxation times.

2. THE SCALE OF VALUES OF CONDUCTIVITY AND THE MAJOR ROLE OF WATER AT THE SURFACE OF THE EARTH

2.1. At the nil frequency, i.e., in the static condition, there are man-made bodies which have very low conductivity values :

Body	Conductivity σ_s ($\Omega^{-1} \text{ m}^{-1}$)
Melted quartz	$< 2 \times 10^{-17}$
Common glass	10^{-12}

are

But there/also metals with high conductivity values

Steel	$0.5 \text{ at } 1 \times 10^7$
Copper	5.7×10^7

The ratio of the orders of magnitude in powers of ten is 24.

Bodies and materials, in general non-homogeneous and even heterogeneous that are found on the Earth's surface or in the top surface layers, have static conductivity values which lie between the two extremal values given in the table above. These are mainly aqueous solutions in their solid or liquid states and rocks. The following approximate values are found :

Body	Conductivity σ_s ($\Omega^{-1} \text{ m}^{-1}$)
Dry basalt	10^{-9}
Pure soft water ice	10^{-8}
Very pure water	10^{-6}
Dry ground (granite)	$10^{-5} \text{ to } 10^{-6}$
Soft water (lakes and rivers)	5×10^{-3}
Sea-water	4 to 5

The ratio of the extremal orders of magnitude (dry basalt and sea-water) in powers of ten is from 9 to 10 maximum.

2.2. Very pure water is a relatively poor conductor, but it is a quasi-universal solvent. Practically all known chemical compounds dissolve in water, to a measurable degree. The aqueous solutions of the minerals which make up rocks are all more or less conducting.

Certain subterranean layers are highly mineralised. Certain lakes are salt-laden. Such masses of liquid like sea-water, are indeed strong electrolytes.

On one hand water can be seen as a most corrosive agent, reacting with ions and molecules. It infiltrates rocks. It can flow from the surface to a subterranean layer, but can also rise from a subterranean layer to the surface, by capillarity. Its presence directly affects the e.m. characteristics of the Earth's rocks, including so-called "dry" basalt. The Ancient Greek philosopher Aristotle had included water among his four elements, together with earth, air and fire.

To summarize, from an electromagnetic point of view, solid or liquid state water presents the magnetic permeability value of a vacuum μ_0 . Moreover, because it contains free charges, or monopolar charges, i.e., ions, it possesses a certain real conductivity value σ' . An external electric field E applied to a sample causes an orderly displacement of these charges, i.e., a conduction current. Lastly, water has a certain electric permittivity ϵ , which is a result of polarization ; the latter being due mainly to the statistical orientation of permanent dipoles. In the harmonic condition, losses by friction of the orientation of the dipoles in neutral water give rise to an additional conductivity value σ'' , additional to ionic conductivity. The effective conductivity value, for the frequency under consideration, is the sum of the two elementary conductivities.

(45)

$$\sigma = \sigma' + \sigma''$$

3. DISTRIBUTION OF WATER AT THE SURFACE OF THE EARTH (2) :

Water, the most common of bodies, is present everywhere on the Earth's surface. In fact, the planet Earth could more appropriately be called the water planet, since water is probably the most specific substance which distinguishes the Earth from the other planets in the solar system. There is water practically everywhere, on the surface at a relatively shallow depth.

3.1. The total amount represents a volume of $13,5 \times 10^8 \text{ km}^3$ for a total planet surface of $5.09 \times 10^8 \text{ km}^2$. On a spherical model the thickness of the water layer would be 2.650 km.

The approximate global distribution of this water is as follows :

- the oceans : these account for $13 \times 10^8 \text{ km}^3$, i.e., 97 % of the total, for an oceanic surface of $3.6 \times 10^8 \text{ km}^2$. The mean depth of the oceans is therefore 3.610 km.
- the polar ice-caps : the Antarctic plateau holds 2.5 to $2.9 \times 10^7 \text{ km}^3$ of soft water ice, for a geographic surface of $1.5 \times 10^7 \text{ km}^2$. The average thickness of this ice is 1.8 km.

The Arctic only, accounts for $3 \times 10^6 \text{ km}^3$ of total soft water ice.

Despite the considerable quantity of water taken up by the polar ice-caps the edges of the continental masses, the "continental shelves" are covered by sea-water. Even if the axis of rotation of the Earth were to meet the surface in two continents, which would approximately double the amount of ice in the ice-caps, a considerable area of the continental shelves would still be under water, under the prevailing conditions of temperature.

- the upper part of the non-immersed terrestrial crust :

Beneath the continental surfaces (or in direct contact with the air there is approximately $4.8 \times 10^6 \text{ km}^3$ of water, in saturated layers, or in non-saturated rocks.

If the count is limited to 1 km in depth, the quantity of soft water is estimated at $4.1 \times 10^6 \text{ km}^3$.

3.2. On the continents, the quantity of water per unit of surface is likewise unevenly distributed. The following represent the main concentrations :

- glaciers	$2.1 \times 10^5 \text{ km}^3$
- large softwater lakes (Baikal, etc...)	$1.2 \times 10^5 \text{ km}^3$
- large salt-water lakes (Caspian, etc...)	$1.2 \times 10^5 \text{ km}^3$
- surface soil humidity	$25 \times 10^3 \text{ km}^3$
- rivers	$1.2 \times 10^3 \text{ km}^3$

The lower atmosphere contains an equivalent mass of $13 \times 10^3 \text{ km}^3$ of liquid water in the troposphere.

The annual turn-over rate by evaporation of oceans, precipitation and the return flow to the oceans, for the planet as a whole is $3.5 \times 10^5 \text{ km}^3$ per annum.

4. THE ELECTRIC MOMENTS AND MOLECULAR POLARIZABILITY (3)

We have already pointed out that a knowledge of the electric characteristics of material bodies required both a development of the theoretical studies and the experimentations. We are therefore led to giving a rapid recapitulation of the prime bases of the physical theory, before going on to a discussion of more recent progress. Obviously, the properties of water in all its forms depend fundamentally on the structures and properties of isolated molecule.

4.1. The potential of a charge distribution

From an electric point of view, a molecule is made up of positive and negative charges, distributed in the vicinity of the centre of gravity.

In order to understand the dielectric phenomena and the propagation of the e.m. field in matter, it is useful to develop, in a spherical harmonic series, the potential created remotely by the distribution of non-spherical charges and to represent the potential of these charges by the first terms of the development.

Let us, therefore, consider an atom or a molecule made up of a few charges taking up a small volume and let us take the coordinates of centre of gravity of the molecule as the origin.

The potential V at the point $M(X, Y, Z)$ created by the charges $e_1, e_2, \dots, e_i, \dots$ located at points $x_1, y_1, z_1; x_2, y_2, z_2; \dots, x_j, y_j, z_j, \dots$ is given by the equation :

$$(11) \quad V = \frac{1}{4\pi \epsilon_0} \sum_i \frac{e_i}{\left[(X - x_i)^2 + (Y - y_i)^2 + (Z - z_i)^2 \right]^{\frac{1}{2}}}$$

We then have (12)
$$\rho = (X^2 + Y^2 + Z^2)^{\frac{1}{2}}$$

The development of V as a function of the powers of $\frac{1}{\rho}$ can be written :

$$(13) \quad V = \frac{1}{4\pi \epsilon_0} \left[\frac{k_0}{\rho} + \frac{k_1}{\rho^2} + \frac{k_2}{\rho^3} + \dots \right]$$

each coefficient k_0 , k_1 , k_2 only depends on the structure of charge distribution and coordinates (X, Y, Z) .

4.1.1. The monopolar moment

$$(14) \quad k_0 = \sum_i e_i$$

This moment only exists with ionised molecules. For a system which is neuter as a whole, such as a neutral molecule, it disappears. On the contrary, for ions, as a first approximation, the potential comes down to that due to the global charge. It is the basis of the theory for strong electrolytes given by Debye-Hückel. It is all the more justified in that the term k_1 is nil for simple ions and complex symmetrical ions and that, moreover, the term k_2 is nil for simple ions with saturated or pseudo-saturated layers, such as :



4.1.2. The dipolar moment

$$(15) \quad k_1 = \frac{X}{\rho} \sum_i e_i x_i + \frac{Y}{\rho} \sum_i e_i y_i + \frac{Z}{\rho} \sum_i e_i z_i$$

k_2 is only different from zero if one, at least, of the three terms \sum differs from zero, i.e., if the barycentre of the positive charges does not coincide with that of the negative charges even as an average in time. In this case, the molecule is said to be "polar". It possesses an electric moment μ , the component vector :

$$\mu_x = \sum e_i x_i \quad \mu_y = \sum e_i y_i \quad \mu_z = \sum e_i z_i$$

The molecule is equivalent to a dipole formed by the negative charge $-e$ at the origin of the coordinates, and the positive charge $+e$ at the point with coordinates

$$x = \frac{\mu_x}{e} \quad y = \frac{\mu_y}{e} \quad z = \frac{\mu_z}{e}$$

Since the charge e is large enough for x , y and z to be very small, the potential of this dipole is :

$$(16) \quad V \sim \frac{1}{4\pi \epsilon_0 r^2} \left(\mu_x \frac{X}{\rho} + \mu_z \frac{Z}{\rho} \right)$$

An isolated atom does not have a dipolar moment, since the electron cloud is symmetrical with respect to the nucleus. In like manner, a molecule with a centre of symmetry, such as CH_4 , is not polar. On the contrary folded and pyramidal molecules are polar. H_2O is a folded molecule, and therefore is polar.

4.1.3. The quadrupolar moment

$$(17) \quad k_2 = \frac{1}{2} \left(3 \frac{X^2}{\rho^2} - 1 \right) \sum e_i x_i^2 + \frac{1}{2} \left(3 \frac{Y^2}{\rho^2} - 1 \right) \sum e_i y_i^2 + \frac{1}{2} \left(3 \frac{Z^2}{\rho^2} - 1 \right) \sum e_i z_i^2 \\ + 3 \frac{XY}{\rho^2} \sum e_i x_i y_i + 3 \frac{YZ}{\rho^2} \sum e_i y_i z_i + 3 \frac{ZX}{\rho^2} \sum e_i z_i x_i$$

This term may be discussed by taking the following quadric surface equation into account :

$$(18) \quad \xi^2 \sum e_i x_i^2 + \eta^2 \sum e_i y_i^2 + \zeta^2 \sum e_i z_i^2 + 2 \xi \eta \sum e_i x_i y_i + 2 \eta \zeta \sum e_i y_i z_i \\ + 2 \zeta \xi \sum e_i z_i x_i = 1$$

With respect to the molecule, this quadric has a well defined orientation, and is independent of the reference system. Instead of taking random coordinates, let us choose the trihedral $ox'y'z'$ aligned with the main axes of the quadric, in which the rectangular terms are self-cancelling and the term in ρ^{-3} of the potential V then becomes :

$$(19) \quad \frac{1}{2\rho^3} \left[\left(3 \frac{x'^2}{\rho^2} - 1 \right) \sum e_i x_i'^2 + \left(3 \frac{y'^2}{\rho^2} - 1 \right) \sum e_i y_i'^2 + \left(3 \frac{z'^2}{\rho^2} - 1 \right) \sum e_i z_i'^2 \right]$$

$$\text{If the quadric is a sphere (20) : } \sum e_i x_i'^2 = \sum e_i y_i'^2 = \sum e_i z_i'^2$$

Under these conditions, the potential cancels itself, since one can factorise

$$(21) \quad \left(3 \frac{x'^2 + y'^2 + z'^2}{\rho^2} - 3 \right) = 0$$

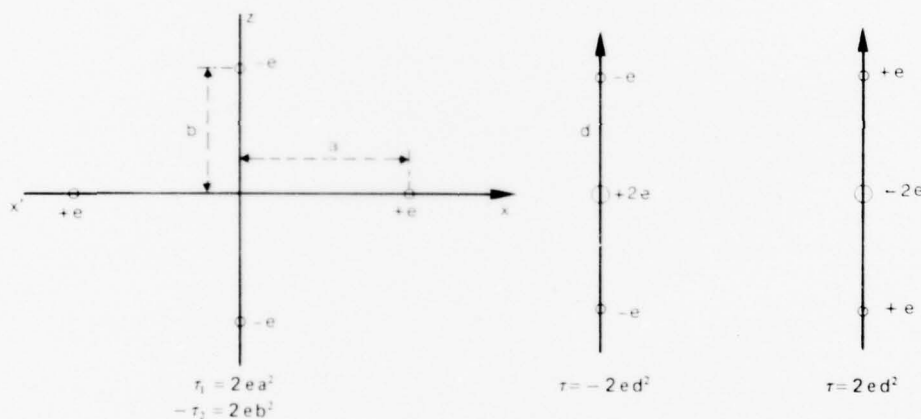
Thus, without changing the potential one can add or subtract a like quantity from each magnitude $\sum e_i x_i'^2$, $\sum e_i y_i'^2$, $\sum e_i z_i'^2$

Let us suppose that (22) $\sum e_i x_i'^2 > \sum e_i y_i'^2 > \sum e_i z_i'^2$, and hence the potential only depends on the two magnitudes

$$(23) \quad Q_1 = \sum e_i x_i'^2 - \sum e_i y_i'^2$$

$$(24) \quad Q_2 = \sum e_i y_i'^2 - \sum e_i z_i'^2$$

The potential may be attributed to a quadripole, i.e., to a system



Quadripole examples

containing 2 positive charges $+e$ with coordinates $\pm \sqrt{\frac{Q_1}{2e}}$, $0, 0$ and 2 negative charges $-e$ with coordinates $0, 0, \pm \sqrt{\frac{Q_2}{2e}}$. (e must be large enough so that the parallelogram thus formed has very small sides).

In practice, the quadric is very often a revolution. We can, therefore, define the effective quadrupolar moment Q carried by the axis of revolution. If $Q > 0$ the quadripole is made up of a $-2e$ charge surrounded by two positive charges $+e$ at the distance d : (25) $Q = 2ed^2$. If $Q < 0$, the sign of the charges will be changed. An atom (or an ion) in which all the electron layers are saturated or pseudosaturated does not have an effective quadrupolar moment.

A complex non-polar molecule, (or an atom) with unfilled electron layers, is equivalent to a quadripole. For a polar molecule such as the water molecule, it may be necessary to take the quadripole and dipole conditions into consideration.

The ρ^{-4} term of the development of V could lead to a definition of an octopole.

4.2. Polarizability of molecules

Let us consider a molecule under the effect of a local electric field E_m , which modifies the relative positions of the nuclei and the movement of the electrons; a result is the creation of a dipolar moment μ which comes in addition to the permanent moment μ_p , if the molecule is polar. In this case we say the molecule is polarized.

If we consider the harmonic condition of the macroscopic field \vec{E} and of the local field \vec{E}_m at a high frequency in the visible spectrum or near ultra-violet, the molecule is not deformed and only "electron polarizability" has an effect. We can define an ellipsoid for electron polarizability and a mean polarizability α_e such that $\vec{\mu}_e = \alpha_e \vec{E}_m$.

In like manner, we can define an ellipsoid for atomic polarizability when the frequency is low enough for it to be necessary to take the deformation of the molecule into account and to define, moreover, a polarizability α_a such that $\vec{\mu}_a = \alpha_a \vec{E}_m$.

4.3. Polarization

Let us suppose we have a static and uniform macroscopic electric field E , in which case the induced polarization in the sample of dielectric material, from equations (6) and (8), is

$$(26) \quad \vec{P} = \epsilon_0 (\epsilon_r - 1) \vec{E}$$

The vector \vec{P} represents the sum of the dipolar moments per unit volume, whether they be due to the orientation of the permanent dipoles associated with electron movement or due to molecular deformation

$$(27) \quad \vec{P} = \vec{P}_p + \vec{P}_a + \vec{P}_e$$

\vec{P}_p corresponds to the orientation of the permanent dipoles and which is disturbed by thermal agitation. \vec{P}_a and \vec{P}_e like α_a and α_e correspond to atomic and electronic polarizations and are due to intramolecular phenomena which are temperature - independent.

In the same way, we can write an expression for the mean dipolar moment $\vec{\mu}_1$, as

$$(28) \quad \vec{\mu}_1 = \vec{\mu}_p + \vec{\mu}_a + \vec{\mu}_e$$

If, lastly, there are $\frac{N_A}{V}$ molecules per unit volume, where N_A is Avogadro's number and V the molar volume, we have :

$$(29) \quad \vec{P} = \frac{N_A}{V} \vec{\mu}_1 = \vec{P}_p + \frac{N_A}{V} \alpha \vec{E}_m$$

Returning now to permanent dipoles, we note that their orientation decreases the thermodynamic degree of disorder. The potential energy of an elementary dipole, rotated through an angle θ , is :

$$(30) \quad U = - \mu_p \cdot E_m \cdot \cos \theta$$

The statistical equilibrium is governed in such a way that the molecules distribute themselves among the various energy levels U , proportionately to $\exp(-U/kT)$, where k is Boltzmann's constant and T the absolute temperature.

We may write :

$$(31) \quad e^{-\frac{U}{kT}} = 1 + \frac{\mu_p E_m}{kT} \cos \theta \quad (T \approx 300^\circ K)$$

Where there is no field, none of the directions is privileged and the number of molecules whose moment has an angle lying between θ and $\theta + d\theta$ with respect to a reference direction and is proportionate to the solid angle $2\pi \sin \theta d\theta$. Each of the molecules contributes $\mu_p \cos \theta$ to the dipolar moment and, thus, we find :

$$(32) \quad P_p = \frac{1}{2} \frac{N_A}{V} \mu_p \int_0^\pi \left[1 + \frac{\mu_p E_m}{kT} \cos \theta \right] \cos \theta \sin \theta d\theta$$

Whence, by integration, we have

$$(33) \quad \vec{P}_p = \frac{N_A}{3V} \frac{\mu_p^2 E_m}{kT}$$

Which formula, with (29) gives

$$(34) \quad \vec{P} = \frac{N_A}{V} \left(\alpha + \frac{\mu^2}{3kT} \right) \vec{E}_m$$

5. THE WATER MOLECULE (2)

In order to explain the known properties of water molecules, we are led to a presupposition regarding this molecule's structure. Basically, it comprises one oxygen atom and two of hydrogen. It still remains to detail the relative positions of the charges and masses which agree with the experimental data relating to the permanent electric moment, to the mechanical inertial moment revealed by infra-red absorption and by the Raman effect, and to anisotropy revealed by polarization of diffused light, etc...

Unfortunately, at the present state of our knowledge, several molecular configurations do, in fact, comply with the corpus of data available. However, all such configurations allow for a folded HOH model which is strongly polar.

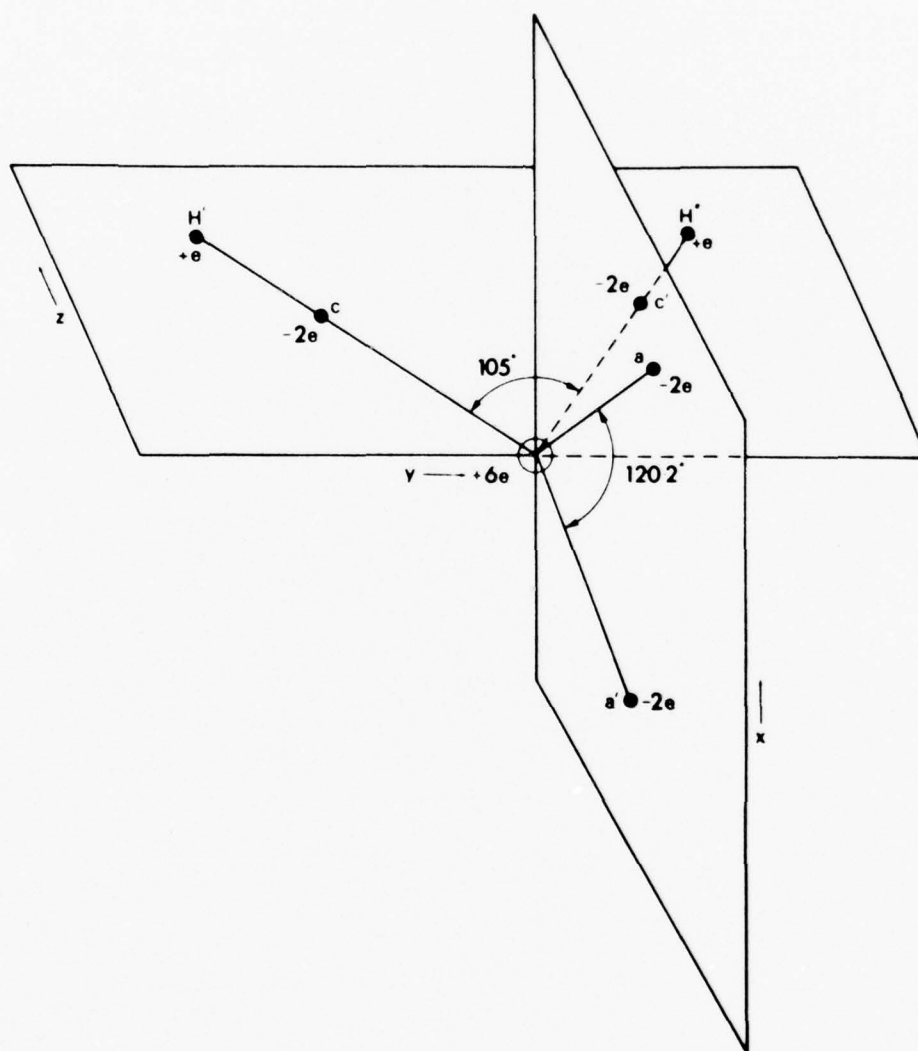


Fig. 1 : Water molecule model proposed by Pople (2)

5.1. The electrical properties of free water molecules

The permanent electric moment of the water molecule H_2O has been deduced from variations in electric permittivity for water vapour as a function of temperature, and from other experiments.

The most probable value is :

$$(35) \quad \mu = 1,83 D = 1,83 \times 10^{-18} \text{ ues cm.}$$

The symbol D stands for a debye. The value of a debye is 3.333×10^{-30} C.m.. The vector $\vec{\mu}$ is carried by the bisector of the angle H-O-H. Its alignment goes from the negative oxygen atom to the positive region between the hydrogen atoms. The length of the OH bonds is 0.96 Å and the value of the HOH bond angle is 104° . The relative values of the free molecule are not found in the liquid state. But one is, however, in a position to tentatively represent the permanent dipole by a wave function.

The quadrupolar moment Q is known by experimentation. Its value is :

$$(36) \quad Q = (-5,6 \pm 1,0) \times 10^{-26} \text{ ues cm}^2$$

The individual values Q_{xx} , Q_{yy} and Q_{zz} are not presently known by experimentation but they can be calculated from the wave functions.

The computed values for individual values of moment are :

$$Q_{xx} = -6,6 \times 10^{-26} \quad Q_{yy} = -5,2 \times 10^{-26} \quad Q_{zz} = -5,7 \times 10^{-26} \text{ ues cm}^2$$

These values relate to a molecule with its centre of gravity at the origin of the coordinates. The signs - indicate that the electron contributions to this moment are greater than nuclear counterpart contributions. The approximate equality of the individual moment values shows that the charge distribution is quasi-spherical.

The molecular polarizability α is known experimentally and its mean value is :

$$(37) \quad \bar{\alpha} = \frac{1}{3} (\alpha_{xx} + \alpha_{yy} + \alpha_{zz}) = 1,44 \times 10^{-24} \text{ cm}^3$$

The tensor components are not known but it would seem that the anisotropy of the polarizability is small.

Another electric constant of molecules that would warrant study and measurement is variation of the dipolar moment in the course of molecular vibration.

5.2. Water molecule configurations (Frank, H.S.) (4)

The molecule in the vapour state can be taken to be free. In the ice state, at low pressures, (forms I_h and I_c) each molecule is surrounded by 4 neighbouring molecules, arranged at the apexes of a regular tetrahedron, each 2.75 Å distant approximately and there are 12 second order molecules, each at 4.5 Å distance. At high pressures (forms II to VI) the tetrahedral configuration is somewhat deformed; the close neighbours are located from 2.75 to 2.9 Å from the reference molecule and the second order molecules are never less than 3.5 Å distant. In the densest form (VII) the configuration is that of a centre cube; the distance from the reference centre to an apex is 2.95 Å.

The interpretation of these discoveries, in terms of the hydrogen bond, is amply confirmed by neutron diffraction studies, by the infra-red Raman spectrum and by the acoustic and electric properties and residual entropy for the disorganized phases.

The importance of the hydrogen bonds linking each molecule to its neighbours has recently been confirmed by quantum mechanics computations and is brought out clearly; the bond angle between the protons is never greatly different from 109° .

Thus, water may be represented by an oxygen atom at the centre of a regular tetrahedron, with a hydrogen nucleus (proton, deuterion or tritium) at two apexes and two pairs of electrons in orbits oriented towards the other two apexes.

Considering the variety of configurations observed in the solid states, we can suppose that in the liquid state a much greater number of disorganized structures can assemble the molecules in tetrahedral configurations with somewhat greater degree of deformation. This does not imply that there is a significant abundance of aggregates that are sufficiently large and regular as to be identifiable. On the contrary, it would seem reasonable to think of there being a great number of irregular configurations which are compatible with the latent heat of fusion.

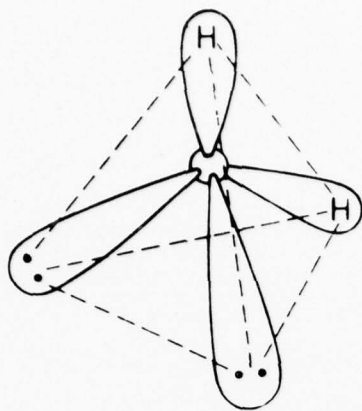


Fig. 2 : Geometric arrangement proposed for nuclei and electron charge distribution in a water molecule (4)

5.3. Isotopes (2)

Strictly speaking, water is a mixture of isotopic combinations ^1H , ^2H , ^3H and ^{16}O , ^{17}O , ^{18}O in the molecular, ionic H and ionic OH forms.

In natural water, the proportions are as follows :

$$\frac{^2\text{H}}{^1\text{H}} = \frac{1}{69\,000}, \quad \frac{^{17}\text{O}}{^{18}\text{O}} = \frac{1}{5}, \quad \frac{^{18}\text{O}}{^{16}\text{O}} = \frac{1}{500}$$

These proportions remain the same everywhere

$$\frac{^3\text{H}}{^1\text{H}} = \frac{1}{10^{18}} \quad \text{Tritium appears in rain and snow}$$

(The half-life is 12.5 years)

6. THE CLAUSIUS MOSSOTTI formula (5)

In order to follow through the theoretical computation on the permittivity in the results of § 4.3., it still remains to find an equation to define the local field E_m acting on the molecule from the applied field E , taking the other molecules, in the vicinity of the molecule under consideration, into account.

6.1. The static condition

Starting from a very simple model (a spherical cavity, on the inner wall of which the charges appear, is centred on the molecule under consideration) Mossotti and Lorentz elaborated the expression :

$$(38) \quad \vec{E}_m = \vec{E} + \frac{\vec{P}}{3\epsilon_0}$$

By eliminating \vec{P} , \vec{E} , and \vec{E}_m from (26), (34) and (38), we find :

$$(39) \quad \frac{\epsilon_r - 1}{\epsilon_r + 2} = \frac{N_A}{V} \frac{1}{3\epsilon_0} \left[\alpha + \frac{\mu_p^2}{3kT} \right]$$

In the absence of permanent dipolar moments, this formula comes down to the Clausius Mossotti formula

$$(40) \quad \frac{\epsilon_r - 1}{\epsilon_r + 2} = \frac{N_A}{V} \frac{\alpha}{3\epsilon_0}$$

6.2. The harmonic condition and the Debye equation

If we use a variable field E , i.e., a standing electromagnetic wave, the electric permittivity, given by Maxwell's equation $\epsilon_r = n^2$ (where n is the refractive index) depends on frequency. When the latter reaches 10^9 Hz, approximately, ϵ_r decreases strongly for substances with polar molecules, since the dipoles do not have the time to orient themselves in the field. ϵ_r varies very rapidly in those absorption bands where the intra-molecular vibrations reach a large amplitude, since they enter resonance with the e.m. wave. The absorption bands in the infra-red correspond to nuclei vibrating and, in the ultra-violet, to electrons vibrating.

At sufficiently low frequencies, i.e., lower than 10^{12} Hz in the case of water, the polarizability can be taken to be instantaneous whereas the dipolar orientation, which largely contributes to polarization, cannot.

Let us suppose, that at time $t = 0$, the electric field \vec{E} is sharply cancelled. Any one of the dipoles will move to take up a new position. Debye supposed that the angle of rotation β decreased from β_0 to zero in compliance with an exponential law, while the polarization \vec{P} follows the same time-dependent law.

$$(41) \quad \vec{P}_p(t) = \vec{P}_p(0) e^{-\frac{t}{\tau}}$$

where τ is a relaxation time

in the harmonic condition, equation (39) becomes :

$$(42) \quad \frac{\bar{\epsilon}_r - 1}{\bar{\epsilon}_r + 2} = \frac{N_A}{V \cdot 3 \epsilon_0} \left[\alpha - \frac{\mu_p}{3kT} \frac{1}{1 + j\omega\tau} \right]$$

Permittivity is therefore a complex function, with an imaginary part to account for the braking effect due to viscosity friction and corresponds to real conductivity.

We can write :

$$(43) \quad \bar{\epsilon}_r = \epsilon' - j\epsilon''$$

The real part ϵ' derives partly from polarizability on one hand and partly from dipolar orientation on the other hand.

$$\text{We may write (44) :} \quad \epsilon'' = \frac{\sigma''}{\omega \epsilon_0}$$

The total conductivity of the medium is the sum of the ionic conductivity σ' due to monopole movement, should there be any, and dipolar conductivity.

$$(45) \quad \sigma = \sigma' + \sigma''$$

To sum up, the specific characteristics of macroscopic polarization obtained in this way are the following :

- i) For a given field E , P is much greater for polar bodies than for non-polar bodies.
- ii) Polarization depends notably on temperature. It increases as temperature is decreased since the thermal agitation decreases.
- iii) The dielectric losses are much greater in polar bodies. During their oscillation, the elementary moments dissipate the energy they receive from the field by way of heat by shock.

6.3. From (42) we write :

$$(46) \quad \frac{\bar{\epsilon}_r - 1}{\bar{\epsilon}_r + 2} = U + \frac{V}{T(1 + j\omega\tau)}$$

$$\text{with (47)} \quad U = \frac{N_A}{V} \frac{\alpha}{3 \epsilon_0}$$

$$\text{and (48)} \quad V = \frac{N_A}{V} \frac{1}{3 \epsilon_0} \frac{\mu_p}{3k}$$

If the molecule is spherical, with radius a and turns in a fluid with viscosity η , from Stoke's law leads to the expression

$$(49) \quad \tau = \frac{\zeta}{2kT} = \frac{0,4 \pi a^3 \eta}{kT}$$

(η is measured in poise and a in meters)

At very low frequencies ($\omega \rightarrow 0$), $\bar{\epsilon}_r$ tends to a real number ϵ_S : the value for static permittivity.

At very high frequencies ($\omega \rightarrow \infty$), $\bar{\epsilon}_r$ also tends to a real number ϵ_∞ : the optical permittivity, which is the square of the refractive index, when the orientation of the permanent dipoles no longer contributes to the polarization and when the polarizability still remains.

$$(50) \quad \frac{\epsilon_S - 1}{\epsilon_S + 2} = U + \frac{V}{T}$$

$$(51) \quad \frac{\epsilon_\infty - 1}{\epsilon_\infty + 2} = U$$

It becomes (Debye's equations) :

$$(52) \quad \begin{aligned} & \left(\begin{aligned} \epsilon' &= \epsilon_\infty + \frac{\epsilon_S - \epsilon_\infty}{1 + x^2} \\ \epsilon'' &= \frac{(\epsilon_S - \epsilon_\infty) x}{1 + x^2} \end{aligned} \right. \end{aligned} \quad \text{or} \quad (53) \quad \epsilon_r = \epsilon_\infty + \frac{\epsilon_S - \epsilon_\infty}{1 + jx}$$

with (54)

$$x = \frac{\epsilon_S + 2}{\epsilon_\infty + 2} \omega \tau$$

$$\text{For } x = 1, \text{ we have (55)} \quad \epsilon' = \frac{\epsilon_S + \epsilon_\infty}{2}$$

$$\epsilon'' \text{ is maximum : (56)} \quad \epsilon''_{\max} = \frac{\epsilon_S - \epsilon_\infty}{2}$$

This situation is called the "point of transition".

The transition wavelength is (57) $\lambda_t = 2\pi c \tau \frac{\epsilon_S + 2}{\epsilon_\infty + 2}$, where c is the speed of light in a vacuum.

One can also write :

$$(58) \quad \epsilon' = \epsilon_\infty + \frac{\epsilon_S - \epsilon_\infty}{1 + \left(\frac{\lambda_t}{\lambda}\right)^2}$$

$$(59) \quad \epsilon'' = \frac{(\epsilon_S - \epsilon_\infty) \frac{\lambda_t}{\lambda}}{1 + \left(\frac{\lambda_t}{\lambda}\right)^2}$$

It is clear that from the formula (52), (53) and (54) one can compute the quantities ϵ' and ϵ'' at any frequency provided one knows ϵ_S , ϵ_∞ and τ or the transition angular frequency.

We shall apply these formula to water. It is first of all necessary to examine the effect of the ions and to know the ionic conductivity σ' since the total conductivity is given by (45) and (46).

7. THE IONIC COMPOSITION OF SEA-WATER (6)

As we mentioned earlier, the ionic conductivity of sea-waters is part of the physical and physico-chemical properties that set it apart from soft water.

These properties are attributable to approximately 11 chemical components which represent more than 99,9 % of the matter dissolved in the water and which are found to almost the same degree of concentration at all points in the ocean, whatever the locality, the temperature and the pressure, as long as one is sufficiently distant from river estuaries, submarine sources and floating ice-masses.

This matter is composed : (cf. table I)

Of the anions Cl^- , SO_4^{--} , HCO_3^- , Br^- and F^-

Of the cations Na^+ , Mg^{++} , Ca^{++} , K^+ and Sr^{++}

and non dissociated H_3BO_3

The dissociation of the salts is almost complete and, therefore, sea-water is a "strong electrolyte" like aqueous acid solutions or strong basic solutions. (There are, however, ionic associations in polyvalency).

On the basis of this ionic composition, it is not possible to say what the composition of the mixture of salts effectively dissolved is. However, if sea-water is dehydrated, we find a mixture of salts, the two main ones being : sodium chloride Na Cl and magnesium chloride Mg Cl_2 .

The total concentration of the salts is termed the "salinity". This is defined as being the weight, in grammes of inorganic matter dissolved in sea-water (after all the bromides and iodides have been replaced by an equivalent addition of chlorides and that the carbonates have been converted to oxides). The "total chloride concentration or chlorinity" can be defined and can be used to serve to characterise a typical composition.

Tableau I

Composition of sea-water. Concentration of constituents in
sea-water having a salinity of 19 o/oo
(from A. Richards)

	g/kg	(g/unit of chlorinity)
Chloride, Cl^-	18.890	0.99894
Sodium, Na^+	10.560	0.5556
Magnesium, Mg^{++}	1.273	0.06695
Sulfate, SO_4^{--}	2.649	0.1394
Calcium, Ca^{++}	0.4104	0.02106
Potassium, K^+	0.380	0.02000
Carbon (as HCO_3^- or CO_3^{--})	28.10^{-3}	0.00735
Bromide, Br^-	65.9×10^{-3}	0.00340
Strontium, Sr^{++}	8.1×10^{-3}	0.0004
Boron, as H_3BO_3	4.6×10^{-3}	0.00137
Silicon, as silicate	$0.01-4.5 \times 10^{-3}$	
Fluoride, F^-	1.4×10^{-3}	0.00007
Nitrogen, as NO_3^-	$0.01-0.80 \times 10^{-3}$	
Aluminium, Al^{+3}	0.5×10^{-3}	
Rubidium, Rb^+	0.2×10^{-3}	
Lithium, Li^+	0.1×10^{-3}	
Phosphorus, as PO_4^{-3}	$0.001-0.1 \times 10^{-3}$	

Trace Elements present in concentrations of 1 to 50 $\mu\text{g/kg}$: barium, iodine, arsenic, iron, manganese, copper, zinc, lead, selenium, caesium, uranium.

Trace elements present in concentrations of less than 1 $\mu\text{g/kg}$: molybdenum, thorium, cerium, silver, vanadium, lanthanum, yttrium, nickel, scandium, cobalt, cadmium, mercury, gold, tin, chromium, radium.

Salinity is a variable characteristic of a certain type of water. In the open ocean stretches, the values lie between 32 and 37 o/oo. In the Red Sea and the Persian Gulf, where the evaporation rate is very high, the values can be in excess of 40 o/oo. The general mean value is 35 o/oo. The mean chloride concentration level is 19 o/oo.

8. THE IONIC CONDUCTIVITY OF SOFT-WATER AND SEA-WATER (5)

8.1. The principle of current flow in the electrolyte (6)

Sea-water is an electrolyte. Its structure, like all electrolytes, is akin to that of a plasma. However, dissociation in an electrolyte only brings out the ions and excludes the electrons. These ions are heavy and slow. The lightest of them, the proton H^+ is still 1830 times more inert than the electron. It only has in common with the electron its single charge, but the absolute value is the same, the signs are opposite.

Each ion of the same type presents a mass m and carries a charge q , which is a positive or negative integer multiple of the electron's single $-e$ charge :

$$(60) \quad q = z e$$

z is called the "electrovalency"

The faraday is the electric charge carried by one mole of monovalent ions, such as Na^+ or Cl^- , for example.

$$(61) \quad F = N_A e = (96\,491,2 \pm 1,1) \text{ C/mole}$$

(The mole is the quantity of a body which contains N_A elementary entities, i.e., as many entities as there are atoms in 0.012 kg of carbon 12.)

If the ion is bi-, tri- or z -valent, the charge transported by a mole of ions is $z F$.

The solution being electrically neutral, the sum of the concentration levels of the positive ions is equal to the sum of the concentrations of the negative ions.

The "Molarity" of ion B is a term used to designate the quotient c_B of the number of moles of this ion and the volume of the mixture. Per unit of volume, there are therefore $N_A c_B$ ions of type B which carry the charge $N_A c_B z_B e$.

For a generally neutral mixture, $\sum c_B z_B = 0$ (The sum being extended to all types of ions).

The ions, which have about the same size as water molecules, participate in disorganized thermal agitation, the latter giving rise to no current on the macroscopic scale. But, if there is a statistically organized movement of the charges in the electrolyte there can be a current, the value of which is:

$$(62) \quad \vec{J} = N_A e \sum c_B z_B \vec{V}_B$$

In the presence of the electric field \vec{E} which penetrates the electrolyte, we can suppose that each ion undergoes the force $q_B \cdot \vec{E}$. (It is not necessary to have the polarization and the effective field intervene, since the relations between these vectors are linear). Moreover, each ion undergoes a viscous force or a frictional force mZV , where Z has the dimensions of a frequency and can be termed the collision frequency of the ion.

Moreover, the coefficient of friction mZ is given by Stokes' law

$$(63) \quad mZ = 6\pi\eta a$$

where η designates the coefficient of friction of water and a the radius of the ion.

In the final analysis, the equation of forces applied to ion B is (by cancelling the index B from the notations) :

$$(64) \quad m \frac{d\vec{V}}{dt} + mZ\vec{V} = q\vec{E}$$

In the continuous condition we can suppose that

$$(65) \quad \vec{V} = \frac{q}{mZ} \vec{E}$$

The quantity $u = \frac{q}{mZ}$ is called the "mobility" of the ion.

For this ion, we therefore have :

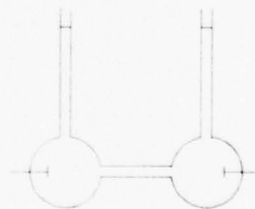
$$(66) \quad \vec{J} = N_A e c |z| u \vec{E}$$

or again : (67)

$$\vec{J} = \sigma' \vec{E}$$

where σ' is the "specific conductivity" due to the presence of the ion B .

This equation contains Ohm's Law.



The "equivalent concentration" C is the product of the molarity c and the absolute value of the electrovalency z

$$(68) \quad C = c |z|$$

For a dissolved salt, the concentration C is the product of (the number of moles per unit volume) and (the sum of the broken valency bonds). Thus, for NaCl

$$C = c \cdot 1$$

$$\text{Hence (69)} \quad \sigma' = N_A e C u$$

The "molar conductivity" Λ_m , can be defined by

$$(70) \quad \Lambda_m = \frac{\sigma'}{c} = N_A e |z| u$$

and the "equivalent conductivity" Λ by :

$$(71) \quad \Lambda = \frac{\sigma'}{C} = N_A e u$$

For a mixture of ions of a dissolved salt, we naturally have

$$(72) \quad \Lambda = N_A e \sum u$$

From (71) we deduce that for each salt, Λ should only be dependent on temperature and not on concentration. Thus, for a given fixed temperature, σ would be proportionate to C .

8.2. Measurement procedures and experimental results :

To measure the conductivity of any liquid electrolyte whatsoever, we can use a vase, as represented in Fig. 3, with a cylindrical section of cross-section s , where the electric field can be taken to be uniform and parallel to the cylinder generators.

The quantity of electricity which flows across unit surface MM' per second is :

$$(73) \quad i = \frac{1}{s} = \sigma' E$$

We can then implement the same measurement methods as for ordinary conductors. In order to avoid the electrodes being polarized, the measurements via the wheatstone bridge are made with alternating current. The electrolyte tube can be calibrated by measuring its resistance when filled with a liquid of known conductivity.

Experimentally, we note that the conductivity of the electrolytes increases with temperature. The relative variation is quite appreciable and is of the order of $1/40$ per degree Celsius. This relative increase is close to $1/\eta$ and is related to the relative decrease in the coefficient of internal friction for water (63).

We also note that the equivalent conductivity Λ decreases when the concentration C increases and insofar as C does not greatly exceed 10, the variation for strong electrolytes obeys KOHLRAUSCH (1900) :

$$(74) \quad \Lambda = \Lambda_0 - b \sqrt{C}$$

The two constants of this experimental law are specific for each salt. Λ_0 is a limit conductivity which characterizes an infinitely low value concentration.

Table II below sets out some of the numerical values in mho/m for equivalent conductivities multiplied by 10^3 for two aqueous solutions at 18°C , taken from H. FALKENHAGEN

Tableau II

C	$\ll 10^{-1}$	10^{-1}	$5 \cdot 10^{-1}$	1	5	10	50	100	500	1 000
NaCl	10.899	10.810	10.718	10.649	10.378	10.195	9.571	9.202	8.094	7.435
MgCl_2	11.088	10.943	10.768	10.635	10.130	9.814	8.848	8.342	6.987	6.145

The conductivity $\sigma' = \Lambda C$ is then seen to be only very roughly proportionate to the concentration value. We may note that for sea-water the overall equivalent concentration is close on 600.

8.3. The ionic concentration of pure water

Even when it is absolutely pure, double-distilled and degassed, water does still have a residual conductivity, which thus points to a very low degree of dissociation. The H^+ and OH^- ion concentration levels are such that we have at $18^\circ C$ and per m^3 :

$$(75) \quad C_1 = C_2 = 0,77 \cdot 10^{-4}$$

Since the pH value is defined by the equation $pH = -\log_{10} C_1/1000$, the pH value of pure water at $18^\circ C$ is approx. 7.1. (For sea-water, the pH value varies from 8.0 to 8.2 at the surface and diminishes to 7.7 in deeper waters, this indicating a slight degree of alkalinity).

$$\text{For a pH value of 7.1 we have} \quad \sigma' = 3,8 \times 10^{-6} \text{ mho/m}$$

$$\text{and for a pH value of 8, we have} \quad \sigma' = 1,1 \times 10^{-5} \text{ mho/m}$$

Fresh-water in lakes and rivers is not pure and has a conductivity of $(1 \text{ to } 5) \times 10^{-3}$ mho/meter. It is, however, a poor conductor.

8.4. The ionic conductivity of sea-water

The value found is the addition of that for pure water plus that for the dissolved salts, the latter being by far the major component.

The problem is in principle solved by application of formula (66). But, one needs to identify those mobilities which themselves vary with the concentration levels. Naturally, one can compute the sum of the mobilities (u_1 and u_2) of a pair of ions of a single dissolved salt by measuring the equivalent conductivity and, by other methods, also the ratio $u_1/(u_1 + u_2)$. One thus arrives at a value for the figures of mobilities themselves. The values found are small, and, for example, the mobility of the H^+ ion in water at $18^\circ C$ is 33×10^{-8} m/s and per Vm. The ions therefore move very slowly indeed.

One could likewise add the various conductivities of each salt present and presuppose that the salts come in a certain composition.

It is of interest to further detail the principle of current flow and to explain the fact that the equivalent conductivity Λ of a strong electrolyte decreases when the concentration level increases. From the theory of electrolyte anomalies by Debye and Hückel, it is found that the movement of a given ion, through the charged particles and not of the medium, is slowed down by the reverse movement of a cloud of ions, of opposite sign, which surround it. This special type of resistance is called "electrophoresis". In addition to this effect there is a second, alternating, one, and which stems from the delay of the ion cloud which is centred about the particular ion under consideration.

Thus, the conductivity Λ is modified. We end up with :

$$(76) \quad \Lambda = \Lambda_0 - (N_A q^2 \chi / 3\pi\eta) - (f' q^2 \Lambda_0 \chi / 12\pi\epsilon kT)$$

f' is a numerical factor, which depends on q_B/u_B of the salt(s) concerned, and $\chi = \left(\frac{2 N_A q^2}{\epsilon_r kT}\right)^{\frac{1}{2}}$; k is Boltzmann's constant and T the absolute temperature.

The formula above shows that the two correction terms are proportionate to χ and therefore to \sqrt{C} , this explaining Kohlrausch's experimental law.

$$(74) \quad \Lambda = \Lambda_0 - b \sqrt{C}$$

If we now calculate the correction terms for sodium chloride at the concentration level $C = 1$ (1 mole per m^3) at $17^\circ C$, taking $\eta = 1.09 \times 10^{-2}$ and $\frac{1}{\chi} = 9.66 \times 10^{-9}$ m, the first correction term has the value 0.155 mho/m and the second, the value 0.078 mho/m. Whence, finally, a computed equivalent conductivity of 10.666×10^{-3} whereas the measured equivalent conductivity is : 10.649×10^{-3} . The degree of agreement is therefore very good, given the errors inherent in the measurement.

Equation (75) is perfectly valid up to $C = 10$ and even beyond, as long as one adds correction terms in $\log C$ and $C \log C$.

In an alternating field, the limit equivalent conductivity Λ_0 and the first correction term are not affected ; but, the second correction term depends on the relaxation time and decreases as frequency increases because the ion cloud has not had the time to reach its asymmetric condition. Therefore, Λ slightly increases with frequency and for a sufficiently high frequency, only the electrophoresis correction remains in (22).

At the total equivalent concentration of sea-water $C \approx 620$ (moles/m³), the relaxation time for a salt of the NaCl type would, at 17°C, be

$$(77) \quad \tau = 1.08 \times 10^{-10} \text{ second}$$

But, under such conditions of concentration, and for frequencies higher than $1/\tau$, the variation in ionic conductivity is completely masked by dipolar conductivity.

Thus, to sum up, the events take place as if for radio frequencies the ionic conductivity of sea-water does not depend on frequency, but was dependent only on the factors : concentration, temperature. Bearing this in mind, we shall now return to the experimental results, such as those contained in table II.

Commonly the direct global method is used which generally replaces titration methods as carried out on oceanographic ships and in laboratories.

Empirical relations for temperature, salinity (total chloride content) and conductivity have been put forward by various authors.

Weyl (1964) combined these data in the following expression (2) :

$$(78) \quad \log \sigma' = -0.42373 + 0.892 \log Cl \text{ (o/oo)} \\ - 10^{-4} \tau \left[88.3 + 0.55 \tau + 0.0107 \tau^2 - Cl \text{ (o/oo)} \right. \\ \left. (0.145 - 0.002 \tau + 0.0002 \tau^2) \right]$$

σ' is the conductivity in mho/m

$\tau = 25 - t$, t is the Celsius temperature in °C. The equation is valid for all degrees of salinity from 17 to 20 o/oo (chlorinities) and for temperature between 0 and 25°C at a pressure of 1 atmosphere.

The values of σ' found for sea-water are of the order 3 to 5 mho/m.

9. LIQUID STATE WATER IN HARMONIC CONDITION (5)

9.1. Experimental measurement procedures

We can point out the importance and the utilization of the planar condenser and the voltmeter in a wheatstone bridge. It is clear that these experimental devices can be used in static conditions and at very low frequencies. On the other hand, at high frequencies, when, for example, the separation of the condenser plates is not very small compared with the wavelength in the medium being studied, the equipment is no longer utilisable under the same conditions.

We then use pair-lines (a Lecher line), coaxials or wave-guides, which are partly plunged in water or which are partly filled with water. We then observe, via a standing wave, the wavelength in the water and the coefficient of attenuation.

The Lecher line is a vertical pair-line (Fig. 4), excited in the air by a loop at the frequency f . An alternating voltage measurement instrument is placed in the air at D. The line is plunged into water. The e.m. energy travels downwards as a travelling wave which is partly reflected on the interface impedance discontinuity. Thus, if D is located vertically, we note the presence of standing waves. One can place D a little above the interface, at a voltage node. The travelling wave still goes through the surface and travels along the line in the water, and finally disappears if the line is long enough, whether it be open or closed at a short-circuit C. If the short-circuit point is brought near to the surface B, while the detector D remains at the same place we can plot the graph 2 (b), since the wave reflected at the short-circuit sets up a new standing wave, which is damped in the water. In this way, one can measure the wavelength on the line in water λ_2 and the attenuation $e^{-\beta z}$ on the line. One can deduce, from line theory, the wave impedance in water, this being directly related to the complex permittivity value.

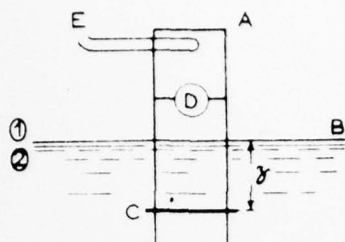


Fig. 4 (a) : Lecher line

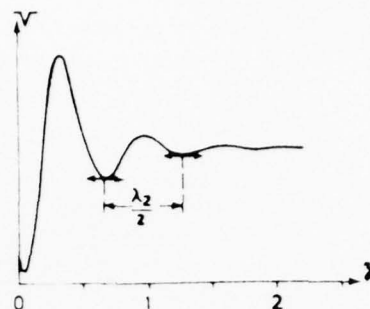


Fig. 4 (b) : Measurement

In the 10 centimeter wavelengths, resonating cavities can be utilized.

In a cavity, the fields present must comply with the wave equation

$$(79) \quad (\Delta + \bar{k}^2) \vec{U} = 0 \quad \text{with} \quad (80) \quad \bar{k}^2 = \mu_0 \epsilon_0 \bar{\epsilon}_r \omega^2$$

and also comply with the limit conditions which coincide with the cavity walls. If the cavity is completely filled with a liquid of conductivity nil and a real permittivity value ϵ_r , giving the propagation constant, the resonance frequency is divided by $\frac{1}{\sqrt{\epsilon_r}}$. In order to get back to the same resonance frequency as before the filling operation began, the dimensions of the cavity must be diminished by a factor $\frac{1}{\sqrt{\epsilon_r}}$. Moreover, if the liquid had a non-nil conductivity value, the overvoltage would decrease even further and the new overvoltage would have the approximate value :

$$(81) \quad \frac{1}{Q} = \frac{\sqrt{\epsilon_r}}{Q_0} + \frac{\epsilon''}{\epsilon'}$$

In practice, a cavity is chosen so as to have a strong overvoltage coefficient Q_0 . A sample of the water one wishes to observe is introduced into the cavity. We then measure a displacement of the resonance frequency of the cavity and a diminution of the overvoltage coefficient which thus enables a computation to be made for the real part and the imaginary part of the sample's complex permittivity value. The sample must be sufficiently small so that the two effects have no bearing, one on the other, and thus lead to independent measurements.

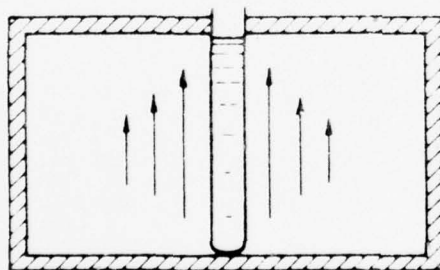


Fig. 5 : Resonant cylindrical cavity in the TM_{010} mode with an axial sample tube.

One can, for example, use the TM_{010} mode of a circular regular cylinder (Fig. 5). In this mode, the electric field has axial symmetry and is maximum along the centre-line of the axis of the cylinder. The cylindric symmetry can be maintained if the sample is inserted in a cylindrical tube centred on the cavity cylinder axis. The resonance frequency only depends on the diameters of the cavity and of the sample tube. It is independent of their respective heights, inasmuch as the height of the tube does not exceed that of the cavity walls.

At centimeter wavelengths, so-called optical methods are used, these consisting of measurement of the coefficient of reflexion at the surface of the liquid at normal or oblique incidence. Small dimension e.m. antennae or projectors are used. Both $R_{||}$ and R_{\perp} are measured. The appa-

ratus can be calibrated by replacing the water in the test-cavity by mercury. Absorption values can be measured separately by transmission through a "slice" of water of known thickness. The quantities measured are related to the main e.m. characteristics of the medium.

At submillimetric wavelengths (HASTED, J.B.) (2), we use a source radiating a continuum. The radiation is directed on to a Michelson interferometer with two beams. The sample of matter is placed within one arm of the interferometer. For heavily absorbing materials such as water, the mirror in one of the arms is replaced by a plane surface of the specimen. An extended interferogram is recorded, as a function of path difference. From this one can deduce the phase refractive index (real \bar{n}) and the attenuation index χ applicable over a wide frequency range, for the Fourier transform of the interferogram.

The interferometer developed by the British National Physics Laboratory is shown in Fig.6. Movement of mirror M increases the difference X of the optical paths from $-D$ to $+D$ and provides a slowly varying signal, the variable part of which forms the interferogram. If the mirror M is jittered with an amplitude $\lambda/8$, where λ is the mean wavelength detected, the signal variation resulting is recorded. The recording is termed the phase-modulated interferogram.

In the absence of the sample W, the reference interferogram $G_{O\phi}(x)$ is recorded. When the sample is introduced, an interferogram $G_{\phi}(x)$ is observed. This is the convolution product of the impulse response function of the sample $V(x)$ with the background interferogram :

$$(82) \quad G_{\phi}(x) = V(x) \star G_{O\phi}(x)$$

From the properties of Fourier transforms it follows

$$(83) \quad \bar{S}_{\phi}(\nu) = \bar{R}(\nu) \bar{S}_{O\phi}(\nu)$$

$$\text{where : } (84) \quad \bar{R}(\nu) = \left[\bar{n}_w + \bar{n}_L(\nu) \right] / \left[\bar{n}_w - \bar{n}_L(\nu) \right]$$

is the complex reflection factor of the sample.

$\bar{n}_L(\nu)$ is the refractive index of the liquid, \bar{n}_w the refractive index of the transparent window. $\bar{S}_{O\phi}(\nu)$ and $\bar{S}_{\phi}(\nu)$ are the computed complex power spectra evaluated, respectively with or without a sample present.

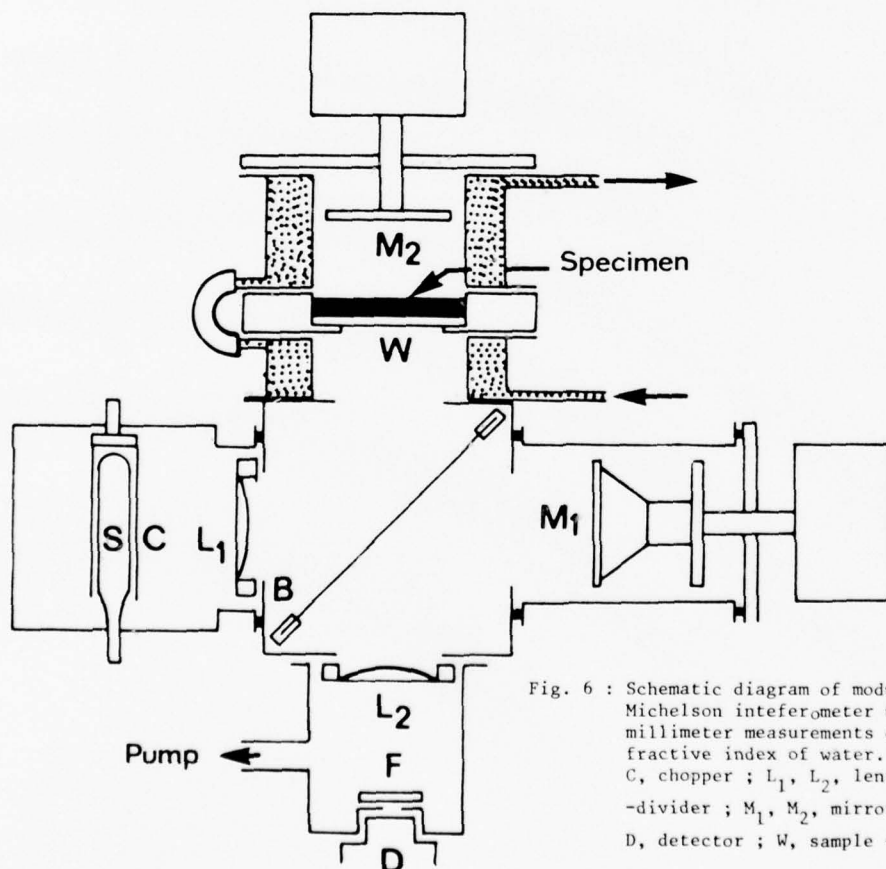


Fig. 6 : Schematic diagram of modular cube Michelson interferometer used for sub-millimeter measurements of complex refractive index of water. S, source ; C, chopper ; L_1 , L_2 , lenses ; B, beam-divider ; M_1 , M_2 , mirrors ; F, filter ; D, detector ; W, sample - holding window.

9.2. Using experimental results associated with the Debye equations (52)(53)(54) :

For pure water, there is good agreement between the experimental results (cf. Fig. 7a and b).

- the value ϵ_S is well-known (Saxton, Lane, Hasted, Ritson, and others ...)

The studies by Malmberg and Maryott (10) lead to formula (82), at atmospheric pressure :

$$(85) \quad \epsilon_S = 87.740 - 0.4008 t + 9.398 \times 10^{-4} t^2 - 1.410 \times 10^{-6} t^3$$

where t is the temperature in $^{\circ}\text{C}$ between 0 and 100° . The maximum error is ± 0.005

ONSAGER (9), KIRKWOOD (7), FROHLICH (8) and other authors have largely contributed to improving the initial theory, by consideration, in particular, of the effect of the dipolar moments of the neighbouring molecules on the molecule under consideration.

- the value ϵ_{∞} comes under closer scrutiny. The best estimation seems to be $\epsilon_{\infty} = 5.5$.

The transition wavelength is a function of temperature.

For example, we find

$t^{\circ}\text{C}$	0	20	40
λ_t (cm)	3,15	$1,75 \pm 0,05$	1,05

We may cite the results of Y. LEGRAND (5) calculated for pure water at a temperature of 17°C .

The experiment gives $\epsilon_S = 81.5$

by taking $\epsilon_{\infty} = 5.5$

$$\text{and } \lambda_t = 1,8 \text{ cm } (\tau = 0,841 \times 10^{-12} \text{ s})$$

thus yielding the results contained in table III.

For sea-water, unfortunately, we do not have sufficient experimental case-studies to draw on. Nonetheless, the results strongly favour the theory. We can take it that the attenuation index χ and the absorption coefficient β depend, above all, on the ionic conductivity values at frequencies below a few Gigahertz. We may note, for example, the results presented in Fig. 8 (a) and (b) (6). In Fig. 8 (a) we see that the results obtained for various concentration levels of NaCl agree exactly in their alignment on a straight line through the origin. In like manner, the results for sea-water also are aligned, but the straight line is a translation of the NaCl line. This displacement is certainly due to the presence of other ions. The fact that the straight line for sea-water samples does not go through the origin, leads us to concluding that there is a component in sea-water which cannot be represented by an equivalent chloride concentration and which is contributory to the dielectric properties of this type of water (15).

Nevertheless, the measurements do confirm that the dielectric properties of sea-water ϵ' and ϵ'' can be taken as deriving from a single characteristic : salinity.

Let us further cite, as an example the results of Y. LEGRAND for sea-water measured at 17°C as contained in table IV.

9.3. Liquid water at frequencies below 1 000 GHz.

Pure water (Fig. 9) :

For all frequencies below 1 GHz, ϵ' only depends on temperature (at 17°C , $\epsilon' = 81.5$)

When the frequency increases from 1 to 1 000 GHz, ϵ' decreases and tends to 5.5. Absorption increases and goes through a maximum around 17 GHz before decreasing.

Sea-water (Fig. 10) :

For all frequencies below 1 GHz, ϵ' only depends on temperature and has almost the same value as for pure water (at 17°C , $\epsilon' = 80.5$) and ϵ'' only varies slightly.

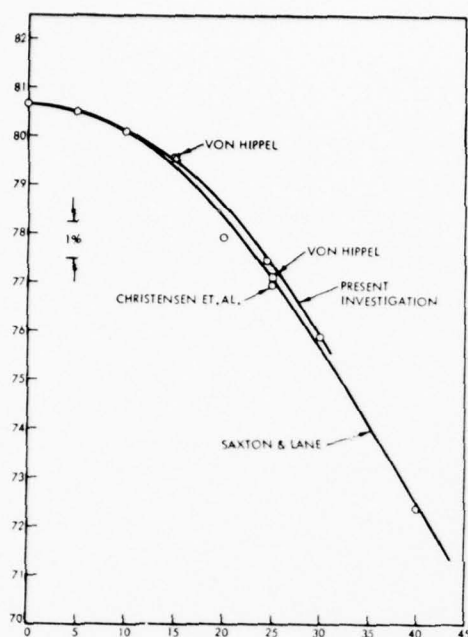


Fig. 7 (a) : ϵ' for pure water as a function of temperature at 2.653 GHz. (NASA - CR 1960) (15)

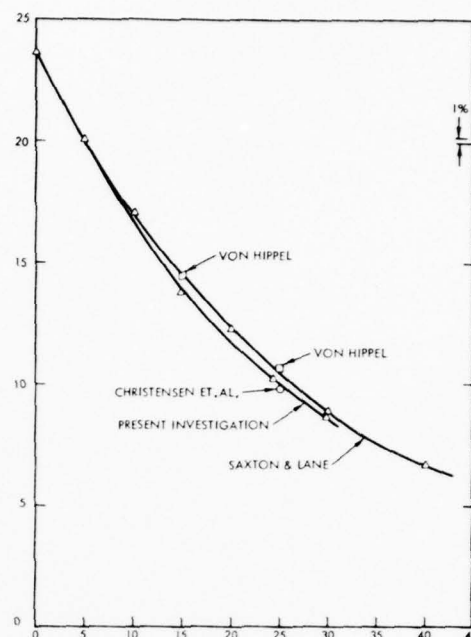


Fig. 7 (b) : ϵ'' for pure water as a function of temperature at 2.653 GHz. (NASA - CR 1960) (15)

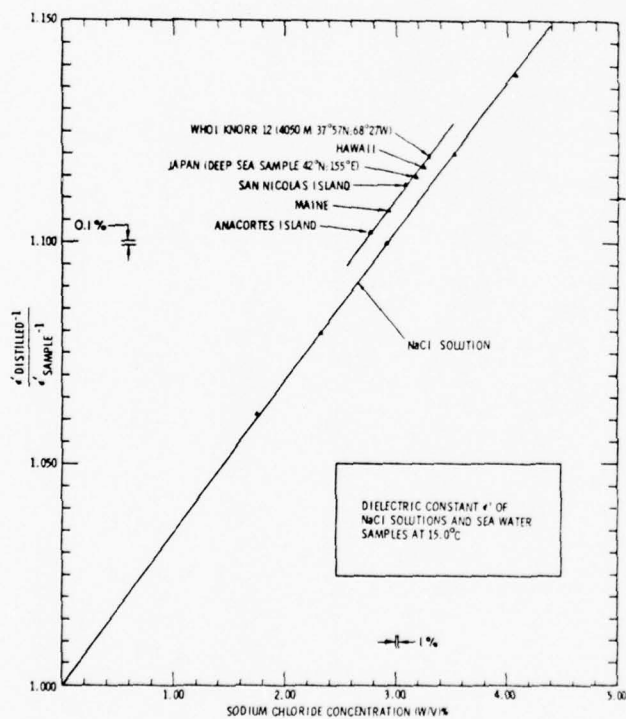


Fig. 8 (a) : Values of $\epsilon' - 1$ relative to the value $\epsilon' - 1$ for pure water as a function of the degree of salinity at 15°C for sodium chloride solutions and for sea-water samples, at 2.653 GHz. (NASA - CR 1960) (15)

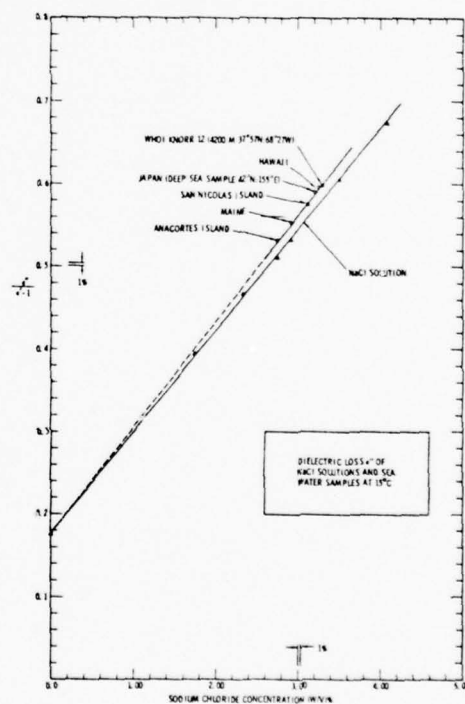


Fig. 8 (b) : $\epsilon''/(\epsilon' - 1)$ for NaCl solutions and for sea-water samples, at 15°C, at 2.635 GHz. (NASA - CR 1960) (15)

TABLE III

FREQUENCY f (Hz)	WAVELENGTH λ	PERMITTIVITY		DIPOLAR CONDUCTIVITY σ'' (mho/m)
		ϵ'	ϵ''	
0	∞	81,5	0	0
10^7	30 m	81,5	0,0	$0,25 \cdot 10^{-4}$
$2 \cdot 10^7$	15	81,5	0,1	$1,01 \cdot 10^{-4}$
$5 \cdot 10^7$	6	81,5	0,2	$0,60 \cdot 10^{-3}$
10^8	3	81,5	0,5	$0,25 \cdot 10^{-2}$
$2 \cdot 10^8$	1,5	81,5	0,9	$1,01 \cdot 10^{-2}$
$5 \cdot 10^8$	0,6	81,4	2,3	$6,33 \cdot 10^{-2}$
10^9	30 cm	81,2	4,5	$2,51 \cdot 10^{-1}$
$2 \cdot 10^9$	15	80,4	9,0	$9,96 \cdot 10^{-1}$
$5 \cdot 10^9$	6	75,2	20,9	5,75
10^{10}	3	61,4	33,5	18,5
$1,7 \cdot 10^{10}$	1,8 (λ_t)	43,5	38,0	34,8
$5 \cdot 10^{10}$	0,6	13,1	22,8	62,7
10^{11}	3 mm	7,6	12,3	67,6
$2 \cdot 10^{11}$	1,5	6,0	6,2	68,6
$5 \cdot 10^{11}$	0,6	5,6	2,5	69,6
10^{12}	0,3	5,5	1,3	69,6
∞	0	(5,5)	0	(69,6)

Permittivity and dipolar conductivity of pure water at 17°C as a function of frequency (5)

TABLE IV

FREQUENCY f (Hz)	WAVELENGTH λ	PERMITTIVITY		DIPOLAR CONDUCTIVITY (mho/m)		
		ϵ'	ϵ''	ionic σ'	dipolar σ''	total σ
0	∞	80,5	∞	4,54	0	4,54
10^8	3 m	80,5	818	4,54	0,00	4,54
$2 \cdot 10^8$	1,5	80,5	410	4,54	0,01	4,55
$5 \cdot 10^8$	0,6	80,4	166	4,54	0,07	4,61
10^9	30 cm	80,3	86,6	4,55	0,26	4,81
$2 \cdot 10^9$	15	79,3	50,1	4,56	1,01	5,57
$5 \cdot 10^9$	6	73,5	37,6	4,64	5,81	10,45
10^{10}	3	59,5	42,2	4,75	18,69	23,44
$1,7 \cdot 10^{10}$	1,5	42,1	43,3	4,84	35,26	40,10
$5 \cdot 10^{10}$	0,6	12,6	24,6	5,00	63,32	68,32
10^{11}	3 mm	7,3	13,2	5,08	68,35	73,43
$2 \cdot 10^{11}$	1,5	5,8	6,7	5,13	69,30	74,43
$5 \cdot 10^{11}$	0,6	5,4	2,7	5,19	70,34	75,53
10^{12}	0,3	5,3	1,4	5,22	70,34	75,55
∞	0	(5,3)	0	(5,29)	(70,36)	(75,65)

Permittivity and dipolar conductivity of sea-water at 17°C as a function of frequency (5)

(ϵ'' designates the imaginary part of $\bar{\epsilon}_r$)

N.B. - The European multiplier point (.) reads (x) and the decimal (,) reads (.)

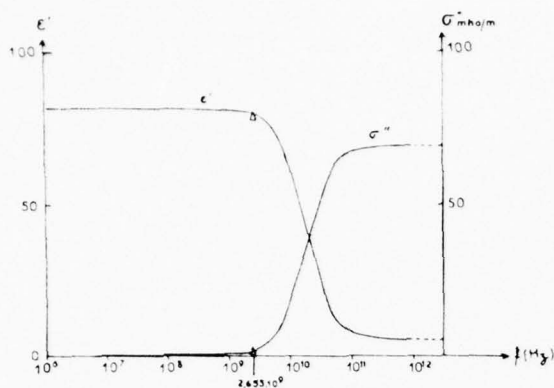


Fig. 9 :

Real permittivity ϵ' and dipolar conductivity of pure water σ'' at 17°C as a function of frequency. (Cf. table III. The points plotted at 2.653 GHz are deduced from NASA observations (6)).

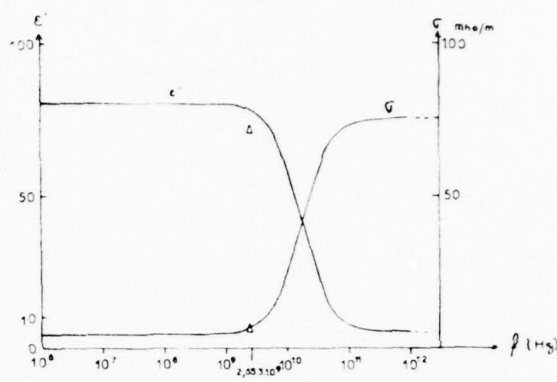


Fig. 10 :

Real permittivity ϵ' and conductivity of sea-water σ at 17°C as a function of frequency. (Cf. table IV. The points at 2.653 GHz are taken from a NASA plot. We note the discrepancy between the theoretical value ϵ' and the observed value. There is a substance in sea-waters which is not sodium chloride and which modifies the real permittivity value.).

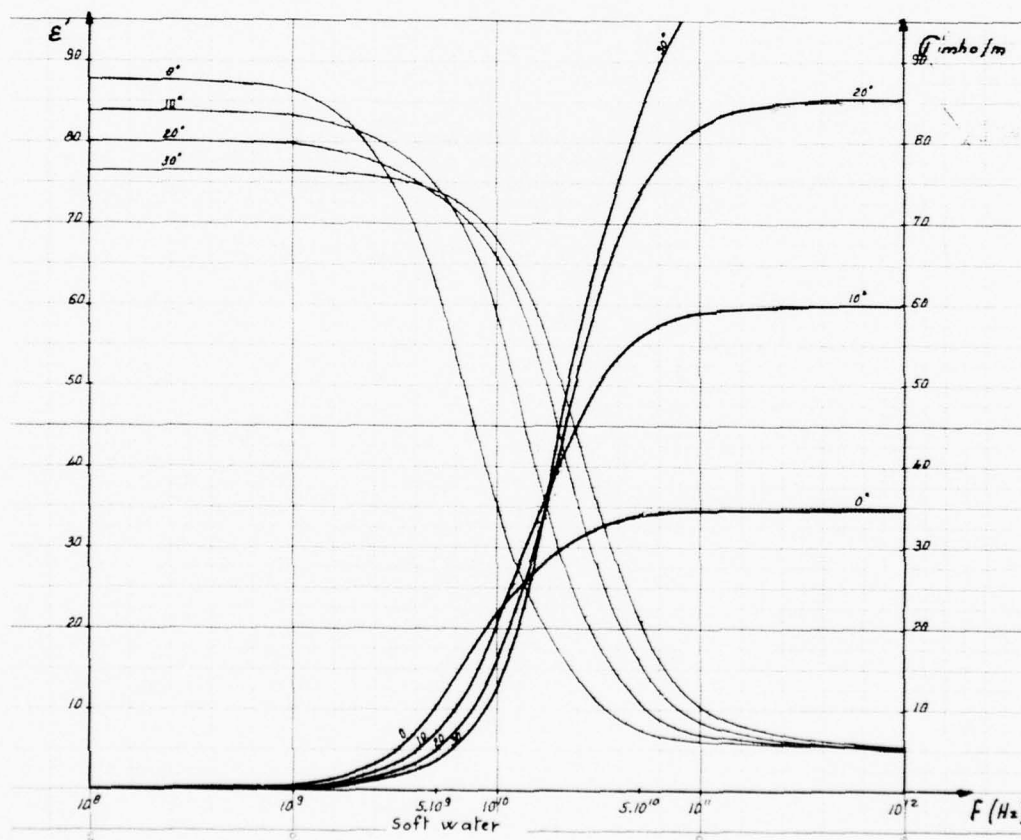


Fig. 11 :

Real permittivity ϵ' and dipolar conductivity of pure water σ'' between 10^8 and 10^{12} Hz , computed using Debye's equation (53) for ϵ_S given by equation (85), $\epsilon_\infty = 5.5$ and τ equal to 1.96×10^{-12} at 0°C ; 1.13×10^{-12} at 10°C ; 0.79×10^{-12} at 20°C and 0.63×10^{-12} at 30°C .

When the frequency rises from 1 to 1 000 GHz, ϵ' and ϵ'' show approximately the same variation as for pure water. The total conductivity σ increases. The dipolar conductivity σ'' exceeds the value for ionic conductivity as soon as the frequency is greater than 4 GHz.

9.4. Liquid water at frequencies greater than 1 000 GHz (Fig. 12).

The Debye equations with a single relaxation time prove inadequate. Their application supposes one takes a certain spread of the relaxation time into account.

K. COLE and R. COLE (13) put forward a general version for Debye's equation, by writing :

$$(86) \quad \epsilon_r = \epsilon_\infty + \frac{\epsilon_s - \epsilon_\infty}{1 + (j\omega\tau_0)^{1-\alpha}} \quad \text{avec} \quad (87) \quad \tau_0 = \frac{\epsilon_s + 2}{\epsilon_\infty + 2} \tau$$

where α is an empirical parameter the value of which lies between 0 and 1. Generally the value taken is $\alpha \approx 0.02$ (14).

The results are then measurably improved and approach the experimental results at 313 and 152 μm .

λ (μm)	ϵ'	ϵ''
313	4.0	2.33
152	3.95	1.57
117	4.09	1.43
109	4.02	1.24
92	3.80	1.35
63	2.74	1.84
52	2.57	1.57

Table V

Complex electric permittivity of pure water at 20°C, with real and imaginary parts at submillimetric wavelengths, the values being taken from various sources (11)

SAXTON (12), in order to the better describe the variations of ϵ' and ϵ'' at submillimeter wavelengths based his findings on FRÖHLICH'S theory, as regards absorption resonance values. In effect, the question arises as to whether it is preferable to consider one or several relaxation times for the molecule or whether to consider that the absorption process results rather from resonance.

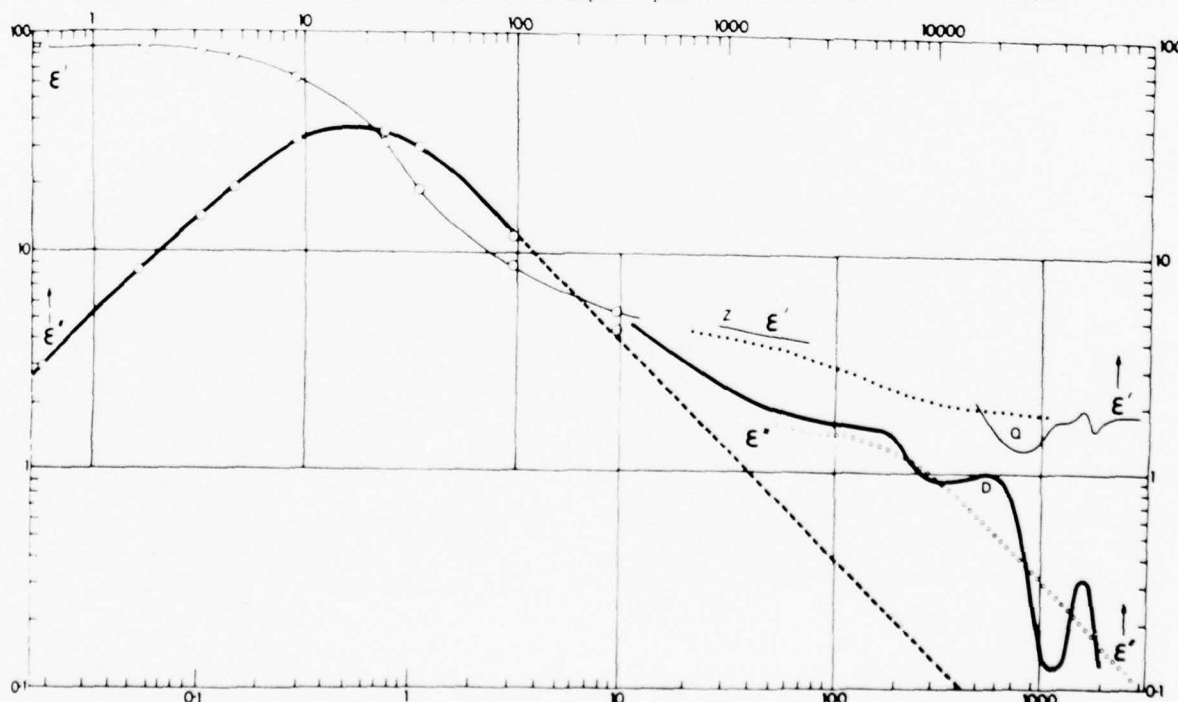


Fig. 12 : Logarithmic diagram for ϵ' (thin line) and for ϵ'' (thick line) for pure water at 20°C as a function of the frequency ν .

The dotted line shows the value of ϵ'' calculated using the Debye formula with a single relaxation time. The small circles show the values of ϵ' and ϵ'' calculated with a second relaxation time : $\lambda_r = 0.008$ cm.

Z, Q, D present the experimental results ; Z and Q for ϵ' and D for ϵ'' (HASTED, J.B.) (2).

At frequencies above 1 000 GHz, the ionic conductivity is also affected by the mechanical inertia and tends to disappear.

Ion movement can, in effect, be represented by the equation :

$$(64) \quad m \frac{d\vec{V}}{dt} + mZ\vec{V} = q \vec{E}$$

In the harmonic condition $\vec{E} = \vec{E}_0 e^{j\omega t}$ and $\vec{V} = \vec{V}_0 e^{j\omega t}$

Equation (65) is not applicable at high frequencies

$$\text{But } \vec{V}_0 = q \vec{E}_0 m (Z + j\omega) = u \vec{E}_0 (1 + j\omega\tau)$$

with the relaxation time $\tau = \frac{1}{Z} = \frac{qm}{u}$

For each ion, this time can be calculated. For Na, for example, the value found is 1.1×10^{-13} second. The transition wavelength is 0.2 mm. The last entries of table IV are therefore under the influence of ion inertia.

0. THE ELECTRIC CHARACTERISTICS OF ICE (2)

The mechanisms by which molecules, atoms and ions can move, in or through ice, give scientists difficult problems to solve. Despite the progress in modern experimental techniques and the results obtained, it is still most difficult to interpret and understand aspects of molecular movement and the relaxation phenomenon observed.

10.1. Ice at frequencies below 1 GHz

The ionic conductivity of soft-water ice is low. Measurement is difficult. Among the values recently measured at -10°C .

$$\sigma' = (1.1 \pm 0.5) \times 10^{-8} \text{ mho/m}$$

The measurements of ϵ'_S and $\epsilon(\omega)$, at different frequencies, provides data concerning dipole orientation in the net and hence concerning relaxation time τ .

The measurements of ϵ_S from 60 to 0°C show that ϵ_S increases as temperature decreases and that ϵ_S , measured perpendicular to the c -axis of the crystal, is 10 % smaller than ϵ_S measured parallel to the same c -axis.

At 0°C , ϵ_S for polycrystalline ice is 10 % higher than for liquid water.

DAVIDSON and WALLEY found that the value of ϵ_S increases with pressure rise for all varieties of polymorphous ice, except phase II and phase VIII in the table below.

Values for ϵ_S , ϵ_∞ and τ are set out in table VI. We note that dipolar mobility is maintained at high pressures.

Table VI - Dielectric characteristics of ice (FRANKS, F.) (2).

Ice (phase)	Temperature ($^\circ\text{C}$)	Pressure (k bar)	ϵ_S	ϵ_∞	τ ($\mu\text{s.}$)
I	- 23.4	6×10^{-6}	97.5	3.1	168
	- 23.4	1.6	101	-	213
	- 30	6×10^{-6}	99	3.2	-
II	- 30	2.3	3.66	3.66	-
III	- 30	2.3	117	4.1	2.75
	- 100	2.3	-	3.96	-
V	- 30	5	144	4.6	7.2
VI	- 30	8	193	5.1	≈ 6
	22	21	-	-	48
VII	22	21.4	-	-	0.25
IX	- 100	2.3	3.74	3.74	-

We may recall that temperature and pressure conditions at the Earth's surface, or in the immediate vicinity, are such that only phase I ice is present. The other phases II, III, etc., are the result of high pressure technology in laboratories.

Table VI give documentary data on the dielectric properties of these ices.

We can note that ice-types II and IX have low values of ϵ_S and also that the values of ϵ_∞ are equal to those of ϵ_S ; this means that the molecular dipoles are frozen or blocked and cannot be oriented under the influence of an external electric field. Such ices are consequently transparent to a large extent to e.m. waves. ϵ' is identically nil and only ionic conductivity σ' has any bearing.

For ice I, which is practically the only one of interest, it is possible to apply the Debye equations and to compute the values for ϵ' and ϵ'' in a wide frequency band, up to approximately 1 GHz.

However, the equations with one or several relaxation times do not enable satisfactory descriptions to be given for experimental data measured at 10^{10} Hz (i.e., at a 3 cm wavelength)

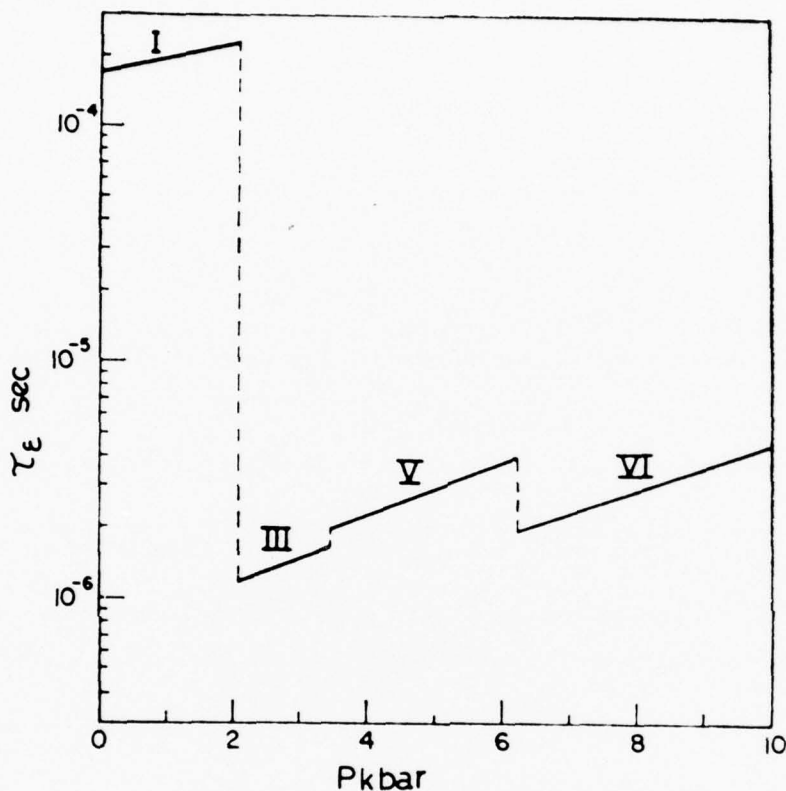


Fig. 13 : Relaxation time at -23.4°C for ice-types I, II, V and VI as a function of pressure. Note the similitude in the behaviours of types III, V and VI, due most probably to their similar structures (FRANKS, F.) (2).

By applying KIRKWOOD'S theory, although strictly speaking it should not be applicable to a medium such as ice, and by taking three layers of neighbouring molecules into account (in total 84), we reach the following values $\mu = 2.6$ D for ice in phase I (KIRKWOOD'S correlation factor $g = 3$).

10.2. Ice and snow at 10 GHz.

Very few measurements have been made for frequencies in excess of 10^{10} Hz. Table VII and VIII give the values for the index of refraction at 3.2 cm for ice and snow.

Table VII - Values for the real part $R_e(n)$ and for the imaginary part $I_m(n) = \chi$ of the complex refractive index of ice at various densities ρ for various temperatures $t^\circ\text{C}$, measured at wavelength $\lambda = 3.2 \text{ cm}$ (17).

ρ (g/cm ³)	$R_e(n)$	$\chi \cdot 10^4 \text{ to } t^\circ\text{C}$									
		0	- 2	- 4	- 6	- 8	- 10	- 12	- 14	- 16	- 18
0.916	1.78	23.0	16.0	12.0	10.5	8.9	7.7	7.1	6.6	6.3	6.1
0.76	1.65	14.8	10.7	8.7	7.4	6.4	5.8	5.4	4.9	4.7	4.4
0.60	1.50	10.3	7.5	6.0	5.2	4.5	4.3	3.9	3.7	3.3	3.0
0.46	1.38	6.9	4.8	4.1	3.4	3.1	2.8	2.6	2.5	2.5	2.5
0.38	1.31	5.2	3.9	3.3	2.6	2.4	2.3	2.2	2.1	2.0	1.8
0.34	1.27	5.0	3.7	3.0	2.3	2.0	1.9	1.8	1.6	1.4	1.3

Note = $R_e(n)$ does not depend on temperature. In effect, at these high frequencies

$$\epsilon' = R_{e2}^2(n) + \chi^2 \text{ is very close to } \epsilon_\infty, \text{ which does not depend on temperature.}$$

We note, finally χ is small compared with $R_e^2(n)$.

Table VIII - Values for the real part $R_e(n)$ and the imaginary part $I_m(n) = \chi$ for wet snow at 0°C , as a function of the weight per unit volume, on one hand and of the percentage water p (in weight), on the other hand, measured at the wavelength $\lambda = 3.2 \text{ cm}$ (17)

ρ (g/cm ³)	$R_e(n)$	$\chi \cdot 10^4 \text{ at } p \%$								
		0	0.2	0.4	0.6	0.8	1.0	1.2	1.4	1.6
0.38	1.31	5.2	13.7	26.2	38.0	54.4	73.4	89.7	112.0	134.0
0.76	1.65	14.8	33.8	55.3	90.1	131.3	179.0	242.0	304.0	371.0

It appears that ice and a layer of snow of the same density have essentially the same value of dielectric constant.

R E F E R E N C E S

-
- 1 STRATTON, J.A. Théorie de l'électromagnétisme
 (traduit par HEBENSTREIT J.) - Dunod - Paris 1961
 - 2 FRANKS, F. Water a comprehensive treatise
 Volume 1 - The physics and physical chemistry of water
 Plenum Press - New York, London 1972
 - 3 GUINIER, G. Eléments de physique moderne théorique
 Bordas - Paris 1950
 - 4 LUCK, W.A.P. Structure of water and aqueous solutions
 Proc. of the international symposium held at Marburg
 in July 1973
 Verlag chemie, Physic verlag
 - 5 HALLEY, P.M. Introduction à l'électromagnétisme des mers
 AGARD Lecture Series N° 61
 OPTICS OF THE SEA
 - 6 RICHARDS, F.A. Chemical and biological factors in the marine environment
 Chap. 8 of OCEAN ENGINEERING - Bratz, editor - Wiley
 - 7 DARMOIS, E. Electrochimie theorique
 DARMOIS, G. Masson, Paris 1960
 - 8 KIRKWOOD, J.G. J. Chem. Phys. 4,592 (1936)
 - 9 FRÖHLICH, H. "Theory of dielectrics"
 Oxford university press (1949)
 - 10 ONSAGER, L. J. Am. Chem. Soc. 58, 1486 (1936)
 - 11 MALMBERG, C.G. J. Res. Natl. Bur. Std. 56,1 (1956)
 - MARYOTT, A.A.
 - 12 MAGAT, M.M. On the dielectric dispersion of liquid water
 J. Chimie physique, Physico-chimie biologique
 Vol. 45, N° 4 (1948)
 - 13 SAXTON, J.A. Dielectric Dispersion in pure polar liquids at very
 high radio frequencies
 II Proc. Roy. Soc., Ser. A, Vol. 213 N° 1115 (1952)
 - 14 COLE, K. Dispersion and absorption in dielectrics
 COLE, R. J. Chem. Phys. Vol. 9, N° 4 (1941)
 - 15 HASTED, J.B. Dielectric properties of water
 Progress in dielectrics, Vol. 3 (1961)
 - 16 HIDY, GM Development of a satellite microwave radiometer to sense
 HALL, W.F. the surface of the world oceans
 and others NASA Report CR - 1960 (1972)
 - 17 CUMMING, W.A. The dielectric properties of ice and snow at 3,2 cm
 J. Appl. Phys., Vol 23 N° 7 (1952)
 - 18 EVANS, S. Dielectric properties of ice and snow. A review
 J. Glaciol. Vol. 42 p. 773 - 792 (1965)

Les propriétés électromagnétiques de l'eau
aux fréquences inférieures à 1 000 GHz, sous les
diverses formes rencontrées à la surface de la terre

par

P.M. HALLEY

Centre National d'Etudes des Télécommunications
38-40, rue du Général Leclerc - 92131 Issy-les-Moulineaux

Plan de l'exposé

1. Les trois caractéristiques e.m. fondamentales des milieux physiques
2. L'échelonnement des valeurs de la conductivité et le rôle majeur de l'eau sur ces valeurs à la surface de la terre
3. La répartition de l'eau à la surface de la terre
4. Les moments électriques et la polarisabilité des molécules
 - 4.1. Le potentiel d'une distribution de charges
 - 4.2. La polarisation
5. La molécule d'eau
 - 5.1. Les propriétés électriques de la molécule d'eau libre
 - 5.2. Les arrangements de molécules d'eau
 - 5.3. Les isotopes
6. La formule de Clausius Mossotti
 - 6.1. Le régime statique
 - 6.2. Le régime harmonique et l'équation de Debye
7. La composition ionique de l'eau de mer
8. La conductivité ionique de l'eau douce et de l'eau de mer :
 - 8.1. Le mécanisme de passage du courant dans l'électrolyte
 - 8.2. Méthodes de mesure et résultats expérimentaux
 - 8.3. La conductivité de l'eau pure
 - 8.4. La conductivité de l'eau de mer
9. L'eau liquide en régime harmonique :
 - 9.1. Les méthodes expérimentales de mesure des caractéristiques e.m. de l'eau
 - 9.2. L'exploitation des résultats expérimentaux associés aux équations de Debye
 - 9.3. L'eau aux fréquences inférieures à 1 000 GHz
 - 9.4. L'eau aux fréquences supérieures à 1 000 GHz
10. Les caractéristiques diélectriques de la glace :
 - 10.1. La glace aux fréquences inférieures à 1 GHz
 - 10.2. La glace et la neige à 10 GHz

Quelques notations

α	Polarisabilité moléculaire
σ	Conductivité mho/m
σ'	Conductivité ionique
σ''	Conductivité dipolaire
ϵ	Permittivité (constante diélectrique)
ϵ_0	Permittivité de l'espace libre
ϵ_r	Permittivité relative $\epsilon_r = \epsilon/\epsilon_0$
$\bar{\epsilon}_r$	Permittivité relative complexe

$$\bar{\epsilon}_r = \epsilon_r - j \frac{\sigma}{\omega \epsilon_0}$$

$$\bar{\epsilon}_r = \epsilon' - j \epsilon'' - j \frac{\sigma'}{\omega \epsilon_0} \equiv \epsilon' - j \frac{\sigma' + \sigma''}{\omega \epsilon_0}$$

ϵ'	Partie réelle de $\bar{\epsilon}_r$
ϵ''	Partie imaginaire de $\bar{\epsilon}_r$ due à la polarisation
ϵ'_S	$\epsilon'(0)$ partie réelle de $\bar{\epsilon}_r$ en régime statique
ϵ'_∞	$\epsilon'(\infty)$ partie réelle théorique de $\bar{\epsilon}_r$ pour une fréquence infiniment grande
μ_0	Perméabilité magnétique de l'espace libre

$$\mu_0 = 4\pi \cdot 10^{-7} \text{ (H m}^{-1}\text{)}$$

μ	Perméabilité magnétique et moment électrique dipolaire
β	Coefficient d'absorption $A = A_0 e^{-\beta z}$
n	Indice de réfraction
\vec{P}	Polarisation électrique
T	Température absolue ($^{\circ}\text{K}$)
t	Température Celsius ou temps
ω	Pulsation de travail
τ	Temps de relaxation

Les propriétés électromagnétiques de l'eau
aux fréquences inférieures à 1 000 GHz, sous les
diverses formes rencontrées à la surface de la terre

par

P. Halley

Sommaire

L'eau est la matière la plus répandue à la surface de la terre où elle est presque omni-présente.

En régime statique, on connaît très bien les propriétés diélectriques de l'eau et la conductivité des électrolytes aqueux, tels que l'eau des mers. Des théories récentes sont en cours de développement (Kirkwood - Fröhlich).

En régime harmonique, l'application d'une théorie relativement simple (Debye, Onsager) fournit des résultats convenablement satisfaisants.

Ces théories sont étroitement liées à un modèle de molécule d'eau coudée et fortement polaire et aux actions mutuelles entre molécules.

Le corps naturel le plus étendu et le plus homogène à la surface de la terre est l'Océan. Ses caractéristiques sont convenablement connues jusqu'à 10^{12} Hz. Son opacité aux ondes e.m. est très grande.

Les calottes glaciaires sont moins homogènes, leurs caractéristiques sont moins bien connues et jusqu'à 10^{11} Hz seulement. La glace aux basses températures est moins opaque aux ondes e.m. que l'Océan.

1. - LES TROIS CARACTERISTIQUES e.m. FONDAMENTALES DES MILIEUX PHYSIQUES (1) :

La plupart des problèmes d'électromagnétisme macroscopique où l'on ne considère pas d'effets non-linéaires, peuvent être résolus en admettant qu'au voisinage du point considéré certaines relations linéaires entre les vecteurs du champ sont acceptables. Ce sont :

$$(1) \quad \vec{D} = \epsilon \vec{E}$$

$$(2) \quad \vec{H} = \frac{1}{\mu} \vec{B}$$

$$(3) \quad \vec{J} = \sigma \vec{E}$$

Les coefficients s'appellent

ϵ : la permittivité électrique ou pouvoir inducteur spécifique ou constante diélectrique

μ : la perméabilité magnétique

σ : la conductivité

Ils sont à déterminer au voisinage du point et à la fréquence considérés, uniquement à partir des propriétés physiques du milieu en faisant appel à la théorie et à l'expérience.

Bien entendu, à partir des trois caractéristiques fondamentales ϵ , μ , σ , on peut en définir d'autres mieux adaptées à certains problèmes.

Dans le cadre de l'étude qui nous occupe nous allons, dans un premier temps, examiner sommairement l'importance relative des caractéristiques en cause et l'ordre de grandeur des valeurs connues. Puis nous approfondirons l'étude des caractéristiques essentielles des eaux et des glaces.

1.1. La perméabilité magnétique μ

A la surface du globe terrestre et sauf exception, on n'a pratiquement pas à se préoccuper de la perméabilité magnétique, si l'on exclut les matières ferromagnétiques et l'on peut admettre que la perméabilité magnétique μ est partout égale à celle de l'espace libre ou vide μ_0 .

Dans le système MKS (A) que nous adoptons (sauf exception signalée dans le texte)

$$(4) \quad \mu_0 = 4\pi \cdot 10^{-7} \text{ (H m}^{-1}\text{)}$$

1.2. La permittivité électrique ϵ

Cette caractéristique est variable à la surface de la terre, non seulement d'un corps à l'autre mais en fonction de la fréquence.

$$\text{La permittivité électrique du vide est (5) } \epsilon_0 = \frac{1}{c^2 \mu_0} \text{ (F m}^{-1}\text{)}$$

ou c est la vitesse de la lumière dans le vide.

On peut définir pour chaque corps matériel une permittivité électrique relative à celle du vide, par la relation :

$$(6) \quad \epsilon_r = \frac{\epsilon}{\epsilon_0}$$

De plus, les équations de Maxwell permettent d'établir en régime harmonique la relation (7) $\epsilon_r = n^2$, où n est l'indice de réfraction du milieu.

Enfin, il est commode d'introduire un vecteur polarisation électrique induite, défini par l'équation

$$(8) \quad \vec{P} = \vec{D} - \epsilon_0 \vec{E}$$

Le vecteur \vec{P} s'annule dans le vide et il s'annule en l'absence de champ. Il représente donc la matière.

1.3. La conductivité électrique σ

C'est la caractéristique e.m. la plus variable et de beaucoup, partant la plus importante.

L'espace libre ou vide est le seul milieu physique qui présente une conductivité identiquement nulle. Pour cette raison, le vide est parfaitement transparent aux ondes électromagnétiques. Les autres milieux physiques, dits matériels, présentent tous une certaine opacité, c'est-à-dire qu'ils présentent une conductivité équivalente σ finie et non-nulle. C'est pourquoi la caractéristique e.m. la plus importante d'un milieu de propagation est sa conductivité ! On l'évalue en siemens par mètre ou mho par mètre. Bien entendu σ est fonction de la fréquence.

1.4. La permittivité électrique complexe

Les équations de Maxwell permettent de rassembler les deux caractéristiques ϵ et σ d'un corps non ferromagnétique, dans le domaine de l'espace où l'on considère le champ et en régime harmonique défini par l'opérateur (9) $\frac{\partial}{\partial t} \equiv j\omega$, en une seule caractéristique la permittivité électrique complexe

$$(10) \quad \bar{\epsilon}_r = \frac{\epsilon}{\epsilon_0} - j \frac{\sigma}{\omega \epsilon_0} = \epsilon_r (1 - jp)$$

Grâce à cette écriture, on n'a plus à parler que d'une seule caractéristique, en distinguant toutefois la partie réelle et la partie imaginaire, ou bien en distinguant la permittivité relative ϵ_r d'une part et la tangente de l'angle de pertes p , d'autre part.

La permittivité électrique d'un corps est directement liée à la structure de sa molécule. Le moment électrique dipolaire est l'une des plus importantes constantes moléculaires. La polarisabilité est une autre caractéristique importante. Ces quantités peuvent l'une comme l'autre être obtenues à partir des mesures diélectriques.

Récemment, un effort d'analyse théorique des diélectriques a permis d'améliorer l'interprétation des propriétés des milieux condensés et d'exploiter les mesures faites sur des vapeurs ou des solutions étendues.

La permittivité électrique complexe dépend de la fréquence ; c'est aussi d'un grand intérêt au sujet des processus d'orientation de la molécule et de la connaissance des temps de relaxation.

2.1. ECHELONNEMENT DES VALEURS DE LA CONDUCTIVITE ET LE ROLE MAJEUR DE L'EAU SUR CES VALEURS A LA SURFACE DE LA TERRE

2.1. A fréquence nulle, c'est-à-dire en régime statique, l'industrie humaine produit des corps très peu conducteurs :

Corps	Conductivité σ_s ($\Omega^{-1} \text{ m}^{-1}$)
Quartz fondu	$< 2 \cdot 10^{-17}$
Verre ordinaire	10^{-12}

Mais elle produit aussi des métaux dont les conductivités sont élevées :

Acier	$0,5 \text{ à } 1 \cdot 10^7$
Cuivre	$5,7 \cdot 10^7$

Le rapport des ordres de grandeur en puissance de dix est 24.

Les corps et matériaux, en général inhomogènes et même hétérogènes, que l'on rencontre à la surface ou dans les couches superficielles de la terre ont des conductivités statiques qui se situent entre les deux extrêmes indiqués ci-dessus. Ce sont principalement des solutions aqueuses sous phase solide ou liquide et des roches. On trouve les valeurs approximatives suivantes :

Corps	Conductivité σ_s ($\Omega^{-1} \text{ m}^{-1}$)
Basalte sec	10^{-9}
Glace d'eau douce pure	10^{-8}
Eau très pure	10^{-6}
Sols secs (granit)	$10^{-5} \text{ à } 10^{-6}$
Eau douce (lacs et fleuves)	$5 \cdot 10^{-3}$
Eau de mer	4 à 5

Le rapport des ordres de grandeur extrêmes (basalte sec et eau de mer) en puissance de 10 est de 9 à 10, au plus.

2.2. L'eau très pure est relativement peu conductrice, mais c'est un solvant presque universel. Presque tous les composés chimiques connus se dissolvent dans l'eau, d'une quantité décelable. Les solutions aqueuses des minéraux qui composent les roches sont toutes plus ou moins conductrices.

Certaines nappes souterraines sont fortement minéralisées. Certains lacs sont salés. Ces masses liquides sont comme l'eau des mers de véritables électrolytes forts.

D'autre part l'eau est une substance des plus corrosives, qui réagit avec les ions et les molécules. Elle s'infiltre dans les roches. Elle peut s'écouler de la surface vers une nappe souterraine, mais aussi monter d'une nappe souterraine vers la surface par capillarité. Sa présence conditionne directement les caractéristiques e.m. des roches de la terre, y compris le basalte dit "sec". Le philosophe grec de l'antiquité Aristote avait inclus l'eau parmi les quatre éléments, à côté de la terre, de l'air et du feu.

En résumé, du point de vue électro-magnétique, l'eau solide ou liquide présente la perméabilité magnétique du vide μ_0 . Elle présente de plus, parce qu'elle contient des charges libres ou monopôles c'est-à-dire des ions, une certaine conductivité réelle σ' . Un champ électrique extérieur E appliqué à un échantillon provoque un mouvement ordonné de ces charges, c'est-à-dire un courant de conduction. Enfin, l'eau présente une certaine permittivité électrique ϵ , qui résulte de sa polarisation, laquelle est due principalement à l'orientation statistique de dipôles permanents. En régime harmonique les pertes par frottement dans l'orientation des dipôles de l'eau neutre se traduisent par une conductivité supplémentaire σ'' , qui s'ajoute à la conductivité ionique. La conductivité effective, à la fréquence considérée, est alors la somme des deux conductivités élémentaires

(45)

$$\sigma = \sigma' + \sigma''$$

3. LA REPARTITION DE L'EAU SUR LE GLOBE (2) :

L'eau, corps le plus ordinaire, est omniprésent à la surface de la terre. En fait, la planète terre pourrait s'appeler plus justement la planète des mers ou la planète de l'eau, car l'eau est probablement la substance qui distingue le plus la terre des autres planètes du système solaire. Il y a de l'eau à peu près partout à la surface ou à profondeur relativement faible.

3.1. Le total représente un volume de $13,5 \times 10^8 \text{ km}^3$, pour une surface planétaire de $5,09 \times 10^8 \text{ km}^2$. Sur un modèle sphérique l'épaisseur du film d'eau serait de 2,650 km.

La répartition globale approximative de cette eau est la suivante :

- Les océans : Ils représentent $13 \times 10^8 \text{ km}^3$, soit 97 % du total, pour une surface océanique de $3,6 \times 10^8 \text{ km}^2$. L'épaisseur moyenne des océans est donc de 3,610 km.

- Les calottes polaires : L'Antarctique supporte $2,5 \text{ à } 2,9 \times 10^7 \text{ km}^3$ de glace d'eau douce, pour une surface géographique de $1,5 \times 10^7 \text{ km}^2$. L'épaisseur moyenne de cette glace est de 1,8 km.

L'Arctique ne contribue que pour $3 \times 10^6 \text{ km}^3$ au stockage de la glace d'eau douce.

Malgré l'importance de la quantité d'eau soustraite aux océans par les calottes polaires, les bords des croûtes continentales sont cependant couverts par la mer sur les "plateaux continentaux". Même si l'axe de rotation de la terre perçait sa surface sur deux continents, ce qui doublerait approximativement le stock des glaces polaires, une grande partie des plateaux continentaux serait encore couverte d'eau, dans les conditions actuelles de température.

- La partie supérieure de la croûte terrestre émergée :

En dessous des surfaces continentales (ou immédiatement au contact de l'air) se trouve approximativement $4,8 \times 10^6 \text{ km}^3$ d'eau, dans des nappes saturées ou des roches non-saturées.

Si on se limite à 1 km de profondeur, la quantité d'eau douce est estimée à $4,1 \times 10^6 \text{ km}^3$.

3.2. Sur les continents, la quantité d'eau par unité de surface est très inégalement répartie. Voici les principales concentrations :

- les glaciers	$2,1 \times 10^5 \text{ km}^3$
- les grands lacs d'eau douce (Baïkal, etc..)	$1,2 \times 10^5 \text{ "}$
- les grands lacs d'eau salée (Caspienne, etc..)	$1,2 \times 10^5 \text{ "}$
- l'humidité superficielle des sols	$25 \times 10^3 \text{ "}$
- les fleuves et les rivières	$1,2 \times 10^3 \text{ "}$

La basse atmosphère contient, dans la troposphère, l'équivalent de $13 \times 10^3 \text{ km}^3$ d'eau liquide.

Le renouvellement par évaporation des océans, précipitation et retour aux océans, pour le globe entier, est de $3,5 \times 10^5 \text{ km}^3$ par an.

4. LES MOMENTS ELECTRIQUES ET POLARISABILITE DES MOLECULES (3)

Nous avons déjà exposé que la connaissance des caractéristiques électriques des corps matériels exigeait tout autant le développement de l'étude théorique que celui de l'expérimentation. Nous sommes donc conduits à rappeler rapidement les bases premières de la théorie physique, avant d'aborder la discussion de ses plus récents progrès. Bien entendu les propriétés de l'eau sous toutes ses phases dépendent fondamentalement de la structure et des propriétés de la molécule isolée.

4.1. Le potentiel d'une distribution de charges

Au point de vue électrique une molécule est constituée par des charges positives et négatives, réparties au voisinage de son centre de gravité.

Pour la compréhension des phénomènes diélectriques et la propagation du champ e.m. dans la matière, il est utile de développer en série d'harmoniques sphériques le potentiel créé, à distance, par une distribution de charges non-sphérique et de représenter le potentiel de ces charges par les premiers termes du développement.

Considérons donc un atome ou une molécule constituée par quelques charges qui occupent un petit volume et prenons pour origine des coordonnées le centre de gravité de la molécule.

Le potentiel V au point $M(X, Y, Z)$ créé par les charges $e_1, e_2, \dots, e_i, \dots$ situées aux points $x_1, y_1, z_1; x_2, y_2, z_2; \dots, x_j, y_j, z_j, \dots$ est fourni par l'expression :

$$(11) \quad V = \frac{1}{4\pi\epsilon_0} \sum_i \frac{e_i}{\left[(X - x_i)^2 + (Y - y_i)^2 + (Z - z_i)^2 \right]^{\frac{1}{2}}}$$

Posons (12)

$$\rho = (X^2 + Y^2 + Z^2)^{\frac{1}{2}}$$

Le développement de V suivant les puissances de $\frac{1}{\rho}$ s'écrit :

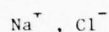
$$(13) \quad V = \frac{1}{4\pi \epsilon_0} \left[\frac{k_0}{\rho} + \frac{k_1}{\rho^2} + \frac{k_2}{\rho^3} + \dots \right]$$

chaque coefficient k_0 , k_1 , k_2 ne dépend que de la structure de la distribution de charges et des coordonnées (X, Y, Z).

4.1.1. Le moment monopolaire

$$(14) \quad k_0 = \sum_i e_i$$

Il n'existe que pour les molécules ionisées. Pour un système neutre dans son ensemble, tel qu'une molécule neutre, il disparaît. Au contraire, pour les ions en première approximation le potentiel se réduit à celui dû à la charge globale. C'est la base de la théorie des électrolytes forts de Debye-Hückel. Cela est d'autant plus justifié que le terme k_1 est nul pour les ions simples et les ions complexes symétriques et qu'en outre le terme k_2 est nul pour les ions simples à couches électroniques saturées ou pseudosaturées, comme :



4.1.2. Le moment dipolaire

$$(15) \quad k_1 = \frac{X}{\rho} \sum_i e_i x_i + \frac{Y}{\rho} \sum_i e_i y_i + \frac{Z}{\rho} \sum_i e_i z_i$$

k_2 ne diffère de zéro que si l'un au moins des trois termes \sum diffère de zéro, c'est-à-dire que si le barycentre des charges positives ne coïncide pas avec celui des charges négatives même en moyenne dans le temps. Dans ce cas, la molécule est "polaire". Elle possède un moment électrique μ , vecteur de composantes :

$$\mu_x = \sum e_i x_i \quad \mu_y = \sum e_i y_i \quad \mu_z = \sum e_i z_i$$

Elle équivaut à un dipôle formé, par exemple, de la charge $-e$ à l'origine des coordonnées et de la charge $+e$ au point de coordonnées

$$x = \frac{\mu_x}{e} \quad y = \frac{\mu_y}{e} \quad z = \frac{\mu_z}{e}$$

La charge e étant assez grande pour que x , y et z soient très petits, le potentiel de ce dipôle est :

$$(16) \quad V \sim \frac{1}{4\pi \epsilon_0 \rho^2} \left(\mu_x \frac{X}{\rho} + \mu_y \frac{Y}{\rho} + \mu_z \frac{Z}{\rho} \right)$$

Un atome isolé n'a pas de moment dipolaire, car le nuage électronique est symétrique par rapport au noyau. De même une molécule présentant un centre de symétrie comme CH_4 n'est pas polaire. Au contraire, les molécules coudées ou pyramidales sont polaires. H_2O est une molécule coudée, donc polaire.

4.1.3. Le moment quadrupolaire

$$(17) \quad k_2 = \frac{1}{2} \left(3 \frac{X^2}{\rho^2} - 1 \right) \sum e_i x_i^2 + \frac{1}{2} \left(3 \frac{Y^2}{\rho^2} - 1 \right) \sum e_i y_i^2 + \frac{1}{2} \left(3 \frac{Z^2}{\rho^2} - 1 \right) \sum e_i z_i^2 \\ + 3 \frac{XY}{\rho^2} \sum e_i x_i y_i + 3 \frac{YZ}{\rho^2} \sum e_i y_i z_i + 3 \frac{ZX}{\rho^2} \sum e_i z_i x_i$$

Ce terme peut se discuter en considérant la quadrique :

$$(18) \quad \xi^2 \sum e_i x_i^2 + \eta^2 \sum e_i y_i^2 + \zeta^2 \sum e_i z_i^2 + 2 \xi \eta \sum e_i x_i y_i + 2 \eta \zeta \sum e_i y_i z_i \\ + 2 \xi \zeta \sum e_i z_i x_i = 1$$

Cette quadrique a, par rapport à la molécule, une orientation bien déterminée, indépendante du système de référence. Au lieu de prendre des axes de coordonnées quelconques, choisissons le trièdre $ox'y'z'$ des axes principaux de la quadrique, les termes rectangles s'annulent et le terme en ρ^{-3} du potentiel V devient :

$$(19) \quad \frac{1}{2\rho^3} \left[\left(3 \frac{x'^2}{\rho^2} - 1\right) \sum e_i x_i'^2 + \left(3 \frac{y'^2}{\rho^2} - 1\right) \sum e_i y_i'^2 + \left(3 \frac{z'^2}{\rho^2} - 1\right) \sum e_i z_i'^2 \right]$$

$$\text{Si la quadrique est une sphère (20) : } \sum e_i x_i'^2 = \sum e_i y_i'^2 = \sum e_i z_i'^2$$

Dans ces conditions, le potentiel s'annule, puisqu'on peut mettre en facteur

$$(21) \quad \left(3 \frac{x'^2 + y'^2 + z'^2}{\rho^2} - 3\right) = 0$$

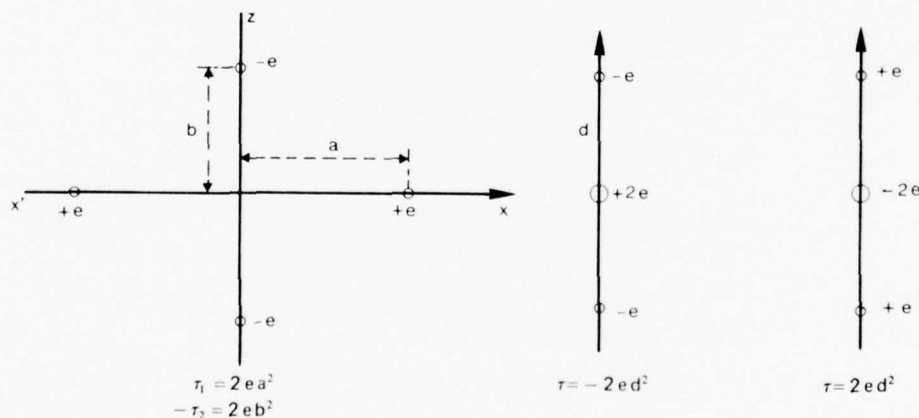
Ainsi, sans changer le potentiel on peut ajouter ou retrancher une même quantité aux trois grandeurs $\sum e_i x_i'^2$, $\sum e_i y_i'^2$, $\sum e_i z_i'^2$

Supposons que (22) $\sum e_i x_i'^2 > \sum e_i y_i'^2 > \sum e_i z_i'^2$, le potentiel ne dépend que des deux grandeurs

$$(23) \quad Q_1 = \sum e_i x_i'^2 - \sum e_i y_i'^2$$

$$(24) \quad Q_2 = \sum e_i y_i'^2 - \sum e_i z_i'^2$$

Il peut être attribué à un quadrupôle, c'est-à-dire à



Exemples de quadrupôles

un ensemble de 2 charges positives $+e$ de coordonnées $\pm \sqrt{\frac{Q_1}{2e}}$, 0, 0 et de 2 charges négatives $-e$ de coordonnées 0, 0, $\pm \sqrt{\frac{Q_2}{2e}}$. (e doit être assez grand pour que le parallélogramme ainsi formé ait des côtés très petits).

En pratique la quadrique est très souvent de révolution. On peut alors définir le moment quadrupolaire effectif Q porté par l'axe de révolution. Si $Q > 0$ le quadrupôle est formé d'une charge $-2e$ entourée de deux charges $+e$ à la distance d : (25) $Q = 2e d^2$. Si $Q < 0$, changer le signe des charges. Un atome ou un ion dont toutes les couches électroniques sont saturées ou pseudosaturées n'a pas de moment quadrupolaire effectif.

Une molécule complexe non-polaire ou un atome à couches électroniques non complètes équivalent à un quadrupôle. Pour une molécule polaire comme celle de l'eau, il peut être nécessaire de tenir compte du quadrupôle en même temps que du dipôle.

Le terme en ρ^{-4} du développement de V pourrait permettre de définir un moment octopolaire.

4.2. La polarisabilité des molécules

Considérons une molécule soumise à un champ électrique local E_m , qui modifie les positions relatives des noyaux et le mouvement des électrons, il en résulte la création d'un moment dipolaire μ qui s'ajoute au moment permanent μ_p , si la molécule est polaire. On dit qu'il y a polarisation de la molécule.

Si on considère le régime harmonique du champ macroscopique \vec{E} et du champ local \vec{E}_m à une fréquence élevée, dans le visible ou le proche u.v., la molécule ne se déforme pas et seule intervient la "polarisabilité électronique". On peut définir un ellipsoïde de polarisabilité électronique et une polarisabilité moyenne α_e telle que $\mu_e = \alpha_e E_m$.

On peut définir de façon analogue un ellipsoïde de polarisabilité atomique lorsque la fréquence est assez faible pour qu'il soit nécessaire de tenir compte de la déformation de la molécule et définir de plus une polarisabilité α_a telle que $\mu_a = \alpha_a E_m$.

4.3. La polarisation

Supposons un champ électrique macroscopique E statique et uniforme la polarisation induite dans l'échantillon de matière diélectrique est d'après les équations (6) et (8)

$$(26) \quad \vec{P} = \epsilon_0 (\epsilon_r - 1) \vec{E}$$

Le vecteur \vec{P} représente la somme des moments dipolaires par unité de volume, qu'ils soient dus à l'orientation des dipôles permanents au mouvement des électrons ou à la déformation de la molécule

$$(27) \quad \vec{P} = \vec{P}_p + \vec{P}_a + \vec{P}_e$$

\vec{P}_p correspond à l'orientation des dipôles permanents qui est gênée par l'agitation thermique. \vec{P}_a et \vec{P}_e comme α_a et α_e correspondent aux polarisations atomique et électronique et sont dues à des phénomènes intramoléculaires indépendants de la température.

On peut écrire de même le moment dipolaire moyen $\bar{\mu}_1$ de la molécule sous la forme

$$(28) \quad \bar{\mu}_1 = \mu_p + \mu_a + \mu_e$$

Enfin, s'il y a $\frac{N_A}{V}$ molécules par unité de volume, N_A étant le nombre d'Avogadro et V le volume molaire :

$$(29) \quad \vec{P} = \frac{N_A}{V} \bar{\mu}_1 = \vec{P}_p + \frac{N_A}{V} \alpha E_m$$

Revenons aux dipôles permanents. Leur orientation diminue le désordre thermodynamique. L'énergie potentielle d'un dipôle élémentaire, ayant tourné de l'angle θ , est :

$$(30) \quad U = - \mu_p \cdot E_m \cdot \cos \theta$$

L'équilibre statistique est régi de façon telle, que les molécules se répartissent, entre

les différents niveaux d'énergie U , proportionnellement à $e^{-\frac{U}{kT}}$, où k est la constante de Boltzmann et T la température absolue.

$$\text{On écrit : } (31) \quad e^{-\frac{U}{kT}} = 1 + \frac{\mu_p E_m}{kT} \cos \theta \quad (T \approx 300^\circ K)$$

En l'absence de champ, aucune direction n'est privilégiée et le nombre de molécules dont le moment fait avec une direction fixe un angle compris entre θ et $\theta + d\theta$ est proportionnel à l'angle solide $2\pi \sin \theta d\theta$. Chacune des molécules contribuant pour la part $\mu_p \cos \theta$ au moment dipolaire, on trouve :

$$(32) \quad P_p = \frac{1}{2} \frac{N_A}{V} \mu_p \int_0^\pi \left[1 + \frac{\mu_p E_m}{kT} \cos \theta \right] \cos \theta \sin \theta d\theta$$

D'où en intégrant

$$(33) \quad \vec{P}_p = \frac{N_A}{3V} \frac{\mu_p^2 E_m}{kT}$$

Ce qui donne avec (29)

$$(34) \quad \vec{P} = \frac{N_A}{V} \left(\alpha + \frac{\mu^2}{3kT} \right) \vec{E}_m$$

5. LA MOLECULE D'EAU (2)

Pour expliquer les propriétés connues de la molécule d'eau, on est conduit à admettre que cette molécule présente une certaine structure. Elle est essentiellement composée d'un atome d'oxygène et de deux atomes d'hydrogène. Il reste à préciser les positions respectives des charges et des masses qui satisfont aux données expérimentales le moment électrique permanent, le moment d'inertie mécanique connu par l'absorption dans l'infra-rouge et par l'effet Raman, l'anisotropie connue par la polarisation de la lumière diffusée, etc..

Malheureusement, dans l'état actuel de nos connaissances, plusieurs configurations de molécules sont compatibles avec l'ensemble des données. Cependant, toutes ces configurations admettent un modèle coudé HOH et fortement polaire.

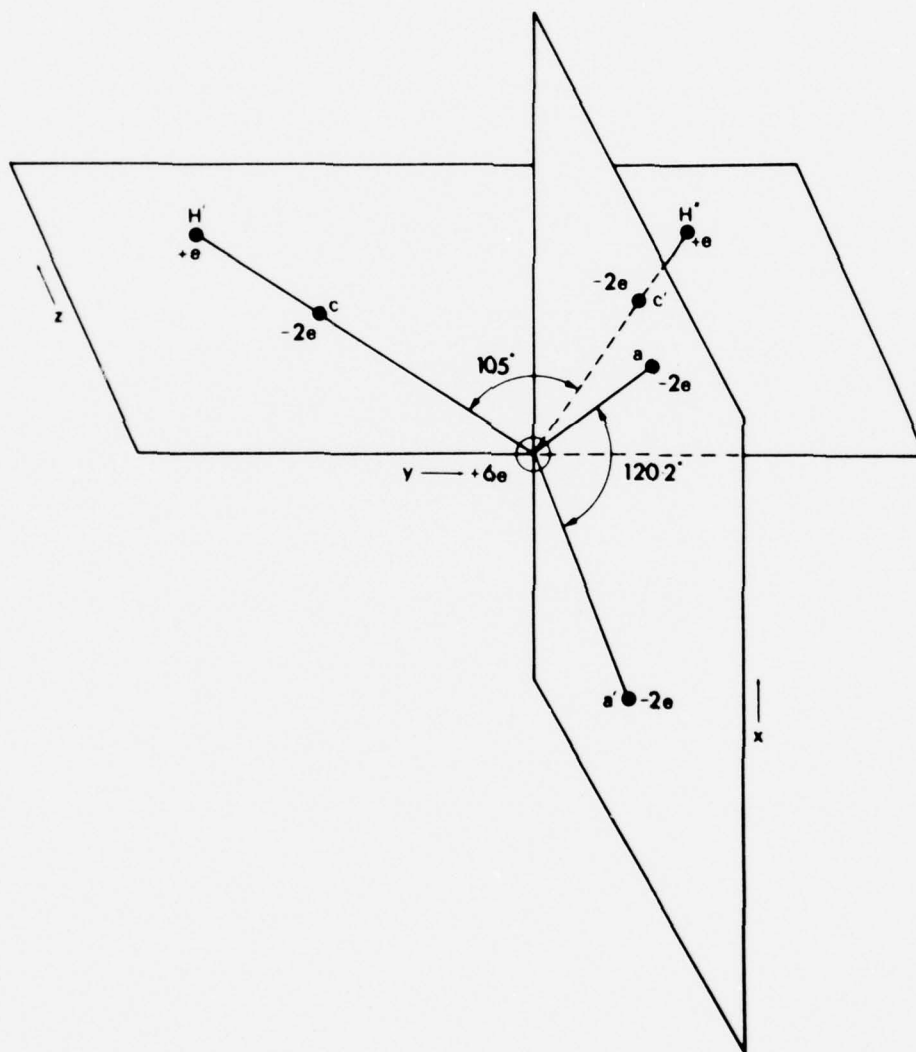


Fig. 1 : Modèle de molécule d'eau proposé par Pople (2)

5.1. Les propriétés électriques de la molécule d'eau libre

Le moment électrique permanent de la molécule d'eau H_2O a été déduit de la variation de la permittivité électrique de la vapeur d'eau en fonction de la température, ainsi que d'autres expériences.

La valeur la plus probable est :

$$(35) \quad \mu = 1,83 D = 1,83 \times 10^{-18} \text{ ues cm.}$$

Le symbole D désigne le debye. Un debye vaut $3,333 \times 10^{-30}$ C.m.. Le vecteur $\vec{\mu}$ est porté par la bisectrice de l'angle H-O-H. Il est orienté de l'atome négatif d'oxygène vers la région positive entre les atomes d'hydrogène. La longueur des liaisons OH est de 0,96 Å et l'angle de liaison HOH vaut 104° . Les valeurs relatives à la molécule libre ne se retrouvent pas dans le liquide. Mais on peut tenter de représenter le dipôle permanent par une fonction d'onde.

Le moment quadrupolaire Q est connu à partir de l'expérience. Il vaut :

$$(36) \quad Q = (-5,6 \pm 1,0) \times 10^{-26} \text{ ues cm}^2$$

Les valeurs individuelles Q_{xx} , Q_{yy} et Q_{zz} ne sont pas actuellement connues expérimentalement mais peuvent être calculées à partir des fonctions d'onde.

Les valeurs calculées des moments individuels sont alors :

$$Q_{xx} = -6,6 \times 10^{-26} \quad Q_{yy} = -5,2 \times 10^{-26} \quad Q_{zz} = -5,7 \times 10^{-26} \text{ ues cm}^2$$

Ces valeurs se rapportent à la molécule ayant son centre de gravité à l'origine des coordonnées. Les signes - indiquent que les contributions des électrons à ce moment sont plus importantes que celles du noyau. L'égalité approximative des moments individuels montre que la distribution des charges est presque sphérique.

La polarisabilité moléculaire α est connue expérimentalement, sa valeur moyenne est :

$$(37) \quad \bar{\alpha} = \frac{1}{3} (\alpha_{xx} + \alpha_{yy} + \alpha_{zz}) = 1,44 \times 10^{-24} \text{ cm}^3$$

Les composantes du tenseur ne sont pas connues mais il semble que l'anisotropie de la polarisabilité soit petite.

Une nouvelle constante électrique de la molécule à étudier et à mesurer serait la variation du moment dipolaire pendant la vibration moléculaire.

5.2. Les arrangements de molécules d'eau (Frank, H.S.) (4)

La molécule dans la vapeur peut être considérée comme libre. Dans la glace, aux faibles pressions (formes I_h et I_c) chaque molécule est entourée de 4 voisines, disposées aux sommets d'un tétraèdre régulier à une distance de 2,75 Å environ et il existe 12 voisines de second rang à la distance de 4,5 Å chacune. Aux pressions élevées (formes II à VI) la disposition en tétraèdres est quelque peu déformée ; les molécules voisines sont séparées par des distances de 2,75 à 2,9 Å et les voisines de second rang n'approchent pas à moins de 3,5 Å. Dans la forme la plus dense (forme VII) l'arrangement est cubique centré ; la distance entre le centre et un sommet étant de 2,95 Å.

L'interprétation de ces découvertes, en termes de liaison hydrogène, est amplement confirmée par les études de diffraction des neutrons, le spectre Raman infrarouge et pour les phases désordonnées par les propriétés acoustiques et électriques et les entropies résiduelles.

L'importance des liaisons hydrogène connectant chaque molécule à ses voisines a été récemment confirmée par des calculs de mécanique quantique et apparaît clairement ; l'angle de liaison entre les protons n'est jamais très différent de 109° .

Ainsi, l'eau peut être représentée par un atome d'oxygène au centre d'un tétraèdre régulier, qui posséderait un noyau d'hydrogène (proton, deutéron ou triton) en deux sommets et deux paires d'électrons en orbites dirigés vers les deux autres sommets.

En considérant la variété des configurations observées dans les phases solides, on peut admettre que dans le liquide un beaucoup plus grand nombre de structures désordonnées peuvent assembler les molécules en arrangements tétraédriques un peu plus déformés. Ceci ne signifie pas qu'il y ait une abondance significative d'agrégats assez grands et réguliers pour être identifiés. Au contraire, il paraît raisonnable de penser qu'il y a en présence les unes des autres beaucoup de configurations irrégulières compatibles avec la chaleur de fusion.

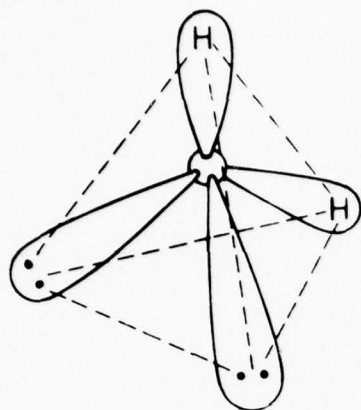


Fig. 2 : Disposition géométrique proposée des noyaux et de la distribution de charges électroniques dans une molécule d'eau (4)

5.3. Les isotopes (2)

Strictement parlant, l'eau est un mélange de combinaisons d'isotopes ^1H , ^2H , ^3H et ^{16}O , ^{17}O , ^{18}O sous forme de molécules, d'ions d'hydrogènes et d'ions OH

Dans les eaux naturelles les proportions sont les suivantes :

$$\frac{^2\text{H}}{^1\text{H}} = \frac{1}{69\,000}, \quad \frac{^{17}\text{O}}{^{18}\text{O}} = \frac{1}{5}, \quad \frac{^{18}\text{O}}{^{16}\text{O}} = \frac{1}{500}$$

Ces proportions sont partout les mêmes.

$$\frac{^3\text{H}}{^1\text{H}} = \frac{1}{10^{18}} \quad \text{Le tritium apparaît dans la pluie et la neige}$$

(La période de décroissance moitié est de 12,5 années)

6. LA FORMULE DE CLAUSIUS MOSSOTTI (5)

Afin de poursuivre le calcul théorique de la permittivité sur les résultats du § 4.3., il reste à trouver une relation déterminant le champ local E_m agissant sur la molécule à partir du champ appliqué E en tenant compte de la présence des autres molécules au voisinage de la molécule considérée.

6.1. Le régime statique

En partant d'un modèle simpliste (Une cavité sphérique sur la face interne de laquelle apparaissent des charges est centrée sur la molécule considérée) Mossotti et Lorentz parviennent à l'expression :

$$(38) \quad \vec{E}_m = \vec{E} + \frac{\vec{P}}{3\epsilon_0}$$

En éliminant \vec{P} , \vec{E} , et \vec{E}_m entre (26), (34) et (38), on trouve :

$$(39) \quad \frac{\epsilon_r - 1}{\epsilon_r + 2} = \frac{N_A}{V} \frac{1}{3\epsilon_0} \left[\alpha + \frac{\mu^2}{3kT} \right]$$

En l'absence de moments dipolaires permanents, la formule se réduit à l'expression de Clausius Mossotti

$$(40) \quad \frac{\epsilon_r - 1}{\epsilon_r + 2} = \frac{N_A}{V} \frac{\alpha}{3\epsilon_0}$$

6.2. Le régime harmonique et l'équation de Debye :

Si on utilise un champ E variable, c'est-à-dire une onde électromagnétique entretenue, la permittivité électrique donnée par la relation de Maxwell $\epsilon_r = n^2$ (où n est l'indice de réfraction) dépend de la fréquence. Lorsque celle-ci atteint 10^9 Hz environ, ϵ_r diminue fortement pour les substances à molécules polaires, car les dipôles n'ont pas le temps de s'orienter dans le champ. ϵ_r varie très rapidement dans les bandes d'absorption où les vibrations intra-moléculaires prennent une grande amplitude car elles sont en résonance avec l'onde e.m. Les bandes d'absorption de l'infra-rouge correspondent aux vibrations des noyaux et celles de l'ultra-violet aux vibrations électroniques.

Aux fréquences suffisamment basses, c'est-à-dire pour l'eau inférieures à 10^{12} Hz, la polarisabilité peut passer pour instantanée tandis que l'orientation dipolaire, qui apporte à la polarisation une part principale, ne l'est pas.

Supposons qu'à l'instant $t = 0$, le champ \vec{E} s'annule brusquement. L'un quelconque des dipôles va se mouvoir pour gagner une nouvelle position. Debye a supposé que l'angle de rotation β décroissait de β_0 à zéro suivant une loi exponentielle, la polarisation \vec{P} suivant la même loi temporelle

$$(41) \quad \vec{P}_p(t) = \vec{P}_p(0) e^{-\frac{t}{\tau}}$$

ou τ est un temps de relaxation

en régime harmonique l'équation (39) devient :

$$(42) \quad \frac{\bar{\epsilon}_r - 1}{\bar{\epsilon}_r + 2} = \frac{N_A}{V \cdot 3 \epsilon_0} \left[\alpha - \frac{\mu_p}{3kT} \frac{1}{1 + j\omega\tau} \right]$$

La permittivité est donc complexe, elle possède une partie imaginaire qui rend compte du freinage par le frottement de viscosité et qui correspond à une conductivité réelle.

On peut poser :

$$(43) \quad \bar{\epsilon}_r = \epsilon' - j\epsilon''$$

La partie réelle ϵ' provient d'une part de la polarisabilité d'autre part de l'orientation dipolaire.

La partie imaginaire ϵ'' provient de l'orientation dipolaire.

$$\text{On peut poser (44) :} \quad \epsilon'' \equiv \frac{\sigma''}{\omega \epsilon_0}$$

La conductivité totale du milieu est la somme de la conductivité ionique σ' due aux mouvements des monopoles, s'il y en a, et de la conductivité dipolaire.

$$(45) \quad \sigma = \sigma' + \sigma''$$

En résumé, les caractères distinctifs de la polarisation macroscopique ainsi obtenue sont les suivants :

- i) A champ \vec{E} donné, \vec{P} est nettement plus grand pour les corps polaires que pour les corps non polaires.
- ii) La polarisation dépend notablement de la température. Elle augmente quand on diminue la température parce que l'agitation thermique décroît.
- iii) Les pertes diélectriques sont beaucoup plus grandes dans les corps polaires. Au cours de leur oscillation, les moments élémentaires dissipent en chaleur, par choc, l'énergie qu'ils reçoivent du champ.

6.3. On écrit à partir de (42) :

$$(46) \quad \frac{\bar{\epsilon}_r - 1}{\bar{\epsilon}_r + 2} = U + \frac{V}{1 + j\omega\tau}$$

$$\text{avec (47)} \quad U = \frac{N_A}{V} \frac{\alpha}{3 \epsilon_0}$$

$$\text{et (48)} \quad V = \frac{N_A}{V} \frac{1}{3 \epsilon_0} \frac{\mu_p}{3k}$$

Si la molécule est sphérique de rayon a et tourne dans un fluide de viscosité η , la loi de Stokes conduit à l'expression

$$(49) \quad \tau = \frac{\zeta}{2kT} = \frac{0,4 \pi a^3 \eta}{kT}$$

(η étant mesuré en poises et a en mètres)

Aux fréquences très basses ($\omega \rightarrow 0$), $\bar{\epsilon}_r$ tend vers un nombre réel ϵ_S : la permittivité statique.

Aux fréquences très élevées ($\omega \rightarrow \infty$), $\bar{\epsilon}_r$ tend aussi vers un nombre réel ϵ_∞ : la permittivité optique, qui est le carré de l'indice de réfraction, lorsque l'orientation des dipôles permanents ne contribue plus à la polarisation et que la polarisabilité subsiste.

$$(50) \quad \frac{\epsilon_S - 1}{\epsilon_S + 2} = U + \frac{V}{T}$$

$$(51) \quad \frac{\epsilon_\infty - 1}{\epsilon_\infty + 2} = U$$

Il vient (équation de Debye) :

$$(52) \quad \begin{cases} \epsilon' = \epsilon_\infty + \frac{\epsilon_S - \epsilon_\infty}{1 + x^2} \\ \epsilon'' = \frac{(\epsilon_S - \epsilon_\infty) x}{1 + x^2} \end{cases} \quad \text{ou} \quad (53) \quad \bar{\epsilon}_r = \epsilon_\infty + \frac{\epsilon_S - \epsilon_\infty}{1 + jx}$$

avec (54) $x = \frac{\epsilon_S + 2}{\epsilon_\infty + 2} \omega \tau$

Pour $x = 1$ on a (55) $\epsilon' = \frac{\epsilon_S + \epsilon_\infty}{2}$

ϵ'' est maximum : (56) $\epsilon''_{\max} = \frac{\epsilon_S - \epsilon_\infty}{2}$

Cette situation est appelée "point de transition".

La longueur d'onde de transition est (57) $\lambda_t = 2\pi c \tau \frac{\epsilon_S + 2}{\epsilon_\infty + 2}$, où c est la vitesse de la lumière dans le vide.

On peut encore écrire :

$$(58) \quad \epsilon' = \epsilon_\infty + \frac{\epsilon_S - \epsilon_\infty}{1 + \left(\frac{\lambda_t}{\lambda}\right)^2}$$

$$(59) \quad \epsilon'' = \frac{(\epsilon_S - \epsilon_\infty) \frac{\lambda_t}{\lambda}}{1 + \left(\frac{\lambda_t}{\lambda}\right)^2}$$

Il est clair qu'à partir des formules (52), (53) et (54) on peut calculer les quantités ϵ' et ϵ'' à toutes les fréquences à condition de connaître ϵ_S , ϵ_∞ et τ ou la pulsation de transition.

Nous appliquerons ces formules à l'eau. Il est tout d'abord nécessaire d'examiner l'effet des ions et de connaître la conductivité ionique σ' puisque la conductivité totale est fournie par (44) et (45).

7. LA COMPOSITION IONIQUE DE L'EAU DE MER (6)

La conductivité ionique de l'eau des mers fait partie, comme nous l'avons déjà dit, de l'ensemble des propriétés physiques et physico-chimiques qui la différencient de l'eau douce.

Ces propriétés sont attribuables à environ 11 constituants chimiques qui représentent plus de 99,9 % de la matière dissoute dans l'eau et que l'on retrouve, à très peu près dans les mêmes proportions, en tout point des océans, quelles que soient le lieu, la température et la pression, à condition de s'éloigner suffisamment des estuaires fluviaux, des sources sous-marines et des banquises.

Cette matière comprend : (Voir tableau I)

Les anions Cl^- , SO_4^{--} , HCO_3^- , Br^- et F^-

Les cations Na^+ , Mg^{++} , Ca^{++} , K^+ et Sr^{++}

et non dissocié H_3BO_3

La dissociation des sels étant presque totale, l'eau de mer est un "électrolyte fort" comme les solutions aqueuses d'acides ou de bases fortes. (Il existe cependant des associations ioniques des polyvalents).

A partir de cette composition ionique, il n'est pas possible de dire quelle est la composition du mélange des sels qui sont effectivement dissous. Cependant, si l'on déshydrate de l'eau de mer, on retrouve un mélange de sels dont les deux principaux sont : le chlorure de sodium NaCl et le chlorure de magnésium MgCl_2 .

La concentration totale des sels est appelée "Salinité". Elle est définie comme étant le poids, en gramme, de la matière inorganique dissoute dans l'eau de mer (après que tous les bromures et les iodures ont été remplacés par un apport équivalent de chlorures et que les carbonates ont été convertis en oxydes). La "concentration totale en chlorures" ou "chlorinité" peut être définie et servir à caractériser la quantité de sels dissous au même titre que la salinité.

Tableau I

Composition de l'eau de mer. Concentration partielle des constituants
d'une eau de mer ayant une chlorinité de 19 o/oo
(d'après A. Richards)

	g/kg	rapport à la chlorinité
Chlore Cl^-	18,890	0,99894
Sodium Na^+	10,560	0,5556
Magnésium Mg^{++}	1,273	0,06695
Sulfate SO_4^{--}	2,649	0,1394
Calcium Ca^{++}	0,4104	0,02106
Potassium K^+	0,380	0,02000
Carbone (comme HCO_3^- ou CO_3^{--})	$28 \cdot 10^{-3}$	0,00735
Brome Br^-	$65,9 \cdot 10^{-3}$	0,00340
Strontium Sr^{++}	$8,1 \cdot 10^{-3}$	0,0004
Bore, comme H_3BO_3	$4,6 \cdot 10^{-3}$	0,00137
Silicium, comme silicates	$0,01-4,5 \cdot 10^{-3}$	
Fluor F^-	$1,4 \cdot 10^{-3}$	0,00007
Azote dans NO_3^-	$0,01-0,80 \cdot 10^{-3}$	
Aluminium Al^{+3}	$0,5 \cdot 10^{-3}$	
Rubidium Rb^+	$0,2 \cdot 10^{-3}$	
Lithium Li^+	$0,1 \cdot 10^{-3}$	
Phosphore dans PO_4^{--3}	0,001-0,1	

Traces d'éléments présents en concentrations comprises entre 1 à 50 $\mu\text{g/kg}$: barium, iode, arsenic, fer, manganèse, cuivre, zinc, plomb, sélénium, césium, uranium.

Traces d'éléments présents en concentrations inférieures à 1 $\mu\text{g/kg}$: molybdène, thorium, cérium, argent, vanadium, lanthane, yttrium, nickel, scandium, cobalt, cadmium, mercure, or, étain, chrome, radium.

La salinité est une variable caractéristique d'une certaine eau. En plein océan, les valeurs restent comprises entre 32 et 37 o/oo. En Mer Rouge et dans le golfe Persique, où l'évaporation est très intense, elles peuvent dépasser 40 o/oo. La moyenne générale est de 35 o/oo. La concentration moyenne en chlorures est de 19 o/oo.

8. LA CONDUCTIVITE IONIQUE DE L'EAU DOUCE ET DE L'EAU DE MER (5)

8.1. Le mécanisme du passage du courant dans l'électrolyte (6) :

L'eau de mer est un électrolyte. Sa structure comme celle de tous les électrolytes se rapproche beaucoup de celle d'un plasma. Cependant, la dissociation dans un électrolyte ne fait apparaître que des ions, à l'exclusion des électrons. Ces ions sont lourds et lents. Le plus léger d'entre eux, le proton H^+ , est encore 1 830 fois plus inerte que l'électron. Il ne porte que la charge $+e$ égale en valeur absolue à celle de l'électron $-e$.

Chaque ion d'un même type présente une masse m et porte une charge q , qui est un multiple entier positif ou négatif de la charge élémentaire $-e$ de l'électron :

$$(60) \quad q = z e$$

z s'appelle "électrovalence"

Le faraday est la charge électrique transportée par une mole d'ions monovalents, tels que Na^+ ou Cl^- par exemple.

$$(61) \quad F = N_A e = (96\,491,2 \pm 1,1) \text{ C/mole}$$

(La mole est la quantité d'un corps qui contient N_A entités élémentaires, c'est-à-dire autant de ces entités qu'il y a d'atomes dans 0,012 kg de carbone 12.).

Si l'ion est bi, tri ou z -valent, la charge transportée par une mole d'ions est zF .

La solution étant électriquement neutre dans son ensemble, la somme des concentrations des ions positifs est égale à la somme des concentrations des ions négatifs.

On appelle "Molarité" de l'ion B le quotient c_B du nombre de moles de cet ion par le volume du mélange. Par unité de volume, il y a donc $N_A c_B$ ions du type B qui portent la charge $N_A c_B z_B e$.

On a, pour un mélange neutre dans son ensemble, $\sum c_B z_B = 0$ (la somme étant étendue à tous les types d'ions).

Les ions, qui ont à peu près la même taille que les molécules d'eau, participent à l'agitation thermique désordonnée, dont il ne résulte aucun courant à l'échelle macroscopique. Mais, s'il existe dans l'électrolyte un mouvement statistiquement ordonné des charges il peut en résulter un courant dont la densité s'écrit :

$$(62) \quad \vec{J} = N_A e \sum c_B z_B \vec{V}_B$$

En présence du champ électrique \vec{E} qui pénètre l'électrolyte, on admet que chaque ion est soumis à la force $q_B \cdot \vec{E}$. (Il n'est pas nécessaire de faire intervenir la polarisation et le champ effectif, puisque les relations entre ces vecteurs sont linéaires). Chaque ion est d'autre part soumis à une force visqueuse ou de frottement $mZ\vec{V}$, où Z a les dimensions d'une fréquence et peut être appelé fréquence de collision de l'ion.

D'autre part, le coefficient de frottement mZ est donné par la loi de Stokes

$$(63) \quad mZ = 6\pi\eta a$$

η désignant le coefficient de viscosité de l'eau et a le rayon de l'ion.

En définitive, l'équation des forces appliquées à l'ion B est (en supprimant dans l'écriture l'indice B) :

$$(64) \quad m \frac{d\vec{V}}{dt} + mZ\vec{V} = q\vec{E}$$

En régime continu on peut admettre

$$(65) \quad \vec{V} = \frac{q}{mZ} \vec{E}$$

La quantité $u = \frac{q}{mZ}$ s'appelle "mobilité" de l'ion.

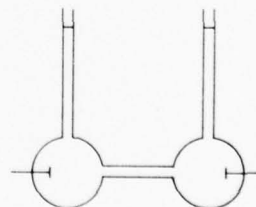
On a donc pour cet ion :

$$(66) \quad \vec{J} = N_A e c |z| u \vec{E}$$

$$\text{ou bien } (67) \quad \vec{J} = \sigma' \vec{E}$$

où σ' est la "conductivité spécifique" due à la présence de l'ion B.

Cette relation est l'expression de la loi d'Ohm.



On appelle "concentration équivalente" C le produit de la molarité c par la valeur absolue de l'électrovalence z

$$(68) \quad C = c |z|$$

Pour un sel dissous, la concentration C est le produit du (nombre de moles par unité de volume) par (la somme des valences rompues). Ainsi, pour NaCl

$$C = c \cdot 1$$

$$\text{D'où (69)} \quad \sigma' = N_A e C u$$

On peut définir la "conductivité molaire" Λ_m par :

$$(70) \quad \Lambda_m = \frac{\sigma'}{c} = N_A e |z| u$$

et la "conductivité équivalente" Λ par :

$$(71) \quad \Lambda = \frac{\sigma'}{C} = N_A e u$$

Pour le mélange d'ions d'un sel dissous, on a bien entendu

$$(72) \quad \Lambda = N_A e \sum u$$

Il résulte de (71) que, pour chaque sel, Λ ne devrait dépendre que de la température et non de la concentration. Ainsi, à température fixe, σ' serait proportionnel à C .

8.2. Méthodes de mesure et résultats expérimentaux :

Pour mesurer la conductivité d'un électrolyte liquide quelconque, on peut utiliser un vase dont la forme est représentée sur la figure 3 possédant une partie cylindrique de section s , où le champ électrique peut être considéré comme uniforme et parallèle aux génératrices du cylindre.

La quantité d'électricité qui traverse par seconde l'unité de surface MM' est :

$$(73) \quad i = \frac{I}{s} = \sigma' E$$

On met alors en oeuvre les mêmes méthodes de mesure que pour les conducteurs ordinaires. Pour éviter le phénomène de polarisation des électrodes, on emploie dans les mesures au pont de Wheatstone un courant alternatif. On peut étalonner le tube à électrolyte en mesurant sa résistance lorsqu'il est rempli par une solution de conductivité connue.

Expérimentalement, on constate bien que la conductivité des électrolytes augmente avec la température. La variation relative est assez considérable et de l'ordre de $1/40$ par degré Celsius. Cette augmentation relative est voisine de celle de $1/\eta$ et liée à la diminution relative du coefficient de frottement interne de l'eau (63).

On constate de plus, que la conductivité équivalente Λ diminue quand la concentration C augmente et tant que C ne dépasse pas beaucoup 10, la variation suit, pour les électrolytes forts, la loi de KOHLRAUSCH (1900) :

$$(74) \quad \Lambda = \Lambda_0 - b \sqrt{C}$$

Les deux constantes de cette loi expérimentale sont propres à chaque sel. Λ_0 est une conductivité limite qui caractérise une concentration infiniment petite.

Le tableau II, ci-dessous, indique quelques valeurs numériques en mho/m des conductivités équivalentes multipliées par 10^3 de deux solutions aqueuses à 18°C , d'après H. FALKENHAGEN

Tableau II

C	$\ll 10^{-1}$	10^{-1}	$5 \cdot 10^{-1}$	1	5	10	50	100	500	1000
NaCl	10,899	10,810	10,718	10,649	10,378	10,195	9,571	9,202	8,094	7,435
MgCl ₂	11,088	10,943	10,768	10,635	10,130	9,814	8,848	8,342	6,987	6,145

La conductivité $\sigma' = \Lambda C$ n'est donc qu'assez grossièrement proportionnelle à la concentration. Noter que pour l'eau de mer la concentration globale équivalente est voisine de 600.

8.3. La conductivité ionique de l'eau pure

Même parfaitement propre, bidistillée et privée de gaz, l'eau possède une conductibilité résiduelle qui révèle une très faible dissociation. Les concentrations des ions H^+ et OH^- sont telles que l'on ait à 18°C et par m^3 :

$$(75) \quad C_1 = C_2 = 0,77 \cdot 10^{-4}$$

Comme le pH est défini par l'expression $pH = -\log_{10} C_1/1000$, le pH de l'eau pure à 18°C est 7,1 environ. (Pour l'eau de mer, le pH varie entre 8,0 et 8,2 à la surface et décroît jusqu'à 7,7 en profondeur, ce qui signifie une légère alcalinité).

$$\begin{aligned} \text{Pour un pH de 7,1, on obtient} \quad \sigma' &= 3,8 \cdot 10^{-6} \text{ mho/m} \\ \text{et pour un pH de 8, on obtient} \quad \sigma' &= 1,1 \cdot 10^{-5} \text{ mho/m} \end{aligned}$$

L'eau douce des lacs et des rivières qui n'est pas pure, présente une conductivité de (4 à 5) $\cdot 10^{-3}$ mho/mètre. C'est un conducteur médiocre.

8.4. La conductivité ionique de l'eau de mer

C'est celle de l'eau pure à laquelle s'ajoute celle produite par les sels dissous, de beaucoup principale.

Le problème est en principe résolu par la formule (66). Mais, il faut déterminer les mobilités qui varient elles-mêmes avec les concentrations. On peut, bien entendu, déterminer la somme des mobilités ($u_1 + u_2$) d'une paire d'ions d'un sel unique dissous, en mesurant la conductivité équivalente et, par d'autres méthodes, le rapport $u_1/(u_1 + u_2)$. On détermine ainsi les mobilités elles-mêmes. On trouve des valeurs petites, par exemple dans l'eau à 18°C la mobilité de l'ion H^+ est $33 \cdot 10^{-8}$ m/s et par V/m. Les ions se déplacent donc lentement.

On peut également, additionner les conductivités provenant de chaque sel en admettant une certaine composition en sels.

Il a paru intéressant de préciser davantage le mécanisme du passage du courant et d'expliquer le fait que la conductivité équivalente Λ d'un électrolyte fort diminue quand la concentration augmente. De la théorie des anomalies des électrolytes de Debye et Hückel, il résulte que le mouvement d'un ion particulier, à travers les particules chargées ou non du milieu, est ralenti par le mouvement en sens inverse du nuage d'ions de l'autre signe, qui l'entourent. Cette résistance particulière a été appelée "électrophorèse". A ce premier effet s'en ajoute un second, en régime alternatif, qui est dû au retard que prend le nuage d'ions qui se trouve centré en arrière de l'ion particulier considéré.

Ainsi, la conductivité Λ_0 est modifiée. On a finalement :

$$(76) \quad \Lambda = \Lambda_0 - (N_A q^2 \chi / 3\pi n) - (f' q^2 \Lambda_0 \chi / 12\pi \epsilon kT)$$

f' est un facteur numérique, qui dépend des q_B/u_B du ou des sels en cause, et $\chi = \left(\frac{2 N q^2}{\epsilon_r kT} \right)^{\frac{1}{2}}$; k est la constante de Boltzmann et T la température absolue.

La formule ci-dessus montre que les deux termes correctifs sont proportionnels à χ donc à \sqrt{C} , ce qui explique la loi expérimentale de Kohlrausch

$$(74) \quad \Lambda = \Lambda_0 - b \sqrt{C}$$

Si on calcule les termes correctifs de la formule pour le chlorure de sodium à la concentration $C = 1$ (une mole par m^3) et à 17°C en prenant $\eta = 1,09 \cdot 10^{-2}$ et $1/\chi = 9,66 \cdot 10^{-9}$ m, le premier terme vaut 0,155 mho/m et le second 0,078 mho/m. D'où finalement, une conductivité équivalente calculée de $10,666 \times 10^{-3}$ alors que la conductivité équivalente mesurée est de : $10,649 \times 10^{-3}$. L'accord est très bon, aux erreurs de mesure près.

L'équation (75) est parfaitement valable jusqu'à $C = 10$ et même au-delà, à condition d'ajouter des termes correctifs en $\log C$ et $C \log C$.

Dans un champ alternatif, la conductivité équivalente limite Λ_0 et le premier terme correctif ne sont pas affectés ; mais, le second terme correctif qui dépend du temps de relaxation diminue quand la fréquence augmente parce que la dissymétrie du nuage d'ions n'a plus le temps de s'établir. Λ augmente donc un peu avec la fréquence et pour une fréquence suffisamment élevée il ne subsiste plus dans (22) que la correction d'électrophorèse.

A la concentration équivalente totale de l'eau de mer $C \approx 620$ (moles/m³) le temps de relaxation d'un sel du type NaCl serait à 17°C

$$(77) \quad \tau = 1,08 \cdot 10^{-10} \text{ seconde}$$

Mais dans ces conditions de concentration, et aux fréquences supérieures à $1/\tau$, la variation de conductivité ionique est complètement masquée par la conductivité dipolaire.

Donc, en résumé, tout paraît se passer comme si, aux fréquences radio, la conductivité ionique de l'eau de mer ne dépendait pas de la fréquence ; mais, dépendait seulement de la concentration et de la température. Ceci étant, on peut en revenir aux résultats expérimentaux tels que ceux qui ont été présentés au tableau II.

On utilise couramment la mesure directe globale qui a largement remplacé les procédés de titration sur la plupart des navires océanographiques et dans les laboratoires.

Des relations empiriques entre la température, la salinité (la concentration totale en chlorures) et la conductivité ont été présentées par différents auteurs.

Weyl (1964) a rassemblé ces données par la relation suivante (2) :

$$(78) \quad \log \sigma' = -0,42373 + 0,892 \log Cl \text{ (o/oo)} \\ - 10^{-4} \tau \left[88,3 + 0,55 \tau + 0,0107 \tau^2 - Cl \text{ (o/oo)} \right. \\ \left. (0,145 - 0,002 \tau + 0,0002 \tau^2) \right]$$

σ' est la conductivité en mho/m

$\tau = 25 - t$, t est la température Celsius. La relation est valide pour les salinités (chlorinités) de 17 à 20 o/oo et les températures de 0 à 25°C, à la pression de 1 atm.

Les valeurs de σ' que l'on rencontre pour l'eau de mer sont de l'ordre de 3 à 5 mho/m.

9. L'EAU LIQUIDE EN REGIME HARMONIQUE (5)

9.1. Les méthodes expérimentales de mesure des caractéristiques e.m. de l'eau

Nous pouvons signaler l'importance de l'emploi du condensateur plan et du voltamètre dans un pont de Wheatstone. Ces dispositifs expérimentaux sont clairement utilisables en régime statique et aux très basses fréquences. Par contre, aux fréquences élevées lorsque par exemple l'écart entre les armatures du condensateur n'est plus très petit devant la longueur d'onde dans le milieu étudié, l'appareillage n'est plus utilisable dans les mêmes conditions.

On utilise alors des lignes bifilaires (ligne de Lecher), des coaxiaux ou des guides d'onde, qu'on fait plonger partiellement dans l'eau ou qu'on remplit partiellement d'eau. On observe alors, par l'intermédiaire d'une onde stationnaire, la longueur d'onde dans l'eau et le coefficient d'affaiblissement.

La ligne de Lecher (figure 4) est une ligne bifilaire verticale, excitée dans l'air par une boucle, à la fréquence f . On place dans l'air, en D, un appareil de mesure de tension alternative. La ligne plonge dans l'eau. L'énergie e.m. progresse vers le bas en une onde progressive qui est partiellement réfléchiée sur la discontinuité d'impédance à l'interface. Donc, si on place D verticalement, on constate des ondes stationnaires. On peut placer D un peu au-dessus de l'interface, à un noeud de tension. L'onde progressive franchit cependant la surface et progresse sur la ligne dans l'eau, où elle se perd si la ligne est suffisamment longue, qu'elle soit ouverte ou fermée sur un court-circuit C. Si on rapproche le court-circuit C de la surface B, en laissant immobile le détecteur D, on peut construire par points le graphique 2 (b), car l'onde réfléchiée sur le court-circuit crée une nouvelle onde stationnaire, amortie dans l'eau. On mesure ainsi la longueur d'onde sur la ligne dans l'eau λ_2 et l'atténuation $e^{-\alpha z}$ sur la ligne. On en déduit, d'après la théorie des lignes, l'impédance d'onde dans l'eau qui est directement liée à la permittivité complexe.

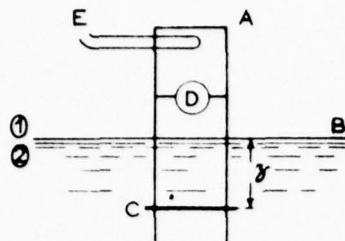


Fig. 4 (a) : Ligne de Lecher

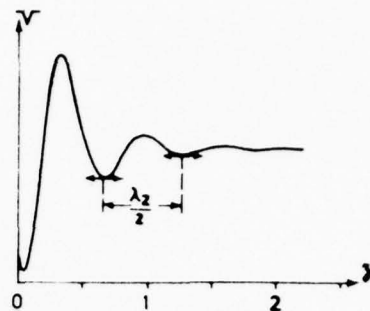


Fig. 4 (b) : Graphique de mesure

Aux longueurs d'onde décimétriques on peut utiliser des cavités résonnantes.

Dans une cavité, les champs doivent satisfaire l'équation d'onde

$$(79) \quad (\Delta + \bar{k}^2) \vec{U} = 0 \quad \text{avec} \quad (80) \quad \bar{k}^2 = \mu_0 \epsilon_0 \epsilon_r \omega^2$$

et satisfaire aux conditions aux limites sur les parois. Si la cavité est entièrement remplie d'un liquide de conductivité nulle et de permittivité réelle ϵ_r , la constante de propagation étant donnée, la fréquence de résonance est divisée par $\frac{1}{\sqrt{\epsilon_r}}$. Pour retrouver la même fréquence de résonance qu'avant le remplissage, il faudrait réduire les dimensions de la cavité dans le rapport $\frac{1}{\sqrt{\epsilon_r}}$. Ce faisant, on augmenterait les pertes par effet Joule dans les parois. En effet, ces pertes sont proportionnelles à σ/ℓ (σ étant la conductivité et ℓ une dimension de la cavité). Ainsi, la surtension serait réduite dans le rapport $\frac{1}{\sqrt{\epsilon_r}}$. En outre, si le liquide avait une conductivité non nulle, la surtension serait diminuée encore et la nouvelle surtension aurait pour valeur approximative :

$$(81) \quad \frac{1}{Q} = \frac{\sqrt{\epsilon_r}}{Q_0} + \frac{\epsilon''}{\epsilon'}$$

Pratiquement, on choisit une cavité de fort coefficient de surtension Q_0 . On y introduit un échantillon de l'eau à observer. On mesure alors un déplacement de la fréquence de résonance de la cavité et une diminution du coefficient de surtension ce qui permet de calculer la partie réelle et la partie imaginaire de la permittivité complexe de l'échantillon. L'échantillon doit être suffisamment petit pour que les deux effets soient bien découplés et permettent deux mesures indépendantes.

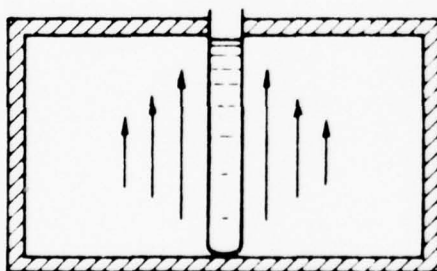


Fig. 5 : Cavité résonnante cylindrique en mode TM_{010} avec un tube échantillon axial.

On peut utiliser par exemple le mode TM_{010} du cylindre circulaire droit (figure 5). Dans ce mode, le champ électrique présente une symétrie axiale et est maximum au centre le long de l'axe de la cavité. La symétrie cylindrique peut être maintenue en introduisant l'échantillon dans un tube cylindrique centré sur l'axe. La fréquence de résonance ne dépend que des diamètres de la cavité et du tube échantillon. Elle est indépendante de leur hauteur, aussi longtemps que le tube d'échantillon ne dépasse pas les parois de la cavité.

Aux longueurs d'ondes centimétriques, on utilise des méthodes dites optiques qui consistent à mesurer le coefficient de réflexion à la surface du liquide en incidence normale ou en oblique. On utilise des antennes ou projecteurs e.m. de dimensions réduites. On mesure $R_{||}$ et R_{\perp} . On peut étalon-

ner l'appareillage en remplaçant dans la cuve l'eau par du mercure. On mesure l'absorption séparément par la traversée d'une lame d'eau d'épaisseur fixe. Les quantités mesurées sont liées aux caractéristiques e.m. principales du milieu.

Aux longueurs d'onde submillimétriques (HASTED, J.B.) (2) on utilise une source rayonnant un continuum. La lumière de la source est dirigée sur un interféromètre de Michelson à deux faisceaux. L'échantillon de matière est placé dans un des bras de l'interféromètre. Pour les matériaux très absorbants comme l'eau on remplace le miroir de l'un des bras par une surface plane de l'échantillon. On enregistre un interférogramme, qui est fonction de la différence des chemins. On déduit l'indice de réfraction (Réel \bar{n}) et l'indice d'extinction χ , sur une large bande de fréquences de la transformée de Fourier de l'interférogramme.

L'interféromètre développé par le laboratoire national britannique de physique est représenté sur la figure (6). Le mouvement du miroir M_1 , augmente la différence x des chemins optiques de $-D$ à $+D$ et produit un signal lentement variable dont la partie variable est appelée interférogramme. Si le miroir M_2 est déplacé de $\lambda/8$, où λ est la longueur d'onde, la variation de signal qui en résulte est enregistrée. L'enregistrement est appelé interférogramme modulé en phase.

En l'absence de l'échantillon W , l'interférogramme de référence $G_0(x)$ est enregistré. Quand l'échantillon est introduit un interférogramme $G(x)$ est observé. C'est le produit de convolution de la fonction réponse de l'échantillon $V(x)$ et de l'interférogramme de référence :

$$(82) \quad G_\phi(x) = V(x) \star G_{0\phi}(x)$$

Il résulte des propriétés des transformées de Fourier que :

$$(83) \quad \bar{S}_\phi(v) = \bar{R}(v) \bar{S}_{0\phi}(v)$$

$$\text{où : } (84) \quad \bar{R}(v) = \left[\bar{n}_w + \bar{n}_L(v) \right] / \left[\bar{n}_w - \bar{n}_L(v) \right]$$

est le coefficient de réflexion complexe de l'échantillon.

$\bar{n}_L(v)$ est l'indice de réfraction complexe du liquide, \bar{n}_w l'indice de réfraction de la fenêtre transparente. $\bar{S}_{0\phi}(v)$ et $\bar{S}_\phi(v)$ sont les spectres de puissance en l'absence et en présence de l'échantillon, respectivement.

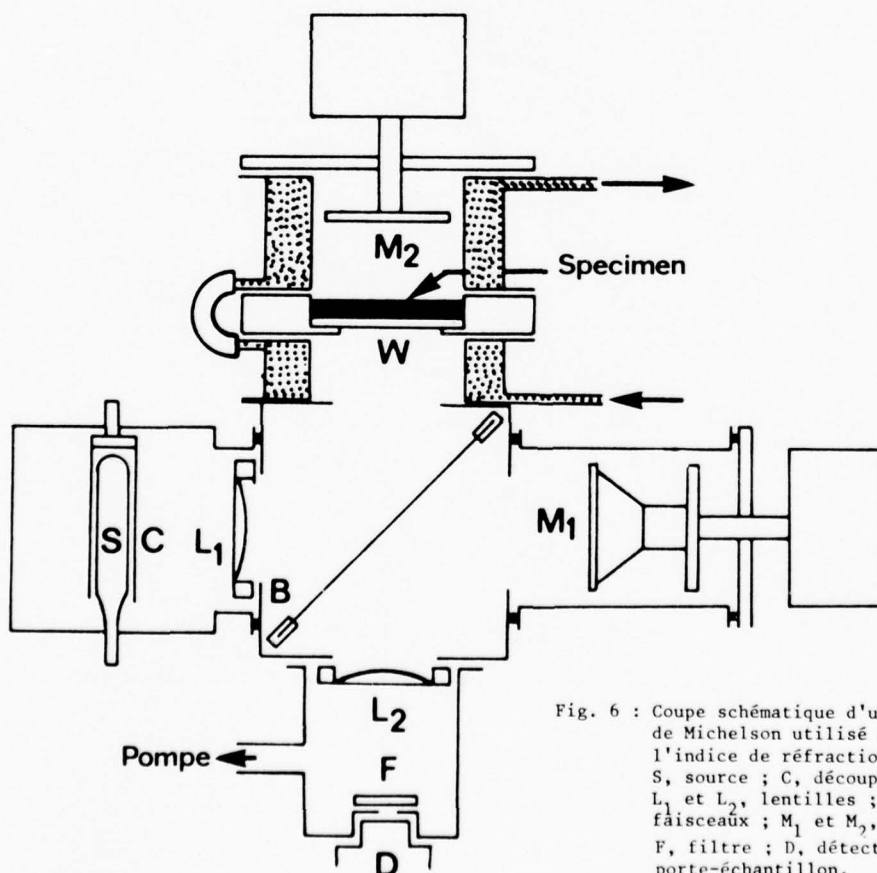


Fig. 6 : Coupe schématique d'un interféromètre de Michelson utilisé pour la mesure de l'indice de réfraction complexe de l'eau. S, source ; C, découpeur mécanique ; L_1 et L_2 , lentilles ; B séparateur de faisceaux ; M_1 et M_2 , miroirs ; F, filtre ; D, détecteur ; w, fenêtre porte-échantillon.

9.2. L'exploitation des résultats expérimentaux associés aux équations de Debye (52)(53)(54) :

Pour l'eau pure il existe un bon accord entre les résultats expérimentaux (voir figures 7-a et b).

- La valeur ϵ_S est bien connue (Saxton, Lane, Hasted, Ritson, et autres ...)

Les travaux de Malmberg et Margott (10) conduisent à la formule (82), à la pression atmosphérique :

$$(85) \quad \epsilon_S = 87,740 - 0,4008 t + 9,398 \times 10^{-4} t^2 - 1,410 \times 10^{-6} t^3$$

où t est la température en $^{\circ}\text{C}$ entre 0 et 100° . L'erreur maximale est de $\pm 0,005$

ONSAGER (9), KIRKWOOD (7), FROHLICH (8) et d'autres auteurs ont largement amélioré la théorie initiale, en considérant en particulier l'effet des moments dipolaires des molécules voisines sur la molécule considérée.

- La valeur ϵ_{∞} est plus discutée. La meilleure estimation paraît être $\epsilon_{\infty} = 5,5$

La longueur d'onde de transition est une fonction de la température.

On trouve par exemple :

$t^{\circ}\text{C}$	0	20	40
λ_t (cm)	3,15	$1,75 \pm 0,05$	1,05

Citons à titre d'exemple les résultats de Y. LEGRAND (5) calculés pour l'eau pure à la température de 17°C .

L'expérience donnant $\epsilon_S = 81,5$

, en adoptant $\epsilon_{\infty} = 5,5$

et $\lambda_t = 1,8 \text{ cm}$ ($\tau' = 0,96 \cdot 10^{-11} \text{ s.}$)

, il trouve les résultats présentés dans le tableau III

Pour l'eau de mer, on ne dispose malheureusement pas d'un aussi grand nombre d'expériences. Les résultats sont néanmoins nettement en faveur de la théorie. On peut admettre que l'indice d'extinction χ et le coefficient d'absorption δ dépendent surtout de la conductivité ionique aux fréquences inférieures à quelques Gigahertz. Voir, à titre d'exemple, les résultats présentés sur les figures 8 (a) et (b) (6). On constate, sur la figure 8 (a), que les résultats obtenus pour les différentes concentrations de NaCl sont exactement alignés sur une droite passant par l'origine. Les résultats pour l'eau de mer sont également alignés, mais sur une droite déduite de la droite NaCl par une translation. Ce déplacement est certainement dû à la présence des autres ions. Le fait que la droite des échantillons de mer ne passe pas par l'origine des coordonnées, laisse penser qu'il existe dans l'eau de mer un composant qui ne peut être représenté par une concentration en chlorures équivalents et qui contribue aux propriétés diélectriques de cette eau (15).

Cependant, les mesures confirment bien que les propriétés diélectriques de l'eau de mer ϵ' et ϵ'' peuvent être rattachées à une seule caractéristique : la salinité.

Citons encore, à titre d'exemple, les résultats de Y. LEGRAND calculés pour l'eau de mer à la température de 17°C présentés dans le tableau IV.

9.3. L'eau liquide aux fréquences inférieures à 1 000 GHz

L'eau pure (figure 9) :

À toute fréquence inférieure à 1 GHz, ϵ' ne dépend que de la température (à 17°C , $\epsilon' = 81,5$).

Lorsque la fréquence augmente de 1 à 1 000 GHz, ϵ' diminue et tend vers 5,5. L'absorption augmente, passe par un maximum vers 17 GHz puis diminue.

L'eau de mer (figure 10) :

À toute fréquence inférieure à 1 GHz, ϵ' ne dépend que de la température et a presque la même valeur que pour l'eau pure (à 17°C , $\epsilon' = 80,5$) et σ' varie très peu.

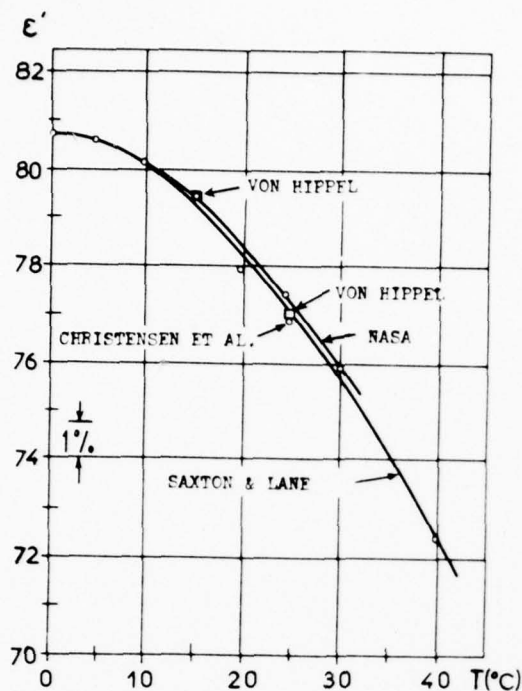


Fig. 7 (a): ϵ' pour l'eau pure en fonction de la température à 2,653 GHz (NASA - CR 1960) (15)

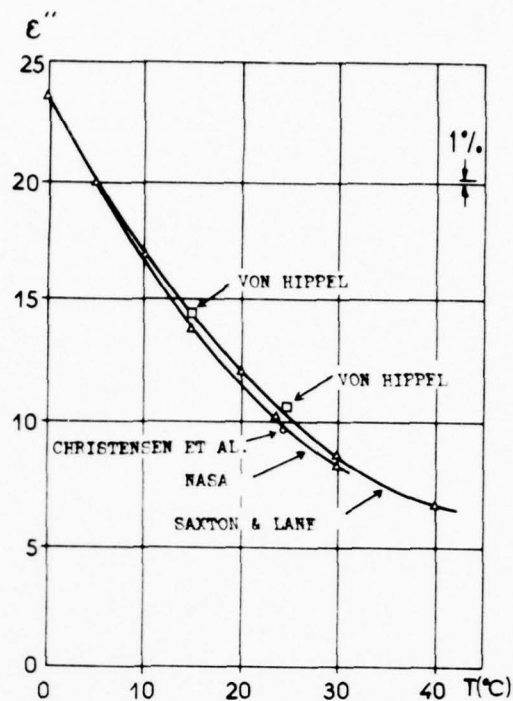


Fig. 7 (b): ϵ'' pour l'eau pure en fonction de la température à 2,653 GHz (NASA - CR 1960) (15)

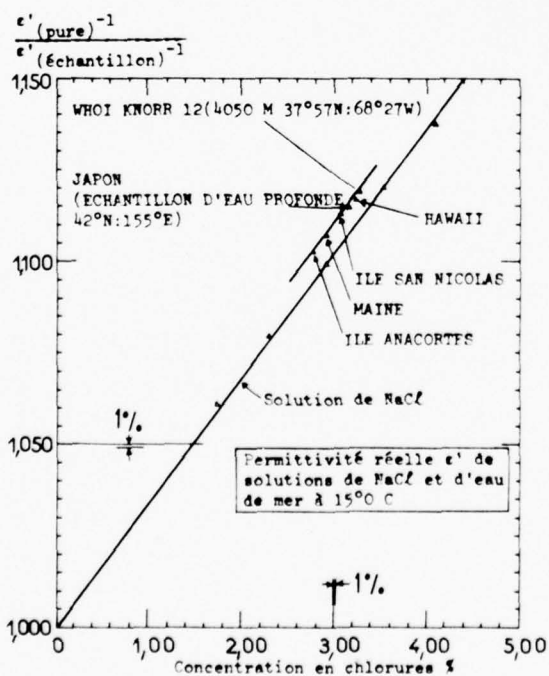


Fig. 8 (a):

Valeurs de $\epsilon' - 1$ relatives à la valeur $\epsilon' - 1$ de l'eau pure en fonction de la salinité à 15°C pour des solutions de chlorure de sodium et pour des échantillons d'eau de mer, à 2,653 GHz (NASA - CR 1960) (15)

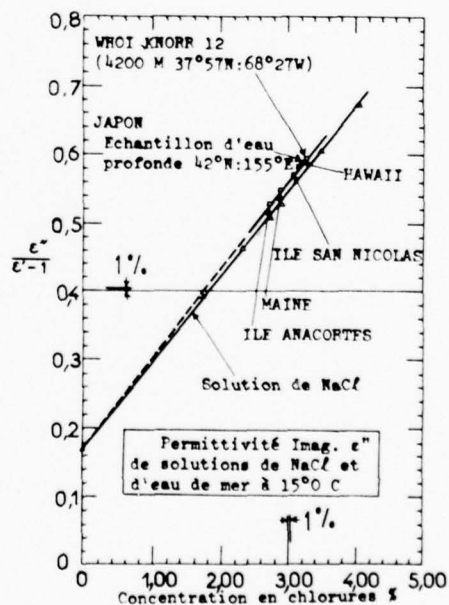


Fig. 8 (b):

$\epsilon''/(\epsilon' - 1)$ pour des solutions de NaCl et des échantillons d'eau de mer) 15°C, à 2,653 GHz (NASA - CR 1960) (15)

TABLEAU 111

Fréquence f (Hz)	Longueur d'onde λ	Permittivité		Conductivité dipolaire σ'' (mho/m)
		ϵ'	ϵ''	
0	∞	81,5	0	0
10^7	30 m	81,5	0,0	$0,25 \cdot 10^{-4}$
$2 \cdot 10^7$	15	81,5	0,1	$1,01 \cdot 10^{-4}$
$5 \cdot 10^7$	6	81,5	0,2	$0,60 \cdot 10^{-3}$
10^8	3	81,5	0,5	$0,25 \cdot 10^{-2}$
$2 \cdot 10^8$	1,5	81,5	0,9	$1,01 \cdot 10^{-2}$
$5 \cdot 10^8$	0,6	81,4	2,3	$6,33 \cdot 10^{-2}$
10^9	30 cm	81,2	4,5	$2,51 \cdot 10^{-1}$
$2 \cdot 10^9$	15	80,4	9,0	$9,96 \cdot 10^{-1}$
$5 \cdot 10^9$	6	75,2	20,9	5,75
10^{10}	3	61,4	33,5	18,5
$1,7 \cdot 10^{10}$	$1,8 (\lambda_c)$	43,5	38,0	34,8
$5 \cdot 10^{10}$	0,6	13,1	22,8	62,7
10^{11}	3 mm	7,6	12,3	67,6
$2 \cdot 10^{11}$	1,5	6,0	6,2	68,6
$5 \cdot 10^{11}$	0,6	5,6	2,5	69,6
10^{12}	0,3	5,5	1,3	69,6
∞	0	(5,5)	0	(69,6)

Permittivité et conductivité dipolaire de l'eau pure à 17°C en fonction de la fréquence (5)

TABLEAU IV

Fréquence f (Hz)	Longueur d'onde λ	Permittivité		Conductivités (mho/m)		
		ϵ'	ϵ''	ionique σ'	dipolaire σ''	totale σ
0	∞	80,5	∞	4,54	0	4,54
10^8	3 m	80,5	818	4,54	0,00	4,54
$2 \cdot 10^8$	1,5	80,5	410	4,54	0,01	4,55
$5 \cdot 10^8$	0,6	80,4	166	4,54	0,07	4,61
10^9	30 cm	80,3	86,6	4,55	0,26	4,81
$2 \cdot 10^9$	15	79,3	50,1	4,56	1,01	5,57
$5 \cdot 10^9$	6	72,5	37,6	4,64	5,81	10,45
10^{10}	3	59,5	40,2	4,75	18,69	23,44
$1,7 \cdot 10^{10}$	1,5	42,1	43,3	4,84	35,26	40,10
$5 \cdot 10^{10}$	0,6	12,6	24,6	5,00	63,32	68,32
10^{11}	3 mm	7,3	13,2	5,08	68,35	73,43
$2 \cdot 10^{11}$	1,5	5,8	6,7	5,13	69,30	74,43
$5 \cdot 10^{11}$	0,6	5,4	2,7	5,19	70,34	75,53
10^{12}	0,3	5,3	1,4	5,22	70,34	75,55
∞	0	(5,3)	0	(5,29)	(70,36)	(75,65)

Permittivité et conductivité de l'eau de mer à 17°C en fonction de la fréquence (5)

(ϵ'' désigne la partie imaginaire de $\bar{\epsilon}_r$ due à la polarisation)

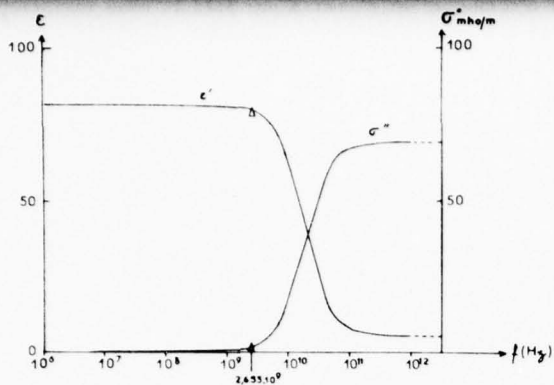


Fig. 9 :

Permittivité réelle ϵ' et conductivité dipolaire σ'' de l'eau pure à 17°C en fonction de la fréquence. (Voir tableau III. Les points à 2,653 GHz sont déduits des observations de la NASA (6)).

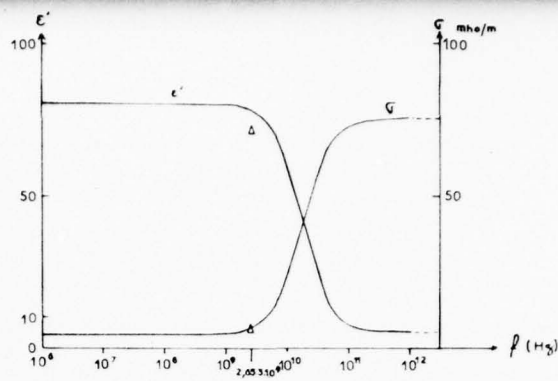


Fig. 10 :

Permittivité réelle ϵ' et conductivité σ de l'eau de mer à 17°C en fonction de la fréquence. (Voir tableau IV. Les points à 2,653 GHz sont ceux de la NASA. On remarquera l'écart entre la valeur ϵ' théorique et la valeur observée. Il y a dans l'eau des mers une substance qui n'est pas le chlorure de sodium et qui modifie la permittivité réelle.).

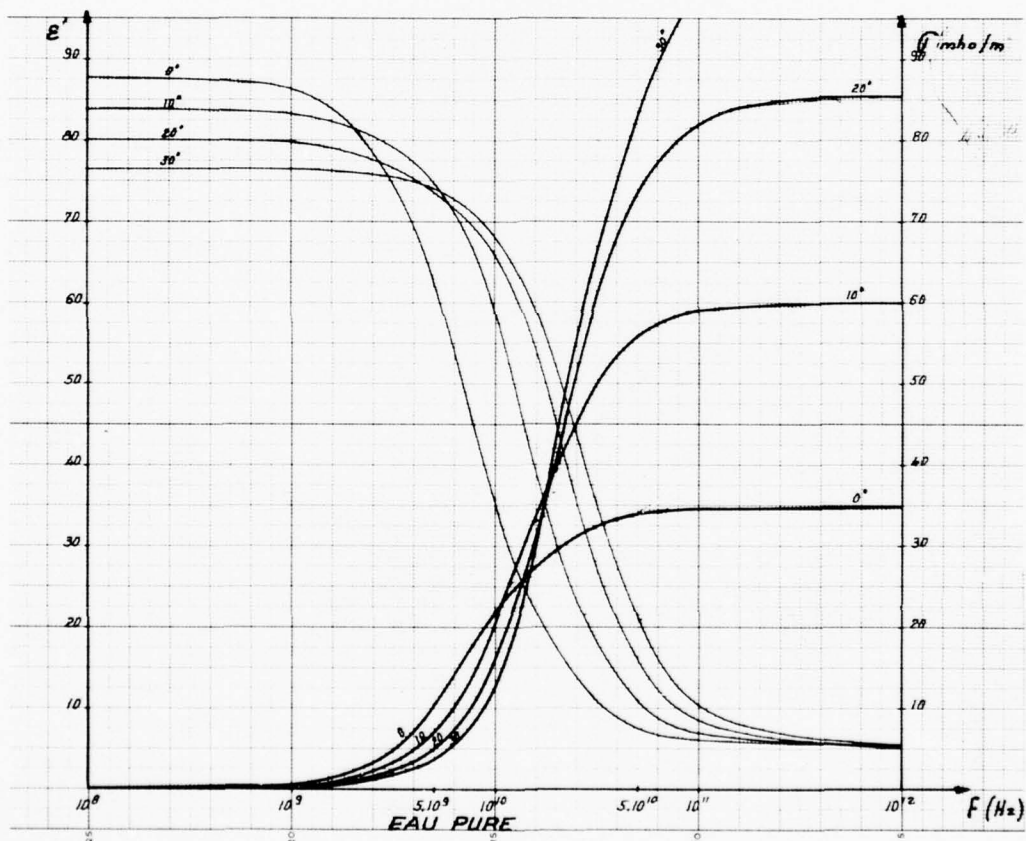


Fig. 11 :

Permittivité réelle ϵ' et conductivité dipolaire σ'' de l'eau pure entre 10^8 et 10^{12} Hz calculées au moyen de l'équation de Debye (53) pour : ϵ_s fourni par l'équation (85), $\epsilon_\infty = 5,5$ et τ égale $1,96 \times 10^{-12}$ à 0° ; $1,13 \times 10^{-12}$ à 10° ; $0,79 \times 10^{-12}$ à 20° et $0,63 \times 10^{-12}$ à 30°.

Lorsque la fréquence augmente de 1 à 1 000 GHz, ϵ' et σ'' ont à peu près la même variation que pour l'eau pure. La conductivité totale σ augmente. La conductivité dipolaire σ'' devient supérieure à la conductivité ionique lorsque la fréquence devient supérieure à 4 GHz.

9.4. L'eau liquide aux fréquences supérieures à 1 000 GHz (figure 12) :

Les équations de Debye à un seul temps de relaxation deviennent insuffisantes. Leur application conduit à supposer un certain étalement du temps de relaxation.

K. COLE et R. COLE (13) ont proposé de généraliser l'équation de Debye en écrivant la relation :

$$(86) \quad \epsilon_r = \epsilon_\infty + \frac{\epsilon_s - \epsilon_\infty}{1 + (j\omega\tau_0)^{1-\alpha}} \quad \text{avec} \quad (87) \quad \tau_0 = \frac{\epsilon_s + 2}{\epsilon_\infty + 2} \tau$$

où α est un paramètre empirique dont la valeur est comprise entre 0 et 1. On prend en général $\alpha = 0,02$ (14).

Les résultats sont alors sensiblement améliorés et on se rapproche des résultats expérimentaux à 313 et 152 μm .

λ (μm)	ϵ'	ϵ''
313	4,0	2,33
152	3,95	1,57
117	4,09	1,43
109	4,02	1,24
92	3,80	1,35
63	2,74	1,84
52	2,57	1,57

Tableau V

Permittivité électrique complexe de l'eau pure à 20 °C partie réelle et partie imaginaire aux longueurs d'onde submillimétriques, d'après différents auteurs (11).

SAXTON (12) pour mieux décrire la variation de ϵ' et ϵ'' aux longueurs d'ondes inférieures au mm., s'est appuyé sur la théorie de FRÖHLICH, au sujet des résonances d'absorption. On peut en effet, se poser la question de savoir s'il est préférable de considérer un ou plusieurs temps de relaxation de la molécule ou bien de considérer que le processus d'absorption se fait plutôt par résonance.

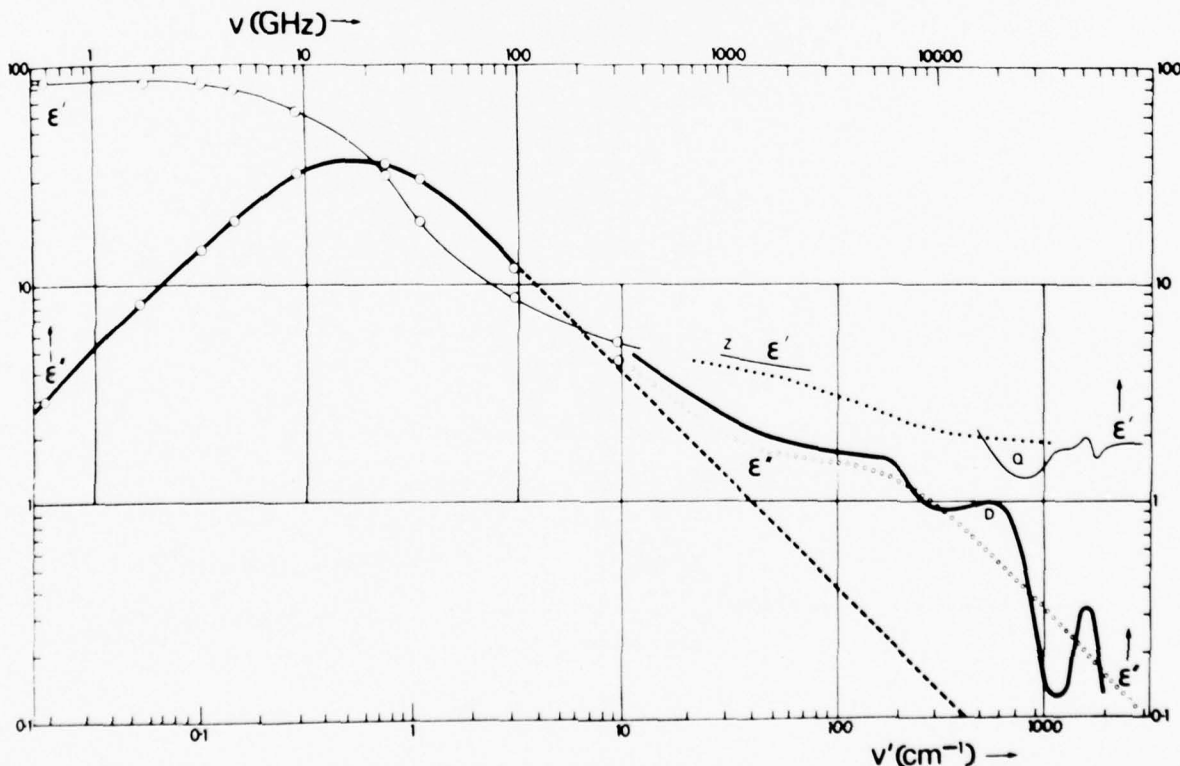


Figure 12 : Diagramme logarithmique de ϵ' (en trait de simple épaisseur) et de ϵ'' (en trait de double épaisseur) pour l'eau pure à 20 °C en fonction de la fréquence ν .

La ligne tiretée indique les valeurs de ϵ'' calculées au moyen de l'équation de Debye à un seul temps de relaxation. Les petits cercles indiquent les valeurs de ϵ' et ϵ'' calculées avec un deuxième temps de relaxation : $\lambda_2 = 0,008$ cm
Z, Q, D présentent des résultats expérimentaux. Z et Q pour ϵ' et D pour ϵ'' (HASTED, J.B.) (2).

Aux fréquences supérieures à 1 000 GHz la conductivité ionique est, elle aussi, affectée par l'inertie mécanique et tend à disparaître.

Le mouvement de l'ion a, en effet, pour équation :

$$(64) \quad m \frac{d\vec{V}}{dt} + mZ\vec{V} = q \vec{E}$$

En régime harmonique $\vec{E} = \vec{E}_0 e^{j\omega t}$ et $\vec{V} = \vec{V}_0 e^{j\omega t}$

L'équation (65) n'est pas admissible aux fréquences élevées.

$$\text{Mais} \quad \vec{V}_0 = q \vec{E}_0 m (Z + j\omega) = u \vec{E}_0 (1 + j\omega\tau)$$

avec le temps de relaxation $\tau = \frac{1}{Z} = \frac{qm}{u}$

Pour chaque ion on peut calculer ce temps. Pour Na par exemple, on trouve $1,1 \cdot 10^{-13}$ seconde. La longueur d'onde de transition est de 0,2 mm. Les dernières valeurs du tableau IV sont donc déjà affectées par l'inertie des ions.

10. LES CARACTERISTIQUES ELECTRIQUES DE LA GLACE (2) :

Les mécanismes suivants lesquels des molécules, des atomes ou des ions, peuvent se mouvoir dans ou à travers la glace posent au scientifique des problèmes difficiles. Malgré les progrès des techniques expérimentales modernes et leurs résultats, il est encore très difficile d'interpréter et de comprendre les aspects du mouvement de la molécule et du phénomène de relaxation que l'on observe

10.1. La glace aux fréquences inférieures à 1 GHz

La conductivité ionique de la glace d'eau douce est faible. Les mesures sont difficiles. Parmi les valeurs récemment mesurées on relève à -10°C

$$\sigma' = (1,1 \pm 0,5) \times 10^{-8} \text{ mho/m}$$

Les mesures de ϵ'_S et de $\epsilon(\omega)$, à différentes fréquences, procurent une information sur l'orientation des dipôles dans le réseau et partant sur le temps de relaxation τ .

Les mesures de ϵ'_S de -60 à 0°C montrent que ϵ'_S augmente lorsque la température diminue et que ϵ'_S mesuré perpendiculairement à l'axe c du cristal est plus petit de 10 % que ϵ'_S mesuré parallèlement à l'axe c.

A 0°C , ϵ'_S pour la glace polycristalline est de 10 % plus grand que pour l'eau liquide.

DAVIDSON et WALLEY ont trouvé que la valeur de ϵ'_S augmente avec la pression pour toutes les variétés de glace polymorphes à l'exception de la glace II et de la glace VIII.

Des valeurs de ϵ'_S , ϵ_∞ et τ sont présentées dans le tableau VI. On constate que la mobilité dipolaire se maintient aux pressions élevées.

Tableau VI - Caractéristiques diélectriques de la glace (FRANKS, F.) (2).

Glacé (phase)	Température (°C)	Pression (kbar)	ϵ'_S	ϵ_∞	τ ($\mu\text{S.}$)
I	- 23,4	6×10^{-6}	97,5	3,1	168
	- 23,4	1,6	101	-	213
	- 30	6×10^{-6}	99	3,2	-
II	- 30	2,3	3,66	3,66	-
III	- 30	2,3	117	4,1	2,75
	- 100	2,3	-	3,96	-
V	- 30	5	144	4,6	7,2
VI	- 30	8	193	5,1	≈ 6
	22	21	-	-	48
VII	22	21,4	-	-	0,23
IX	- 100	2,3	3,74	3,74	-

Rappelons que les conditions de température et de pression à la surface de la terre, ou au voisinage, sont telles, que seule la première forme I de la glace s'y trouve. C'est la technologie des hautes pressions qui permet de produire en laboratoire les glaces II, III, etc..

Le tableau VI fournit, à titre documentaire, des informations sur les caractéristiques diélectriques de ces glaces.

Pour les glaces II et IX on peut remarquer, d'une part que les valeurs de ϵ_S sont faibles, d'autre part que les valeurs de ϵ_∞ sont égales à celles de ϵ_S ; ce qui signifie que les dipôles moléculaires sont gelés ou bloqués et ne peuvent pas s'orienter sous l'action d'un champ électrique extérieur. Ces glaces sont, par conséquent, largement transparentes aux ondes e.m.. ϵ'' est identiquement nul et seule peut intervenir la conductivité ionique σ' .

Pour la glace I qui est pratiquement la seule intéressante, il est possible d'appliquer les équations de Debye et de calculer les valeurs de ϵ' et ϵ'' dans une large bande de fréquences et jusqu'à 1 GHz environ.

Cependant, les équations à un ou plusieurs temps de relaxation ne permettent pas de décrire les données expérimentales recueillies à 10^{10} Hz (soit 3 cm de longueur d'onde) d'une manière satisfaisante

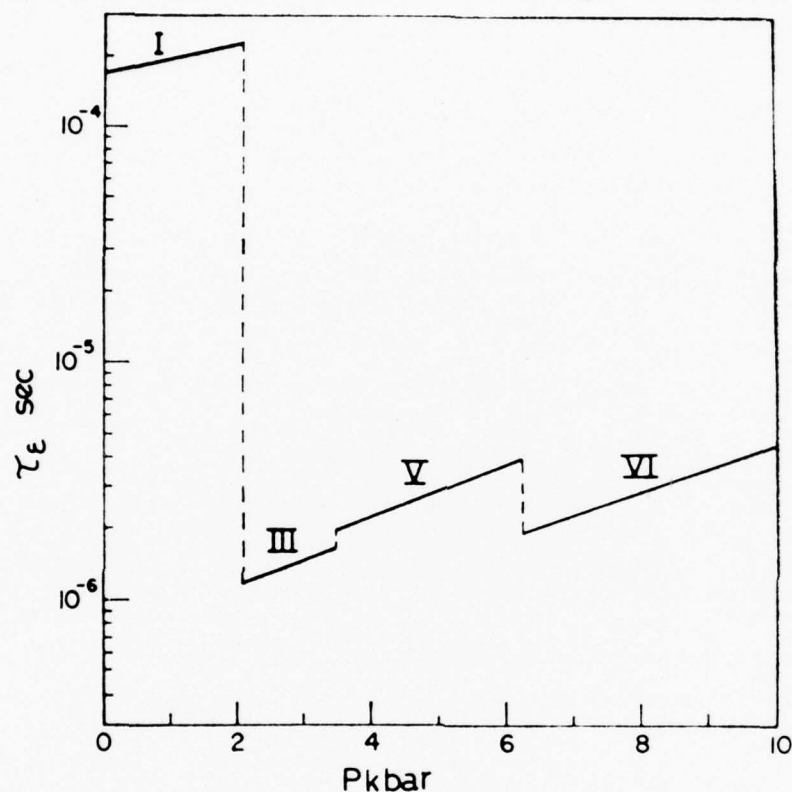


Figure 13 : Temps de relaxation à $-23,4^\circ\text{C}$ pour les glaces I, III, V et VI en fonction de la pression. Noter le comportement similaire des glaces III, V et VI dû probablement à des structures similaires (FRANKS, F.) (2).

En appliquant la théorie de KIRKWOOD, bien que strictement parlant elle ne soit pas applicable à un milieu tel que la glace et en tenant compte de trois couches de molécules voisines (au total 84), on parvient aux valeurs suivantes $\mu = 2,6$ D pour la glace I (paramètre de corrélation de KIRKWOOD $g \approx 3$).

10.2. La glace et la neige à 10 GHz :

Les mesures aux fréquences supérieures à 10^{10} Hz sont très peu nombreuses. Les tableaux VII et VIII fournissent les valeurs de l'indice de réfraction à 3,2 cm pour la glace et la neige.

Tableau VII - Valeurs de la partie réelle $R_e(n)$ et de la partie imaginaire $I_m(n) = \chi$ de l'indice de réfraction complexe de la glace à différentes densités ρ pour différentes températures $t^\circ\text{C}$, mesurées à la longueur d'onde $\lambda = 3,2 \text{ cm}$ (17)

ρ (g/cm ³)	$R_e(n)$	$\chi \cdot 10^4$ à $t^\circ\text{C}$									
		0	- 2	- 4	- 6	- 8	- 10	- 12	- 14	- 16	- 18
0,916	1,78	23,0	16,0	12,0	10,5	8,9	7,7	7,1	6,6	6,3	6,1
0,76	1,65	14,8	10,7	8,7	7,4	6,4	5,8	5,4	4,9	4,7	4,4
0,60	1,50	10,3	7,5	6,0	5,2	4,5	4,3	3,9	3,7	3,3	3,0
0,46	1,38	6,9	4,8	4,1	3,4	3,1	2,8	2,6	2,5	2,5	2,5
0,38	1,31	5,2	3,9	3,3	2,6	2,4	2,3	2,2	2,1	2,0	1,8
0,34	1,27	5,0	3,7	3,0	2,3	2,0	1,9	1,8	1,6	1,4	1,3

Nota : $R_e(n)$ ne dépend pas de la température. En effet, à ces fréquences élevées

$$\epsilon' = R_{e2}^2(n) + \chi^2 \text{ est voisin de } \epsilon_\infty, \text{ qui ne dépend pas de la température.}$$

Enfin χ^2 est petit devant $R_{e2}^2(n)$.

Tableau VIII - Valeurs de la partie réelle $R_e(n)$ et de la partie imaginaire $I_m(n) = \chi$ de la neige humide à 0°C , en fonction du poids par unité de volume d'une part et du pourcentage p d'eau (en poids) d'autre part, mesurées à la longueur d'onde $\lambda = 3,2 \text{ cm}$. (17)

ρ g/cm ³	$R_e(n)$	$\chi \cdot 10^4$ à $p \%$								
		0	0,2	0,4	0,6	0,8	1,0	1,2	1,4	1,6
0,38	1,31	5,2	13,7	26,2	38,0	54,4	73,4	89,7	112,0	134,0
0,76	1,65	14,8	33,8	55,3	90,1	131,3	179,0	242,0	304,0	371,0

Il apparaît que la glace et une couche de neige de même densité ont essentiellement la même constante diélectrique.

REFERENCES

- 1 STRATTON, J.A. Théorie de l'électromagnétisme
 (traduit par HEBENSTREIT J.) - Dunod - Paris 1961
- 2 FRANKS, F. Water a comprehensive treatise
 Volume 1 - The physics and physical chemistry of water
 Plenum Press - New York, London 1972
- 3 GUINIER, G. Eléments de physique moderne théorique
 Bordas - Paris 1950
- 4 LUCK, W.A.P. Structure of water and aqueous solutions
 Proc. of the international symposium held at Marburg
 in July 1973
 Verlag chemie, Physic verlag
- 5 HALLEY, P.M. Introduction à l'électromagnétisme des mers
 AGARD Lecture Series N° 61
 OPTICS OF THE SEA
- 6 RICHARDS, F.A. Chemical and biological factors in the marine environment
 Chap. 8 of OCEAN ENGINEERING - Bratz, editor - Wiley
- 7 DARMOIS, E.
 DARMOIS, G. Electrochimie theorique
 Masson, Paris 1960
- 8 KIRKWOOD, J.G. J. Chem. Phys. 4,592 (1936)
- 9 FRÖHLICH, H. "Theory of dielectrics"
 Oxford university press (1949)
- 10 ONSAGER, L. J. Am. Chem. Soc. 58, 1486 (1936)
- 11 MALMBERG, C.G.
 MARYOTT, A.A. J. Res. Natl. Bur. Std. 56,1 (1956)
- 12 MAGAT, M.M. On the dielectric dispersion of liquid water
 J. Chimie physique, Physico-chimie biologique
 Vol. 45, N° 4 (1948)
- 13 SAXTON, J.A. Dielectric Dispersion in pure polar liquids at very
 high radio frequencies
 II Proc. Roy. Soc., Ser. A, Vol. 213 N° 1115 (1952)
- 14 COLE, K.
 COLE, R. Dispersion and absorption in dielectrics
 J. Chem. Phys. Vol. 9, N° 4 (1941)
- 15 HASTED, J.B. Dielectric properties of water
 Progress in dielectrics, Vol. 3 (1961)
- 16 HIDY, GM
 HALL, W.F.
 and others Development of a satellite microwave radiometer to sense
 the surface of the world oceans
 NASA Report CR - 1960 (1972)
- 17 CUMMING, W.A. The dielectric properties of ice and snow at 3,2 cm
 J. Appl. Phys., Vol 23 N° 7 (1952)
- 18 EVANS, S. Dielectric properties of ice and snow. A review
 J. Glaciol. Vol. 42 p. 773 - 792 (1965)

DISCUSSION

H.J. Albrecht: Referring to lake-water impurity and possible effects of large lakes upon propagation paths, would present information be adequate and significant for communication-link planning?

P.M. Halley: Certainement, dans la mesure où la surface du lac intervient dans la propagation. Les coefficients de réflexion par exemple peuvent être calculés à partir de la permittivité électrique $\epsilon(\omega)$. Il faut connaître la température T et, pour au moins une température, connaître la conductivité ionique par une mesure statique σ_s . Pour les lacs de montagne dont l'eau est pure et pour les lacs salés on peut se contenter d'une estimation de σ_s . Les lacs d'eau douce peuvent recevoir pendant et après la pluie des eaux de ruissellement qui apportent temporairement une abondance supplémentaire d'ions provenant d'éléments minéraux.

REVIEW PAPER: DETERMINATION OF THE EARTH'S RESISTIVITY BY SURFACE MEASUREMENTS

H. Flathe
Federal Institute for Geosciences
and Natural Resources (BGR)
Stilleweg 2, Alfred Bentz Haus
3000 Hannover 51
Germany

SUMMARY

The resistivity distribution below the earth's surface is of more or less high interest for many branches of natural science and engineering as well. In geoscience great efforts have been made by geophysicists to get quantitative insight into the geological structure of the subsurface by using the electric resistivity as physical parameter. Measuring techniques and interpretation methods having been developed since half a century resulted to a very high standard to-day. Analysing a layered earth regarding its resistivity distribution down to several hundred meters depth is no problem. This fact often not well known in neighbour disciplines is demonstrated in this review paper outlining the possibilities and limitations of the methods available nowadays. After a short introduction into the principle of geoelectrical sounding practical results are shown by case histories from some selected parts of the world. The main conclusion is that low resistivities ($< 50 \text{ ohm.m}$) predominate at the surface even in arid areas and deserts. The reason for this surprising fact is the clayey and saline component within the top-layers. It is discussed in detail with respect to draw near surface resistivity map from large areas.

1. INTRODUCTION

Geophysicists working within a geological survey are often asked for a regional or even world-wide map of geoelectric near-surface resistivities. The aim of this paper is after giving a short insight into the modern techniques of direct current resistivity sounding to outline the difficulties in preparing such general maps. From selected case histories the reader may study the different situations and draw his own conclusions.

2. THE PRINCIPLE OF DIRECT CURRENT RESISTIVITY SOUNDING

To determine the electric resistivity ϱ (ohm.m) of the subsoil WENNER (1916) and C. and M. SCHLUMBERGER (1920) proposed the so-called "four-point"-method. This method was developed during the following decades to a nearly perfect standard with regard to instruments, field techniques and interpretation as well. Today there is no limit in matching field data recorded above any number of underground layers quantitatively down to any depth z^+ . Routine work is done since nearly half a century to solve mainly hydrogeological problems, i.e. geoelectrical prospecting on a more or less horizontally stratified underground down to a depth of several hundred meters. Although this paper is not the right place to explain the method at least the principle should be shown because without knowing what a "sounding graph" means a reader not accustomed to the method may not understand the following case histories.

Looking at Fig. 1 we see the artificial electrical field built up in a homogeneous earth by introducing a direct current of intensity I (Amp.) via two current electrodes A and B. The "current lines" are marked by arrows. Perpendicular equipotential lines cause a potential distribution at the earth's surface which depends on the resistivity ϱ of the homogeneous underground. From recording the voltage U (Volt) between two potential electrodes M and N in the center between A and B we can calculate from Maxwell's theory the resistivity ϱ by

$$\varrho = K \frac{U}{I} \quad \text{with} \quad K = \frac{\pi}{a} \left[(L/2)^2 - (a/2)^2 \right] \quad (1)$$

where $L = \overline{AB}$ and $a = \overline{MN}$. K is known as the "geometric factor".

The step from the homogeneous earth to a layered one may be demonstrated in Fig. 2. This way is as simple as it is important for understanding the fundamental physical process in the underground. Two layers with resistivities ϱ_1 and $\varrho_2 \gg \varrho_1$ are separated by a plain horizontal interface at depth h . The current flow from A to B is marked by dotted lines in the vertical sections (on the left side of the figure) for different values of the depth h assuming $\varrho_2 = \infty$ (insulator). Looking at the current density j at the surface in the center of the arrangement (M and N are not plotted) we observe that by decreasing h the current is "pressed" against

z^+ f.i. recently down to the Upper Mantle in SE-Africa ($\overline{AB} = 1300 \text{ km}$; see below)

the surface. From Maxwell's equations we know that

$$U_{MN} = j \varrho_1 \quad (2)$$

This is Ohm's Law in infinitesimal form, generally written as $\vec{E} = \vec{j} \varrho$, where \vec{E} is the electric field vector and \vec{j} the vector of the current density.

As ϱ_1 is constant in our case the voltage U_{MN} recorded at the surface between the potential electrodes M and N is directly proportional to the current density j between M and N "just below our feet". And this is the only information we get from the subsoil; nothing else!

Looking at the right hand side of Fig. 2 we find the same situation but concerning now the reality of geology: The depth h is fixed! On the left hand side L was fixed and h decreased, enlarging the current density j between M and N and proportionally the voltage U . On the right hand side h is fixed. Enlarging L we get the same ratio $\frac{L}{h}$. And this is the fundamental principle of electrical sounding: Prospecting a layered earth we pull the deeper underground upwards simply by enlarging the distance L of the current electrodes A and B. KRAJEV (1952) mentioned this fundamental fact in a short note (without any figure) in his textbook (German edit. 1957). In anglo-american textbooks we read that enlarging the current electrode spacing means "deeper penetration" of the current and this is the reason why during recording in the field geologists always ask: "How deep are you now?" -

Krajew has clearly demonstrated that a resistivity sounding is somehow "zooming" the layered earth by enlarging $AB = L$. Consequences drawn from this principle are:

- 1) the logarithmic scale, because ratios are concerned
- 2) the "smooth" sounding graph, because "zooming" is a steady process.

Here is a break because until now there has not been defined the sounding graph. Formula (1) gives an expression for the resistivity ϱ of a homogeneous earth. Formula (2) shows that U is changing when zooming a layered underground. Setting this U from (2) into (1) we will get an ascending branch of $\varrho (\frac{L}{2}/h)$. ϱ from formula (1) is no more a constant as it was in the case of a homogeneous earth. It smoothly ascends from ϱ_1 to ϱ_2 as demonstrated at the bottom of Fig. 2. This means that we are using a wrong formula resulting only asymptotically in "true" values of ϱ at the beginning (ϱ_1) and at the end (ϱ_2). In between the graph calculated by formula (1) shows "apparent" resistivities depending on the electrode configuration (L , a) and the soil parameters (ϱ_1, ϱ_2, h). Per definition we get the formula for the "apparent" resistivity ϱ_a)*

$$\varrho_a^{(a)}(L/2)_{\text{def.}} = K \frac{U}{I} \quad (3)$$

This definition was chosen because in the case of a homogeneous underground it results into formula (1).

Finally a four layer-case is shown in Fig. 3 demonstrating the zooming as a "push-pull" process caused by the layer sequence from its true parameters ϱ_i and h_i . An explanation in detail is not necessary. On top of this figure we find the vertical section with its influence on the current density j between M and N. In the lower part of the figure we see the smooth sounding graph. Here the $L/2$ -scale is (on top) taken as depth-scale simultaneously. This is done by convention, but the reader will observe that the interfaces at 2,6 and 26 m are not corresponding with the maximum and minimum in the sounding graph. To find out sharp boundaries between the layers from a smooth graph is the problem of the interpreters. Some remarks on this mathematical problem are given in the next chapter.

3. INTERPRETATION

The problem to be solved is the calculation of the "true" resistivity distribution in a layered earth $\varrho(z)$, where z is the depth, from the "apparent" resistivities $\varrho_a(L/2)$ recorded at the earth's surface. This is done by theoretically calculated master curves published either in Wenner arrangement ($a = L/3$) or in Schlumberger configuration ($a \rightarrow 0$), i.e. either $\varrho_a^{(L/3)}$ or $\varrho_a^{(0)}$. In the following we refer only to Schlumberger: $MN = a$ is infinitesimally small compared with $AB = L$ ($a \ll L$) and introduce $\varrho_a^{(0)} = \varrho_a$ (or ϱ_s in some case histories). Since 1930 nearly all theoretical work is based on STEFANESCU'S integral

$$\varrho_a(L/2) = \varrho_1 \left[1 + 2(L/2)^2 \int_0^\infty \theta(\lambda, h_i, \varrho_i) J_1(\lambda \cdot L/2) \lambda d\lambda \right] \quad (4)$$

where J_1 is the Bessel-function of the 1st order. The integral reduces to zero if a homogeneous earth is concerned. The kernel function θ is mathematically rather complicated. It was given only for the 3-layer case by Stefanescu himself. A quarter of a century later a recursion formula for θ was found in 1955 for the general n -layer case ($n > 3$) and started a new area in computing master curves for interpretation. A 10-layer graph takes less than 30 sec. today on a computer of the size of a type-writer. The computer belongs in between already to the field equipment; the interpretation

$$\varrho_a(L/2) \rightarrow \varrho(z)$$

is mathem.-physically nearly perfectly solved. The problem not yet solved is the translation

)* in German literature we shall find ϱ_s ("scheinbarer" Widerstand)

$$\rho(z) \longrightarrow \text{geology}$$

There is, compared with perhaps gravity and seismics, a wide scale. The variation of resistivities covers about 10 powers (0,1 - 10.000 ohm.m) thus being very sensitive against changes in petrography if a geological concept exists. This problem seems to be without interest to EM-wave propagation, because the question was to get first a picture of Ohm's resistivity ρ (DC). But from discussions the question is extended to AC. We must know whether a low resistivity is caused by saline or clayey sediments. What has to be done in future cannot be decided by the DC-geophysicist. In any case he can provide neighbour disciplines with information using his modern tools. The following chapters may be an offer for interdisciplinary cooperation.

4. CASE HISTORIES

To answer the question after providing interested disciplines with maps of the near-surface resistivity distribution the following examples are presented, selected from typical cases in different parts of the world. Since 1959 when the BGR was founded geoelectric prospecting mainly on groundwater was done all over the world. To select typical examples just concerning AGARD's problems was rather a hard job. The result is presented in a couple of figures. Each example states a special aspect. The author is not sure whether these aspects cover the scale of questions. It may, however, be regarded as an attempt to do something. -

As it is impossible to present a world-map showing the sites of these case histories the reader may look into special maps available. A short description will be given at the beginning of each case. The resumé will briefly be outlined at the end.

4.1. Kota Bharu/Kelantan (Malaysia).

The growing city of Kota Bharu lies in NE-Malaysia within the Delta of the Kelantan River close to the South China Sea. Here a geoelectrical survey, carried out in 1974 detected a deep freshwater aquifer not known before under clayey and saltwater bearing sands in the overburden. Fig. 4 shows a vertical section along a profile near to the coast of the South China Sea. It is the result of an interpretation of the set of sounding graphs given in Fig. 5)* using the geological concept from Fig. 6. Please notice the wide scale from 2 to 1000 ohm.m within the upper 10 m and below generally a good conductor to be seen in the curve minima. The true resistivities are plotted in the vertical section in Fig. 4. The ascending rear branches are caused by the deep freshwater aquifer.

This example demonstrates the degree of solution by modern geoelectrics (up to seven layers) and results in a top layer with resistivities between 2 and 1000 ohm.m underlain by a series consisting of saline beds and clay (1 - 20 ohm.m) down to an average depth of 50 - 70 m. Our question: Which resistivity values should be plotted in a resistivity map? The photos in Fig. 7 and 8 illustrate the situation at the surface.

4.2. Gunung Sewu/Java (Indonesia).

In Central Java SE of Djokjakarta a dry limestone area shows a morphology having no pendant all over the world. Karst in form of "sinoids" up to 60 m height cover a large area. The geological situation is shown in Fig. 9 and the photo in Fig. 10. The hills with the sinus-contour have of course high resistivities. The valleys in between, however, show low resistivities (< 15 ohm.m) down to a depth of 10 - 20 m as may be seen from the sounding graphs in Fig. 11. Comparing these curves with the curve set from Kota Bharu in Fig. 5 we ask again: Which resistivity values should be plotted in a resistivity map? The photo in Fig. 11 shows the field situation.

4.3. Chaco Boreal (Paraguay).

In 1959 a geoelectrical survey was carried out in central South America. The Gran Chaco is well known from the war between Bolivia and Paraguay in 1933-35, the war in the "green hell", i.e. high temperatures and no water. Looking at the map in Fig. 12 you will find in the left part of the area of investigation the name "Mariscal Estigarribia". This man won the final battle against the Bolivian troops. From this place - a military station now - a geoelectric profile was run via "km 260" and "km 145" in eastern direction to Puerto Cassado at the Rio Paraguay. The result is shown as a vertical section in Fig. 13. Some typical sounding graphs are given in Fig. 14. The surprising fact in 1959 was the low resistivity of the subsoil decreasing below 1 ohm.m in a few meters depth in spite of the difficulty to push a current electrode by hammer into the hard ground. The resistivities plotted in Fig. 14 reach low values of 0.6 ohm.m. Comparing this with the water resistivities ρ_w in Fig. 6 we are within the range of the ocean water. Our conclusion: There is nearly no difference in resistivity between ocean surface water and the surface of wide regions in central South America. This was a surprising result in 1959 because before bringing an equipment into the Chaco Boreal we were told that we would waste money, because there would be no chance to get any current into this hard underground. Looking

)* The overlapping of the o-branches and the +-branches is typical for the Schlumberger arrangement because starting with $a = 1$ m the voltage U will reach a technical low limit making a change to $a = 10$ m necessary.

at the photos in Fig. 15-17 this opinion had to be expected. And the answer to our question concerning the resistivity map: Here we are able to plot values for a large region: $< 1 \text{ ohm.m.}$

4.4. Jordan Valley (Jordan).

In 1963/64 a geoelectrical survey was carried out north of the Dead Sea (Totes Meer) by measuring on profiles across the valley (see Fig. 18). The level of the Dead Sea is about 400 m below m.s.l. (m.s.l. = main level of the Mediterranean Sea). Fig. 18 shows the true resistivities on a horizontal section. The resistivities are decreasing from the graben-margins to the river. The sounding graphs recorded along profile 9 from Jericho to Shuna are represented in Fig. 19 together with two observation wells. These graphs clearly show the sensitivity of electrical measurements. The horizontal section in Fig. 18 could be used for constructing a resistivity map but only for the region of the valley. The photo in Fig. 20 shows the arid plain near Shuna.

5. CONCLUSIONS

Four case histories were presented with figures and photos. What was really demonstrated? Drawing a world-wide near-surface resistivity map cannot be done without geological aspects. Experience from geoelectrics show what I should like to call the "near-surface resistivity paradoxon", i.e. low resistivities in arid regions, high resistivities in humid regions. The latter fact could be demonstrated by many case histories from Northern Europe. In forests the near-surface resistivities are normally higher than 1000 ohm.m. A possible reason may be found in ARCHIE's formula given in Fig. 6. As a ionic conductivity is concerned the electrolytic content in the water is an important factor in the resistivity of the groundwater. In forests these electrolytes are extracted by the trees causing high values of σ_w . In arid areas, however, σ_w is decreased because the sunshine and the low air-humidity cause a high evaporation and thus a concentration of the electrolytic content in the small amount of water infiltrated into the ground. The last photo in Fig. 21 shows the Iran highlands: $< 20 \text{ ohm.m.}$

6. REFERENCES

6.1. Textbooks.

BHATTACHARY, P.K. & PATRA, H.P., 1968, "Direct current geoelectrical sounding", 135 p., Elsevier, Amsterdam, (in English).

LASFARGUES, P., 1957, "Prospection Électrique par courants continus", 290 p., Masson, Paris, (in french).

KRAJEV, A.P., 1952, "ОСНОВЫ ГЕОЭЛЕКТРИКИ", German Edit. VEB-Tech., Berlin, 1957.

SCHNEIDER, H., 1973, "Die Wassererschliessung", Kap. 4 "Geophysik" (H.FLATHE u. J. HOMILIUS), p. 201-277, Vulkan, Essen, (in German).

6.2. Original papers.

BENDER, F. & FLATHE, H., 1961, "Groundwater conditions in the Chaco Boreal of Paraguay", Publ. Assoc.Int.Hydrol.Scient., 57, p. 173-185, Gentbrugge.

FLATHE, H., 1955, "A practical method of calculating geoelectrical model graphs for horizontally stratified media", Geophys.Prospect., 3, p. 268-295.

FLATHE, H., 1968, "Geoelektrische Untersuchung der Grundwasserversalzung im südlichen Jordantal", Geol.Jb., 85, p. 767-782, Hannover.

FLATHE, H., 1970, "Interpretation of geoelectrical resistivity measurements for solving hydrogeological problems", Min. Groundwater Geophys./1967, Ottawa, Econ. Geol. Rep., 26, p. 580-597.

FLATHE, H., 1976, "The role of a geologic concept in geophysical research work for solving hydrogeological problems", Geoexploration, 14, p. 195-206, Amsterdam.

FLATHE, H. u. PFEIFFER, D., 1965, "Grundzüge der Morphologie, Geologie und Hydrogeologie im Karstgebiet Gunung Sewu/Java (Indonesien)", Geol. Jb., 83, p. 533-562, Hannover.

SCHLUMBERGER, C., 1920, "Étude sur la Prospection Électrique du Sous-Sol", Gauthier-Villars, Paris.

WENNER, F., 1916, "A method of measuring earth-resistivity", Bull. U.S. Bureau Stand., 12, p. 469-478.

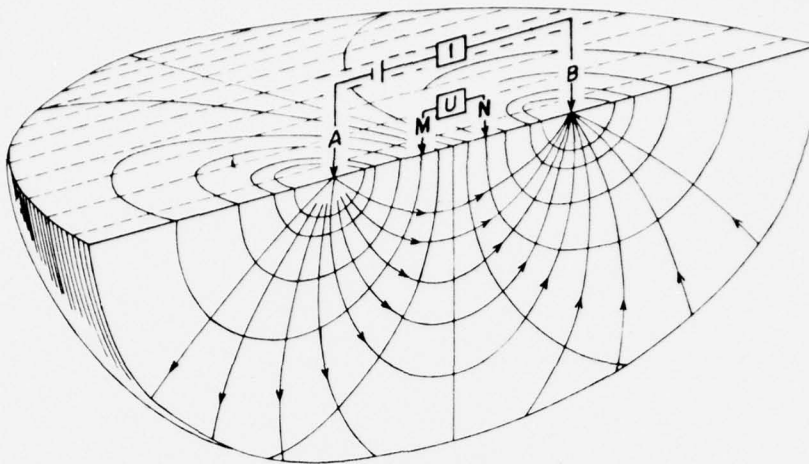


Fig. 1 Four-point arrangement AMNB with current (I)-lines and potential distribution (U) in a homogeneous earth.

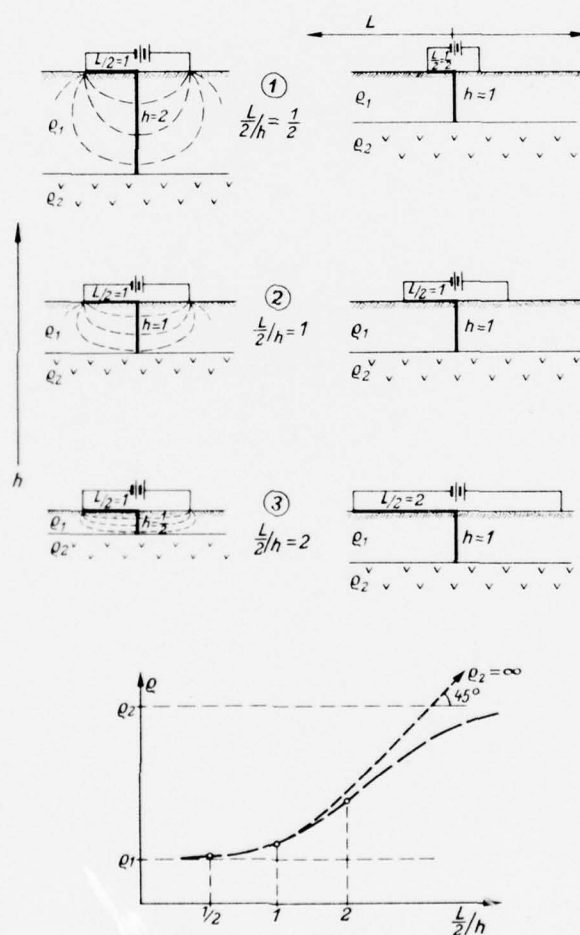


Fig. 2 The fundamental principle of direct current geoelectric sounding.

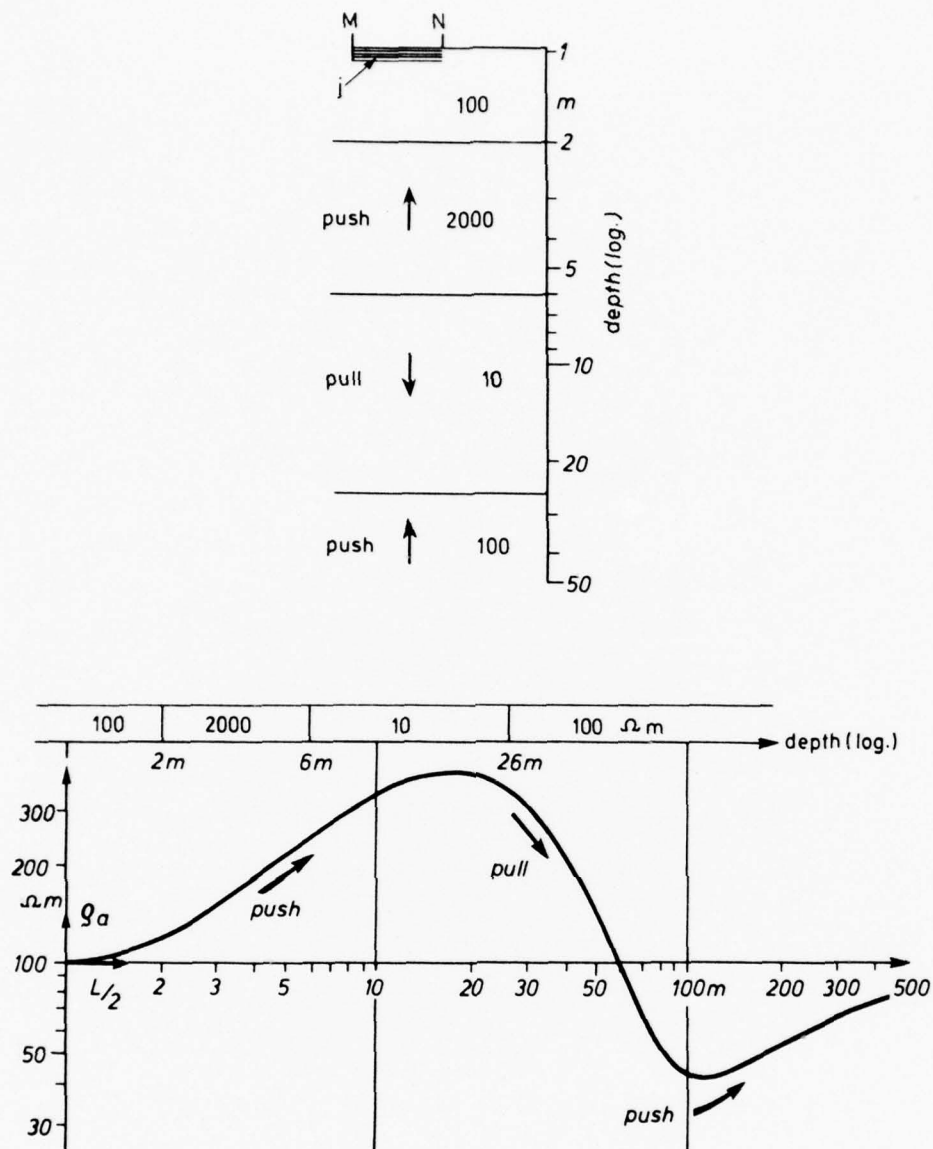


Fig. 3 Four-layer sounding graph resulting from "zooming" the underground.

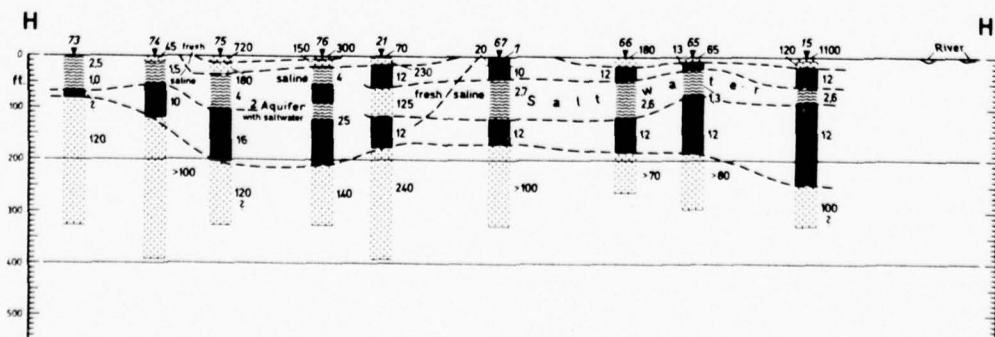


Fig. 4 Kota Bharu/Malaysia: Vertical section near to the South-China-Sea with resistivities (ohm.m) of layers and geological interpretation.

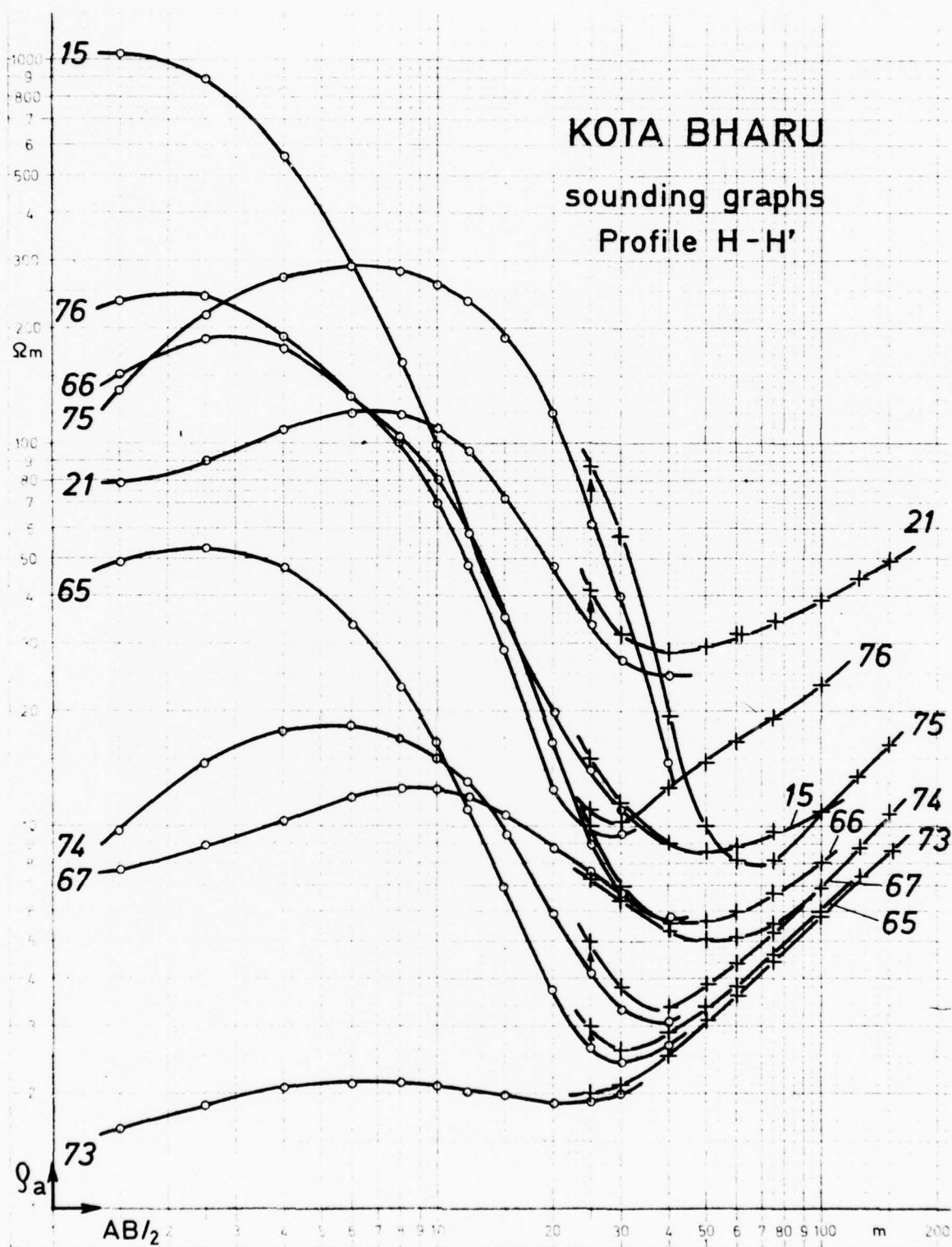


Fig. 5 Original soundings recorded on profile H-H' in Fig. 4.

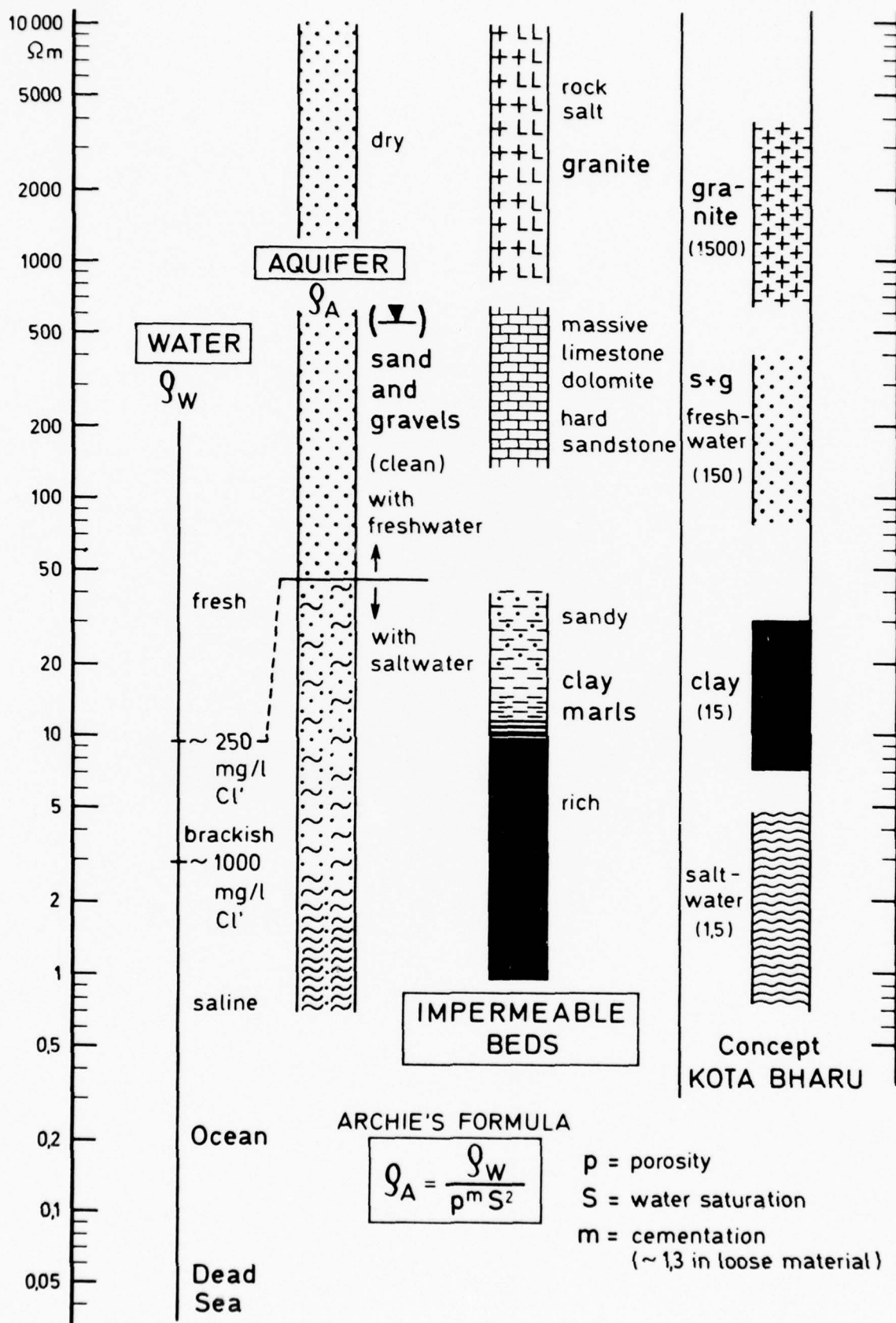


Fig. 6 Geological concept for interpretation of the sounding graphs in Fig. 5 resulting into the vertical section in Fig. 4.



Fig. 7 The Kelantan-River near Kota Bharu/Malaysia running from the granitic hills in the background towards the South-China-Sea.



Fig. 8 Preparing a geoelectrical measurement in a rubber-plant near Kota Bharu.

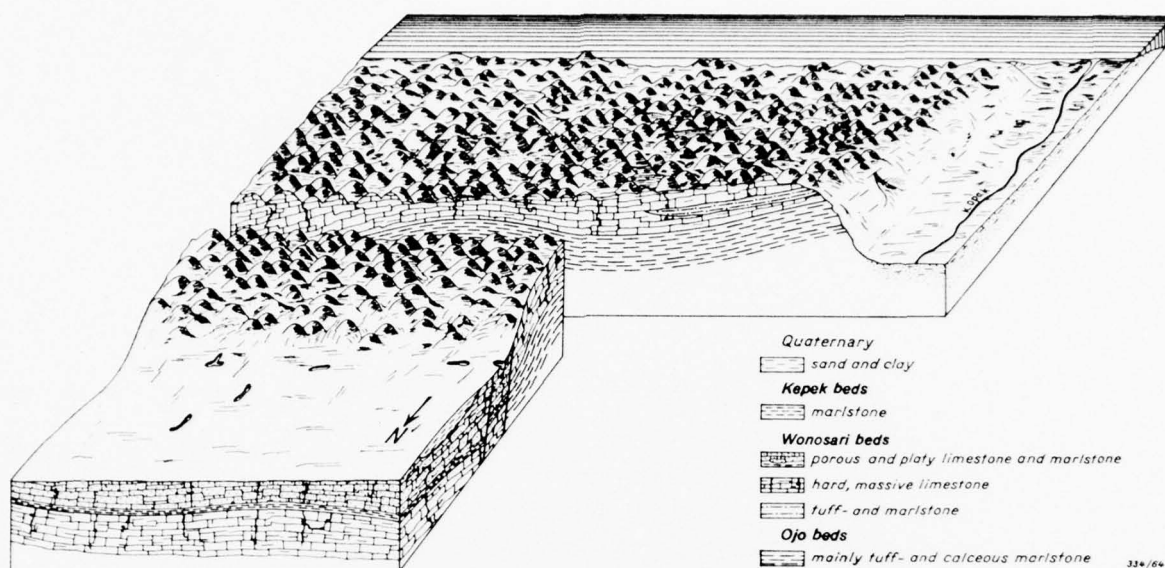


Fig. 9 Geological situation in the karstic area of the Gunung Sewu/
 Java (Indonesia).

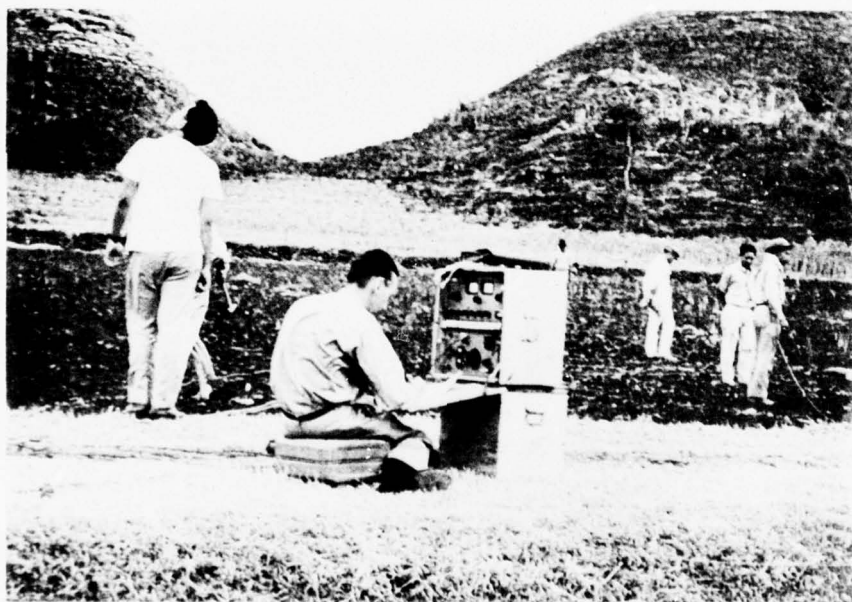


Fig. 10 Geoelectrical field work within the Gunung Sewu.

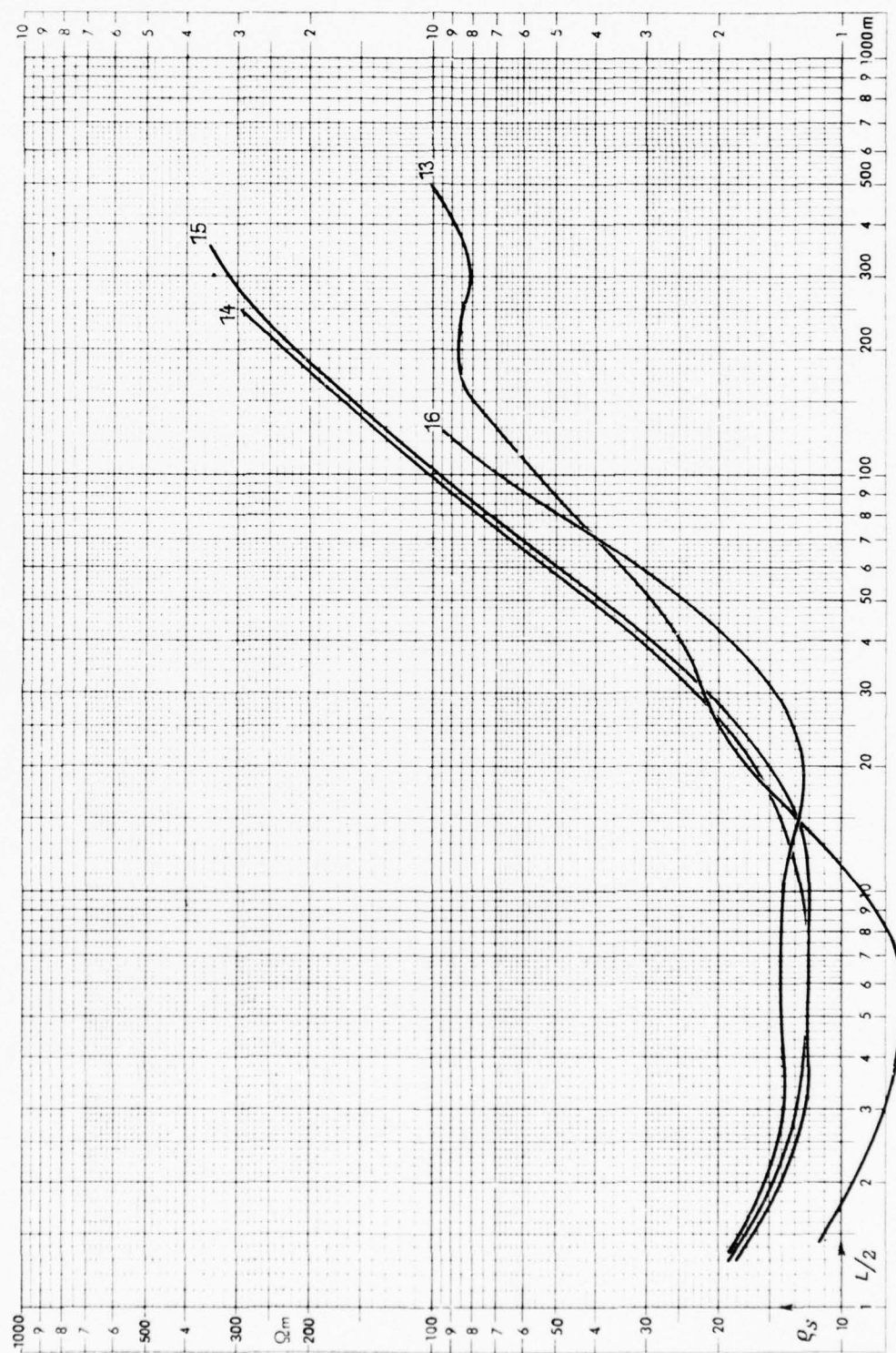


Fig. 11 Typical sounding graphs from the Gunung Sewu-area.

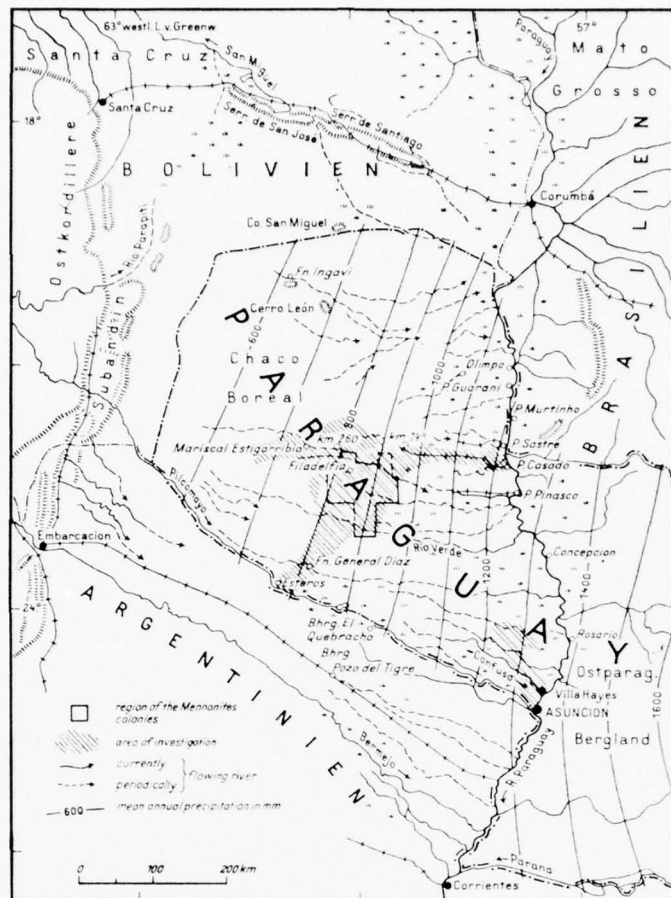


Fig. 12 Chaco Boreal/Paraguay: Map of investigation.

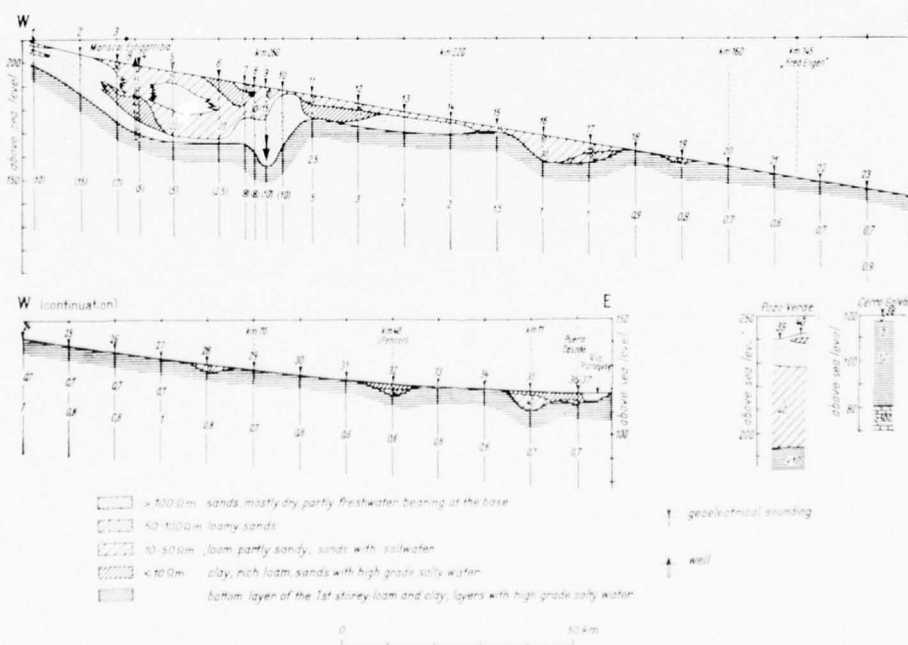


Fig. 13 W-E vertical section in the Chaco Boreal/Paraguay showing the low resistivities (ohm.m) in the saline underground.

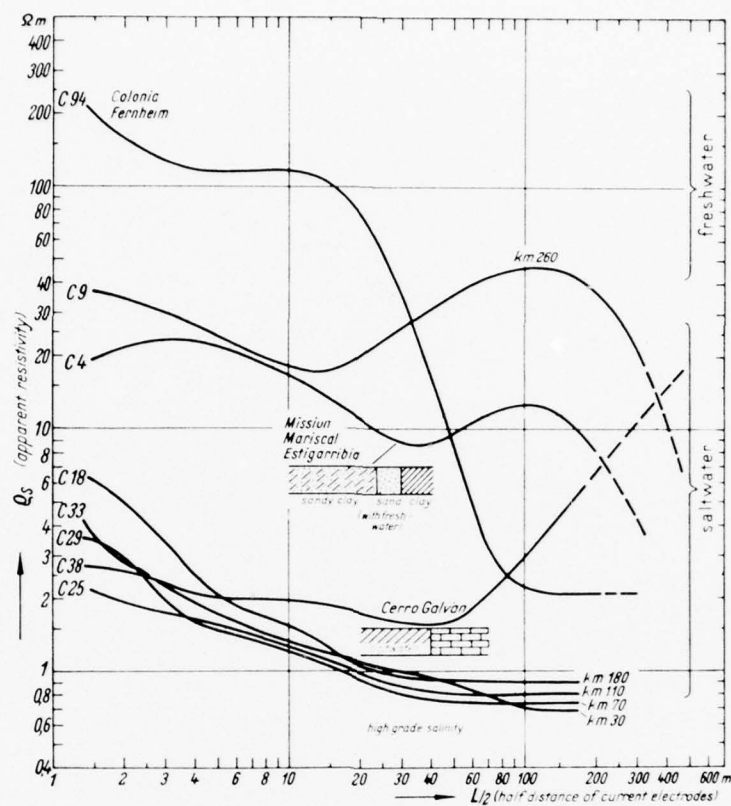


Fig. 14 Typical sounding graphs along the profile in Fig. 13.



Fig. 15 Mennonite village in the Central Chaco with dry cotton fields cut into the bush.



Fig. 16 Landscape in the Chaco Boreal.



Fig. 17 Geoelectrical measurement in the dry Chaco.

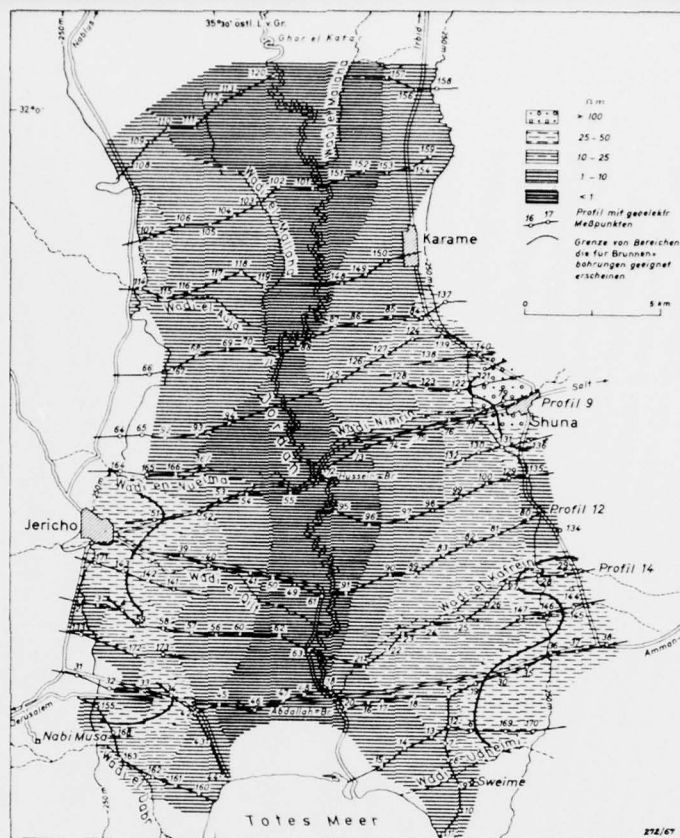


Fig. 18 Jordan Valley: Horizontal section in -400 m.s.l. with resistivities calculated from geoelectrical measurements.

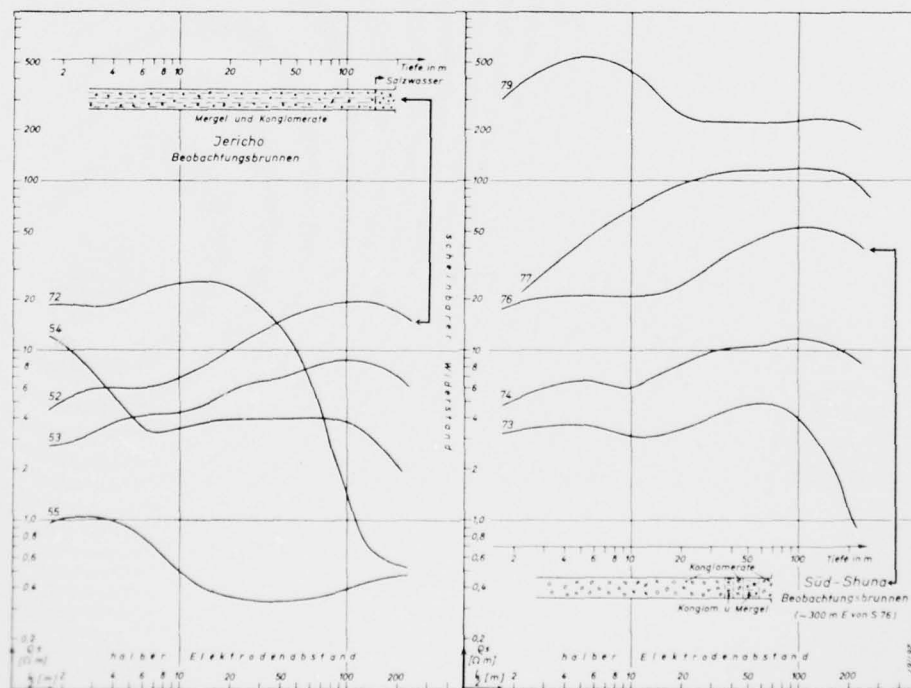


Fig. 19 Sounding graphs recorded on profile 9 between Jericho and Shuna (see Fig. 18).



Fig. 20 Measuring car in the Lysan marls near Shuna in the Jordan valley.



Fig. 21 Iran highlands: 20 ohm.m.

ELECTROMAGNETIC WAVE PROPAGATION FROM SOURCES IN COMPOSITE MEDIA

Albert W. Biggs
Electrical Engineering Department
University of Kansas
Lawrence, Kansas 66045, USA

SUMMARY

Space, ground, and surface wave expressions are developed for a four layer medium. The four layer medium consists of an upper layer of air above a three layered earth. A horizontal electric dipole antenna is the source considered here. Boundary conditions and Fourier transforms are applied to the Hertz vector potential wave equations in each layer of the multilayer terrain. Integral expressions for the horizontal and vertical components of the Hertz vector potential are found for each layer. The electric and magnetic fields are functions of the media parameters.

The antenna is located in the upper layer of the stratified earth. Variations in the media parameters allow results for upper layers of water, ice, dry earth, wet earth, or an earth formed by mixtures of different materials. Similar combinations are available for the lower two layers.

Surface wave phenomena are observed for suitable combinations of layer parameters. In addition to material variations, the frequency and layer depths can also be considered. Applications to buried rhombic antennas and traveling wave antennas can be made with the preceding results. Square loop antennas can also be synthesized. When arrays of buried horizontal antennas are examined, a frequency steerable antenna can be developed.

1. INTRODUCTION

This paper is a review of the electromagnetic wave propagation from sources in composite media. The electromagnetic waves include space, ground, and surface waves. They can be formulated with respect to the composite media, which is an upper layer of air or free space above a three layer earth. The Cartesian coordinate system appears in Figure 1, where the x-y plane at $z = 0$ is the air-ground interface and the x-y planes at $z = -D_1$ and $z = -(D_1 + D_2)$ are the interfaces in the layered ground. The space wave is in the air, region (0), and the ground and surface waves are on the x-y plane between region (0) and region (1). Since these radiation fields were derived for antennas in the Antarctic region (BIGGS, A. W., 1968), region (1) is ice or dry soil, region (2) is sea water or wet soil, and region (3) is granite or dry soil. These media correspond to sea ice floating above sea water, with a bottom layer of granite or comparatively dry soil. There are transition regions between each of these regions where the conductivities and dielectric constants blend from one to the other medium. These transition regions are considered to be small in the layered model, where the changes are more pronounced. The sources in region one are horizontal and vertical electric dipoles. They are assumed to be very small in comparison with the wavelength of the radiation fields. The current distribution is assumed to be constant instead of linear or sinusoidal. These assumptions allow application of the results to traveling wave antennas and other forms of linear antennas. The depth of burial, h , allows the observation of these influences to be included in the radiation field expressions.

The propagation constant for region (0) is

$$k_0^2 = \omega^2 \mu_0 \epsilon_0, \quad (1)$$

where ω is the radian frequency, μ_0 is the permeability of free space ($4\pi \times 10^{-7}$ henries per meter) and ϵ_0 is the dielectric constant of free space ($1/36 \times 10^{-9}$ farads per meter). In the ground, region (1) is described by

$$k_1^2 = \omega^2 \mu_0 \epsilon_1 + i\omega \mu_0 \sigma_1 \quad (2)$$

with similar forms for regions (2) and (3). The differences between region (0) and the other regions lie in the dielectric constant and the conductivity, ϵ_1 and σ_1 , respectively. When the medium is ice or snow at low frequencies, the behavior of the electrical parameters follow the empirical forms from dielectric relaxation theories (AUTY, R. P. and COLE, R. H., 1952). In the form of relative dielectric constants and loss factor, the complex relative dielectric constant ϵ^* is

$$\begin{aligned} \epsilon^* &= \epsilon' + i\epsilon'' \\ &= \epsilon_\infty + (\epsilon_0 - \epsilon_\infty)/(1 - i\omega\tau), \end{aligned} \quad (3)$$

where ϵ_∞ and ϵ_0 are the equilibrium and high frequency limit values and τ is the relaxation time. At -0.1°C , ϵ_0 , ϵ_∞ , and τ are 91.5, 3.10, and 2.2×10^{-5} , respectively. At -65.8°C , they increase to 100, 3.10, and 4.5×10^{-2} , respectively. The variation of the components of the relative complex dielectric constant appears in Figure 2 for ice at -0.1°C .

The dielectric relaxation phenomena present in ice at low frequencies is also present in water at microwave frequencies. The relative dielectric constant and loss factor for water appear in Figure 3 for microwave frequencies.

2. INTEGRAL EQUATIONS

The electric and magnetic field intensities are expressed with the Hertz vector potential Π as

$$\vec{E} = \nabla(\nabla \cdot \vec{\Pi}) + k^2 \vec{\Pi}, \quad (4)$$

$$\vec{H} = -\frac{ik}{\eta} \nabla \times \vec{\Pi}, \quad (5)$$

with a time dependence $(-i\omega t)$ and the intrinsic impedance η ,

$$k\eta = \omega\mu \quad (6)$$

and the intrinsic admittance ζ ,

$$k\zeta = \omega\epsilon + i\sigma. \quad (7)$$

The source appears in the inhomogeneous wave equation

$$(\nabla^2 + k_1^2)\vec{\Pi}_1 = -i \frac{\vec{J}}{k_1 \zeta_1}, \quad (8)$$

where \vec{J} is the current density vector for the dipole source,

$$\vec{J} = a_x Idl \delta(x) \delta(y) \delta(z+h), \quad (9)$$

where $\delta(x)$, $\delta(y)$, and $\delta(z+h)$ are delta functions (PANOFSKY, W. and PHILLIPS, M., 1955). The dipole moment is Idl and it is oriented in the x-direction in region (1). The other wave equations are homogeneous in the form

$$(\nabla^2 + k_1^2)\vec{\Pi}_{x1} = 0, \quad (10)$$

where the source is not included and

$$(\nabla^2 + k_1^2)\vec{\Pi}_{z1} = 0, \quad (11)$$

with the z-component being necessary to satisfy boundary conditions. Similar expressions are present for region (0) in the form

$$(\nabla^2 + k_o^2)\vec{\Pi}_{xo} = 0, \quad (12)$$

$$(\nabla^2 + k_o^2)\vec{\Pi}_{zo} = 0, \quad (13)$$

and replacing the subscript (0) by (2) and (3) for those in the other regions.

Boundary conditions at each interface have the form

$$k_1^2 \vec{\Pi}_{x1} = k_o^2 \vec{\Pi}_{xo}, \quad (14)$$

$$\frac{\partial \vec{\Pi}_{x1}}{\partial x} + \frac{\partial \vec{\Pi}_{z1}}{\partial z} = \frac{\partial \vec{\Pi}_{xo}}{\partial x} + \frac{\partial \vec{\Pi}_{zo}}{\partial z}, \quad (15)$$

for the tangential electric field and

$$k_1^2 \frac{\partial \vec{\Pi}_{x1}}{\partial z} = k_o^2 \frac{\partial \vec{\Pi}_{xo}}{\partial z}, \quad (16)$$

$$k_1^2 \vec{\Pi}_{z1} = k_o^2 \vec{\Pi}_{zo}, \quad (17)$$

for the tangential magnetic field. Similar forms are found at the other interfaces.

The Fourier transform,

$$F(\xi, \eta, \zeta) = \iiint_{-\infty}^{\infty} \Pi(x, y, z) e^{-i(\xi x + \eta y + \zeta z)} dx dy dz, \quad (18)$$

is applied to the homogeneous and inhomogeneous wave equations. The resulting expressions are transformed into integral equations with the inverse Fourier transform,

$$\Pi(x, y, z) = \frac{1}{(2\pi)^3} \iiint_{-\infty}^{\infty} F(\xi, \eta, \zeta) e^{i(\xi x + \eta y + \zeta z)} d\xi d\eta d\zeta, \quad (19)$$

and the integral equations are evaluated by use of the boundary conditions in Equations (14) to (17). The electric field intensities obtained are (BIGGS, A. W., 1968).

$$\begin{aligned} E_{\theta} = & -30 k_o^2 I dl \sin \theta \cos \theta \cos \phi \\ & \cdot \int_{-\infty}^{\infty} M(h) \frac{\gamma_1 k_o^2 M_{123}}{\gamma_o k_1^2 + \gamma_1 k_o^2 M_{123}} \frac{e^{-\gamma_o z + i\lambda p}}{\lambda} \\ & \cdot [H_o^{(1)}(\lambda p) e^{-i\lambda p}] d\lambda, \end{aligned} \quad (20)$$

$$\begin{aligned} E_{\phi} = & -i 30 k_o I dl \sin \phi \int_{-\infty}^{\infty} N(h) \frac{1}{\gamma_o + \gamma_1 N_{123}} \\ & \cdot e^{-\gamma_o z + i\lambda p} [H_o^{(1)}(\lambda p) e^{-i\lambda p}] \lambda d\lambda. \end{aligned} \quad (21)$$

The depth functions, $M(h)$ and $N(h)$ are (WAIT, J. R., 1967)

$$M(h) = \frac{\gamma_1 k_2^2 \sinh \gamma_1 (D_1 - h) + \gamma_2 k_1^2 M_{23} \cosh \gamma_1 (D_1 - h)}{\gamma_1 k_2^2 \sinh \gamma_1 D_1 + \gamma_2 k_1^2 \cosh \gamma_1 D_1}, \quad (22)$$

$$N(h) = \frac{\gamma_1 \cosh \gamma_1 (D_1 - h) + \gamma_2 N_{23} \sinh \gamma_1 (D_1 - h)}{\gamma_1 \cosh \gamma_1 D_1 + \gamma_2 \sinh \gamma_1 D_1} \quad (23)$$

and the layer functions M_{123} and N_{123} are

$$M_{123} = \frac{\gamma_2 k_1^2 M_{23} + \gamma_1 k_2^2 \tanh \gamma_1 D_1}{\gamma_1 k_2^2 + \gamma_2 k_1^2 \tanh \gamma_1 D_1}, \quad (24)$$

$$N_{123} = \frac{\gamma_2 N_{23} + \gamma_1 \tanh \gamma_1 D_1}{\gamma_1 + \gamma_2 N_{23} \tanh \gamma_1 D_1}, \quad (25)$$

where M_{23} and N_{23} are

$$M_{23} = \frac{\gamma_3 k_2^2 + \gamma_2 k_3^2 \tanh \gamma_2 D_2}{\gamma_2 k_3^2 + \gamma_3 k_2^2 \tanh \gamma_2 D_2}, \quad (26)$$

$$N_{23} = \frac{\gamma_3 + \gamma_2 \tanh \gamma_2 D_2}{\gamma_2 + \gamma_3 \tanh \gamma_2 D_2}. \quad (27)$$

3. RADIATION FIELD EXPRESSIONS

The saddle point method is applied to the evaluation of the integrals in Equations (20) and (21) to obtain the space wave field expressions (BIGGS, A. W. and SWARM, H. M., 1968)

$$E_{\theta} = i 60 k_0 I dl M(h) \frac{M_{123} \cos \phi \cos \theta \sqrt{n_1^2 - \sin^2 \theta}}{n_1^2 \cos \theta + M_{123} \sqrt{n_1^2 - \sin^2 \theta}} \frac{e^{ik_0 R}}{R}, \quad (28)$$

$$E_{\phi} = -i 60 k_0 I dl N(h) \frac{\sin \phi \cos \theta}{\cos \theta + N_{123} \sqrt{n_1^2 - \sin^2 \theta}} \frac{e^{ik_0 R}}{R}, \quad (29)$$

where n_1^2 is the index of refraction for the first layer or region (1).

The modified saddle point method is applied to the same integrals to obtain the surface and ground wave field expressions. The surface wave is created when the upper layer has a lower index of refraction than the composite index of refraction of the lower layers. The composite index of refraction for three layers is

$$n_{123} = \frac{n_1}{M_{123}} \quad (30)$$

and the effect of layer thickness, D_1 , can be observed in Equation (24). As D_1 increases, M_{123} approaches unity and

$$n_{123} \approx n_1 \quad (31)$$

for distances in excess of a quarter wavelength of the radiated wave, measured in free space or air. Another impact of depth changes, indicated in Figure 4, occurs with the case where D_1 , the upper layer depth, is almost zero. When this occurs, the pole location is the value of λ satisfying the Sommerfeld equation,

$$\gamma_0 k_2^2 + \gamma_2 k_0^2 M_{23} = 0, \quad (32)$$

and the pole is

$$\lambda = +k_2 \sqrt{\frac{n_2^2 - M_{23}^2}{n_2^4 - M_{23}^2}}. \quad (33)$$

As D_1 increases to D_2 , the Sommerfeld equation changes to

$$\gamma_0 k_1^2 + \gamma_1 k_0^2 M_{123} = 0, \quad (34)$$

and the pole is

$$\lambda = +k_1 \sqrt{\frac{n_1^4 - M_{123}^2}{n_1^4 - M_{123}^2}} \quad (35)$$

With D_1 approaching deep distances, the Sommerfeld equation is

$$\gamma_0 k_1^2 + \gamma_1 k_0^2 = 0 \quad (36)$$

and the pole is

$$\lambda = +k_1 \sqrt{\frac{n_1^2 - 1}{n_1^4 - 1}} = +k_1 \frac{1}{\sqrt{n_1^2 + 1}} \quad (37)$$

The pole location in Equation (33) may be on either side of the $+k_0$ branch cut on the complex λ -plane in Figure 5, which shows the path of steepest descents used in the saddle point method of integration. Pole loci for two layered media in Figure 6 move counterclockwise with increasing depths D_1 for upper layers of soil in the first two curves and for an upper layer of ice in the third curve. The composite soil conductivity below the first layer is 0.01 mho per meter and the frequency is 10 kHz. In crossing the $+k_0$ branch cut, normalized to 1.0, the "virtual" poles become real poles. When real poles are trapped by deformation of the integration path, a residue term is created. The resulting electric field intensity is

$$E_\theta = 160 k_0 I d l \cos \phi M_{123} \frac{n_1^5 (n_1^2 - 1)}{(n_1^4 - M_{123}^2)^2} \frac{k_0}{\lambda_p} F(x_0) \frac{e^{ik_0 R}}{R} \quad (38)$$

where $F(x_0)$, the ground wave attenuation function, is

$$F(x_0) = 1 + i \sqrt{\pi x_0^2 / 2} e^{-1/2 x_0^2} \operatorname{erfc}(i x_0 / \sqrt{2}) \quad (39)$$

Oscillations in phase and amplitude in $F(x_0)$ are presented in Figures 7 and 8. These occur when the phase angle of $1/2 x_0^2$, or p , varies from 0° to -90° in stratified media where the upper layer has a smaller refractive index than the lower layer (WAIT, J. R., 1958; BIGGS, A. W. and SWARM, H. M., 1965).

4. CONCLUSIONS

The extension of the above method to vertical dipoles is relatively simple. This permits superposition of results from short dipoles to any linear system of antennas as long as any interaction effects are considered. In a traveling wave antenna or in a rhombic antenna, the composite refractive index can be applied to the layered media so that the velocity of the slow wave on the antenna can be calculated.

5. REFERENCES

- AUTY, R.P., and COLE, R.H., 1952, "Dielectric Properties of Ice and Snow," J. Chem. and Phys., vol. 20, pp. 1309-1314.
- BIGGS, A.W., 1968, "Dipole Antenna Fields in Stratified Antarctic Media," IEEE Trans. Ant. and Prop., vol. AP-16, pp. 445-448.
- BIGGS, A.W., and SWARM, H.M., 1965, "Analytical Study of the Radiation Fields from an Electric Dipole in Stratified and Inhomogeneous Antarctic Terrain," Tech. Report No. 98, Univ. of Wash., Seattle, Washington 98195.
- BIGGS, A.W., and SWARM, H.M., 1968, "Radiation Fields from an Electric Dipole Antenna in Homogeneous Antarctic Terrain," IEEE Trans. Ant. and Prop., vol. AP-16, pp. 201-208.
- PANOFSKY, W., and PHILLIPS, M., 1955, Classical Electricity and Magnetism, Addison-Wesley.
- WAIT, J.R., 1958, "Transmission and Reflection of Electromagnetic Waves in the Presence of Stratified Media," J. Res. NBS (Radio Prop), vol. 61, pp. 205-232.

WAIT, J.R., 1967, "Asymptotic Theory for Dipole Radiation in the Presence of a Lossy Slab Lying on a Conducting Half-Space," IEEE Trans. Ant. and Prop., vol. AP-15, pp. 645-648.

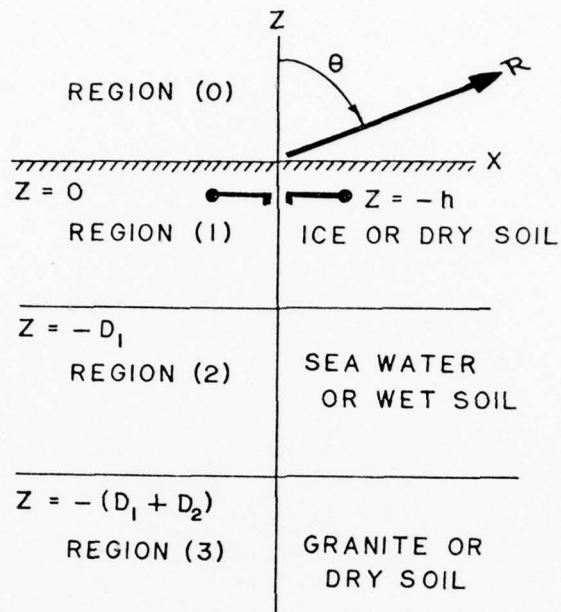


Fig.1 Coordinate system for a dipole source in a layered medium

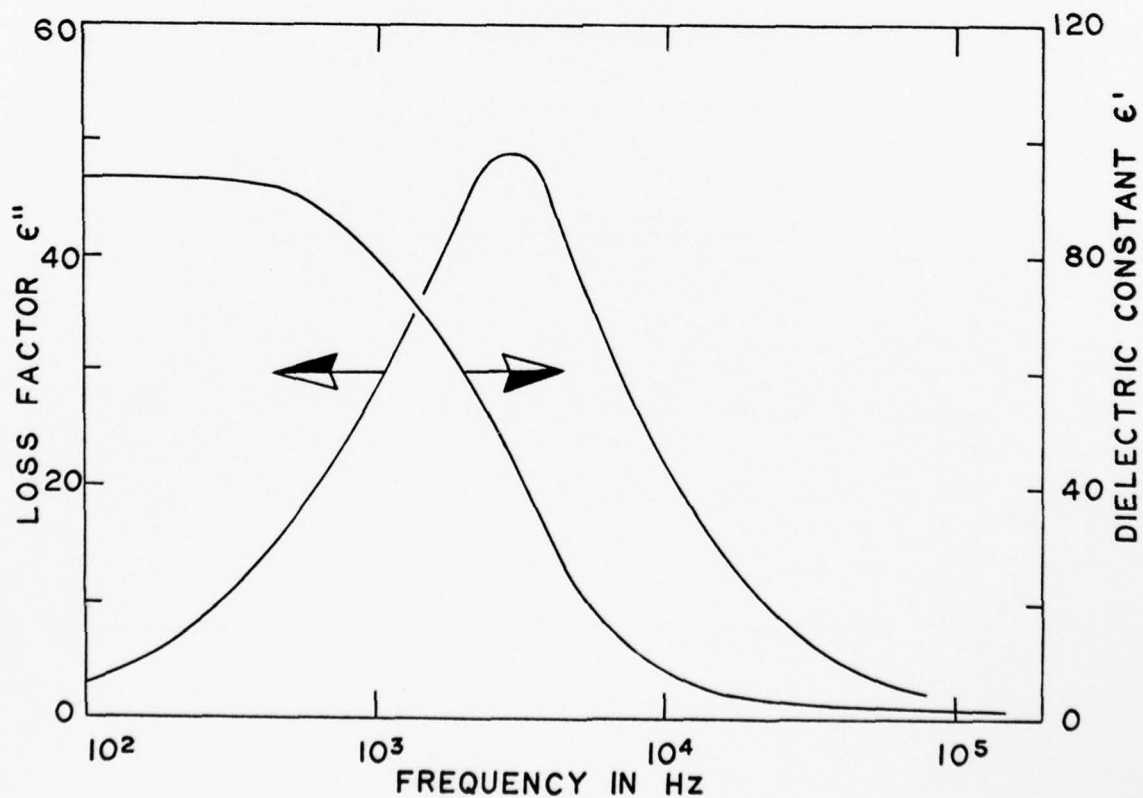


Fig.2 Loss factor and dielectric constant of ice at very low frequencies

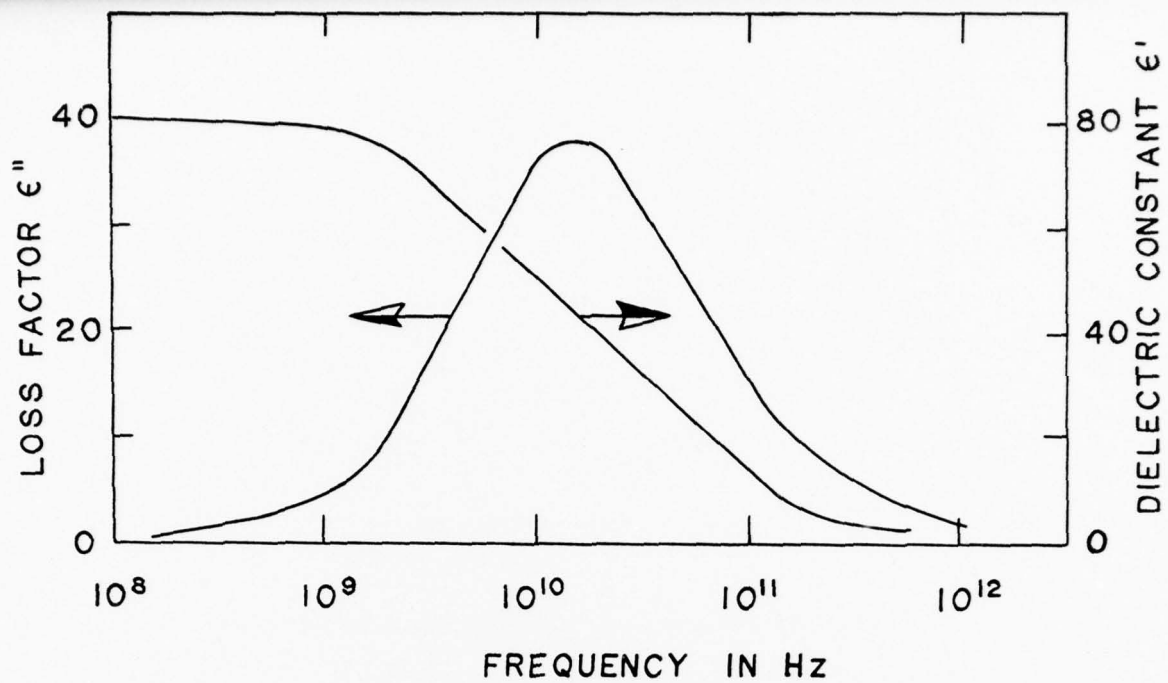


Fig.3 Loss factor and dielectric constant of water at microwave frequencies

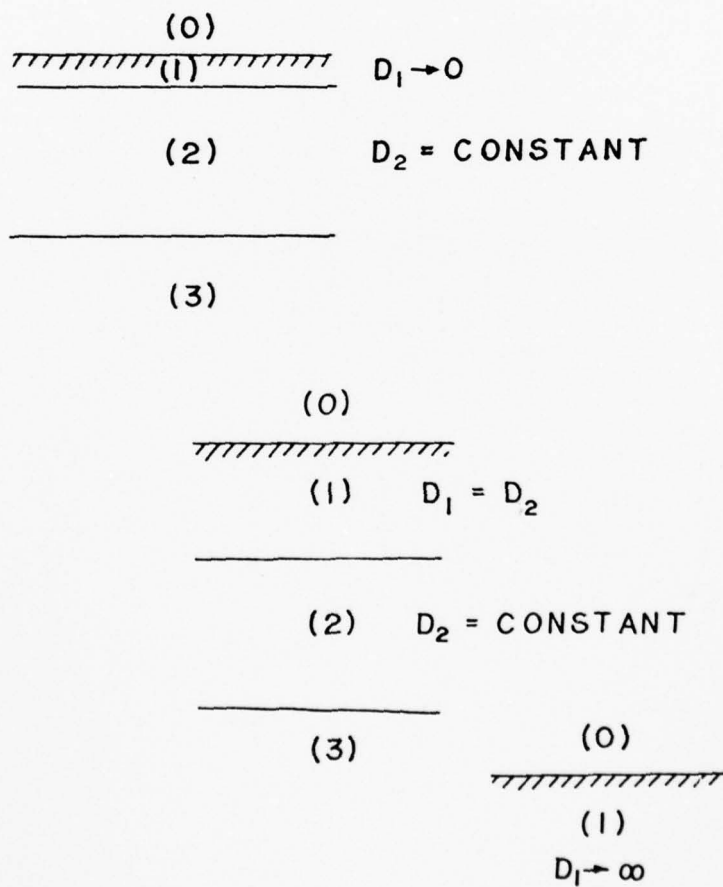


Fig.4 Variation of depth D_1 of the upper layer

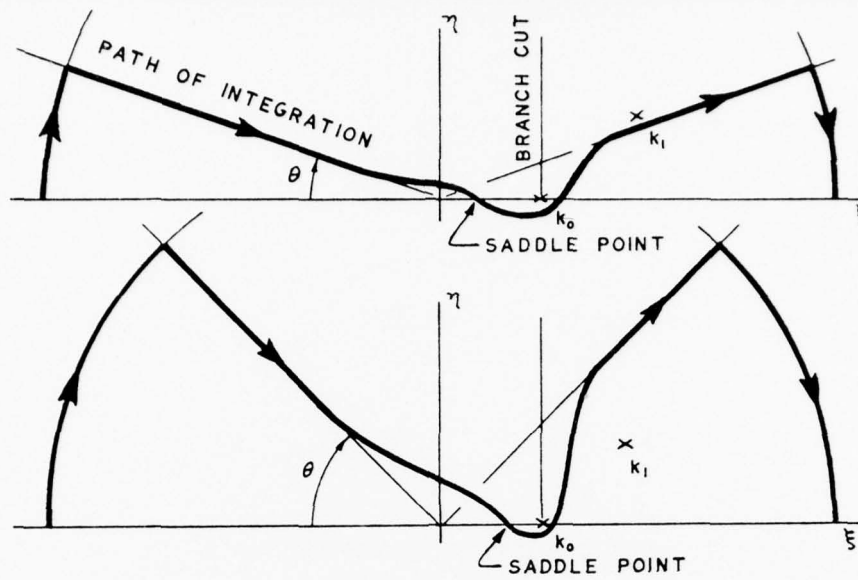


Fig.5 Path of steepest descents for two polar angles in the saddle point region

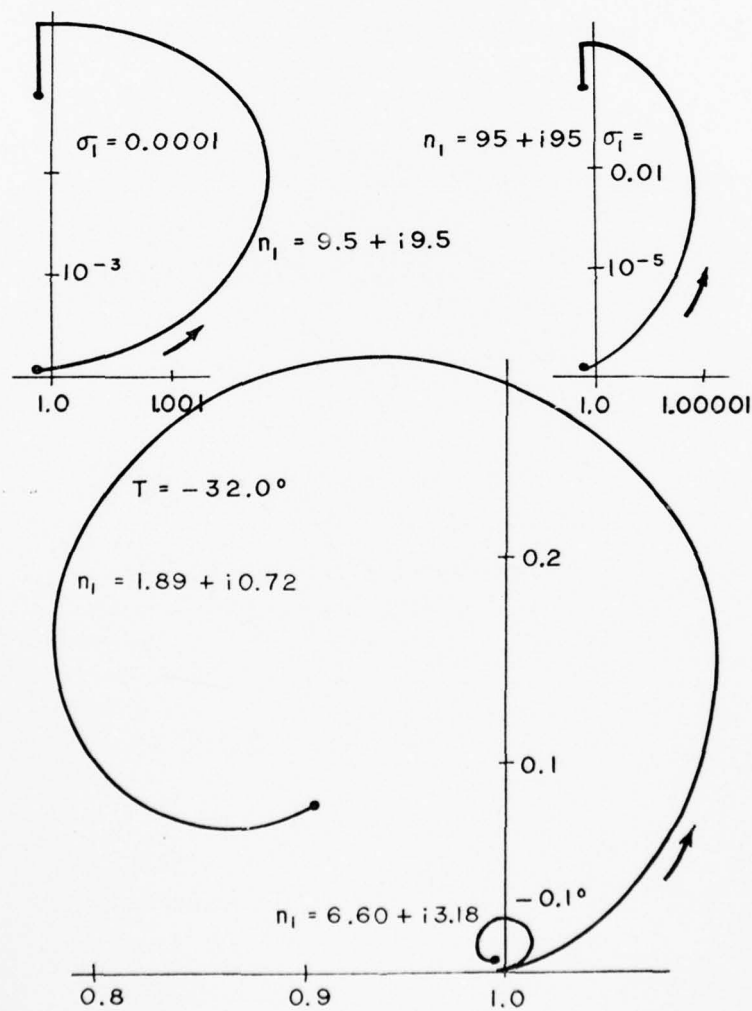


Fig.6 Loci of the poles for increasing depth D_1

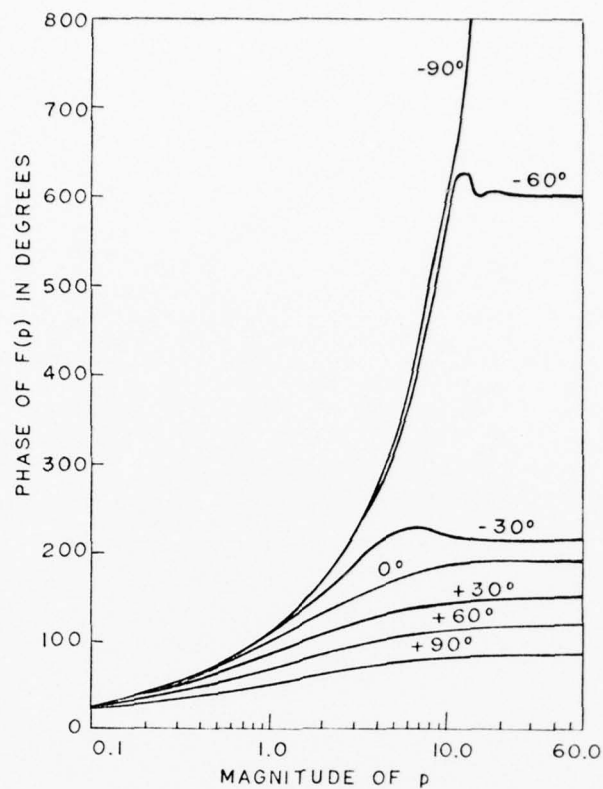


Fig.7 Phase of the ground wave attenuation function $F(p)$ as a function of the numerical distance p

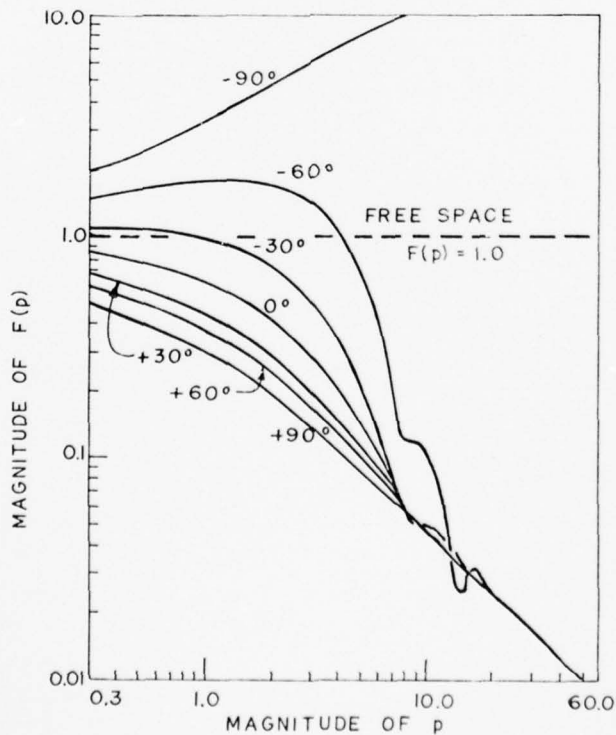


Fig.8 Magnitude of the ground wave attenuation function $F(p)$ as a function of the numerical distance p

DISCUSSION

K.J. Langenberg: Are there not any poles due to the denominator of your integrands which give rise to propagating damped modes?

A.W. Biggs: The poles exist on two of the four Riemann sheets formed by four branch cuts. They are virtual poles, not real poles, for homogeneous media. With layered media where the upper layer has a smaller refractive index than the lower layer, the virtual poles migrate to the Riemann sheet where they become real as the layer depth increases. As the depth continues to increase, they recross the branch cut and cease to exist as real poles.

L.B. Felsen: You have stated that when the number of layers in the medium is increased, then the number of branch cuts in the complex λ -plane is likewise increased. I should like to point out that this commonly accepted notion is incorrect. Branch joints and branch cuts appear only for semi-infinite layers. Therefore, the maximum number of branch joints and branch cuts is four, when the top and bottom layers extend to infinity and have different dielectric constants. The proof appears in the book L.B. Felsen and N. Marcuvitz, "Radiation and Scattering of Waves" (Prentice Hall, 1973), Chapter 5.

A.W. Biggs: I agree with L.B. Felsen's interpretation of this problem.

RECENTS PROGRES DANS QUELQUES PROCÉDES ELECTROMAGNETIQUES DE DETECTION

D'HETEROGENEITES

M. CAUTERMAN, P. DEGAUQUE, B. DEMOULIN et R. GABILLARD

Université de LILLE, Département Electronique, B.P. 36, 59650 Villeneuve d'Ascq
FRANCE

RESUME

Pour apprécier les caractéristiques électriques du sol et pour détecter des anomalies de résistivité, plusieurs méthodes peuvent être utilisées suivant la nature du terrain et la profondeur de l'hétérogénéité. Une de ces techniques consiste à émettre une onde électromagnétique basse fréquence, à l'aide d'une antenne électrique ou d'un dipôle magnétique placé à la surface du sol. Dans cet article, nous mettons en évidence les récents progrès théoriques de la méthode de détection dipôle-dipôle placés au voisinage de l'interface air-sol. En effet, en présence d'une anomalie, l'interprétation des mesures se faisait souvent à l'aide d'un modèle analogique. Compte-tenu des difficultés rencontrées, certains auteurs ont élaboré des modèles numériques tridimensionnels permettant de rendre compte de l'influence d'une anomalie de résistivité de forme quelconque, placée dans un demi-milieu homogène. La solution se présente sous la forme d'un système d'équations intégrales que vérifie le champ électromagnétique en tout point du sol. En se ramenant à un système matriciel, une solution numérique est obtenue. Après avoir exposé les principes de base, nous illustrons cette théorie sur quelques exemples.

1. INTRODUCTION

Les recherches sur les antennes susceptibles d'établir des communications à très grande distance sur des fréquences très basses connaissent actuellement un regain d'intérêt. Techniquement, il existe deux types de solutions. La première méthode consiste à utiliser une antenne aérienne verticale. En général, comme il n'est pas possible de lui donner une hauteur h suffisante pour qu'elle puisse résonner en quart d'onde, on construit un réseau de pylones supportant une nappe de fils constituant une capacité terminale.

Le terrain, au dessus duquel est tendu ce réseau, doit être très conducteur car il y a dans ce cas réflexion des ondes et l'antenne rayonne comme un élément de courant vertical, de hauteur $2h$. Pour ce type d'antenne, l'influence de la nature du sous-sol peut toujours être masquée en disposant à la surface du sol un réseau de grillages métalliques et on est ainsi ramené, approximativement, au cas d'un sol très conducteur.

La deuxième solution, pour émettre des ondes très basses fréquences, consiste à utiliser une longue antenne horizontale. On peut employer un fil posé sur la surface du sol ou encore, enterré à faible profondeur. Dans ce cas, la structure du sous-sol est très importante. Le terrain doit être isolant et il n'est donc plus possible de s'affranchir par un grillage conducteur, comme pour les antennes verticales, de l'influence de la structure géologique du sous-sol sur lequel est implanté ce type d'antenne. La recherche d'un site favorable nécessite la mise en oeuvre de méthodes géophysiques capables de déceler des zones de terrain conductrices, susceptibles d'avoir un effet sur le rayonnement à longue distance de l'antenne horizontale. Ce sont ces méthodes électromagnétiques de détection d'hétérogénéités situées dans le sous-sol que nous allons étudier.

Il est évident que ces méthodes ne servent pas uniquement à choisir des sites d'antennes mais qu'elles ont de nombreuses applications en génie civil. On peut envisager, par exemple, la recherche de filons de minerai métallifères correspondant à des anomalies conductrices, ou la détection de cavités souterraines plus ou moins remblayées et qui se traduisent par une résistivité locale importante.

Une des techniques classiques de détection consiste à émettre une onde électromagnétique basse fréquence, à l'aide d'une antenne électrique ou d'un dipôle magnétique placé à la surface du sol et à mesurer à une certaine distance de l'émetteur l'affaiblissement de l'onde émise. Ces techniques sont bien connues, mais leur point délicat réside encore dans l'interprétation des mesures obtenues sur le terrain. Il faut généralement faire une hypothèse sur la structure du terrain à partir de laquelle on calcule un affaiblissement théorique. La confrontation de ce résultat avec les mesures sert à infirmer ou à confirmer l'hypothèse faite. Pour déterminer cet affaiblissement théorique, une première solution que nous avons mise en oeuvre a consisté à utiliser un modèle analogique tridimensionnel, schématisé sur la figure 1.

Le milieu conducteur est constitué d'une solution d'eau salée dont la conductivité varie entre 0,1 et 3 mho/m suivant la concentration en sel. Cette solution est contenue dans une cuve cylindrique réalisée en stratifié de laine de verre de 2,4 m de diamètre et de 1,7 m de hauteur. Le dispositif émetteur se compose d'un générateur de courant sinusoïdal à la fréquence de 200 kHz. Ce modèle nous a servi essentiellement à obtenir des informations qualitatives sur l'effet d'une anomalie ; mais, on ne peut simuler pratiquement les conditions exactes de mesures sur le terrain. En effet, on aboutit à une impossibilité à respecter à la fois les rapports de réduction de géométrie et de fréquence. On choisit bien souvent la réduction de géométrie, ce qui revient à supposer, dans la plupart des cas, que l'on travaille sur le terrain à une fréquence voisine de 1/10 Hz. Il en résulte que la cuve analogique doit être considérée comme un modèle en courant continu.

En faisant, malgré tout, abstraction de ces objections, il est difficile sur un tel modèle de faire varier le contraste de résistivité entre le milieu encaissant et l'anomalie. Nous avons donc été amenés à mettre au point un modèle numérique tridimensionnel devant permettre une interprétation quantitative des résultats. Nous allons développer le principe de la méthode en supposant que la source d'émission est une antenne électrique horizontale placée à la surface du sol. D'autres auteurs ont envisagé le cas d'une excitation à partir d'une ligne source (Hohmann, 1971), d'un émetteur lointain (Dey et al., 1972) ou d'un dipole magnétique (Stoyer et Wait, 1975 ; Hohmann, 1975). Nous signalerons les différences existant entre les modèles et notamment entre le modèle d'Hohmann et le notre, tant du point de vue analytique que numérique.

2. ETUDE THEORIQUE

Comme l'indique la figure 2, le sol est assimilé à un demi-milieu homogène, de conductivité σ_1 et de permittivité ϵ_1 , renfermant une anomalie de volume V , limitée par une surface S . Soient σ_2 et ϵ_2 les paramètres électriques de cette inhomogénéité. A l'aide des équations de Maxwell, on peut montrer qu'une anomalie, quelque soit le dispositif émetteur qui l'excite, peut toujours être remplacée par une distribution de dipôles verticaux et horizontaux (Cauterman, 1975 ; Cauterman et al., juin 1975 ; Hohmann, 1975).

La valeur des moments des dipôles équivalents à une homogénéité de volume dv est donnée par les équations suivantes :

$$Id_{leq} = \frac{\mu_2 \sigma_2 - \mu_1 \sigma_1}{\mu_1} E_2 dv \quad (1)$$

$$Id_{Seq} = \frac{\mu_1 - \mu_2}{\mu_1} H_2 dv \quad (2)$$

Dans ces formules, E_2 et H_2 sont les champs électriques et magnétiques existant à l'intérieur du volume dv .

Dans le cas particulier où les milieux ont la même perméabilité que celle du vide, ces équations se simplifient et l'anomalie peut être uniquement remplacée par des dipôles électriques ayant la même direction que le champ électrique E_2 .

Leur moment est donné par :

$$Id_{leq} = (\sigma_2 - \sigma_1) E_2 dv \quad (3)$$

Nous supposons que l'émetteur, constitué par une antenne électrique horizontale, est situé sur la surface du sol. Compte-tenu du domaine basse fréquence dans lequel nous plaçons, les composantes du champ rayonné peuvent être calculées dans l'approximation quasi-statique. Cette approximation revient à supposer que la distance horizontale émetteur-récepteur est faible vis à vis de la longueur d'onde dans l'air, soit :

$$|\gamma_0 r| \ll 1 \quad (4)$$

Le champ électrique en un point quelconque du sol est la somme d'un champ primaire et d'un champ secondaire diffracté par l'anomalie. Les composantes du champ dans le sol sont donc données par :

$$E_x(Q) = E_{xp}(Q) + K(I_{x1} + I_{x2} + I_{x3}) \quad (5)$$

$$E_y(Q) = E_{yp}(Q) + K(I_{y1} + I_{y2} + I_{y3}) \quad (6)$$

$$E_z(Q) = E_{zp}(Q) + K(I_{z1} + I_{z2} + I_{z3}) \quad (7)$$

AD-A044 800

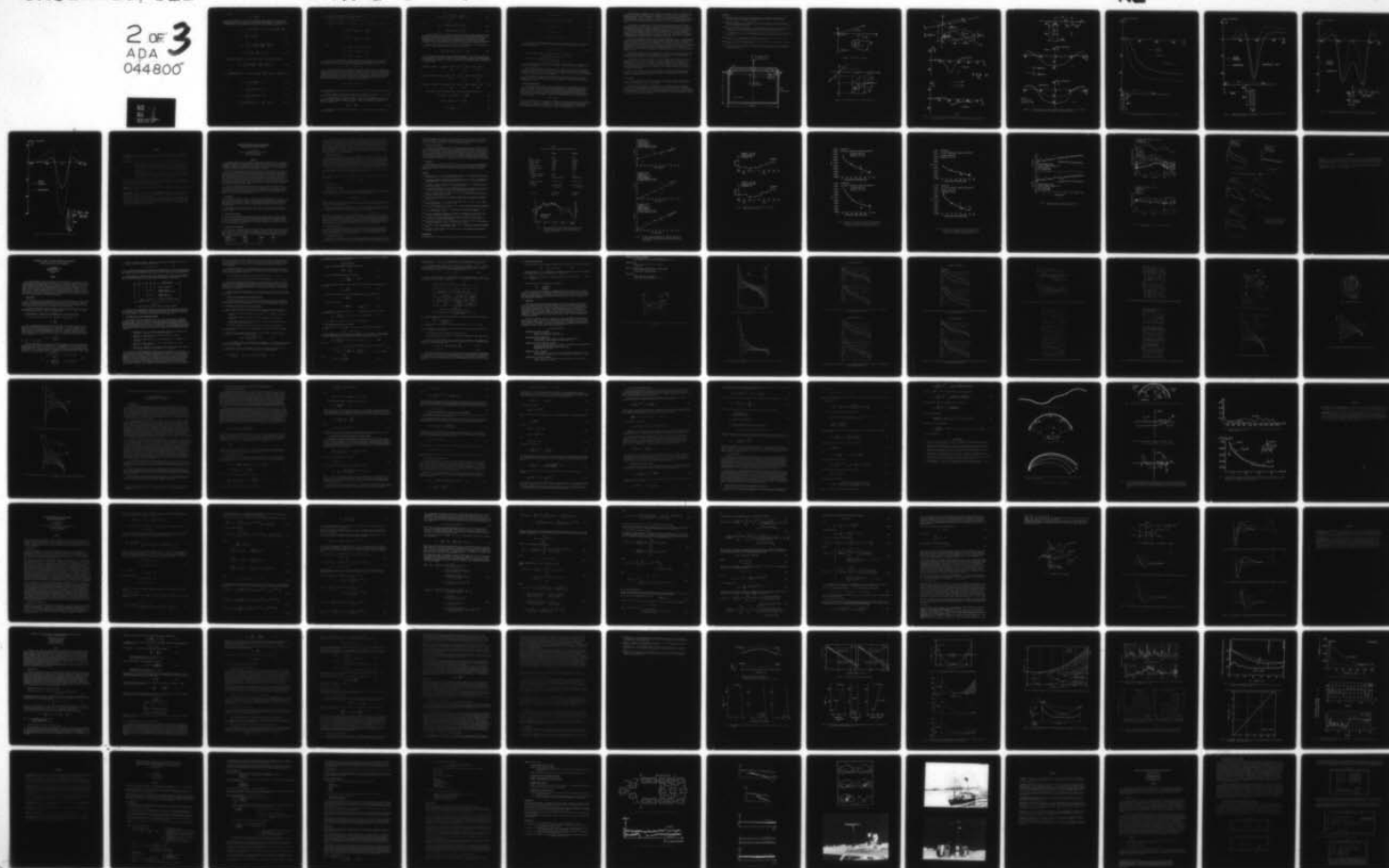
ADVISORY GROUP FOR AEROSPACE RESEARCH AND DEVELOPMENT--ETC F/G 20/14
EM PROPAGATION CHARACTERISTICS OF SURFACE MATERIALS AND INTERFA--ETC(U)

UNCLASSIFIED

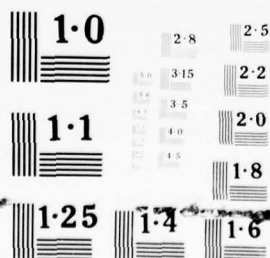
JUN 77 H J ALBRECHT
AGARD-CP-208

NL

2 OF 3
ADA
044800



2 OF 3
ADA
044800



Avec :

$$K = \frac{\sigma_2 - \sigma_1}{4\pi \sigma_1} \quad (8)$$

Dans ces formules, E_{xp} , E_{yp} et E_{zp} sont les champs obtenus dans un demi-milieu homogène. Les termes I_{x1} , I_{x2} et I_{x3} correspondent respectivement à la composante E_x du champ produit par les projections sur les trois axes cartésiens du dipôle équivalent à l'inhomogénéité. Leurs expressions sont données par les relations suivantes :

$$I_{x1} = \int_V E_{2x}(M) \left[\frac{\partial^2}{\partial x^2} (P_1 - P) - \gamma_1^2 (P_1 - P) + \frac{2\partial}{\partial z} \left[\frac{\partial^2 N}{\partial x^2} + \frac{\partial^2 N}{\partial z^2} \right] \dots \right. \\ \left. \dots - 2 \frac{\partial^2 P}{\partial z^2} - 2\gamma_1^2 \frac{\partial N}{\partial z} \right] dv \quad (9)$$

$$I_{x2} = \int_V E_{2y}(M) \left[\frac{\partial^2 P_1}{\partial x \partial y} + \frac{2\partial^3 N}{\partial x \partial y \partial z} - \frac{\partial^2 P}{\partial x \partial y} \right] dv \quad (10)$$

$$I_{x3} = \int_V E_{2z}(M) \frac{\partial^2}{\partial x \partial z} (P_1 - P) dv \quad (11)$$

De même, les termes I_y et I_z sont obtenus à partir des formules suivantes :

$$I_{y1} = \int_V E_{2x}(M) \left[\frac{\partial^2 P_1}{\partial x \partial y} + 2 \frac{\partial^3 N}{\partial x \partial y \partial z} - \frac{\partial^2 P}{\partial x \partial y} \right] dv \quad (12)$$

$$I_{y2} = \int_V E_{2y}(M) \left[\frac{\partial^2}{\partial y^2} (P_1 - P) - \gamma_1^2 (P_1 - P) + \frac{2\partial}{\partial z} \left[\frac{\partial^2 N}{\partial y^2} + \frac{\partial^2 N}{\partial z^2} \right] - 2 \frac{\partial^2 P}{\partial z^2} - 2\gamma_1^2 \frac{\partial N}{\partial z} \right] dv \quad (13)$$

$$I_{y3} = \int_V E_{2z}(M) \frac{\partial^2}{\partial y \partial z} (P_1 - P) dv \quad (14)$$

$$I_{z1} = \int_V E_{2x}(M) \frac{\partial^2}{\partial x \partial z} (P_1 + P) dv \quad (15)$$

$$I_{z2} = \int_V E_{2y}(M) \frac{\partial^2}{\partial y \partial z} (P_1 + P) dv \quad (16)$$

$$I_{z3} = \int_V E_{2z}(M) \left[\frac{\partial^2}{\partial z^2} (P_1 - P) - \gamma_1^2 (P_1 - P) \right] dv \quad (17)$$

Le volume d'intégration est évidemment le volume total de l'anomalie. E_2 est le champ existant en un point quelconque M du volume V (figure 2).

Les fonctions de Green P, P_1 et N sont définies ci-dessous :

$$N = \int_0^\infty e^{u_1(z+z')} \frac{J_0(\lambda r)}{u_1} d\lambda = I_0 \left[\frac{\gamma_1}{2} (R_2 + (z+z')) \right] \cdot K_0 \left[\frac{\gamma_1}{2} (R_2 - (z+z')) \right] \quad (18)$$

$$P_1 = \int_0^\infty e^{-u_1|z-z'|} \frac{J_0(\lambda r)}{u_1} \lambda d\lambda = \frac{e^{-\gamma_1 R_1}}{R_1} \quad (19)$$

$$P = \int_0^\infty e^{u_1(z+z')} \frac{J_0(\lambda r)}{u_1} \lambda d\lambda = \frac{e^{-\gamma_1 R_2}}{R_2} \quad (20)$$

Avec :

$$R_1 = \sqrt{(x-x')^2 + (y-y')^2 + (z-z')^2} \quad (21)$$

$$R_2 = \sqrt{(x-x')^2 + (y-y')^2 + (z+z')^2} \quad (22)$$

$$u_1 = \sqrt{\lambda^2 + \gamma_1^2} \quad \text{où } \operatorname{Re} \{ u_1 \} > 0 \quad (23)$$

Au cours de la démonstration, aucune restriction n'a été imposée à la position du point d'observation Q dans le demi-milieu conducteur. Ce point peut donc être situé à l'intérieur du volume V. Il en résulte dans ce cas que les relations 5 à 7 constituent un système de trois équations intégrales de Fredholm dont les inconnues sont :

$$E_{2x} ; E_{2y} \text{ et } E_{2z}$$

La résolution numérique de ce système a été souvent abordée grâce à la méthode des moments. Cette méthode consiste à ramener le système d'équations intégrales à une équation matricielle en divisant l'anomalie en petits éléments de volume. On choisit leurs dimensions suffisamment faible pour pouvoir supposer que, dans chacun d'eux, le champ électrique est constant et a pour valeur celle prise au centre de l'élément de volume considéré. Certains auteurs, comme Hohmann par exemple, ont appliqué directement cette méthode au système que nous venons d'exposer. Dans ce cas, quelques difficultés mathématiques surgissent. En effet, certaines intégrales à calculer ont une forme donnée par :

$$I(Q) = \int_{\Delta} \frac{\partial P_1}{\partial x} dx' dy' dz' \quad (24)$$

Δ étant la maille élémentaire représentée sur la figure 3 et P_1 la fonction de Green, définie par l'équation (19).

Lorsque le point d'observation Q tend vers M, l'intégrale (24) diverge ; mais on peut montrer analytiquement que sa valeur principale existe (Cauterman, 1975).

La solution adoptée par Hohmann consiste à assimiler le parallélépipède formé par la maille à une sphère de même volume et à intégrer ensuite analytiquement. Nous avons choisi une autre solution obtenue en remarquant que la dérivée de la fonction de Green P_1 satisfait l'équation :

$$\frac{\partial P_1}{\partial x} = - \frac{\partial P_1}{\partial x'} \quad (25)$$

En utilisant cette relation dans l'équation (24), l'intégrale I peut se mettre sous la forme suivante :

$$I(Q) = \int_{z_1}^{z_2} dz' \int_{y_1}^{y_2} \left[\frac{e^{-\gamma_1 R'_1}}{R'_1} - \frac{e^{-\gamma_1 R'_2}}{R'_2} \right] dy' \quad (26)$$

avec :

$$R'_1 = \sqrt{(x-x_1)^2 + (y-y')^2 + (z-z')^2} \quad (27)$$

$$R'_2 = \sqrt{(x-x_2)^2 + (y-y')^2 + (z-z')^2} \quad (28)$$

Ceci montre bien que I a une valeur finie que l'on peut calculer numériquement sans approximation. De plus, il est intéressant de noter qu'en faisant apparaître dans l'intégrant de I une différentielle exacte par rapport à l'une des variables d'intégration, l'intégrale triple se transforme en une intégrale double. Cette remarque va simplifier considérablement la mise en oeuvre du calcul numérique des intégrales de volume des fonctions de Green. Cette démonstration se généralise à toutes les intégrales des dérivées secondes de P_1 qui figurent dans les expressions des composantes du champ électrique.

Enfin, l'autre terme qui peut tendre vers l'infini quand $R_1 \rightarrow 0$ est la fonction P_1 , elle-même. Or, cette fonction vérifie la relation de Helmholtz :

$$\left[\frac{\partial^2}{\partial x^2} + \frac{\partial^2}{\partial y^2} + \frac{\partial^2}{\partial z^2} - \gamma_1^2 \right] P_1 = -4\pi\delta(R_1) \quad (29)$$

En utilisant cette relation, P_1 s'exprime en fonction de ses dérivées secondes par rapport à l'espace. On est ainsi ramené au calcul précédent en ayant rendu régulier tous les intégrants. Si l'anomalie de volume V est discrétisée en n éléments parallélépipédiques ΔV_k , les relations intégrales reliant les composantes du champ électrique se mettent sous la forme suivante :

$$\begin{aligned} \frac{\sigma_2}{\sigma_1} E_{2x}(M_i) &= E_{xp}(M_i) - K \sum_{k=1}^n \{ E_{2x}(M_k) \left[\int_{\Delta V_k} G_x^x dV - E_{2y}(M_k) \int_{\Delta V_k} G_y^x dV - E_{2z}(M_k) \int_{\Delta V_k} G_z^x dV \right] \} \\ \frac{\sigma_2}{\sigma_1} E_{2y}(M_i) &= E_{yp}(M_i) + K \sum_{k=1}^n \{ E_{2x}(M_k) \left[\int_{\Delta V_k} G_x^y dV - E_{2y}(M_k) \int_{\Delta V_k} G_y^y dV + E_{2z}(M_k) \int_{\Delta V_k} G_z^y dV \right] \} \\ \frac{\sigma_2}{\sigma_1} E_{2z}(M_i) &= E_{zp}(M_i) + K \sum_{k=1}^n \{ E_{2x}(M_k) \left[\int_{\Delta V_k} G_x^z dV + E_{2y}(M_k) \int_{\Delta V_k} G_y^z dV - E_{2z}(M_k) \int_{\Delta V_k} G_z^z dV \right] \} \end{aligned} \quad (30)$$

Les fonctions G sont des combinaisons de fonctions de Green, définies par :

$$G_x^x = \frac{\partial^2}{\partial y^2} (P_1 - P) + \frac{\partial^2}{\partial z^2} (P_1 + P) + 2 \frac{\partial^3 N}{\partial^2 y \partial z} \quad (31)$$

$$G_y^x = G_x^y = \frac{\partial^2}{\partial x \partial y} \left[(P_1 - P) + 2 \frac{\partial N}{\partial z} \right] \quad (32)$$

$$G_z^x = \frac{\partial^2}{\partial x \partial z} (P_1 - P) \quad (33)$$

$$G_z^y = \frac{\partial^2}{\partial y \partial z} (P_1 - P) \quad (34)$$

$$G_y^y = \frac{\partial^2}{\partial x^2} (P_1 - P) + \frac{\partial^2}{\partial z^2} (P_1 + P) + 2 \frac{\partial^3 N}{\partial x^2 \partial z} \quad (35)$$

$$G_x^z = \frac{\partial^2}{\partial x \partial z} (P_1 + P) \quad (36)$$

$$G_y^z = \frac{\partial^2}{\partial y \partial z} (P_1 + P) \quad (37)$$

$$G_z^z = \frac{\partial^2}{\partial x^2} (P_1 - P) + \frac{\partial^2}{\partial y^2} (P_1 - P) \quad (38)$$

Les points M_i et M_k correspondent au centre de chacune des mailles ΔV_i et ΔV_k . Pour des points situés dans l'anomalie, les équations du champ se résument sous la forme matricielle suivante :

$$\frac{\sigma_2}{\sigma_1} E_2 = E_p + KA E_2 \quad (39)$$

E_2 est le vecteur champ électrique inconnu dans l'anomalie :

$$E_{2x}(M_i), E_{2y}(M_i), E_{2z}(M_i) \text{ pour } i = 1, n$$

E_p est le vecteur champ électrique primaire :

$$E_{xp}(M_i), E_{yp}(M_i), E_{zp}(M_i) \text{ pour } i = 1, n$$

A est la matrice des intégrales des fonctions de Green étendues aux éléments ΔV_i . Cette matrice, de dimension $3n \times 3n$ est symétrique à condition que tous les éléments de volume ΔV_i soient égaux.

La résolution numérique du système matriciel s'effectue en utilisant l'algorithme de Choleski. L'emploi de cet algorithme pour des systèmes où la matrice A est symétrique se justifie par la rapidité de calcul et la précision des résultats obtenus. Les intégrales définies sont calculées au moyen de l'algorithme de Simpson, tandis que, pour des intégrales de surface, la méthode de Gauss a été choisie.

La résolution de l'équation matricielle nécessite un temps d'environ 1 mn pour une matrice 100×100 . Si l'anomalie est divisée par exemple en 24 mailles, le calcul des intégrales et la résolution du système matriciel demandent un temps voisin de 3 mn sur un ordinateur CII 10070.

3. EXEMPLES D'APPLICATION

Une vérification du modèle a d'abord été faite grâce à une comparaison entre les résultats théoriques et ceux obtenus expérimentalement sur la cuve analogique (Cauterman, et al., Oct. 1975). Comme nous l'avons indiqué précédemment, l'émetteur est placé à la surface de l'eau et, dans le cas du modèle analogique, la composante verticale E_z du champ électrique est mesurée à l'aide d'une sonde. Une plaque isolante a été immergée à une profondeur de 28 cm, la distance émetteur-récepteur étant de 20 et 40 cm. Pour caractériser l'influence de l'hétérogénéité, on définit habituellement un taux d'anomalie par l'équation suivante :

$$\varphi = \frac{V - V_0}{V_0} \quad (40)$$

où V est la tension mesurée en présence de l'anomalie et V_0 celle obtenue en milieu homogène. Les courbes de la figure 4 représentent la variation de φ en fonction de la profondeur du récepteur. Sur la figure (a), l'anomalie est située entre l'émetteur et le récepteur, tandis que sur la figure (b), l'émetteur est situé au dessus du parallélépipède isolant. Nous remarquons un excellent accord entre la théorie et l'expérience.

Pour détecter des anomalies situées à faible profondeur ou lorsque la conductivité du terrain est élevée, l'émetteur et le récepteur peuvent être placés à la surface du sol. Hohmann a appliqué le modèle théorique à la méthode de prospection utilisant des boucles magnétiques. Celles-ci sont déplacées à la surface du sol en maintenant constante la distance émetteur-récepteur. L'anomalie étudiée par Hohmann est représentée sur la figure (5). La résistivité du milieu encaissant est de 100 ou 300 Ωm , celle de l'inhomogénéité étant de 1 Ωm . La distance émetteur-récepteur est fixée à 150 m et la fréquence d'émission à 1 KHz.

Les courbes des figures (5a) et (5b) représentent la réponse de l'anomalie sur la partie en phase et sur la partie en quadrature du champ magnétique mesuré. La distance horizontale x est la distance entre la verticale du centre de l'anomalie et le milieu de l'ensemble dipôle-dipôle. L'anomalie a été divisée, dans ce cas, en 96 mailles. En effet, la convergence du système est souvent obtenue lorsque la taille de chacune des mailles est de l'ordre de grandeur du 1/10 de la profondeur de pénétration dans le sol. Cependant, ce critère n'est pas absolument général et il peut dépendre de la conductivité propre de l'anomalie. Il est donc nécessaire dans bien des cas de tester la convergence en augmentant systématiquement le nombre de mailles. On remarque d'après ces courbes que la composante en quadrature est la plus sensible à la présence de l'anomalie.

Nous allons maintenant envisager la même anomalie qu'Hohmann ; mais en supposant que l'émission et la réception se font à l'aide de dipôles électriques placés à la surface du sol. De plus, nous avons choisi 250 Hz comme fréquence d'émission afin de diminuer le temps calcul. En effet, ceci nous a permis de réduire à 36 le nombre de mailles. La figure 6 représente le taux d'anomalie sur la composante E_r en fonction de la position de l'émetteur. Le récepteur est fixé à la verticale de l'anomalie et les antennes d'émission et de réception sont colinéaires. On remarque, comme pour le dipôle magnétique, que la composante en quadrature est plus sensible à la présence de l'hétérogénéité. De plus, le taux d'anomalie augmente en fonction de la distance émetteur-récepteur pour tendre, à la limite, vers une valeur de 20 %.

Nous supposons maintenant que le récepteur, maintenu fixe, se situe à 150 m du bord de l'hétérogénéité (figure 7). Le taux d'anomalie est maximum lorsque l'émetteur passe au voisinage de cette hétérogénéité. Cependant, comme nous l'avons signalé précédemment, la distance émetteur-récepteur est souvent maintenue constante.

Les courbes de la figure 8 ont été tracées en supposant une distance de 150 m entre les antennes d'émission et de réception. Si l'ensemble dipôle-dipôle se déplace d'une manière continue, on voit qu'une première variation du champ reçu se produit quand l'émetteur est au voisinage de l'anomalie. Lorsque l'hétérogénéité est à égale distance de l'émetteur et du récepteur, on obtient un minimum relatif du taux d'anomalie, puis une nouvelle augmentation de ce taux lorsque le récepteur passe près de la verticale de l'anomalie. Dans cette configuration, l'émetteur et le récepteur jouent donc des rôles pratiquement symétriques.

Enfin, sur la figure 9, nous avons supposé que la distance émetteur-récepteur est réduite à 60 m. Contrairement aux courbes précédentes, il n'apparaît plus qu'un seul extremum du taux d'anomalie qui est obtenu lorsque l'hétérogénéité se situe à égale distance de l'émetteur et du récepteur.

4. CONCLUSION

Les études théoriques qui ont été développées ces dernières années permettent de modéliser sur ordinateur la réponse d'une anomalie de forme quelconque à une excitation fournie par un dipôle électrique ou magnétique.

Nous avons mis en évidence sur quelques exemples l'importance des paramètres de prospection sur l'amplitude du taux d'anomalie et sur la forme des courbes de réponse. Si on recherche des hétérogénéités dont on connaît approximativement soit leur profondeur, soit leur taille, une simulation numérique permet d'obtenir rapidement les valeurs optimum de ces paramètres de prospection et notamment la fréquence et la distance émetteur-récepteur. La comparaison des résultats théoriques et expérimentaux doit ensuite permettre de préciser la position et le volume de l'anomalie.

REFERENCES

- CAUTERMAN, M., 1975, "Etude théorique de l'influence d'une anomalie de résistivité de forme quelconque sur le champ électromagnétique créé par un dipôle en milieu absorbant", Ph. D., Lille Univ., France.
- CAUTERMAN, M., DEGAUQUE, P., et GABILLARD, R., Juin 1975, "Effect of a vertical buried conductor on the subsurface electric field for horizontal electric dipole excitation" IEEE/URSI Meeting, Urbana (Ill.)
- CAUTERMAN, M., DEGAUQUE, P., DEMOULIN, B. et GABILLARD, R., Octobre 1975, "Electromagnetic scattering by a three dimensional inhomogeneity in a dissipative half space for horizontal electric dipole excitation", IEEE/URSI Meeting, Boulder (Col.)
- DEY, A. et MORRISON H.F., 1972, "Electromagnetic response of a two dimensional inhomogeneity in a dissipative half space for TURAM interpretation", geophysics, vol 36, n° 1, pp 340-365
- HOHMANN, G.W., 1971, "Electromagnetic scattering by conductors in the earth near a line source of current", Geophysics, Vol 36, n° 1, pp 101-131
- HOHMANN, G.W., 1975, "Three dimensional induced polarization and electromagnetic modeling", Geophysics, Vol 40, n° 2, pp 309-314
- STOYER, C.H., et WAIT J.R., Octobre 1975, "Numerical study of the effect of two dimensional conductors on the surface fields of a buried vertical magnetic dipole", IEEE/URSI Meeting, Boulder (Col.)

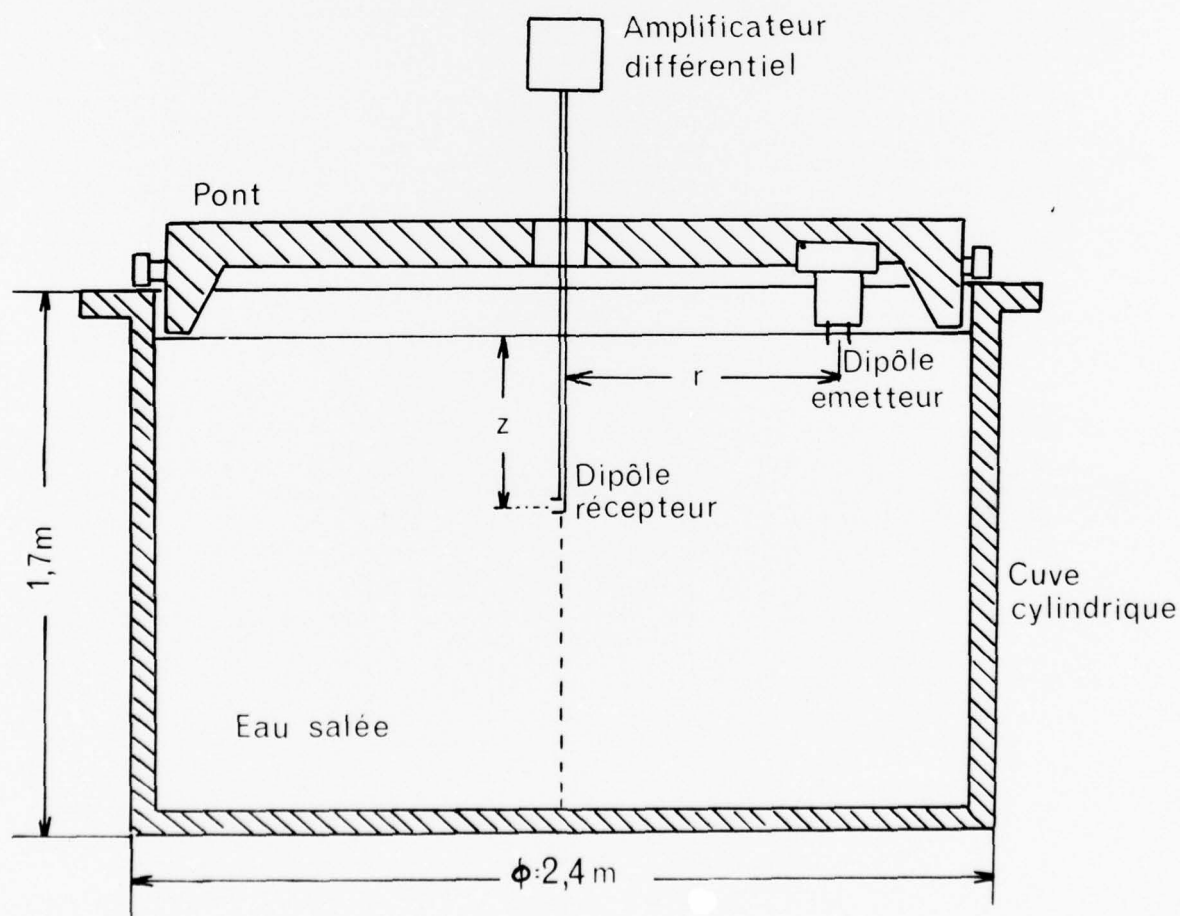


Figure 1 : Modèle analogique

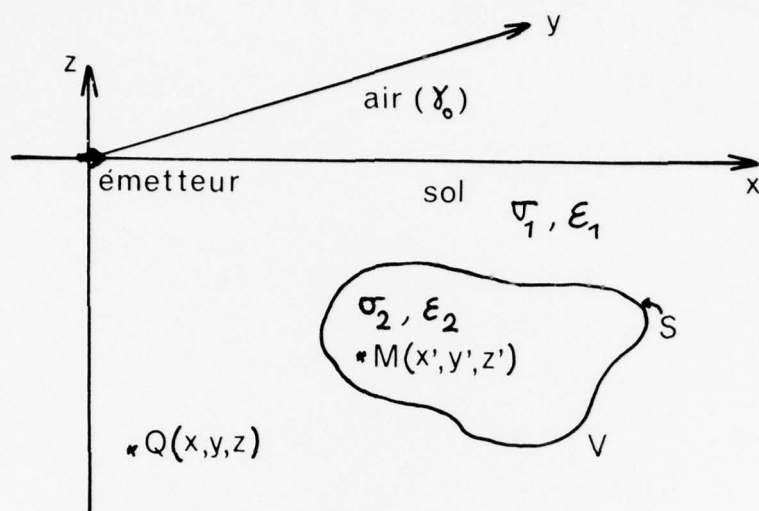


Figure 2 : Système de coordonnées

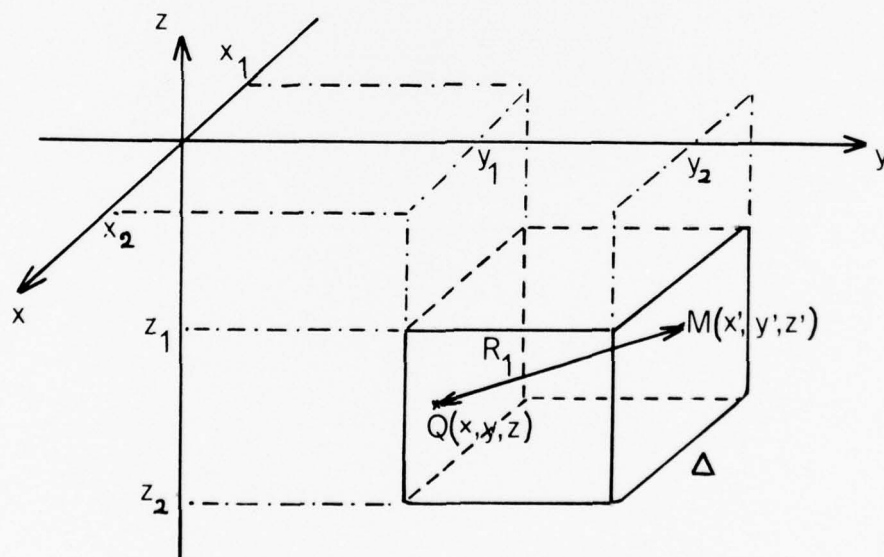


Figure 3 : Maille élémentaire du volume d'intégration

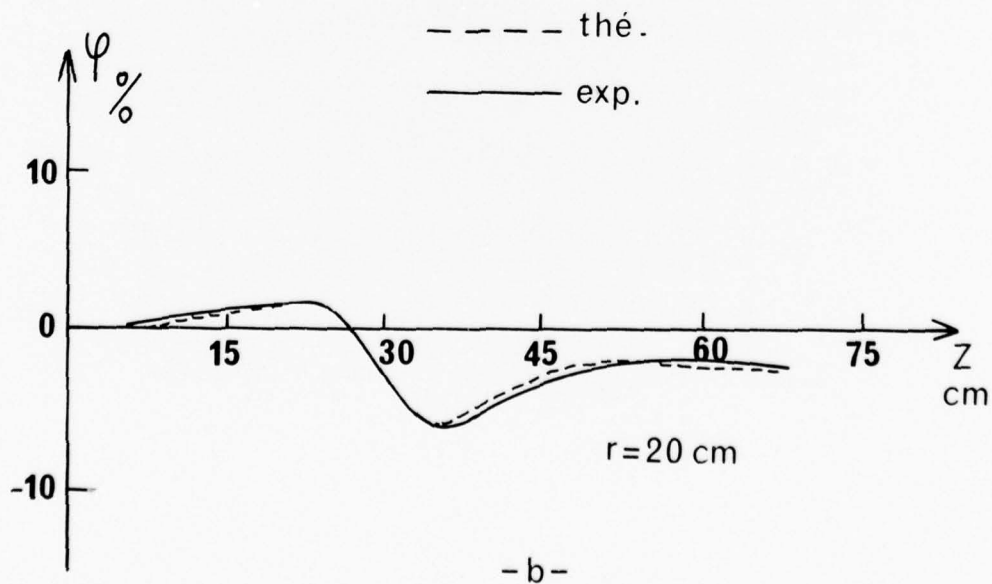
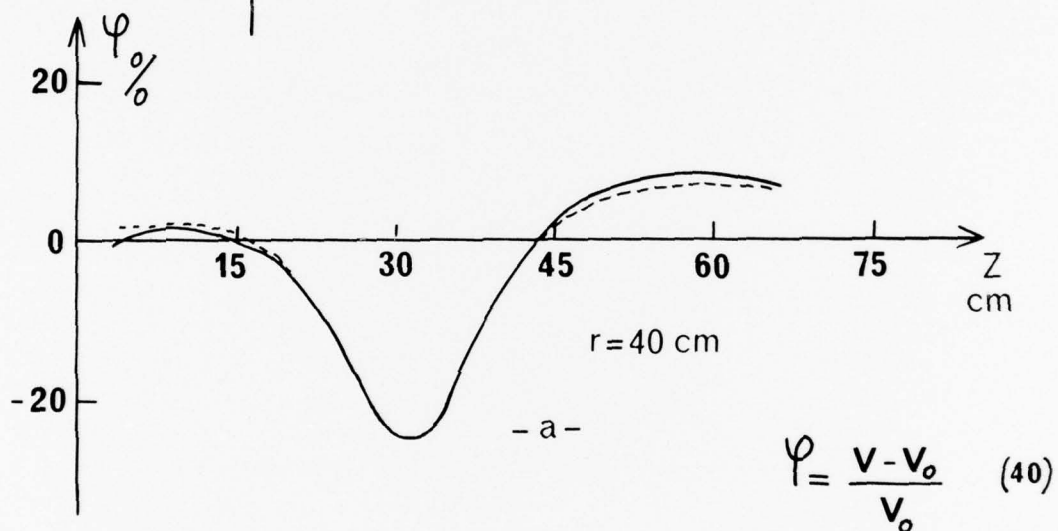
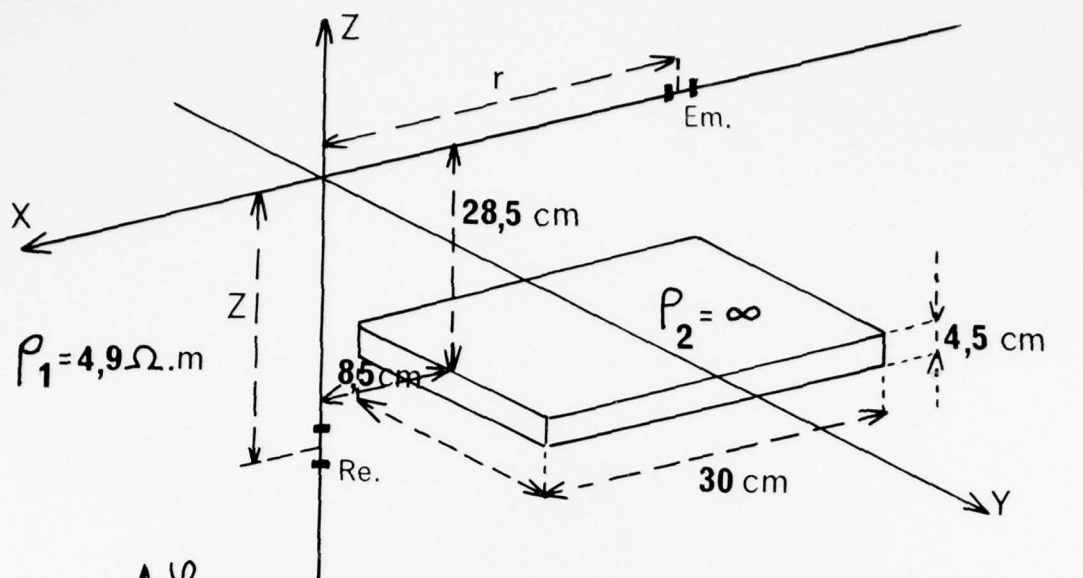
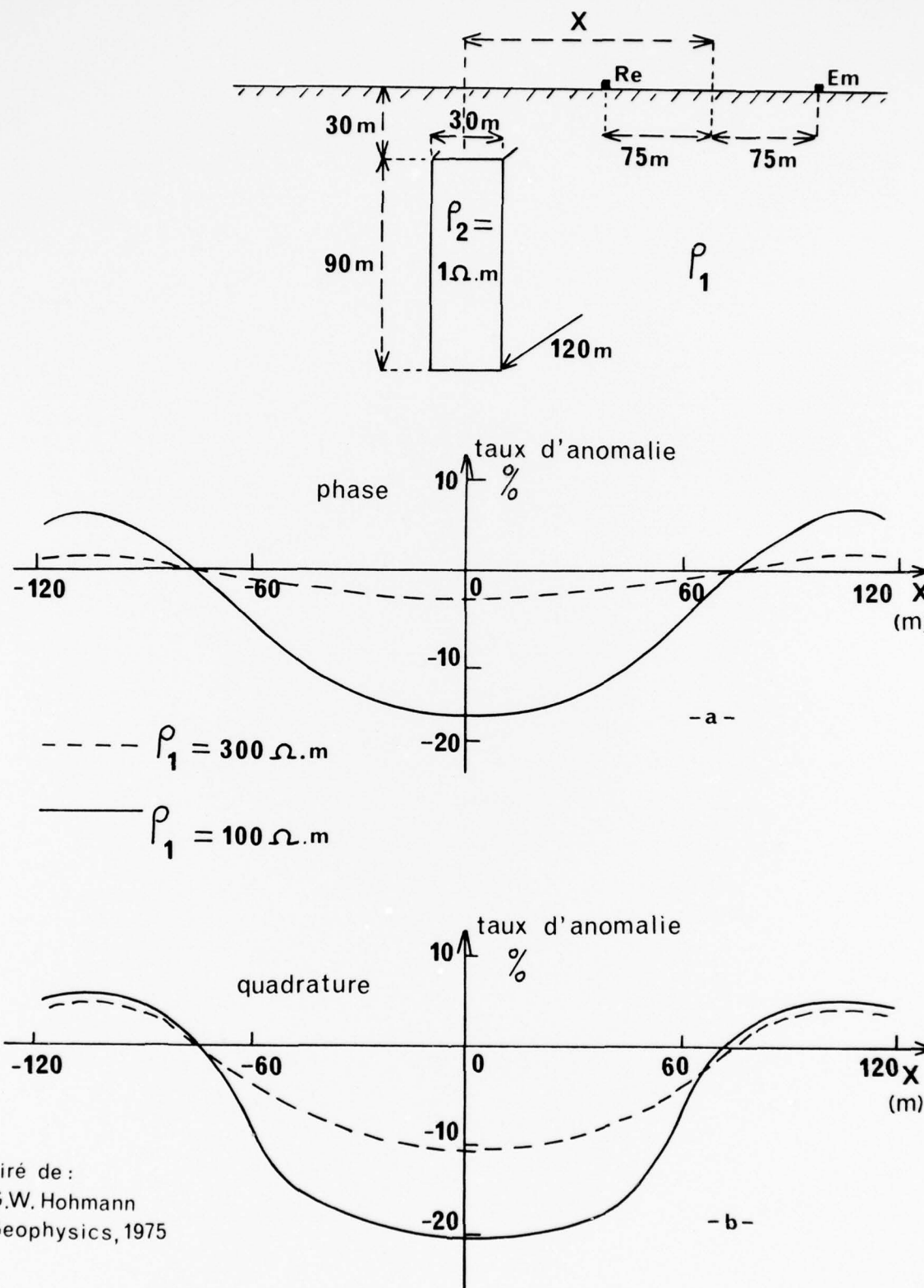


Figure 4 : Taux d'anomalie obtenu expérimentalement à l'aide de la cuve analogique, pour une hétérogénéité de résistivité infinie. Comparaison avec les courbes théoriques.



tiré de :
G.W. Hohmann
Geophysics, 1975

Figure 5 : Prospection du type dipôle magnétique-dipôle magnétique. Taux d'anomalie calculé par Hohmann sur l'amplitude du champ magnétique.

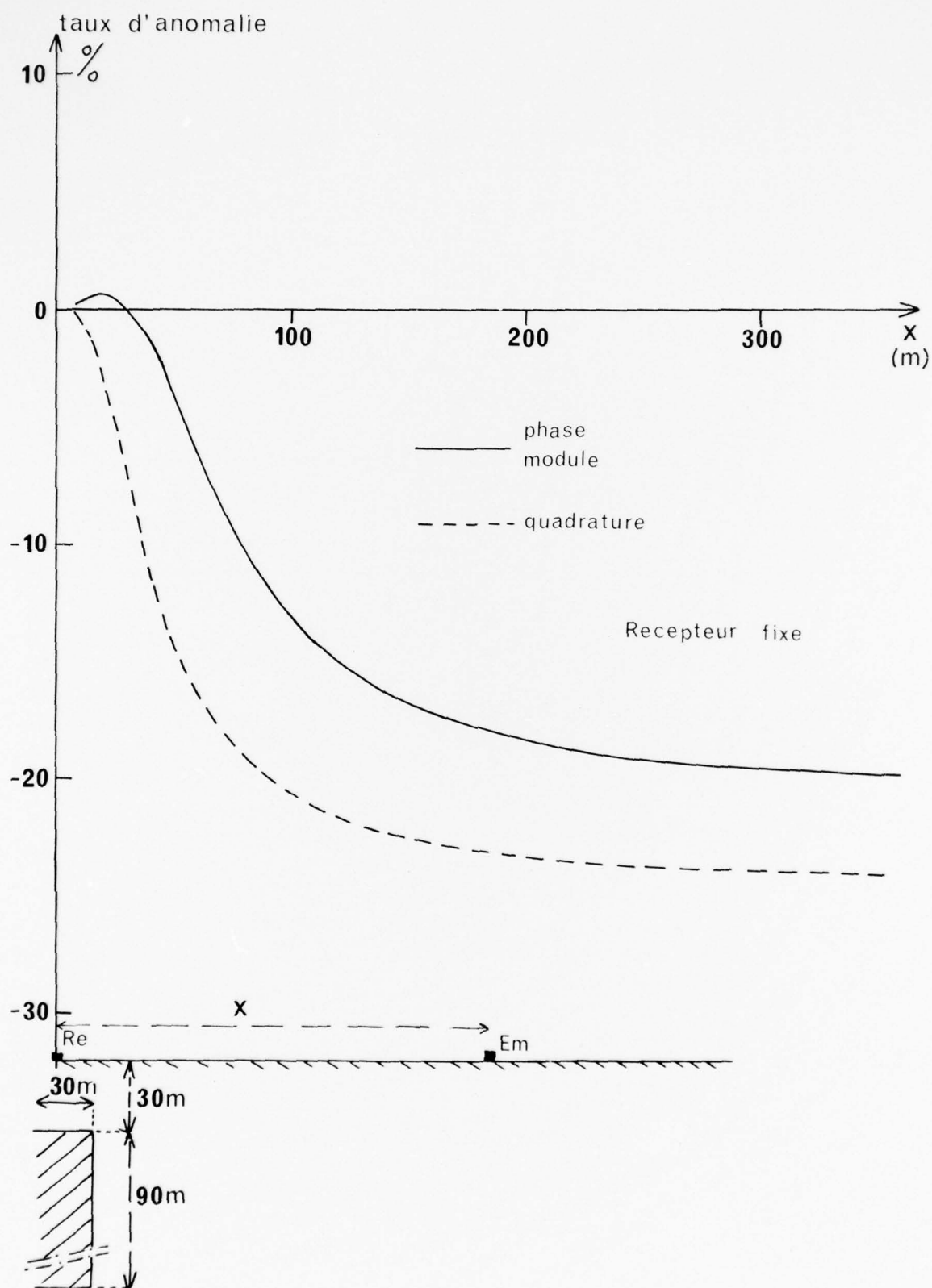


Figure 6 : Prospection du type dipôle électrique-dipôle électrique : influence de la distance émetteur-récepteur.

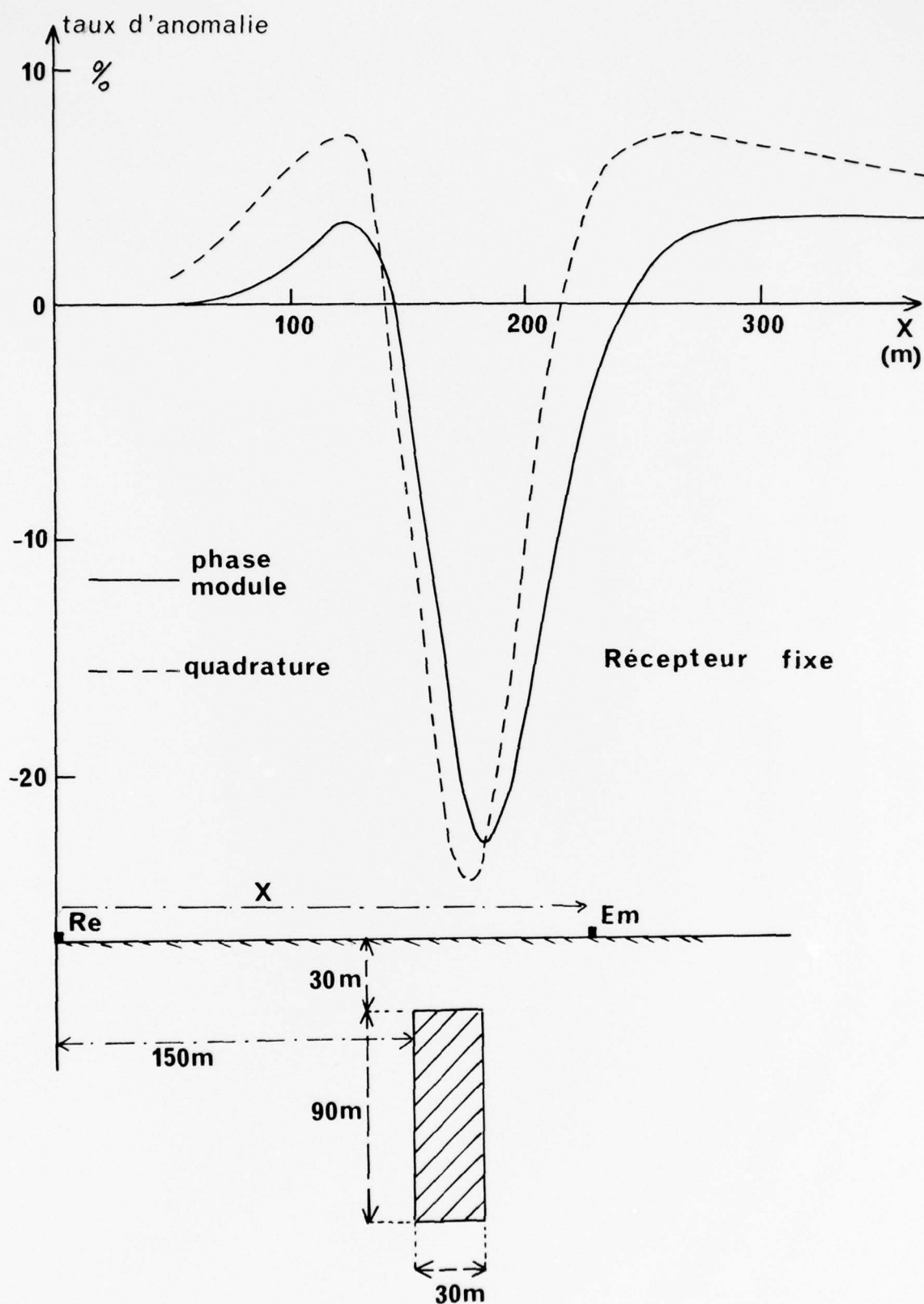


Figure 7 : Récepteur fixe. Influence de la position relative du dipôle électrique émetteur par rapport à l'anomalie.

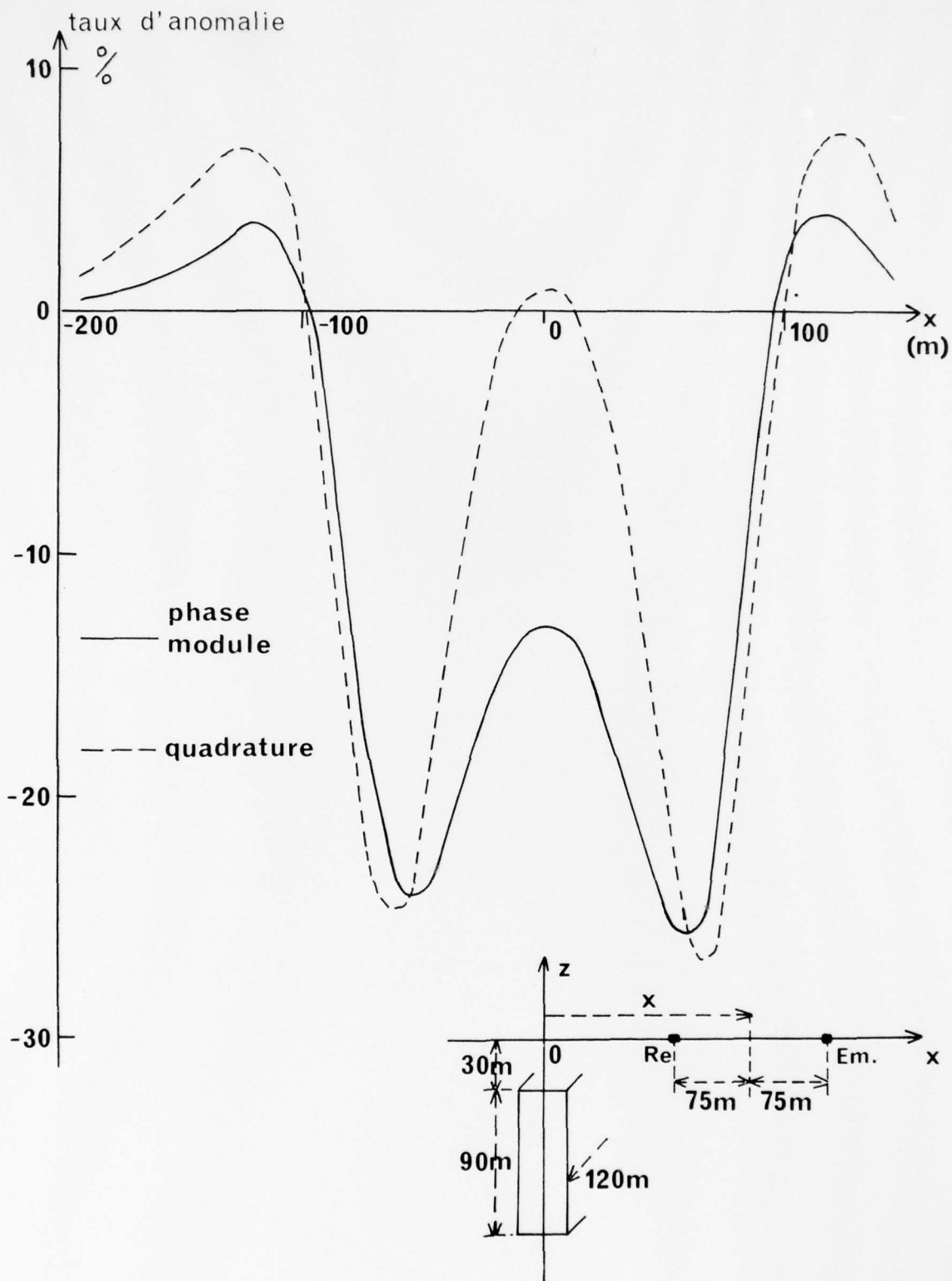


Figure 8 : Distance émetteur-récepteur fixe, égale à 150 m. Variation du taux d'anomalie en fonction de la position de l'ensemble dipôle-dipôle.

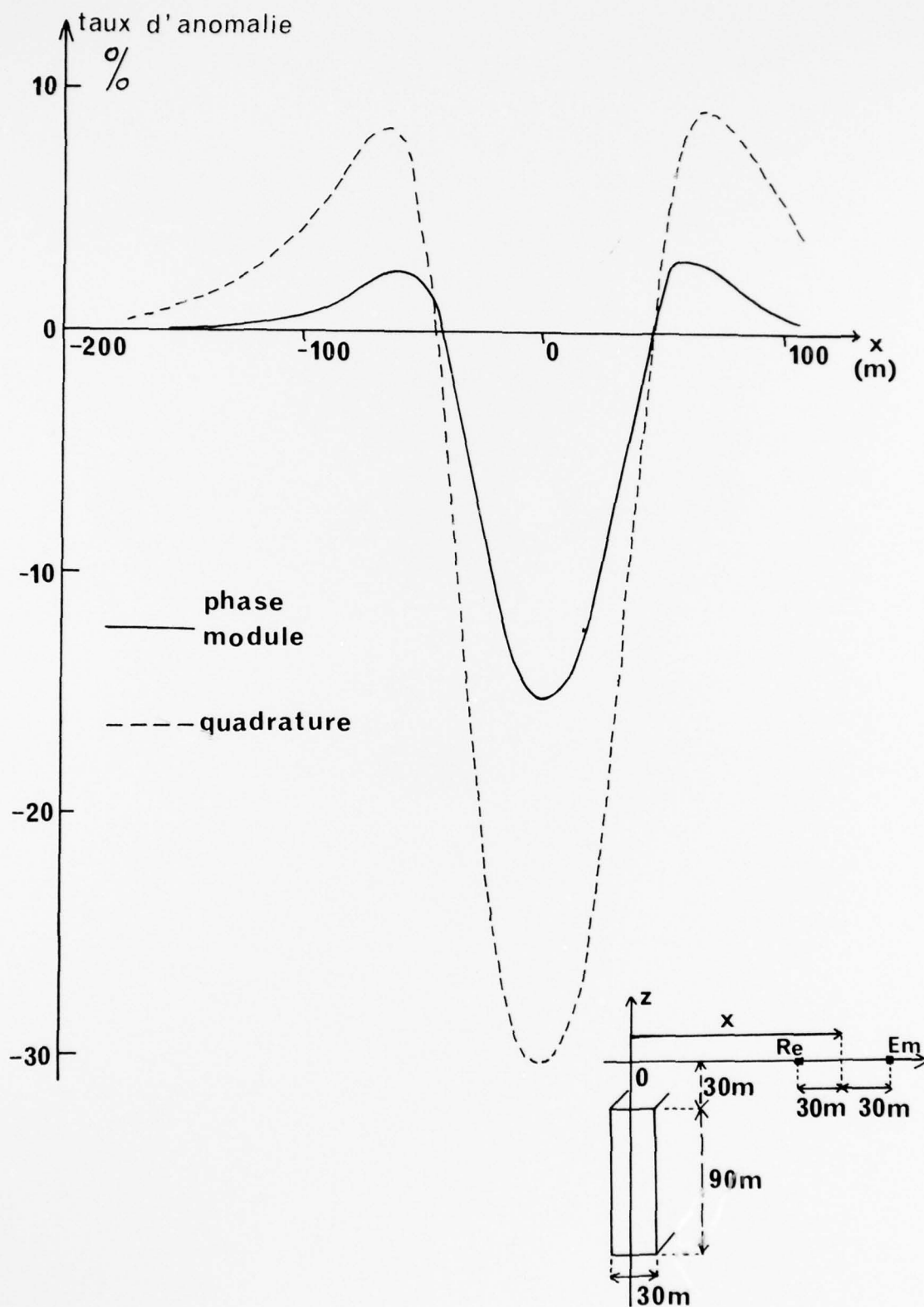


Figure 9 : Distance émetteur-récepteur fixe, égale à 60 m.

DISCUSSION

L.B.Felsen: Since the numerical solution of the integral equation requires constancy of field within each sub-volume, the method can be applied only to inhomogeneities which are not large compared to the local wavelength. Could you comment more precisely on these limitations?

R.Gabillard: For any given frequency there are three wavelengths to consider:

- (1) The atmospheric wavelength: Due to the quasi-static approximation this wavelength is always much greater than any length to be considered.
- (2) The wavelength in the conducting half-space: Due to the attenuation it is impossible to have a path transmitter-inhomogeneities-receiver of an order of magnitude greater than a wavelength in the conducting half-space. Then the inhomogeneity is always small compared to that wavelength.
- (3) The wavelength inside the inhomogeneity: It depends on its conductivity. If this is called σ_2 and σ_1 is the conductivity of the half-space, and if $\sigma_2 \ll \sigma_1$, it is sufficient that each sub-volume length be of the order of $1/10 \lambda_1$ ($\lambda_1 = \lambda/2\pi$). If $\sigma_2 \gg \sigma_1$, one can have each sub-volume length of the order of $0.6 \lambda_2$ ($\sigma_2/\sigma_1 \approx 10^4$).

These conditions have been obtained by the following test: With a given sub-volume one gets a given result. If we divide the sub-volume, for instance by a factor of two, then if the new value obtained differs by no more than a few percent from the preceding one, the sub-volume can be considered sufficiently small. Practically it is possible to divide an inhomogeneity into about 1000 sub-volumes.

A.W.Biggs: We have measured large-scale heterogeneities (objects) in the soil. We have difficulty in computing analytical models. How does your analysis correlate with experimental measurements?

R.Gabillard: As indicated in the answer to L.B.Felsen, large heterogeneities could be numerically simulated without difficulty if the basic hypotheses of the theory are verified. Namely, if the size of each cell is small enough in order to assume that the electric field in each cell is a constant. On the other hand, the theoretical model is a direct one (not an inverse model). Therefore the exact correlation between theory and experiment could be made only if the geometry and the electrical parameters of the structure are approximately known. This verification has been made, as we have outlined in our presentation, on a scale model. Furthermore, many experiments have been made "in situ" and the field variations have the same order of magnitude as those presumed.

VARIATIONS OF TEMPORAL, SPECTRAL AND ANGULAR RADAR
BACKSCATTERING COEFFICIENT OF VEGETATION

Fawwaz T. Ulaby
University of Kansas Center for Research, Inc.
Remote Sensing Laboratory
Lawrence, Kansas 66045

ABSTRACT

The scattering coefficient σ° of a target is the target-sensor transfer function: it is a resultant of the interaction between the interrogating electromagnetic wave (as characterized by its wavelength, polarization and local angle of incidence relative to the target) and the target electrical (dielectric) and geometrical properties. Vegetation is a dynamic target; over the growing cycle of a particular crop, the dielectric properties of the plant change in consequence to variations in its moisture content and its geometrical properties change in terms of height, density and shape.

This paper will review the results of an experimental program at the University of Kansas which over the past five years has succeeded in documenting the variations of the radar backscattering coefficient of a variety of crop types as a function of time, signal frequency (1-18 GHz), angular range (nadir to 80°) and polarization (HH, VV and HV). The systems used are the University of Kansas Microwave Active Spectrometers (MAS); one MAS system covers the 1-8 GHz band and the other system covers the 8-18 GHz band. Each MAS system is mounted on a mobile truck-mounted boom and is operated by a computer controller. To date, these two systems have acquired over 3 million data points from agricultural crops, bare ground and trees. Some of these results have been published in the scientific literature (Battivala and Ulaby, 1976; Bush and Ulaby, 1975; Bush and Ulaby, 1976; Bush et al., 1976; Ulaby, Cihlar and Moore, 1974; Ulaby, 1974; Ulaby, 1975; Ulaby, et al., 1975; Ulaby and Battivala, 1976a; Ulaby and Battivala, 1976b; Ulaby and Bush, 1976a; Ulaby and Bush, 1976b).

In addition to monitoring the temporal variation of σ° over a typically 4-month growing cycle, special experiments were conducted to determine the diurnal variation over the 24-hour cycle. The results indicate that the peak-to-peak diurnal variation in the magnitude of σ° decreases with frequency from about 5 dB at 1 GHz to less than 0.5 dB above 8 GHz. Another experiment was conducted to determine the effect of row direction of the plants on the backscattered return, and yet another experiment compared σ° of trees before and after defoliation.

1.0 INTRODUCTION

Radar backscatter behavior of terrain is defined by the terrain backscattering coefficient, σ° . The acquisition of data to quantify the angular, spectral and polarization variations of σ° of different types of terrain under a variety of conditions, is an important and essential step in many applications. Such a data base is necessary for the design of radar systems for remote sensing applications in the earth sciences, as well as for radar systems intended to detect man-made targets in the presence of a terrain background.

The purpose of this paper is to present, in summary form, the results of the radar backscatter measurements program at the University of Kansas. Due to space limitations, emphasis will be placed on agricultural targets.

2.0 DATA ACQUISITION SYSTEMS

The radar data reported herein were acquired by two truck-mounted Microwave Active Spectrometers, MAS 1-8 and MAS 8-18. Table 1 is a summary of their operational specifications. To reduce signal fading and to insure program representation of the targets under investigation, a combination of frequency and spatial averaging was used. System stability was monitored through the use of a delay line substitution method and absolute determination of σ° was achieved by measuring the radar return from a Luneberg lens of known radar cross section.

3.0 VEGETATION SCATTERING RESPONSE

In general, σ° is a function of the sensor parameters (frequency, polarization and angle of incidence) and the target parameters (geometry and dielectric constant) in a complex fashion, making it very difficult to separate the various dependencies into independent functional relations. It is this complexity that necessitated the acquisition of large volumes of data before a thorough understanding of the target-sensor interaction process could be achieved. To illustrate this point with an example, suppose we quantify the major variables as follows:

Variable	Range	Internal	Number
Frequency	1-18 GHz	1 GHz	19
Angle of Incidence	0° - 80°	10°	9
Polarization	HH, HV, VV	---	3
Time	120 days	3 days	41

Total Number of Measurements: $19 \times 9 \times 3 \times 41 = 21,033$

Thus, to determine the scattering coefficient spectral, angular and polarization response of one crop type over a typical growing period of 4 months, it is necessary to acquire in the neighborhood of 21,000 data points. If these data are to be related to the crop geometrical and dielectrical characteristics, detailed field measurements are also required, contemporaneously with the radar backscatter measurements. The field data usually include crop density and height, vegetation moisture content, soil moisture content, wind speed and direction, etc.. In addition to the above volume of radar backscatter data, experiments should be conducted to determine the effects of crop row direction relative to the incident wave, diurnal variations of σ° , and a variety of other factors. Although several million data points have been acquired to date, we are only at the stage of making observations regarding general trends and dependencies. In the remaining parts of this section, examples of these trends are presented, along with references to more detailed analyses.

3.1 Temporal Variation of Corn

Figure 1 presents the time record of σ_V° (dB) at 17 GHz and at an angle of incidence of 50° (left hand scale) and the time record of the plant water content per unit volume W_V (g/m^3) expressed in dB (relative to $1 g/m^3$), shown on the right hand scale. Comparison of the two records indicates very good agreement over the four month time period. Regression analyses of σ° (dB) on W_V (dB) were performed at several angles, frequencies and polarizations; examples are shown in Figure 2 for σ_V° (dB) at 50° for 8.6, 13.0 and 17.0 GHz. The results are best at 17 GHz where a correlation coefficient of 0.962 was obtained. These results are typical of the dependence of σ° on W_V for angles of incidence higher than 40° . As the angle of incidence approaches nadir, the correlation coefficient decreases due to the domination of the return by the backscatter contribution of the underlying soil (Ulaby and Bush, 1976a).

At angles higher than 40° , where the attenuation by the vegetation almost completely masks the soil backscatter component, σ° can be expressed in the following functional form:

$$\sigma^\circ = C W_V^\beta$$

where C and β are constants for a given frequency-angle-polarization combination. Expressed in dB, σ° takes the form:

$$\sigma^\circ \text{ (dB)} = A + \beta W_V \text{ (dB)}$$

where

$$\begin{aligned} A &= 10 \log C \\ W_V \text{ (dB)} &= 10 \log W_V \end{aligned}$$

3.2 Temporal Variation of Wheat

Whereas in the case of corn σ° appeared to be strongly dependent on W_V , the mass of water per unit volume of the vegetation, σ° of wheat shows a negative exponential dependence on the moisture content of the individual plants, M_p , where M_p is measured on a percentage wet weight basis:

$$M_p = \left(\frac{W_w - W_D}{W_w} \right) \times 100$$

where W_w and W_D are the average wet and dry weights of the individual wheat plants. Thus, M_p represents the mass of water ($W_w - W_D$) relative to the total weight of the plant, in contrast to W_V which is independent of the mass of the plant itself.

Figures 3 illustrate the temporal variation of σ° of wheat at 17 GHz and 50° for HH and VV polarizations (Ulaby and Bush, 1976b). The dependence of σ° on M_p is illustrated in Figures 4 and 5 for 13 and 17 GHz respectively. In functional form, the dependence can be described by:

$$\sigma^\circ = A \exp(B \cdot M_p) \quad [\text{real units}]$$

where A and B are constants for a given frequency-angle-polarization combination. As shown in Figures 4 and 5, B is a negative quantity. Since the dielectric constant of vegetation increases with moisture content (Carlson, 1967), the negative dependence of σ° on M_p cannot be attributed solely to the dielectric constant. A possible explanation of the observed behavior is that the overriding factor responsible for the temporal variation of σ° is the geometrical changes which the plants undergo during the maturation process such as the withering process of the leaves as they lose moisture. Thus, M_p serves as a measurable representative of the geometrical changes which it is related to in a complex manner.

3.3 Spectral Response of Trees

Figure 6 demonstrates the effect of frequency on the difference between Spring (with leaves) and Autumn (partially defoliated) trees (Bush et al., 1976). For the latter, only 8-18 GHz data were acquired. The Spring data indicate an increasing dependence on frequency whereas the Autumn data are almost frequency independent. The difference in behavior suggests that higher frequencies are more sensitive to the temporal variation of deciduous trees.

3.4 Diurnal Variation of Sorghum

Measurements of the radar backscatter from a dense field planted with sorghum indicate that σ° has a cyclic behavior over the 24-hour diurnal cycle (Ulaby and Batlivala, 1976b). Figures 7a and 7b illustrate the diurnal variation of σ° at 2.75 GHz and 7.25 GHz, respectively. The peak-to-peak variation appears to

decrease with frequency and is always smaller for VV polarization than HH polarization. In Figure 8, the angular dependence is presented for the extreme conditions: 6 a.m. and 6 p.m. Note that as the frequency is increased from 2.75 GHz (Figure 8a) to 7.25 GHz (Figure 8b), the difference between the 6 a.m. and 6 p.m. angular responses of σ° has almost completely disappeared.

3.5 The Effect of Row Direction

An experiment to investigate the effect on σ° of row direction relative to look direction (of the radar) was conducted over the 2-8 GHz frequency range (Batlivala and Ulaby, 1976). A field of mature sorghum with an average plant height of 2.5 m was monitored with the look direction parallel and perpendicular to the row direction. Figure 9 presents the angular response of each case at 2.75, 5.25 and 7.25 GHz. As would be expected, the attenuation by the vegetation increases with frequency thereby causing the difference between the two cases to decrease as we progress from Figure 9a to 9c. Furthermore, at nadir both cases give about the same σ° value. In the 10° - 30° angular range, large differences in σ° are observed due to look direction. As the angle of incidence is increased, however, the two angular responses approach one another. Similar observations have been noted on radar by Morain and Coiner (1970).

4.0 CONCLUSIONS

Although the radar response of vegetation is very complex due to its often non-linear dependence on several interdependent variables, the results of the radar measurement program at the University of Kansas indicates that with proper experiment definition and design and a great deal of patience and diligence, considerable information can be obtained to design radar sensor parameters for specific applications.

REFERENCES

- Batlivala, P. P. and F. T. Ulaby, "Radar Look Direction and Row Crops," Photogrammetric Engineering and Remote Sensing, v. 42, n. 2, pp. 233-238, February, 1976.
- Bush, T. F. and F. T. Ulaby, "On the Feasibility of Monitoring Croplands with Radar," Proceedings Tenth International Symposium on Remote Sensing of Environment, University of Michigan, Ann Arbor, October, 1975.
- Bush, T. F. and F. T. Ulaby, "Radar Return from a Continuous Vegetation Canopy," IEEE Transactions on Antennas and Propagation, v. AP-24, n. 3, pp. 269-276, May, 1976.
- Bush, T., F. Ulaby, T. Metzler and H. Stiles, "Seasonal Variations of the Microwave Scattering Properties of Deciduous Trees as Measured in the 1-18 GHz Spectral Range," RSL Technical Report 177-60, University of Kansas Center for Research, Inc., Lawrence, Kansas, June, 1976.
- Carlson, N. L., "Dielectric Constant of Vegetation at 8.5 GHz," Ohio State University, Electro Science Laboratory, Technical Report 1903, 1967.
- Morain, S. and J. Coiner, "Evaluation of Fine Resolution Radar Imagery for Making Agricultural Determinations," RSL Technical Report 177-7, University of Kansas Center for Research, Inc., Lawrence, Kansas, 1970.
- Ulaby, F. T., J. Cihlar and R. K. Moore, "Active Microwave Measurement of Soil Water Content," Remote Sensing of Environment, v. 3, pp. 185-203, 1974.
- Ulaby, F. T., "Radar Measurement of Soil Moisture Content," IEEE Transactions on Antennas and Propagation, v. AP-22, n. 2, pp. 257-265, March, 1974.
- Ulaby, F. T., "Radar Response to Vegetation," IEEE Transactions on Antennas and Propagation, v. AP-23, n. 1, pp. 36-45, January, 1975.
- Ulaby, F. T., T. F. Bush and P. P. Batlivala, "Radar Response to Vegetation II: 8-18 GHz Band," IEEE Transactions on Antennas and Propagation, v. AP-23, n. 5, pp. 608-618, September, 1975.
- Ulaby, F. T. and P. P. Batlivala, "Diurnal Variations of Radar Backscatter from a Vegetation Canopy," IEEE Transactions on Antennas and Propagation, v. AP-24, n. 1, pp. 11-17, January, 1976a.
- Ulaby, F. T. and P. P. Batlivala, "Optimum Radar Parameters for Mapping Soil Moisture," IEEE Transactions on Geoscience Electronics, v. GE-14, n. 2, pp. 81-93, April, 1976b.
- Ulaby, F. T. and T. F. Bush, "Monitoring Wheat Growth with Radar," Photogrammetric Engineering and Remote Sensing, v. 42, n. 4, pp. 557-568, April, 1976a.
- Ulaby, F. T. and T. F. Bush, "Corn Growth as Monitored by Radar," IEEE Transactions on Antennas and Propagation, November, 1976b.

ACKNOWLEDGEMENT

The research reported was sponsored by NASA Johnson Space Center Contracts NAS 9-10261 and NAS 9-14052.

TABLE 1.

MAS 1-8 and MAS 8-18 Nominal System Specifications

	MAS 1-8	MAS 8-18
TYPE	FM-CW	FM-CW
Modulating Waveform	Triangular	Triangular
Frequency Range	1-8 GHz	8-18 GHz
FM Sweep: Δf	400 MHz	800 MHz
Transmitter Power	10 dBm	10 dBm
Intermediate Frequency	50 KHz	50 KHz
IF Bandwidth	10 KHz	10 KHz
Antennas		
Height above ground	20 m	25 m
Reflector diameter	122 cm	46 cm
Feeds	Crossed Log-Periodic	Quad-Ridged Horn
Incidence Angle Range	0° (nadir) - 80°	0° (nadir) - 80°
Calibration:		
Internal	Signal Injection (delay line)	Signal Injection (delay line)
External	Luneberg Lens Reflector	Luneberg Lens Reflector

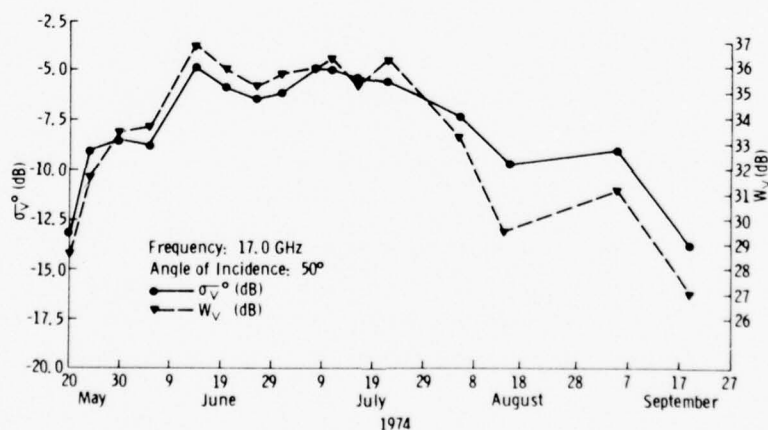


Figure 1. Temporal variations of scattering coefficient of corn σ^0 (dB) (left hand scale) and the corn canopy water mass per unit volume W_v (right hand scale). W_v is expressed in dB (log scale relative to 1 gm/m³).

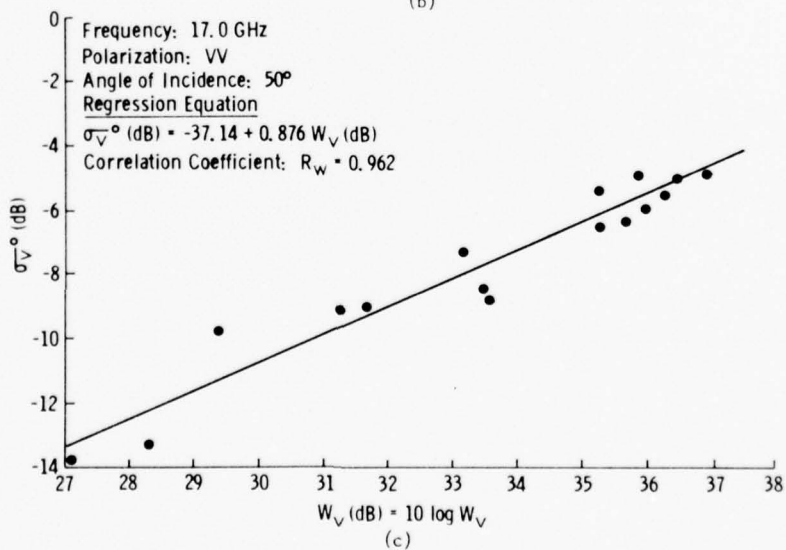
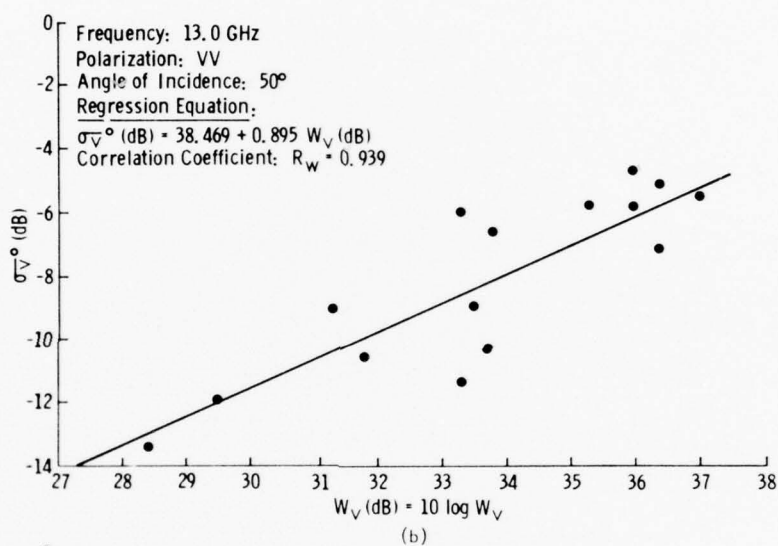
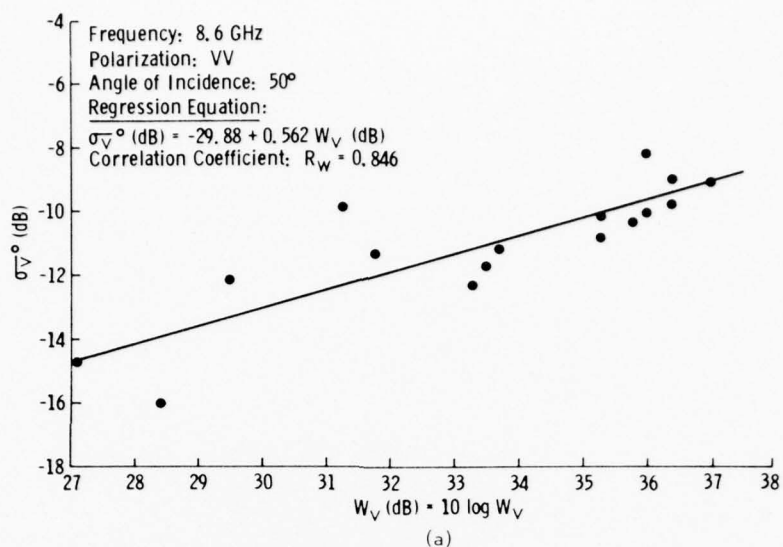


Figure 2. The scattering coefficient of corn σ° (dB) as a function of $W_V \text{ (dB)} = 10 \log W_V \text{ (dB)}$ (where W_V is the water mass per unit volume (g/m^3) of the canopy) at (a) 8.6 GHz, (b) 13.0 GHz, and (c) 17.0 GHz.

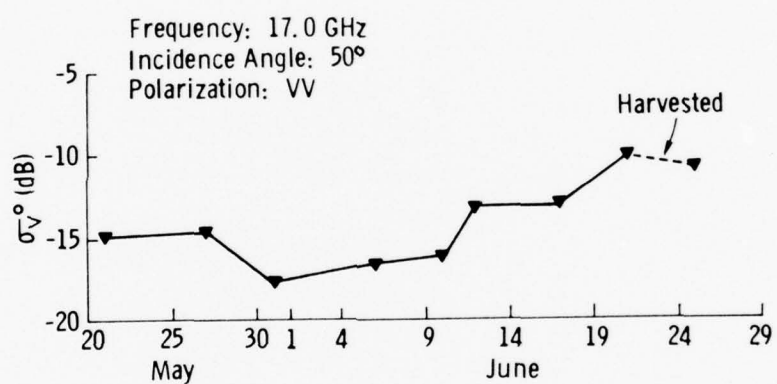
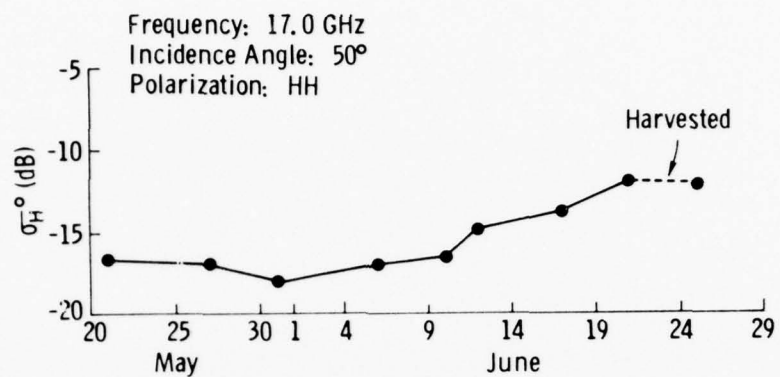


Figure 3. Temporal variations of σ_H^0 (dB) and σ_V^0 (dB) as measured at 50°, 17.0 GHz.

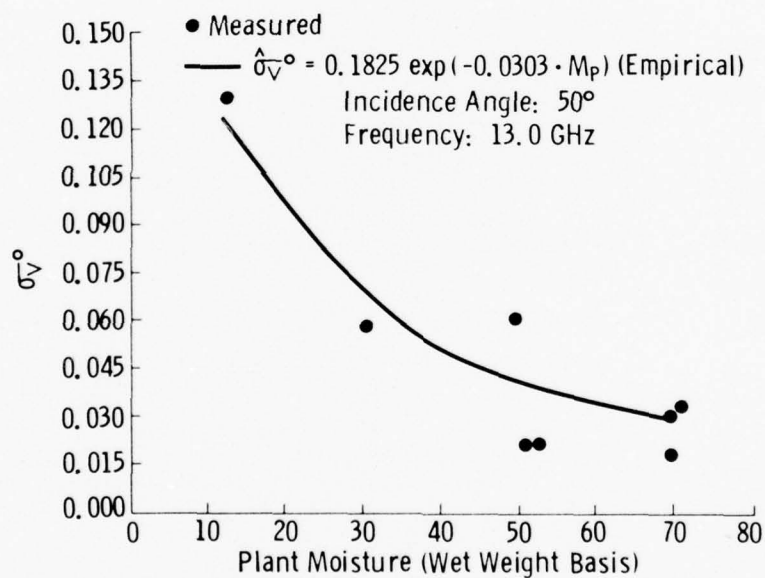
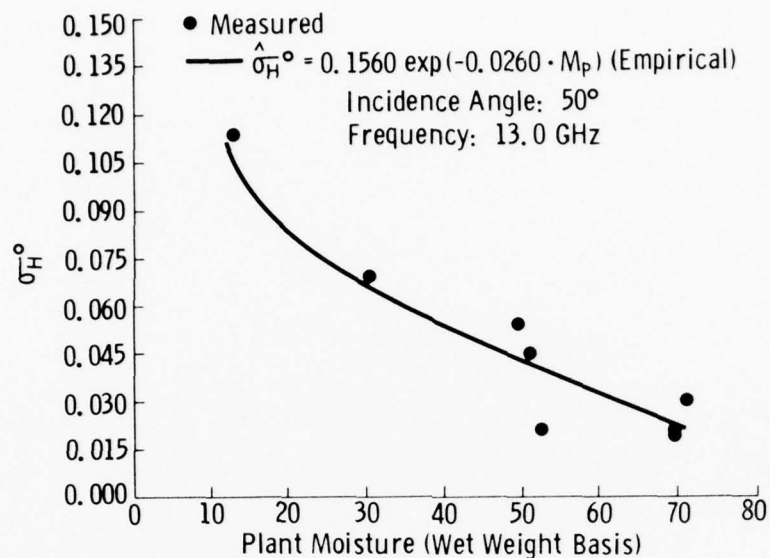


Figure 4. Variations of σ_H° and σ_V° (real units) with plant moisture. The solid lines represent the nonlinear regression curve corresponding to the equation shown with the figure. The frequency is 13.0 GHz and the incidence angle is 50° .

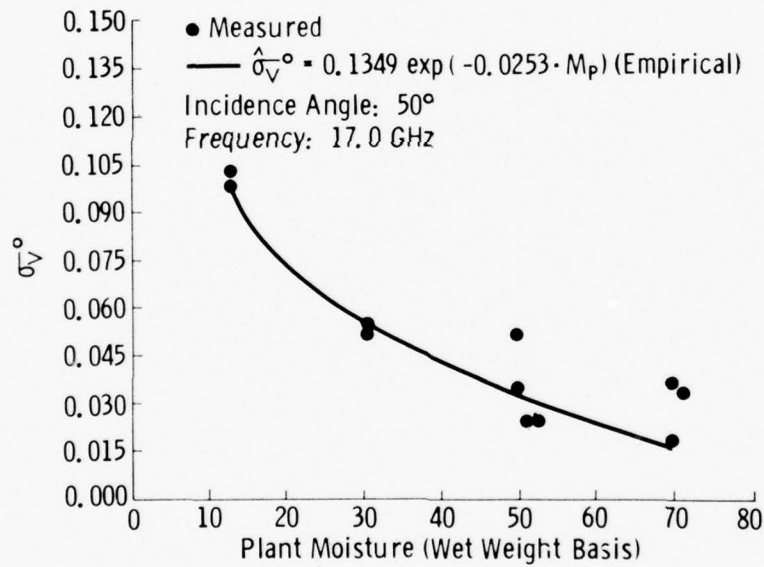
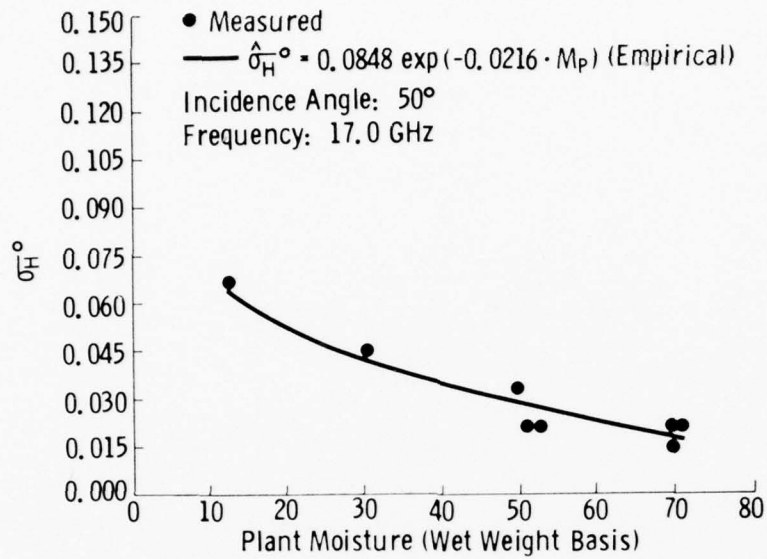


Figure 5. Variations of σ_H° and σ_V° (real units) with plant moisture. The solid lines represent the nonlinear regression curve corresponding to the equation shown with the figure. The frequency is 17.0 GHz and the incidence angle is 50° .

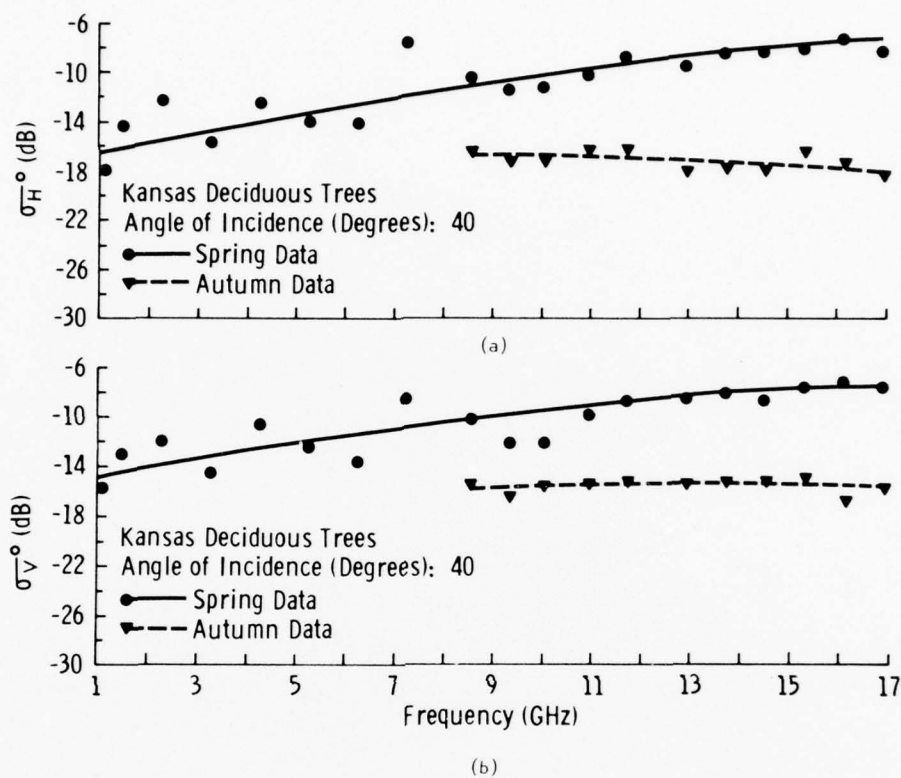
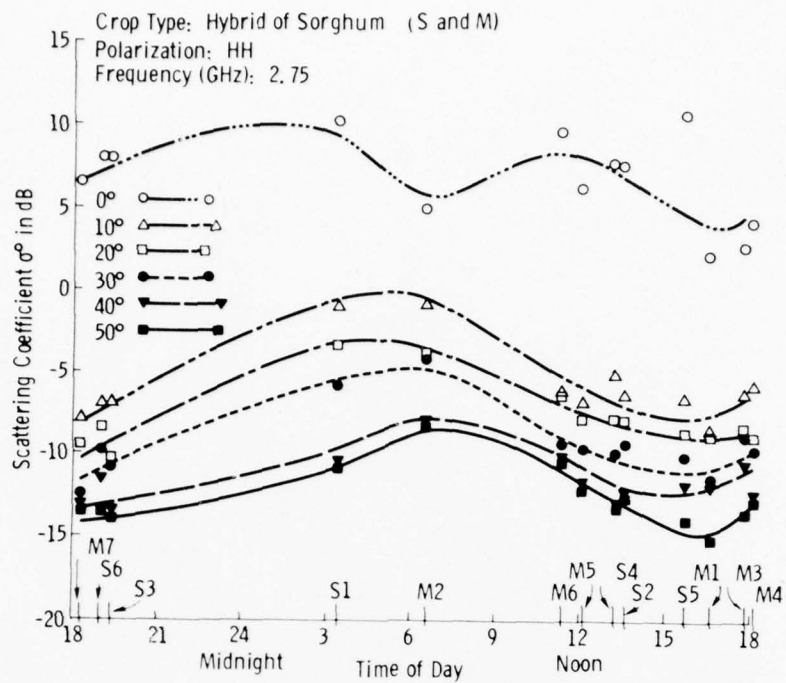
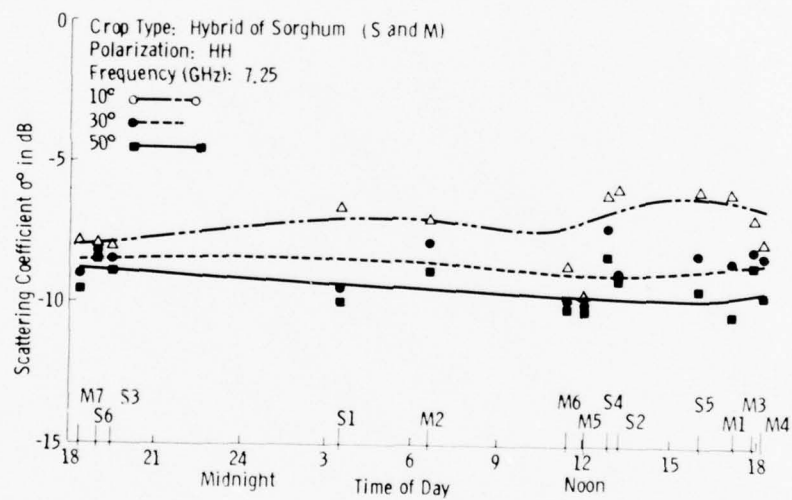


Figure 6. Spectral response of σ_H^0 (a) and σ_V^0 (b) of trees at 40° as measured in the spring and autumn.



(a)



(b)

Figure 7. The diurnal variation of σ^0 at (a) 2.75 GHz and (b) 7.25 GHz.

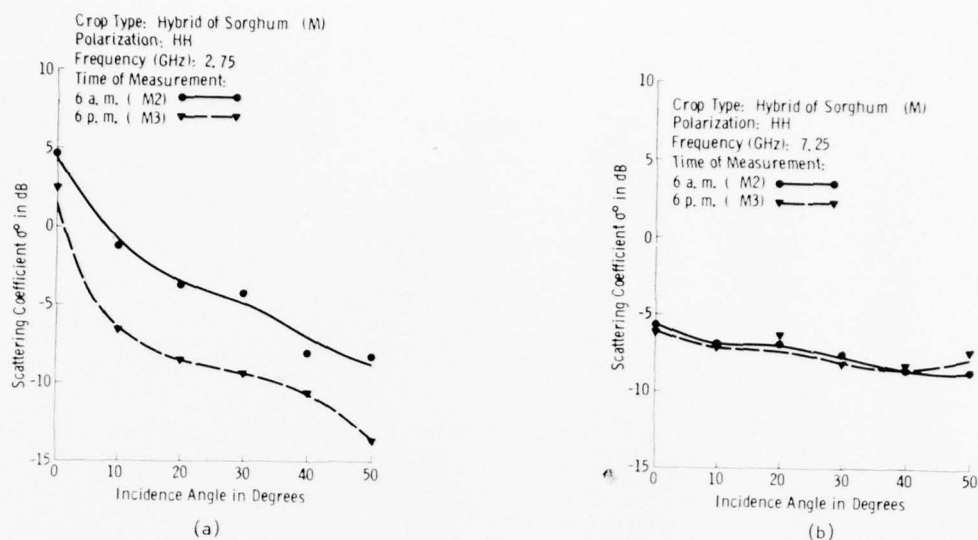


Figure 8. Comparison of the σ^0 angular response for 6 a.m. with 6 p.m. at (a) 2.75 GHz and (b) 7.25 GHz.

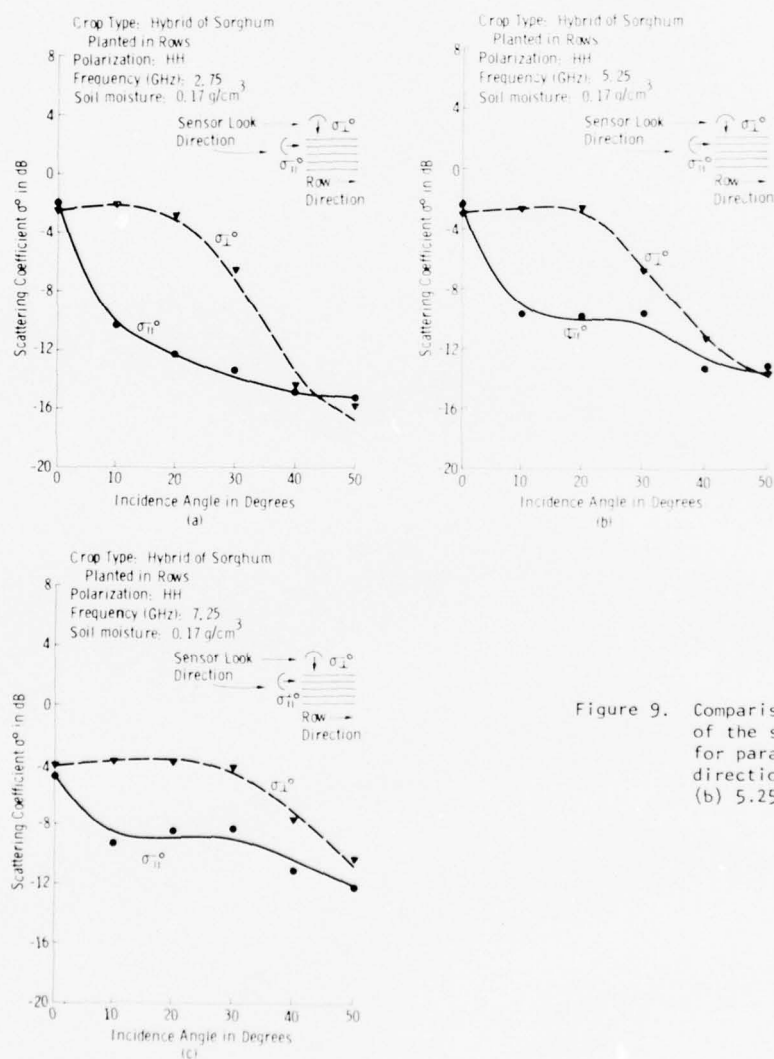


Figure 9. Comparison of the angular response of the scattering coefficient σ^0 for parallel and orthogonal look directions at (a) 2.75 GHz, (b) 5.25 GHz, and (c) 7.25 GHz.

DISCUSSION

W. Keydel: What type of antenna has been used ? - Have the antennae been moved for measurements of angle dependence or were range gates used ? Have circularly polarized equipments been considered or have such experiments been conducted and what has been the result with respect to ground clutter ? - Are the presented σ_c -values mean values ?

A.W. Biggs: Antennae were parabolic dishes with horn feeds. No circular polarization measurements were made. We measure ground scatter from vegetation - which includes "clutter". The σ_c -values are mean values.

AN EMPIRICAL MODEL FOR AVERAGE SCATTERING CROSS SECTION

COMPUTATIONS FOR LAND- AND SEA-SURFACES

W. Keydel
AEG-TELEFUNKEN ULM
Elisabethenstr. 3
7900 Ulm / Donau
Germany

SUMMARY

The paper presents an empirical formula for the mathematical representation of the average backscattering cross section per unit area, σ_0 , for land- and sea-surfaces. There exists no physical explanation for the validity of the formula but comparisons with measurements show that good agreements can be reached and that the formula can be used for clutter computations in case of different surfaces and over a wide frequency range. The model contains as special cases some different still existing models, Lamberts law for example. For a horizontal moving radar with a rotational symmetrical antenna the stated model leads to simple solutions for the spectral power-density and the total power of the ground clutter. The spectral power-density can be expressed as a hypergeometric series. This model can be useful for comparative system analysis of different systems as well as for first clutter estimations in radar system design.

1. INTRODUCTION

For considerations on land- and seaclutter the backscattering cross section per unit area, σ_0 , is the decisive environmental factor. It can only be mathematically assessed with great difficulty and the aim of the present paper is to give a relative simple expression as an empirical model for a mathematical description of the average σ_0 , which allows simple and closed solutions of the so-called clutter integral.

In reality simple models do apply in special cases only; this holds especially for random quantities as σ_0 and for empirical models, however they may be useful for comparative analysis as well as for worst case considerations.

2. ESTABLISHMENT OF A FORMULA FOR THE DEPENDENCE OF σ_0 ON THE GRAZING ANGLE

For σ_0 holds the following definition (Beckmann and Spizzichino, 1963):

$$\sigma_0 = \frac{d\sigma}{dF} \quad (1)$$

In (1) is $d\sigma$ the radar cross section of an element of the earths' surface dF . In agreement with Beckmann and Spizzichino and other authors it will be assumed that σ_0 depends only on the grazing angle and not on the distance r from the radar or on its height h above the ground. Furthermore the experience shows that normally σ_0 increases monotonously with increasing grazing angles. (There are exceptions from this general rule in special cases). In general σ_0 has for land- and sea-surfaces the principal shapes of the dependence on the grazing angle given in Fig. 1. Similar shapes show the curves in Fig. 2 given by:

$$S(\delta) = \frac{\sin^{(\nu+1)} \delta}{\cos^\mu \delta} \quad (2)$$

$\mu \geq 0$ and ν are real numbers.

This is a twoparametric set of curves in which the parameter μ varies the steepness of the function for large grazing angles while the parameter ν varies the steepness for small grazing angles. (Fig. 3). Formula (2) has a singularity for $\delta = 90^\circ$ and in order to eliminate this the curves given by (2) have to be considered for grazing angles less than a limit angle δ_g . In the range $\delta_g \leq \delta \leq 90^\circ$ δ_g should be considered as a constant value. The introduction of a factor δ_μ which allows the adaption of the model function to actual values leads to the following formula for the average of σ_0 :

$$\sigma_0 = \begin{cases} \delta_\mu \frac{\sin^{(\nu+1)} \delta}{\cos^\mu \delta} & \text{for } 0 \leq \delta \leq \delta_g \\ \delta_\mu \frac{\sin^{(\nu+1)} \delta_g}{\cos^\mu \delta_g} & \text{for } \delta_g \leq \delta \leq 90^\circ \end{cases} \quad (3)$$

This is the requested formula. Instead of σ_0 some authors (Beckmann 1963, Ruck 1970, for instance) introduce a quantity γ defined by:

$$\sigma_0 = \gamma \sin \delta \quad (4)$$

μ , γ and γ_μ are functions of the average surface properties, they have to be estimated by comparison with measurements for each type of surfaces in order to obtain optimum agreement between the model and measured results. This shall be done in the following chapter.

A first look on (2) shows that the formula includes some existing well-known empirical and semi-empirical models for average σ_0 of rough surfaces as special cases: (Ruck, Barrik, Stuart, Krichbaum, 1970). Table 1 gives an overlook over such cases:

μ	γ	σ_0	NAME OF MODEL
0	-1	γ_0	Clapps second model
0	0	$\gamma_0 \sin \delta$	Lommel Seeliger, Clapps third model resp.
0	1	$\gamma_0 \sin^2 \delta$	Lamberts law, Clapps first model
0	arbitrary	$\gamma_0 \sin^\gamma \delta$	Generalized Lamberts Model

Table 1
Connection with model (3) and still existing models.

All the still existing models contain one or more arbitrary constants and for most of them there is no satisfactory scattering mechanism which can explain the behavior of the respective model. Nevertheless under certain conditions they may have applicability for certain surfaces. In principle the same holds for the model in (3).

3. THE VERIFICATION OF THE PRESENTED σ_0 -MODEL

The formula (3) giving the dependence of σ_0 on the grazing angle has no physical explanation. The validity of formula (3) for actual cases can be shown by comparison with measurements only. There exist very many measurements on the dependence of σ_0 on the grazing angle, the most important of these published measurements are listed in the References of Nathanson E.E., 1975, Ruck D., Barrik et al., 1970, Beckmann and Spizzichino, 1963. For the purpose of the present paper the following clutter environments and characteristics measured and published by the respective authors shall be considered as representative:

1. Seaclutter in P, L, C, X-Band for different seastates and polarizations (Guinard N. W. and Daley J. C., 1970) Fig. 4 and 5.
2. Landclutter, Land covered with different vegetation C, X-Band (Ulaby F. T., 1975) Fig. 6.
3. Landclutter, Asphaltroads X, Ku, Ka-Band (Earing D. G. and Smith J. A., 1966) Fig. 7.
4. Landclutter, urban industrial areas, S, L-Band (Earing D. G. and Smith J. A., 1966) Fig. 8.
5. Landclutter, mountains and other cases where σ_0 increases with decreasing grazing angle (Earing D. G. and Smith J. A., 1966) Fig. 9.

Some results of these measurements of σ_0 are given in the Figures 4 to 9. These figures show the measured dependence of σ_0 on the grazing angle δ for different conditions and in comparison the empirical adapted model function according to (3). The results represented in Fig. 4 and Fig. 5 show that the model (3) is able to describe the angle-dependence of σ_0 for sea-surfaces in a frequency range from 0.4 GHz up to 8 GHz and for different seastates. The reason for the variance of the measured results shown in these figures is that the measurements have been conducted on different days and therefore for different seastates. In principle the same holds for the results shown in Fig. 6 for the 80 % boundaries of σ_0 in dependence of δ for land-surfaces (Ulaby, 1975). These measurements are conducted for different vegetation and that causes the given variance.

In all cases a sufficient and in some cases an excellent agreement between measurements and the model function (3) can be reached by a proper choice of μ, ν, γ, μ and σ_g . Special cases are represented in Fig. 9. Here are given some cases where σ_g increases for decreasing grazing angle and it can be seen that the model also includes these cases if γ becomes negative.

As a first conclusion it can be established that for different surface conditions and for different frequencies a fit choice of μ and γ leads to good agreements with measured results. The surface characteristics influence the values of μ and γ . As a first result the following can be said:

For the considered sea-surfaces holds approximately $1 \leq \mu \leq 5$, $-0,25 \leq \gamma \leq 1$.

For the considered land-surfaces has been found approximately $0 \leq \mu \leq 1$, $-4 \leq \gamma \leq 2$.

These results lead to the conclusion that for sea-surfaces the quantity μ is important and that for land-surfaces the quantity γ plays the important part. In a future work more detailed comparisons of the here presented σ_g -model with measurements shall be carried out. The aim of this work should be to work out the dependence of the model parameters with the environment characteristics (frequency, polarization, surface-characteristics) more in detail.

However, the here presented results lead to the conclusion that the stated formula (3) for the dependence of the average on the grazing angle describes the reality with satisfaction.

4. THE USE OF THE σ_g -MODEL FOR CLUTTERCALCULATIONS

The stated model can be used for cluttercalculations. Especially the computation of the spectral power-density for a horizontally over ground moving radar with a rotational symmetrical antenna diagram leads to relatively simple mathematical expressions.

4.1. Geometrical considerations and clutter-integrals

The following conditions have to be fulfilled for the calculation of the spectral power-density P_{cf} and of the total power P_c of the groundclutter for a CW-radar:

1. The radar is flying horizontally at a velocity V at a height h above the ground.
2. The antenna diagram of the radar is axially symmetrical to the velocity vector V .
3. The ground is considered to be a plane, the backscattering characteristics of the ground are described by σ_g .
4. Farfield conditions are applicable for both, the radar and the surface.

Fig. 10 shows the geometry of the arrangement taking into account the above mentioned conditions.

From the surface element dF with a radar cross section $d\sigma$ the radar receives a clutterpower dP_c following the radar equation

$$dP_c = \frac{P_1 \eta \lambda^2 g^2 E^4 \cdot d\sigma}{(4\pi)^3 r^4} \quad (5)$$

(P_1 = transmitter power, λ = wavelength of transmitter, g = antenna gain, E = antenna directivity pattern, η = losses due to system and propagation, r = distance between radar and surface element).

One obtains the total clutter power P_c seen by the considered radar from (5) by integration; with respect to (1) and (4) follows after some manipulations:

$$P_c = \frac{P_1 \eta g^2 \lambda^2}{(4\pi)^3 h^2} \iint E^4 \gamma \sin^3 \vartheta \cos^2 \varphi \, d\vartheta \, d\varphi \quad (6)$$

Because of its inherent motion the radar states a doppler -shift f_D of the radiated power with respect to the received power:

$$-f_{Dmax} \leq f_D \leq f_{Dmax}$$

f_{Dmax} is the maximum doppler frequency encountered:

$$f_{Dmax} = \frac{2V}{\lambda} \quad (7)$$

The relative doppler frequency Ω is defined:

$$\Omega = \frac{f_D}{f_{Dmax}} = \cos \vartheta \quad (8)$$

The spectral power-density of the clutter, P_{cf} , with respect to the frequency f is defined as:

$$P_{cf} = \frac{dP_c}{df} \quad (9)$$

This definition leads to the spectral power-density $P_{c\Omega}$ referred to Ω :

$$P_c = \frac{dP_c}{d\Omega} \quad (10)$$

Because of (8) holds:

$$d\Omega = \sin \vartheta d\vartheta = \frac{1}{f_{Dmax}} df_D \quad (11)$$

One obtains for the power-density $P_{c\Omega}$ after the introduction of the filter-characteristic $H(\Omega)$:

$$P_{c\Omega} = \frac{P_1 \gamma g^2 \lambda^2}{(4\pi)^3 h^2} E^y(\Omega) H(\Omega) (1-\Omega^2) \int_{-\pi/2}^{\pi/2} \gamma \cos^2 \varphi d\varphi \quad (12)$$

The integrals in (6) and (12) are called clutter integrals.

4.2. The spectral power-density of clutter

With respect to (4) the integral (12) can be solved. Taking into account the relation

$$\sin \delta = \sin \vartheta \cos \varphi$$

it can be shown that the integral in (12) is identical with the integral representation of the hypergeometric series (Gradshteyn and Ryzhik, 1965) with μ and ν as a part of the parameters. Integration of (12) leads to the following expression for $P_{c\Omega}$:

$$P_{c\Omega} = \frac{P_1 \gamma \lambda^2 g^2}{(4\pi)^3 h^2} E^y(\Omega) H(\Omega) (1-\Omega^2) 2 \delta_\mu \cdot I(\Omega) \quad (13)$$

Herein is:

$$I(\Omega) = \begin{cases} I_{\mu\nu} = \frac{1}{2} (1-\Omega^2) B\left(\frac{1}{2}, \frac{\nu+3}{2}\right) F\left(\frac{\nu+3}{2}, \frac{\mu}{2}, \frac{\nu}{2}+2, 1-\Omega^2\right) & \text{for } \cos \delta_g \leq \Omega \leq 1 \\ I_{\mu\nu} = \int_{\frac{\pi}{2}-\delta_g}^{\pi/2} \frac{\cos^y \varphi}{\sin^u \varphi} d\varphi + \frac{\sin^y \delta_g}{\cos^u \delta_g} \cdot \psi & \text{for } 0 \leq \Omega \leq \cos \delta_g \end{cases} \quad (14)$$

With

$$\psi = \arccos \frac{\sin \delta_g}{\sin \vartheta} \quad (15)$$

In (14) is $B\left(\frac{1}{2}, \frac{\nu+3}{2}\right)$ the Betafunction, F is the hypergeometric series and the remaining integral is solvable by a recursion formula (Gradshteyn and Ryzhik, 1965).

It can be shown that in many cases the choice of $\nu = 0$ and $\mu = 0, 1, 2, \dots$ integer leads to sufficient agreement between the σ_c -model and experimental values. In this case the hypergeometric series in (14) leads to simple algebraic expressions in Ω and to elliptic integrals respectively. For the Betafunction holds:

$$B\left(\frac{1}{2}, \frac{3}{2}\right) = \frac{\pi}{2} \quad (16)$$

Table 2 shows the expressions which result for the hypergeometric series and the integral in (14) in the case $\mu = \text{integer}$ and $\nu = 0$ (Abramowitz and Stegun, 1965, Gradshteyn and Ryzhik, 1965) and for $\sin \psi \approx \psi$.

μ	$F\left(\frac{3}{2}, \frac{\mu}{2}, 1-\Omega^2\right)$	$I_{\mu\nu}^{\delta_g}$
0	1	0
1	$\frac{4}{\pi(1-\Omega^2)} (K'(\Omega^2) - E'(\Omega^2))$	$\frac{\psi}{\cos \delta_g} - \ln \tan \frac{\psi}{2}$
2	$\frac{2}{\Omega(1+\Omega)}$	$-\frac{\pi}{2} + \cot \psi + \psi \left(1 + \frac{1}{\cos^2 \delta_g}\right)$
3	$\frac{4}{\pi(1-\Omega^2)} \left(\frac{E'(\Omega^2)}{\Omega^2} - K'(\Omega^2)\right)$	$\frac{\psi}{\cos^3 \delta_g} + \frac{1}{2\psi^2} + \ln \tan \frac{\psi}{2}$
4	$\frac{1}{\Omega^3}$	$\frac{\psi}{\cos^4 \delta_g} + \frac{1}{3} \cot^3 \psi$

Table 2

Special cases of hypergeometric series

$K'(\Omega^2), E'(\Omega^2) \Delta K(1-\Omega^2), E(1-\Omega^2)$: Elliptic integrals of 1st and 2nd kind resp.

In order to give a normalized representation the normalized spectral power-density $\bar{P}_{c\Omega}$ will be introduced:

$$\bar{P}_{c\Omega} = \frac{P_{c\Omega}}{\frac{P_1 \eta \lambda^2 g^2 \Omega}{(4\pi)^2 h^2}}$$

Fig. 11 gives a representation of $\bar{P}_{c\Omega}$ versus Ω for $E = 1$, $H = 1$, $\nu = 0$ and $\mu = 0, 1, 2, 3, 4$.

In order to work out the influence of the filterfunction $H(\Omega)$ the following conditions are assumed to be fulfilled:

1. The radar shall have an autodyne receiver with $IF = 0$.
2. The filterfunction $H(\Omega)$ shall be a rectangular highpass with lower edge frequency φ . ($0 \leq \varphi \leq 1$).

In order to give more insight into the problem of the influence of the antenna diagram on the clutter received by a moving radar in addition to $E = 1$ the following antenna diagrams are chosen and considered:

$$E = \begin{cases} \cos \vartheta & \text{for } 0 \leq \vartheta \leq 90^\circ \\ 0 & \text{for } 90^\circ < \vartheta \leq 180^\circ \end{cases} \quad (17)$$

$$E = e^{\cos \vartheta} - 1 \quad (18)$$

These antenna characteristics are represented in Fig. 12. The spectral power-density $P_{c\Omega}$ is multiplicative modulated with the function of the antenna diagram and the figures 13 and 14 show the influence of the antenna diagram (17) and (18) on $P_{c\Omega}$. Especially in the region of $\Omega = 0$, the sidelobe region of the antennas, the influence of the sidelobe level on the received clutterpower can be seen by comparison of Fig. 11 with Fig. 13 and Fig. 14.

4.3. The total clutter power

The total clutter power P_c received from the radar is given by the following integral:

$$P_c = \int_{-1}^{+1} P_{cR}(\Omega) d\Omega \quad (19)$$

Considering that $H(\Omega)$ is proposed as a rectangular highpass with lower edge frequency α one obtains from (17) in connection with (14) and (14a):

$$P_c = \frac{P_1 \eta \lambda^2 g^2 2 \delta \mu}{(4\pi)^3 h^2} \left\{ \int_{-1}^{-\alpha} E^4(\Omega) (1-\Omega^2) I(\Omega) d\Omega + \int_{\alpha}^{+1} E^4(\Omega) (1-\Omega^2) I(\Omega) d\Omega \right\} \quad (20)$$

The normalized total clutter power is defined as:

$$\bar{P}_c = \frac{P_c}{\frac{P_1 \eta \lambda^2 g^2 2}{(4\pi)^3 h^2}}$$

For $\mu = 0, 2, 4$ and for the considered antenna diagrams, the integrals in (20) can be solved. The results of this solutions are represented in Fig. 15 which shows the normalized total clutter power \bar{P}_c versus α . It can be seen from the results given in Fig. 15 that with a proper choice of the filterfunction $H(\Omega)$ as well as with the choice of the antenna diagram, especially the sidelobes, the clutter power received by the radar in a wide range can be influenced.

5. CONCLUSION

It has been shown that the empirical σ_0 model given in this paper is able to describe the average power reflection characteristics of the earth surface over land as well as over sea. In contrast to still existing other models the here presented model has no angle limitations, it holds for low grazing angles as well as for mean or large grazing angles. Nevertheless it permits simple computations and with proper choice of the model parameters it can be adapted on different earth surfaces for land and sea respectively. The given examples show that this simple clutter model can be useful for comparative system analysis of different systems and for first clutter estimations in connection with horizontally over ground moving radar systems with rotational symmetrical antenna diagrams.

In a future work more detailed comparisons of the presented σ_0 -model with measurements shall be carried out in order to estimate the model parameters for the most important occurring clutter cases. The aim of this future work shall be to establish a list which contains the dependence of the model parameters $\mu, \nu, \delta g$ and k_μ on the electrodynamic characteristics as frequency and polarisation as well as on geographical characteristics as surface covering, seastate and other surface properties.

References

- Abramowitz, M. and I. A. Stegun
Handbook of Mathematical Functions
Dover Publications, Inc., New York 1965
- Beckmann, P. and A. Spizzichino
The Scattering of Electromagnetic Waves from Rough Surfaces
Pergamon Press, Oxford London, New York, Paris 1963
- Cosgriff R. L., W. H. Peak, R. C. Taylor
Terrain Scattering properties for Sensor System Design (Terrain Handbook II)
Engineering Experiment Station, College
Engineering The Ohio State University, Columbus,
Vo. XXIX, No 3, Mai 1960
- Earing D. G. and I. A. Smith
Target Signatures Analysis Center: Data Compilation Institut of Science
and Technology, The University of Michigan, Rept. AD 489 968, July 1966
- Gradshteyn I. S. and I. M. Rhzhik
Table of Integrals, Series and Products Akademik Press, New York and
London 1965, P. 389, 3.682

Guinard N. W. and I. C. Daley

An Experimental Study of a Seaclutter Model
Proc. I EEE, Vol. 58, No 4, April 1970, PP 543-550

Natanson F. E.

Report of Nato AC-243 (SG 13) Subtask 1
Confidential

Ruck G. T., Barrik D. E., Stuart W. D., C. K. Krichbaum

Radar Cross Section Handbook
Plenum Press, New York, London 1970

Ulabv, F. T.

Radar response to vegetation
I EEE Trans. Ant. and Prop. Vol. AP 23,
No. 1, Jan. 1975, pp. 36-45

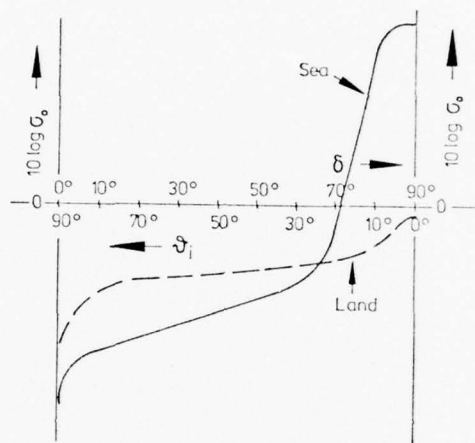


Fig.1 General shapes of the dependence of σ_0 on the grazing angle δ and the incidence angle ν_i for Land — and Sea — Surfaces

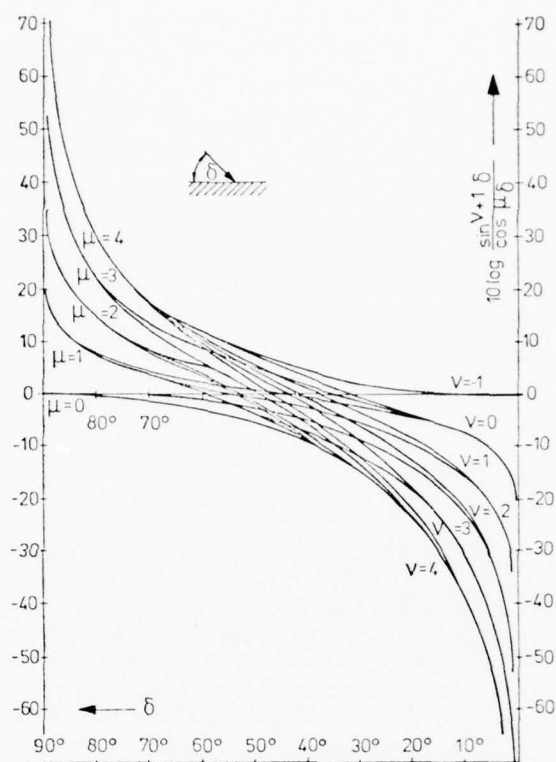


Fig. 2 The function $10 \log \frac{\sin \nu + 1 \delta}{\cos \mu \delta}$ for $-1 \leq \nu \leq 4$, $0 \leq \mu \leq 4$, $\delta \leq 89^\circ$

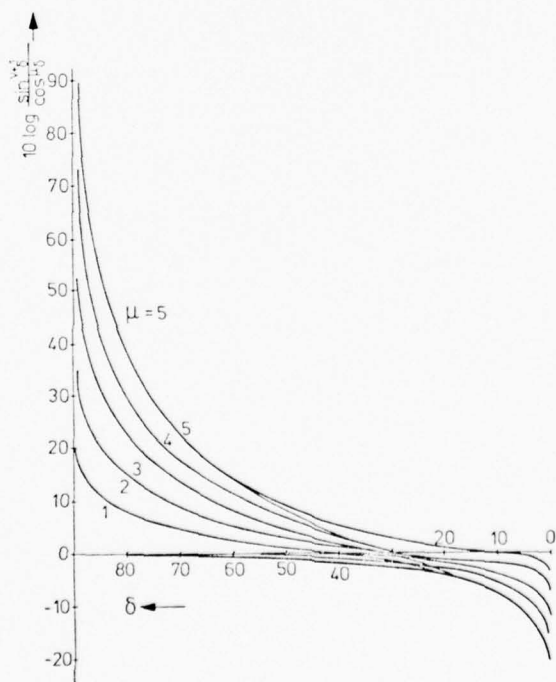


Fig. 3 The function $10 \log \frac{\sin \nu + 1 \delta}{\cos \mu \delta}$ for $0 \leq \mu \leq 5$ and $\nu = 0, -0.25, -0.5, -0.75, -0.9$, $\delta \leq 89^\circ$

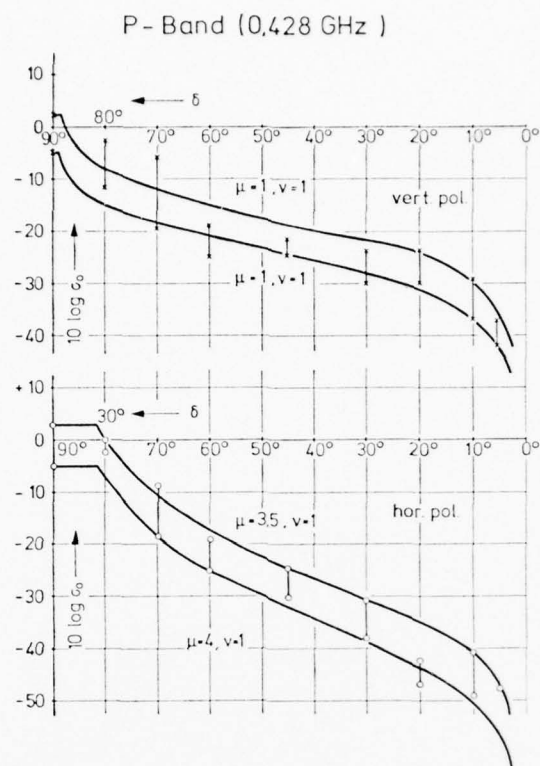


Fig.4(a) Seaclutter characteristics, σ_0 versus grazing angle measured by Guinard and Daley, 1970 for different sea states, comparison with model (3)

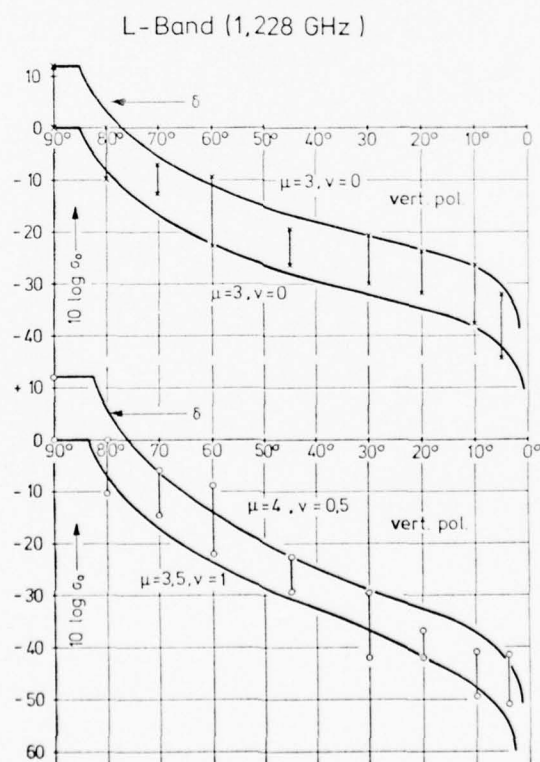


Fig.4(b) Seaclutter characteristics, σ_0 versus grazing angle measured by Guinard and Daley, 1970, for different sea states, comparison with model (3)

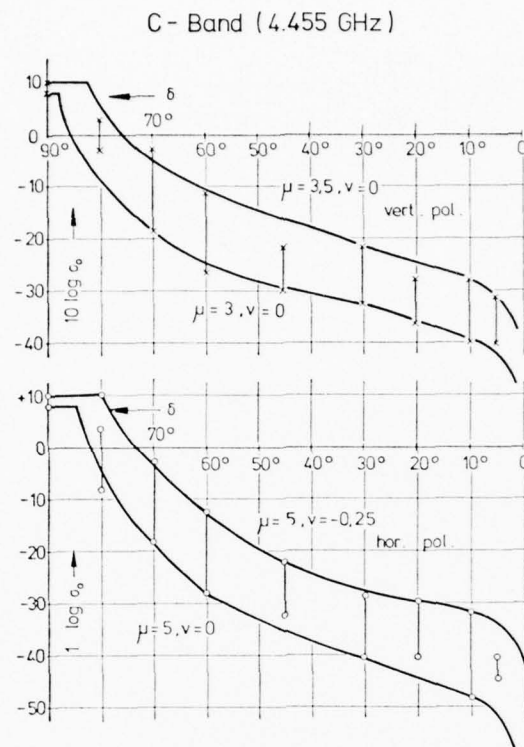


Fig.5(a) Seaclutter-characteristics, σ_0 versus grazing angle measured by Guinard and Daley, 1970, for different sea states, comparison with model (3)

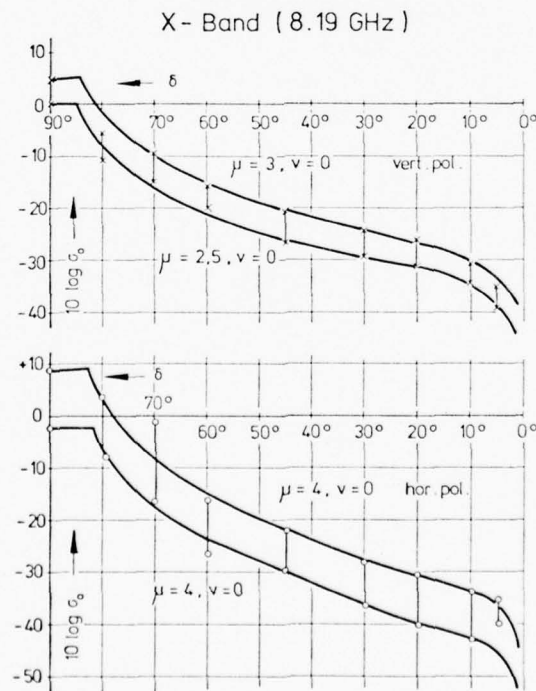


Fig.5(b) Seaclutter-characteristics, σ_0 versus grazing angle measured by Guinard and Daley, 1970, for different sea states, comparison with model (3)

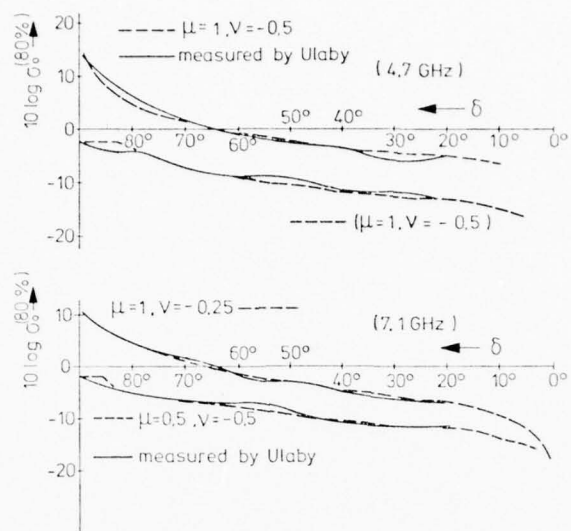


Fig.6 80 percent boundaries of σ_0 measured by Ulaby, 1975, for different vegetation compared with model (3)

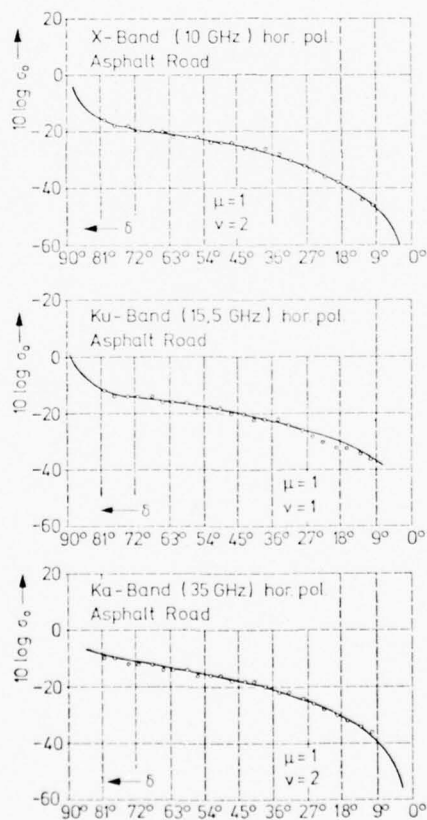


Fig.7 Landclutter-characteristics, measured by Earing and Smith, 1966, comparison with model (3)

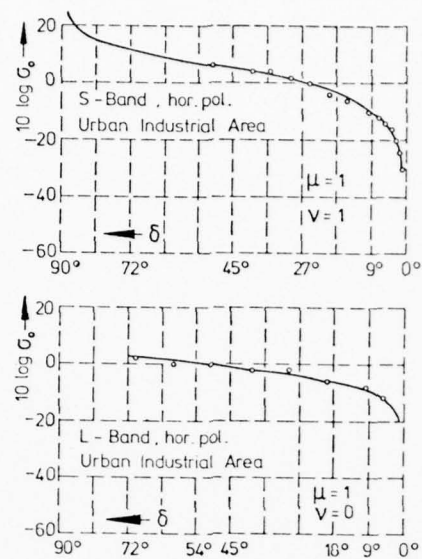


Fig.8 Landclutter-characteristics measured by Earing and Smith, 1966, comparison with model (3)

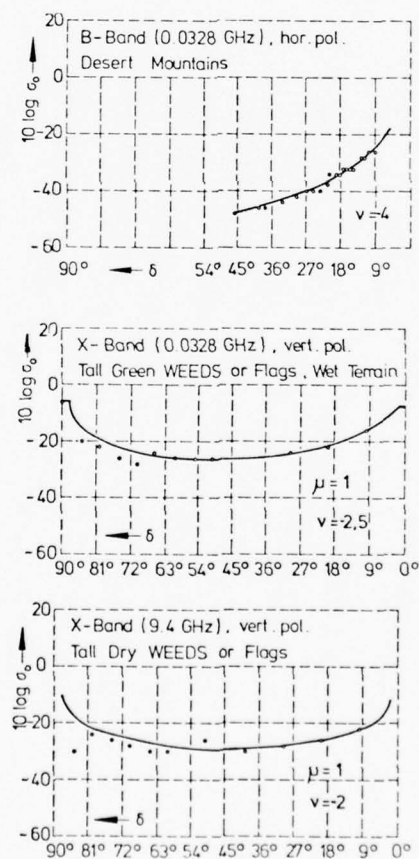


Fig.9 Landclutter-characteristics, increasing σ_0 measured by Earing and Smith, 1966 comparison with model 3

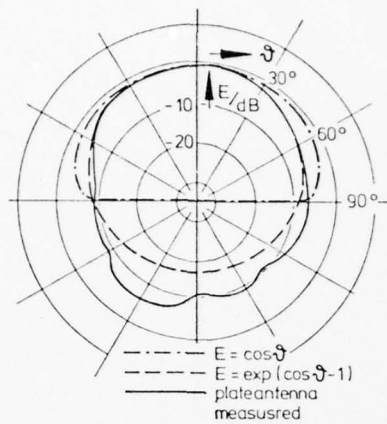
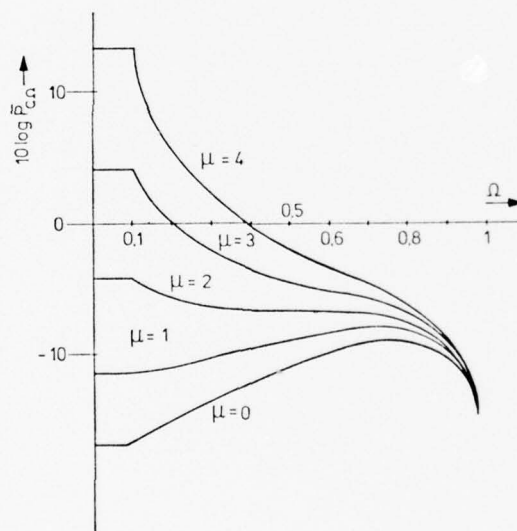


Fig.12 Different antenna diagram

Fig.13 Normalized powerdensity $P_c \Omega$ antenna diagram $E \cdot e^{\cos \theta} - 1$ for $0 \leq \mu \leq 5$

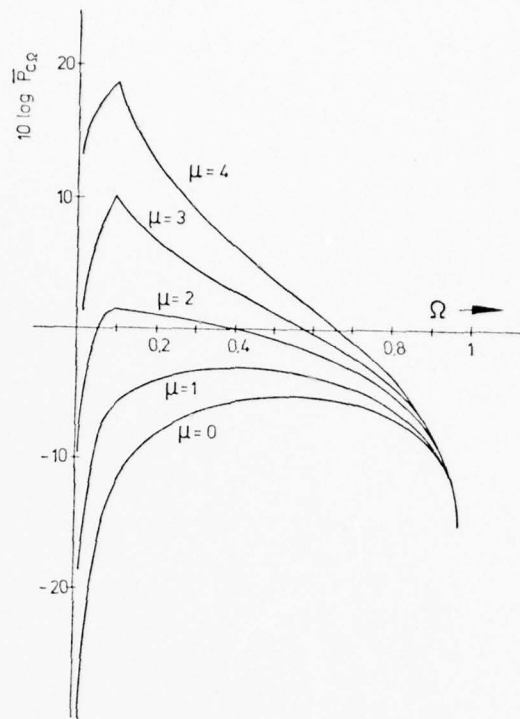


Fig.14 Normalized powerdensity $\bar{P}_c\Omega$ antenna diagram $E = \cos \nu = \Omega$ for $0 \leq \mu \leq 4$

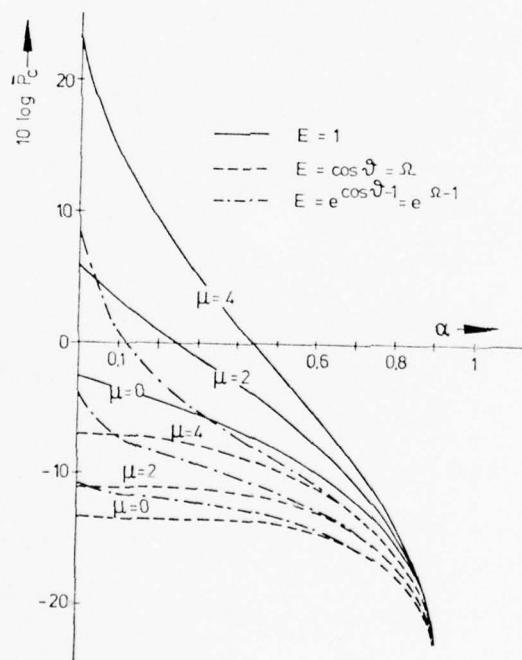


Fig.15 Normalized total clutter power \bar{P}_c versus α influence of filtercharacteristic and antenna diagram for $\mu = 0, 2, 4$

GROUND WAVE PROPAGATION IN THE PRESENCE OF SMOOTH HILLS AND DEPRESSIONS*

L. B. Felsen and A. Green
 POLYTECHNIC INSTITUTE OF NEW YORK
 Farmingdale, N. Y. 11735 USA

I. INTRODUCTION

Electromagnetic waves propagating along the ground-air interface are influenced markedly by terrain features. Previous studies have dealt extensively with abrupt changes in surface properties (modeled in terms of surface impedance), or abrupt changes in height as represented by precipitous hills or valleys, on the convexly curved earth's surface. When the terrain changes gradually, as in the presence of smooth hills or depressions, (Fig. 1), it is necessary to consider the effects of variable concave surface curvature, and more generally those of a gradual changeover from concave to convex, on the signal propagation characteristics. Of special interest are the fields observed on or near the surface when the source is also situated on or near the surface. This paper is concerned with a review of earlier work on the concave surface problem, and with a summary of our current effort to adapt and extend these results to ground wave propagation.

The most fundamental difference between the excitation of concave and convex surfaces of large (compared to the wavelength) radius of curvature is the absence in the former of a geometrical shadow region, from which the source is invisible. This circumstance gives rise not only to a more intricate geometric-optical field comprising multiply reflected rays (Fig. 2) but also, in an alternative guided wave description, to the presence of whispering gallery modes which cling to the surface (Fig. 3) and, in the absence of dissipation, experience no attenuation. Their counterparts on a convex surface, the creeping waves, lose energy by tangential shedding along the propagation path. The problem is complicated further by the fact that ray optics is incapable of providing the field solution since the caustics of multiply reflected rays pile up near the boundary (Fig. 2) and thus invalidate the geometric-optical field evaluation there. A field representation in terms of whispering gallery modes only (with inclusion of a continuous mode spectrum for some surfaces), while valid, is inconvenient for calculation for large separation of source and observation points on a large-radius surface since the number of modes required can be substantial. These problems do not arise on a convex surface where the distant field in the shadow region is represented compactly by the dominant creeping wave.

To gain a better physical as well as quantitative understanding of these aspects of wave propagation on a concave surface, intensive studies have been carried out on the simplest prototype configuration, the interior of a perfectly reflecting circular cylinder (KINBER, B. YE. 1961; BABICH, V. M. and BULDYREV, V. S., 1972; WASYLKIWSKYJ, W., 1975). These two-dimensional field calculations, corresponding to excitation by an axial line source, are reviewed in Section II. A peculiarity of the cylindrical geometry is the presence, in addition to the whispering gallery modes, of a continuous guided mode spectrum which arises because of spurious reflections from the radial coordinate origin. Elimination of these spurious contributions leads to an asymptotic field representation in terms of an integral which can be manipulated so as to exhibit ray-optical contributions, whispering gallery mode contributions, a mixture of these, or a formulation containing a reduced canonical integral analogous to the Fock integral for convex surfaces. The most effective choice depends on the parameters of the problem. The results so obtained can be generalized to apply to arbitrary concave surface shapes provided that the radius of curvature changes slowly over a wavelength interval. The validity of these variable-curvature solutions has been verified by comparison with exact calculations performed for a parabolic contour (BULDYREV, V. M. and LANIN, A. I., 1975). These earlier investigations are reviewed, relevant numerical results presented and their physical implications discussed.

We have extended the analysis to track the field behavior when the radius of curvature of a circular cylindrical surface between fixed source and observation points changes from concave to convex; this transition from a curved to a flat boundary and beyond was not included in the earlier studies. We have also introduced the generalization for a lossy ground modeled by a surface impedance boundary condition (Section III).

The two-dimensional results are useful for the investigation of fields with broad phase fronts that do not vary appreciably along the axial direction of an elongated depression (gully) or smooth ridge. When the incident phase front is strongly curved, as is the case when a dipole radiator is located within or near the ground perturbation, it is necessary to calculate the three-dimensional fields. These modifications are under study.

Still to be explored is the field description along surface contours that vary smoothly from concave to convex. This important problem is presently being investigated, as is the extension of the analysis to three-dimensional ground perturbations exemplified by spherical depressions.

* This work was performed under Contract No. DAHC 04-75-G-0152, U. S. Army Research Office - Durham, N. C.

II. PERFECTLY CONDUCTING CIRCULAR BOUNDARY (TWO-DIMENSIONAL)

A. Green's Function Formulation

We summarize here the results obtained in the literature on the prototype problem of line source radiation inside a perfectly conducting circular cylinder of radius a . To make the analysis relevant to the propagation along concave surfaces in general, it is necessary to remove the azimuthal periodicity imposed on the fields in the cylindrical $\rho = (\rho, \phi)$ geometry, where ρ represents the radial and ϕ the angular (azimuthal) coordinate. This can be done by extending the range of the ϕ coordinate from its physical periodic domain $0 \leq \phi \leq 2\pi$ into an infinite domain $-\infty < \phi < \infty$ (FELSEN, L. B. and MARCUVITZ, N., 1973). Such an extension implies that angularly propagating waves originating at the source point (ρ', ϕ') are outgoing toward $|\phi| = \infty$; this "angular radiation condition" can be realized by placing at some angular location away from the source angle ϕ' a perfect absorber for angularly propagating waves. Such an absorber has, however, the undesired property of generating diffraction at the radial coordinate origin $\rho = 0$. Therefore, when considering propagation phenomena ascribable only to the cylinder surface, it is desirable to remove the spurious diffraction effects from the total field solution.

The line source Green's function $G(\rho, \rho')$ in the cylindrical domain $0 < \rho < a$, $-\infty < \phi < \infty$, can be constructed by the method of separation of variables and expressed in its most general form as a contour integral involving the two one-dimensional characteristic Green's functions g_ρ and g_ϕ for the radial and angular domains, respectively (FELSEN, L. B. and MARCUVITZ, N., 1973). As noted in Section I, when the Green's function is represented in terms of angularly propagating waves, the corresponding eigenmode spectrum in the radial domain involves a discrete (whispering gallery mode) and continuous portion. The latter accounts in part for propagation phenomena associated with the portion of the concave boundary lying between the source and observation points (this is desired contribution), and in part for the spurious diffraction effects of the angular absorber. When the spurious effects are removed and cognizance is taken of the high-frequency nature of the analysis, one may show that the relevant propagation characteristics along the portion of the concave boundary lying between the source point Q and the observation point P in Fig. 2 are contained in the partial Green's function (BABICH, V. M. and BULDYREV, F. S., 1972)

$$G_o(\rho, \rho') = \frac{1}{i(\pi ka)^2} \int_C \frac{e^{i\nu |\phi - \phi'|}}{H'_\nu(2)(ka) J'_\nu(ka)} d\nu \quad (1)$$

where k is the free-space wavenumber, the prime on the cylinder functions denotes the derivative with respect to the argument, and a time factor $\exp(-i\omega t)$ is implied. It has been assumed in (1) that P and Q both lie on the boundary (i.e., $\rho = \rho' = a$) and that the boundary condition requires that the normal derivative of the Green's function vanishes at $\rho = a$; this makes G_o proportional to the axial component of magnetic field. The contour C and the singularities of the integrand in the complex ν -plane are shown in Figure 4. Contributions from the pole singularities ν_m arising from

$$J'_{\nu_m}(ka) = 0, \quad m = 1, 2, \dots \quad (2)$$

are found to describe whispering gallery modes. While (2) has an infinite number of real solutions as indicated in Fig. 4, only those with $\text{Re } \nu_m > 0$ represent spectral contributions in the angular transmission representation which includes also a continuous spectrum.

B. Ray-optical Representation

The integrand in (1) may be dealt with in various ways which exhibit the role of whispering gallery modes, ray-optical fields, or a combination of these, as noted in Section I. If an evaluation is sought by the method of steepest descent, one replaces $H'_\nu(2)$ and $J'_\nu = (H'_\nu(1) + H'_\nu(2))/2$ by their Debye asymptotic forms

$$H'_\nu(1, 2)(ka) \sim \sqrt{\frac{2 \cos w}{\pi ka}} \exp \left\{ \pm ika \left[\cos w - \left(\frac{\pi}{2} - w \right) \sin w \right] \pm i \frac{\pi}{4} \right\} \quad (3)$$

$$\text{Re } w > 0, \quad \left\{ ka \left[\cos w - \left(\frac{\pi}{2} - w \right) \sin w \right] \right\}^{2/3} \gg 1 \quad (3a)$$

where $\nu = ka \sin w$. Utilizing the traveling wave expansion

$$\frac{1}{J'_\nu(ka)} = \frac{2}{H'_\nu(2)(ka)} \sum_{n=0}^{\infty} (-1)^n r^n, \quad r = \frac{H'_\nu(1)(ka)}{H'_\nu(2)(ka)}, \quad |r| < 1, \quad (4)$$

in conjunction with (3), one reduces (1) to a series of integrals

$$G_o \sim \frac{1}{\pi} \sum_{n=0}^{\infty} (-i)^n \int_{C_n} \exp [ika q_n(w)] dw \quad (5)$$

where

$$q_n(w) = |\phi - \phi'| \sin w + 2(n+1) \left[\cos w - \left(\frac{\pi}{2} - w \right) \sin w \right] \quad (6)$$

The saddle points of $q_n(w)$, as obtained from $dq_n/dw = 0$, are

$$w_{sn} = \frac{\pi}{2} - \frac{|\phi - \phi'|}{2(n+1)} \quad , \quad \overline{w}_s = \frac{\pi}{2} \quad , \quad (7)$$

and thus lie on the real w axis between $w = 0$ and $w = \pi/2$. A typical path C_n through the n th saddle point is shown in Figure 5. The original path mapped from the v plane can be deformed into C_n . The Debye approximations in (3) are valid in this relevant region of the complex w -plane. Use of the conventional saddle point formula for evaluation of the integral in (5) then yields the geometrical ray series

$$G_o \sim e^{i\pi/4} \sqrt{\frac{2}{\pi k}} \sum_{n=0}^{\infty} (-1)^n \frac{e^{ikD_n}}{\sqrt{D_n}} \quad (8)$$

where

$$D_n = 2(n+1) a \sin (|\phi - \phi'| / 2(n+1)) \quad , \quad (8a)$$

each term of which corresponds to a direct or multiply reflected ray as depicted in Figure 2(a). The result in (8) could have been constructed directly by ray-optical techniques.

C. Mixed Ray-optical and Whispering Gallery Mode Representation

Although the series in (8) formally contains ray contributions with an arbitrarily large number of reflections, these are suspect since the saddle points, from which they are derived all cluster about $w = \pi/2$. Thus, the asymptotic method, whereby each saddle point is treated as isolated, is inadequate. Moreover, (3) becomes invalid as $w \rightarrow \pi/2$, thereby invalidating the simplification of the integrand, on which the saddle point evaluation is based. It is therefore necessary to truncate the number of legitimate ray-optical terms at some $n = N$ such that w_{sN} is sufficiently less than $\pi/2$. With this in mind, one employs instead of (4) the partial expansion

$$\frac{1}{J'_v(ka)} = \frac{2}{H'_v(2)(ka)} \sum_{n=0}^N (-1)^n r^n + \frac{1}{J'_v(ka)} (-1)^{N+1} r^{N+1} \quad (9)$$

When (9) is substituted into (1), one may write

$$G_o = G_{oN} + R_N \quad (10)$$

where G_{oN} is given by (5) with the series truncated at $n = N$, and

$$R_N = - \frac{i}{\pi^2 ka} \int_{C'} \frac{e^{ika|\phi - \phi'| \sin w}}{H'_v(2)(ka) J'_v(ka)} r^{N+1} (-1)^{N+1} \cos w dw \quad (11)$$

where $v = ka \sin w$. The asymptotic evaluation of G_{oN} evidently yields ray contributions having experienced up to N reflections. The remainder integral R_N incorporates the cumulative effects of ray fields having been reflected more than N times. It should be noted that when the observation point approaches the source point so that $|\phi - \phi'| \rightarrow 0$, one has $w_s \rightarrow \pi/2$ even for $n = 0$ and the ray representation fails altogether.

Several options are open for dealing with R_N . One possibility is to deform the integration path so as to minimize $|R_N|$. If C' is deformed into C_N in Fig. 5, M residues at the poles v_m of the integrand lying between C' and C_N must be extracted. Thus, noting that $r = -1$ at v_m (see (2) and (4)),

$$R_N = G_{oM} + R_{MN} \quad (12)$$

where

$$G_{oM} = \frac{i}{ka} \sum_{m=1}^M e^{i\nu_m |\phi - \phi'|} J_{\nu_m}(ka) \left[\frac{\partial}{\partial \nu} J_{\nu}'(ka) \right]_{\nu_m}^{-1}, \quad (13)$$

with $\nu_m = ka \sin w_m$ and R_{MN} being the same as R_N except for the replacement of C' by C_N . Each term in the series represents precisely one of the whispering gallery modes which make up the discrete spectrum in the previously mentioned Green's function representation in terms of angularly propagating waves. Since $w_m < \pi/2$, one may employ the Debye approximation in (3) to simplify (12). Thus, from (10) and (12),

$$G_o \sim G_{oN} + G_{oM} + R_{MN} \quad (14)$$

D. Whispering Gallery Mode and Continuous Spectrum Representation

The spectral representation comprising the total discrete (whispering gallery mode) portion and a continuous portion may be obtained directly from (1).

As remarked in Section A, only those pole singularities having $\nu_m > 0$ yield spectral contributions in the angular transmission representation. When C in Fig. 4 is deformed into a contour extending along the imaginary ν axis, all necessary pole singularities are picked up and one is left with

$$G_o \sim G_{oM} + \frac{1}{i(\pi ka)^2} \int_{-i\infty}^{+i\infty} \frac{e^{i\nu |\phi - \phi'|} d\nu}{H_{\nu}'^{(2)}(ka) J_{\nu}'(ka)} \quad (15a)$$

where G_{oM} is given by (13) and \hat{M} is the total number of poles satisfying $\text{Re } \nu_m > 0$. The second member of (15a) is the continuous spectrum mentioned in Section A except that the spurious diffraction effects of the angular absorber are not present. By methods similar to Wasyliwskyj (WASYLKIWSKYJ, W., 1975), this integral may be simplified considerably to

$$\frac{1}{\pi} \int_0^{\infty} e^{-ka |\phi - \phi'|} \sinh \nu \, d\nu, \quad ka \gg 1 \quad (15b)$$

which is valid for $|\phi - \phi'|$ arbitrarily small. It is also pointed out that (15b) may be written as

$$\frac{1}{2} [\underline{H}_0(ka |\phi - \phi'|) - Y_0(ka |\phi - \phi'|)] \quad (15c)$$

where \underline{H}_0 is the Struve function and Y_0 the Neumann function which provides the correct singular behavior as $\phi \rightarrow \phi'$.

E. Optimum Mix of Rays and Modes

The utility of the mixed ray - mode representation in (14) depends on the best choice of N and hence M so as to minimize R_{MN} and render it negligible. Utilizing the asymptotic approximations in (3) to simplify the integrand of R_{MN} , Wasyliwskyj (WASYLKIWSKYJ, W., 1975) has concluded that R_{MN} can be neglected at observation points characterized by $w_{sM} \approx (w_M + w_{M+1})/2$, i.e., for saddle points well removed from the pole singularities. The justification is fairly loose and requires further study. It is likely that a precise choice is unimportant for very large ka and large separation of source and observation points. However, for moderate values of ka , or when the observer approaches the source, the problem must be addressed in a different manner.

Returning to the original expression for G_o in (1), one may explore under what conditions the contributing range of the integrand is localized so that approximation methods may be used effectively. To this end, the cylinder functions are first replaced by their uniform asymptotic approximations in terms of Airy functions:

$$H_{\nu}'^{(2)}(ka) \sim -\sqrt{\frac{2 \cos w}{\tau}} \frac{[Ai'(-\tau \Omega^{2/3}) + iBi'(-\tau \Omega^{2/3})]}{\Omega^{2/3}}, \quad \Omega = ka \quad (16)$$

$$J_{\nu}'(ka) \sim -\sqrt{\frac{2 \cos w}{\tau}} \frac{Ai'(-\tau \Omega^{2/3})}{\Omega^{2/3}} \quad (17)$$

$$\tau = \frac{3}{2} (\cos w - (\frac{\pi}{2} - w) \sin w)^{1/3}, \quad \operatorname{Re} w > 0$$

When $\tau^2 (ka)^{2/3} \gg 1$, these representations reduce to those in (3). Examining the behavior of the integrand over the contour C in the ν -plane or the contour C' in the w -plane, Babich and Buldyrev have shown (BABICH, V. M. and BULDYREV, V. S., 1972) that the principal contribution to the integral arises from the vicinity of $\nu = ka$ or $w = \pi/2$ provided that the arc length parameter

$$\gamma = (\frac{ka}{2})^{1/3} \frac{s}{a}, \quad s = a |\phi - \phi'|, \quad (18)$$

is bounded by the inequality*

$$\frac{2}{\sqrt{3} \Delta} \leq \gamma < 2\sqrt{\Delta} (\frac{ka}{2})^\delta, \quad (19)$$

where Δ is a quantity of $O(1)$ for moderate ka and δ is small and positive. Then changing variables to t via

$$\nu = ka + \left[\frac{ka}{2} \right]^{1/3} t \quad (20)$$

and using

$$H_\nu^{(2)}(ka) \sim - \left(\frac{2}{ka} \right)^{2/3} w_2'(t) \quad (20a)$$

$$J_\nu'(ka) \sim - \left(\frac{2}{ka} \right)^{2/3} Ai'(t)$$

where

$$w_2(t) = Ai(t) + i Bi(t) \quad (20b)$$

one may write G_0 in the form

$$G_0 \sim \frac{e^{iks}}{2i\pi^2 ka} \left(\frac{ka}{2} \right)^{2/3} \int_C \frac{e^{i\gamma t}}{w_2'(t) Ai'(t)} dt \quad (21)$$

where the contour \hat{C} in the t -plane is inferred from (20) and Fig. 4 by observing that $\nu = ka$ corresponds to $t = 0$ (note that the mappings t_m and t_p of ν_m and ν_p , respectively, signify the zeros of $Ai'(t)$ and $w_2'(t)$). Extracting ray optical contributions as in (10), when relevant, the form for R_N analogous to (11) becomes

$$R_N = \frac{e^{iks}}{2i\pi^2 ka} \left(\frac{ka}{2} \right)^{2/3} \int_C \frac{(-1)^{N+1}}{Ai'(t) w_2'(t)} \left[\frac{w_1'(t)}{w_2'(t)} \right]^{N+1} e^{i\gamma t} dt \quad (22)$$

Buldyrev and Lanin state as a criterion for the inclusion or not of the ray-optical series G_{0N} the inequality

$$\frac{\gamma}{2\sqrt{\Delta}} \left(\frac{ka}{2} \right)^{-\delta} - 1 < (N+1) \leq \frac{\gamma}{2\sqrt{\Delta}} \left(\frac{ka}{2} \right)^{-\delta}, \quad (23)$$

with δ taken as (1/21). When the left-hand side of the inequality is negative, no ray-optical contributions are included. The canonical integral R_N in (22) has been tabulated for $N = -1, 0, 2$ (BULDYREV, V. M. and LANIN, A. I., 1975).

* Ref. 2 actually deals with the Dirichlet problem $G_0 = 0$ on the boundary. The validity of exactly the same condition for the Neumann function used here remains to be checked.

F. Near Field and Infinite Plane Limits

The preceding results cannot account for the limiting case $\gamma \rightarrow 0$ in (18), which arises either when the observation point approaches the source point ($s \rightarrow 0$ with a fixed) or when the radius of curvature becomes arbitrarily large ($a \rightarrow \infty$ with s arbitrary but fixed). The latter limit traces the transition from a concave to a plane surface and, if a is allowed to become negative, from concave to convex. We have derived the transition functions for these cases.

We begin with G_0 in (21) and use the Wronskian relation for the Airy functions together with Cauchy's theorem applied to the upper half of the t -plane to infer that, equivalently,

$$G_0 \sim -\frac{e^{iks}}{2\pi ka} \left(\frac{ka}{2}\right)^{2/3} \int_{\hat{C}'} e^{i\gamma t} \frac{Ai(t)}{Ai'(t)} dt \quad (24)$$

with the contour \hat{C}' passing below the real t axis. Regarding the integral in (24) as a Laplace integral, the principal contribution for small γ arises from the range of large t . Shifting the contour \hat{C}' so that this is satisfied, and employing large argument expansions, one may show that

$$-\frac{Ai(t)}{Ai'(t)} \sim t^{-1/2} \left(1 - \frac{1}{4}t^{-3/2} + \frac{7}{32}t^{-3} \dots\right), \quad -\pi < \arg t < 0 \quad (25)$$

Then by Laplace inversion of (24),

$$G_0 \sim \frac{i}{2} H_0^{(1)}(ks) \left\{ 1 + \frac{e^{-i\pi/4}}{4} \sqrt{\pi} \gamma^{3/2} - \frac{i7\gamma^3}{60} + O(\gamma^{9/2}) \right\} \quad (26)$$

Actually, the inversion yields for the factor outside the braces the large argument approximation of $(i/2) H_0^{(1)}(ks)$ the Green's function for an infinite perfectly conducting plane. By inserting the exact limiting value for $a \rightarrow \infty$, the formula in (26) may be applied as well in the near field of the source.

To trace the transition from concave to convex curvature when the distance s along the surface remains fixed, we allow a to change continuously from positive to negative values via the complex excursion $0 \leq \arg a \leq \pi$. To keep $a = a|\phi - \phi'|$ positive, it is necessary simultaneously to have $\arg |\phi - \phi'| = -\arg a$. Moreover, one must continuously deform the integration path in the complex t -plane to keep the integral convergent ($\exp(i\gamma t)$ oscillatory) when γ is allowed to become complex according to the rules stated above. These considerations lead to a straight line path along which $\arg t = -\pi/3, 2\pi/3$, when $\arg a = \pi$. Changing variables $t = \mu \exp(i2\pi/3)$, one finds

$$G_0 \sim -\frac{e^{iks}}{2\pi ka} \left(\frac{ka}{2}\right)^{2/3} \int_{C_\mu} \frac{w_1(\mu)}{w_1'(\mu)} e^{i\gamma\mu} d\mu \quad (27)$$

where γ is again given by (18) and the path C_μ proceeds along the real μ axis. The expression in (27) is the known result for the field on the surface of a convex perfectly conducting cylinder. By contour deformation about the singularities μ_p at $w_1'(\mu_p) = 0$, one derives the creeping wave series, and by expansion analogous to (25) and Laplace inversion the limiting transition as $\gamma \rightarrow 0$ (HASSERJIAN, G. and ISHIMARU, A., 1972). Thus, one may track the field continuously as the curvature changes from concave to convex between fixed source and observation points on the surface.

G. Generalization to Variable Curvature

Invoking the principle of locality, which characterizes high frequency propagation and diffraction, one may generalize the preceding results to accommodate concave surfaces with slowly variable radius of curvature $a(s)$. The results are as follows. For the integral representation in (21):

$$G_0 \sim -\frac{e^{iks}}{4\pi [f(0)f(s)]^{1/2}} \int_{\hat{C}'} e^{ikDt} \frac{Ai(t)}{Ai'(t)} dt, \quad (28)$$

where the source point is located at $s = 0$, s is the distance between the source and observation points measured along the surface, and

$$f(s) \approx \left(\frac{ka(s)}{2}\right)^{1/3}, \quad D(s) \approx \frac{1}{2} \int_0^s \frac{d\mu}{f^2(\mu)} \quad (29)$$

R_N in (22) is treated in the same manner (BABICH, V. M. and BULDYREV, V. S., 1972). As $D(s) \rightarrow 0$, with s small, one may derive the generalization of (26),

$$G_o \sim \frac{i}{2} H_o^{(1)}(ks) \left\{ 1 + \frac{e^{-i\pi/4}}{4} \frac{1}{\pi} (kD)^{3/2} + O(kD)^3 \right\} \quad (30)$$

The ray-optical series G_{oN} in (10), with (8), becomes (BABICH, V. M. and BULDYREV, V. S., 1972)

$$G_o \sim e^{i\pi/4} \sqrt{\frac{2}{\pi k}} \sum_{n=0}^{\infty} (-i)^n \frac{e^{ikD_n}}{\sqrt{D_n}} D_n \quad (31)$$

where D_n is the divergence coefficient incorporating the effects of surface curvature,

$$D_1 = \sqrt{\frac{a_1(\ell_1 + \ell_2) \cos \theta_1}{2\ell_1 \ell_2 - a_1(\ell_1 + \ell_2) \cos \theta_1}} \quad (31a)$$

$$D_2 = \sqrt{a_1 a_2 \cos \theta_1 \cos \theta_2 (\ell_1 + \ell_2 + \ell_3)}$$

$$\begin{aligned} \sqrt{} = & \sqrt{4\ell_1 \ell_2 \ell_3 + a_1 a_2 (\ell_1 + \ell_2) \cos \theta_1 \cos \theta_2 - 2\ell_1 \ell_2 a_2 \cos \theta_2} \\ & - 2\ell_3 a_1 (\ell_1 + \ell_2) \cos \theta_1 - 2\ell_1 \ell_3 a_2 \cos \theta_2 + a_1 a_2 \ell_3 \cos \theta_1 \cos \theta_2} \end{aligned} \quad (31b)$$

with a_i the surface radius of curvature and θ_i the ray angle with respect to surface normal of the i -th reflection. Finally, the asymptotically approximated (see (3)) whispering gallery mode series G_{oM} in (13),

$$G_{oM} \sim -\frac{i}{2} \frac{e^{iks}}{[f(0)f(s)]^{1/2}} \sum_M \frac{e^{ikDt_m}}{t_m} \quad (32)$$

It should be noted that (28) cannot be used when $a(s)$ changes continuously from positive to negative values unless the source is located near the inflection point $a = \infty$, where (30) and its convex counterpart applies. The failure of (28) for arbitrary source location on the concave portion arises from the fact that the function $f(s) \rightarrow \infty$ as s nears the inflection point. On the other hand, D remains finite. The coefficient nullifies the finite integral.

H. Numerical Results

Some numerical calculations in the literature illustrate the utility of the various representations for the Green's function G_o . Wasyliwskyj (WASYLKIWSKYJ, W., 1975) has evaluated the field on a concave circular perfectly conducting surface by summing the whispering gallery mode series and the continuous spectrum contribution in (15) (Figure 6). Although he employed this method of computation, the interpretation of the result, as stated by him, is in fact achieved via the ray-optical formulation since the oscillations in the curve are due to interference between the direct ray and reflected rays. Wasyliwskyj observes that the mixed representation in (14), while useful for interpretation, offers no numerical advantage. It appears nevertheless that this aspect would warrant further study. When ka is changed the corresponding curve for $|G_o|$ may be obtained from that in Fig. 6 by a scaling law (WASYLKIWSKYJ, W., 1975), thus making a typical curve universal for other cases.

When ka and (or) γ is relatively small, it is appropriate to explore the representation in (10). This was done by Buldyrev and Lanin (BULDYREV, V. M. and LANIN, A. I., 1975) for a concave surface of parabolic shape, for which the asymptotic results could be checked against the exact series solution. The calculation utilized tabulated values for G_o in (28) or R_N in (22) (when generalized as in (28) to variable curvature), and the ray series in (31), with N determined from (23) (γ there is replaced by kD). One observes from the typical curve in Fig. 7 that the asymptotic representation in (28), when modified to account for the different boundary condition on G_o , does not adequately predict the field for kD so large that a ray-optical term can be separated out. As kD increases further, each formula with a lower N value than permitted is less accurate than that with the correct N value. This demonstration shows indeed the important role played by the geometrical optics field.

III. CONCAVE BOUNDARY WITH SURFACE IMPEDANCE CONDITION

To address the problem of ground wave propagation, we assume that the ground characteristics can be taken into account by a constant surface impedance Z . For the circular cylinder, this implies the

boundary condition

$$\frac{\partial G}{\partial \rho} = i k Z' G \quad \text{at } \rho = a, \quad Z' = \frac{Z}{\xi} \quad (33)$$

where ξ is the impedance of free space. By proceeding as in Section II, one may show that the following modified expressions apply:

Instead of (1),

$$G_o = \frac{1}{i(\pi ka)^2} \int \frac{e^{i\nu} |\phi| d\nu}{\left[H_{\nu}^{(2)}(ka) - iZ' H_{\nu}^{(2)}(ka) \right] \left[J_{\nu}'(ka) - iZ' J_{\nu}'(ka) \right]} \quad (34)$$

Instead of (4), the traveling wave expansion involves

$$\frac{1}{J_{\nu}'(ka) - iZ' J_{\nu}'(ka)} = \frac{2}{H_{\nu}^{(2)}(ka) - iZ' H_{\nu}^{(2)}(ka)} \sum_{n=0}^{\infty} (-1)^n r^n, \quad |r| < 1 \quad (35)$$

$$r = \frac{H_{\nu}^{(1)}(ka) - iZ' H_{\nu}^{(1)}(ka)}{H_{\nu}^{(2)}(ka) - iZ' H_{\nu}^{(2)}(ka)} \quad (35a)$$

with corresponding modification of (5). The saddle points in (7) are unchanged, and the ray-optical series (8) becomes

$$G_o \sim e^{i\pi/4} \sqrt{\frac{2}{\pi k}} \sum_{n=0}^{\infty} (-i)^n \frac{(\Gamma_n)^n \cos^2 w_n}{(\cos w_n + Z')^2} \frac{e^{ikD_n}}{\sqrt{D_n}} \quad (36)$$

where Γ_n is the boundary reflection coefficient for ray species n ,

$$\Gamma_n = \frac{\cos w_n - Z'}{\cos w_n + Z'} \quad (37)$$

and

$$\cos w_n = \sin \frac{|\phi - \phi'|}{2(N+1)}, \quad D_n = 2a(n+1) \sin \frac{|\phi - \phi'|}{2(n+1)} \quad (38)$$

The whispering gallery mode series is

$$G_{oM} = \frac{i}{ka} \sum_{m=1}^M e^{i\nu_m} |\phi - \phi'| J_{\nu_m}'(ka) \frac{\partial}{\partial \nu} \left[J_{\nu}'(ka) - iZ' J_{\nu}'(ka) \right]_{\nu_m}^{-1} \quad (39)$$

where the summation extends over the zeros ν_m defined by

$$J_{\nu_m}'(ka) - iZ' J_{\nu_m}'(ka) = 0 \quad (40)$$

The remainder term (11) becomes

$$R_N = \frac{i}{\pi^2 ka} \oint_C \frac{e^{ika|\phi - \phi'|} \sin w (r^{N+1}) (-1)^{N+1} \cos w dw}{\left[H_{\nu}^{(2)}(ka) - iZ' H_{\nu}^{(2)}(ka) \right] \left[J_{\nu}'(ka) - iZ' J_{\nu}'(ka) \right]} \quad (41)$$

where r is given by (35a). The analogue of (21) becomes

$$G_0 \sim \frac{e^{iks}}{2i\pi^2(ka)} \left(\frac{ka}{2}\right)^{2/3} \int_C \frac{e^{i\gamma t}}{[w_2^1(t) + i\alpha w_2(t)] [Ai^1(t) + i\alpha Ai(t)]} dt \quad (42)$$

where $\alpha = Z^1 \left(\frac{ka}{2}\right)^{1/3}$. Under the same conditions, one has for R_N in (22),

$$R_N \sim \frac{e^{iks}}{2i\pi^2(ka)} \left(\frac{ka}{2}\right)^{2/3} \int_C \frac{(-1)^{N+2}}{w_2^1(t) + i\alpha w_2(t)} \frac{r^{N+1} e^{i\gamma t}}{Ai^1(t) + i\alpha Ai(t)} dt \quad (43)$$

Employing the Wronskian, the field may be put in the form of (24)

$$G_0 \sim -\frac{e^{iks}}{2\pi ka} \left(\frac{ka}{2}\right)^{2/3} \int_C \frac{e^{i\gamma t} Ai(t)}{Ai^1(t) + i\alpha Ai(t)} dt \quad (44)$$

The perturbation expansion

$$-\frac{Ai(t)}{Ai^1(t) + i\alpha Ai(t)} \sim \frac{1}{\sqrt{t}} \left[1 + \frac{i\alpha}{\sqrt{t}} - \frac{\alpha^2}{t} - \left(\frac{1}{4} + i\alpha^3\right) \frac{1}{t^{3/2}} + O(t^{-2}) \right] \quad (45)$$

leads from (44) to the representation

$$G_0 \sim \frac{e^{iks + i\frac{\pi}{4}}}{\sqrt{2\pi ks}} \left[1 - e^{-i\pi/4} \sqrt{\pi} \gamma^{1/2} \alpha - 2i\alpha^2 \gamma + \left(\frac{1}{4} + i\alpha^3\right) \sqrt{\pi} \gamma^{3/2} e^{-i\pi/4} + O(\gamma^2) \right] \quad (46)$$

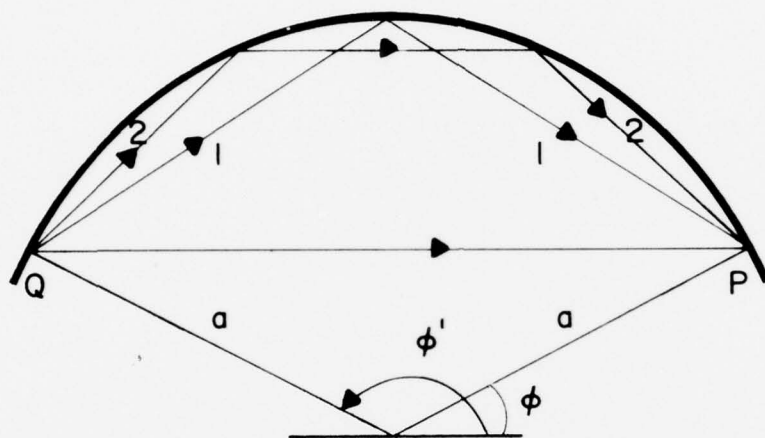
thereby generalizing (26).

REFERENCES

1. BABICH, V. M. and BULDYREV, V. S., 1972, Asymptotic Methods of Short Wave Diffraction, Moscow, USSR: Nauka, Chapter 11, Section 4.
2. BULDYREV, V. M. and LANIN, A. I., Jan. 1975, "Asymptotic Formulas for a Wave Propagating Along a Concave Surface; Limits of Their Applicability," *Radio Tekh. Elektron.* Vol. 20.
3. FELSEN, L. B., and MARCUVITZ, N., 1973, Radiation and Scattering of Waves, Englewood Cliffs, NJ: Prentice Hall, Inc., Sections 3.3, 3.4.
4. HASSERJIAN, G. and ISHIMARU, A., May-June 1962, "Currents Induced on the Surface of a Conducting Circular Cylinder by a Slot," *J. Res. Nat. Bur. Stand.*, Vol. 66D, No. 3, pp. 335-365.
5. KINBER, B. YE., 1961, "On the Diffraction of Electromagnetic Waves by a Concave Surface of a Circular Cylinder," *Radio Tekh. Elektron.* Vol. 6, No. 8, pp. 1273-1283.
6. WASYLKIWSKYJ, W., July 1975, "Exact and Quasi-Optic Diffraction within a Concave Cylinder," *IEEE Transactions on Antennas and Propagation*, Vol. AP-23, No. 4, pp. 480-492.



FIG. 1 General surface contour



a) direct and multiply reflected rays

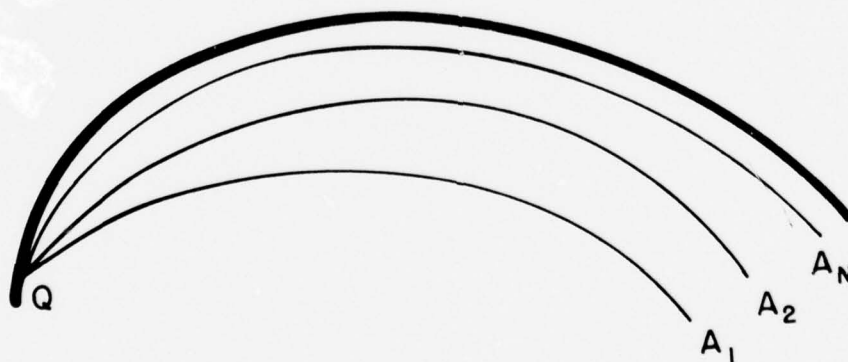
b) caustics A_n for rays reflected N times; these ray contributions are confined to the region between A_n and the boundary

FIG. 2 Rays and caustics for a circular boundary

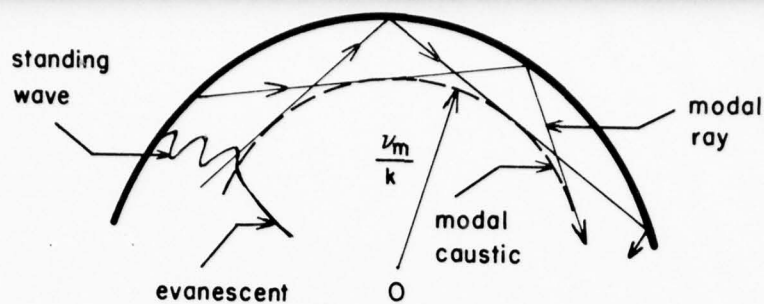


FIG. 3 Whispering gallery mode: modal field, modal rays and caustic ($v_m = ka \sin w_m$)

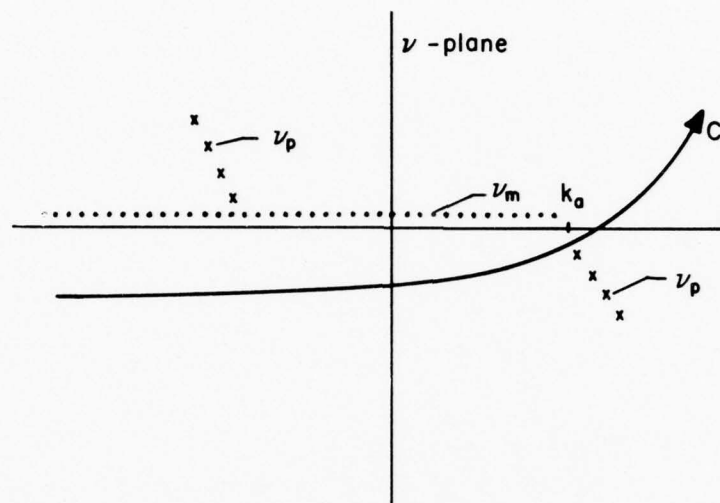


FIG. 4 Integration path and singularities in complex v -plane
 x -- zeros v_p of $H_v^{(2)}(ka)$; \cdot -- zeros v_m of $J_v'(ka)$

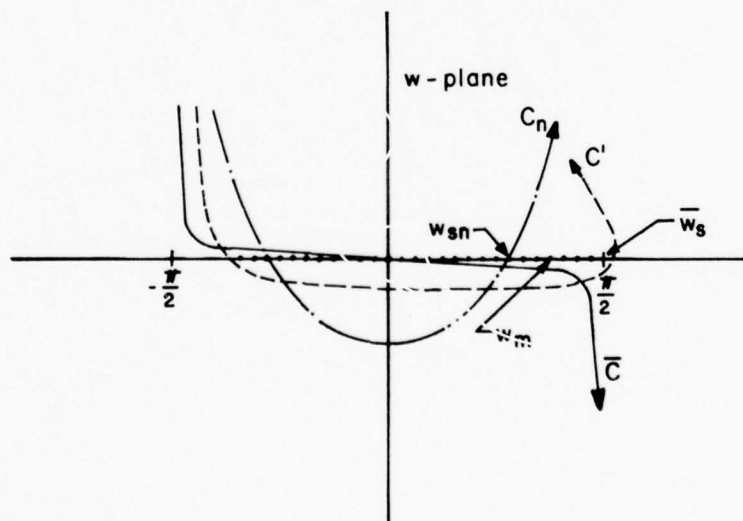


FIG. 5 Integration paths and singularities in complex w plane ($v = ka \sin w$). \bar{C} corresponds to C in Fig. 4 and can be changed to C' because of symmetries in the integrand in (5). C' in turn can be deformed into the steepest descent path C_n through w_{sn} . The pole singularities w_m arising from the zeros of $J_v'(ka)$ do not affect the asymptotic evaluation of (5). The poles w_p are not shown.

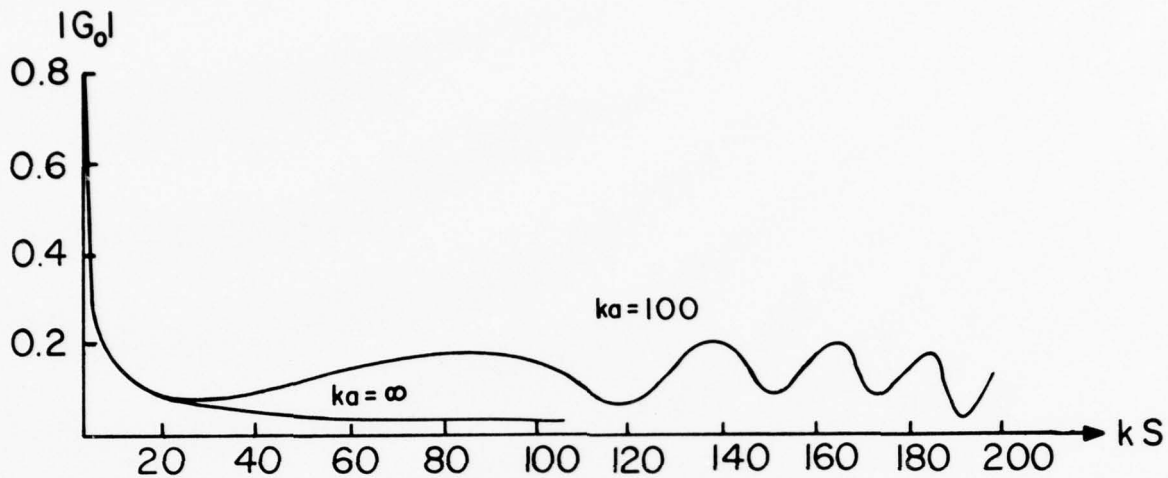


FIG. 6 Magnitude of field on infinite plane ($ka = \infty$) and concave cylindrical surface ($ka = 100$) (WASYLKIWSKYJ, W., 1975)

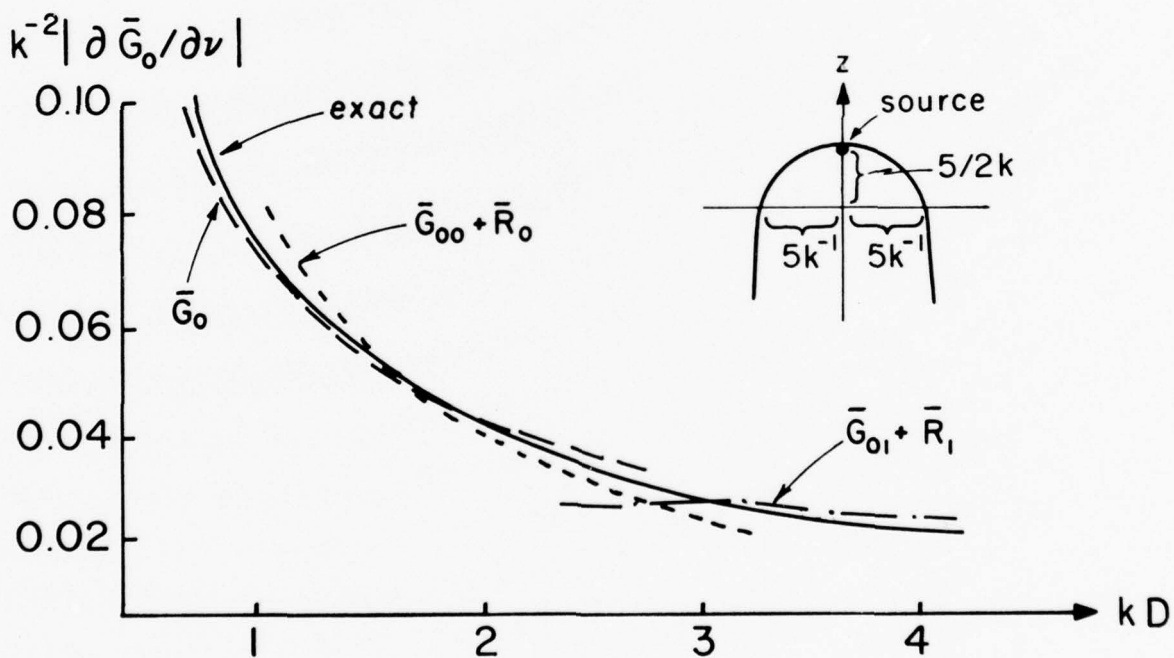


FIG. 7 Magnitude of field ($\partial \bar{G}_0 / \partial \nu$) on parabolic surface (BULDYREV, V. M. and LANIN, A. I., 1975); \bar{G}_0 satisfies the condition $\bar{G}_0 = 0$ on the boundary). The source is located at the apex, and the parameters of the parabola are shown in the figure.

DISCUSSION

K.D.Becker: In 1951, B.Friedman showed that, in the case of an ideally conducting sphere, the continuous spectrum is vanishing. Is there in your case a connection with the sign of curvature of an ideally conducting surface and the existence of a continuous spectrum?

L.B.Felsen: The existence or not of a continuous spectrum depends on the choice of the representative theorem. In the problem which I discussed in cylindrical geometry, the field was represented in terms of angularly propagating waves in an infinity-extended angular space. Therefore, the spectral theorem has to be developed for the radial domain. For the interior of the cylinder, with the origin (cylinder axis) accessible, one finds both, a discrete and a continuous spectrum. When the origin is shielded by another cylindrical boundary, the spectrum is purely discrete.

THE TRANSIENT RESPONSE OF A SLIGHTLY
ROUGH DIELECTRIC SURFACE

K. J. Langenberg
K.-D. Becker
G. Dobmann

Fachbereich 12.2 der Universität des Saarlandes
Fachrichtung Elektrotechnik
D-6600 Saarbrücken
Fed. Rep. Germany

SUMMARY

The source of the electromagnetic field is assumed to be a vertical electric dipole at height ξ above the surface of the plane earth with arbitrary time varying moment. The problem of finding the transient field of this dipole when the earth is allowed to be slightly rough is solved by means of a perturbation analysis, repeated application of integral transforms and their inversion on the base of Cagniard's method with the modification of de Hoop.

1. INTRODUCTION

In both telecommunication and in applied geophysics one is often confronted with the problem of discussing the influence of the earth's roughness on the propagation of electromagnetic waves. The need for the transient response of rough surfaces arises when pulses of nano-second durations are being transmitted; i.e. when these signals may no longer be single frequency harmonics but broadband pulses. This case requires familiarity with propagation induced distortion.

The authors are not aware of any approach to this special theme although the monochromatic problem has been treated in detail (BECKMANN, P., SPIZZICHINO, A., 1963, AGARD); a recent paper (HUGHES, W.J., WAIT, J.R., 1975), for instance, deals with the effective wave tilt over a laterally inhomogeneous two-layer earth. The technique used in this paper involves a perturbation method to find effects of a sinusoidal boundary with small undulations upon an incident plane wave. Here, as in (BECKER, K.-D., et al., 1975) we will discuss the case of a dipole source above a widely arbitrary rough surface separating two media of real wave numbers. We also start with a perturbational series expansion for the total electromagnetic fields which leads to inhomogeneous transition conditions for the disturbed fields alone: the roughness of the earth is transformed into equivalent surface currents. These currents can be given in terms of the flat earth reflected, i.e. undisturbed fields if the perturbation series is truncated after its first term (BECKER, K.-D., et al., 1975), thus yielding results in the time domain which do not describe the early time behavior of the transient response; it can be made physically clear that the truncation of the series is only valid for times greater than the travel time corresponding to the roughness amplitude. Then for the sake of relevant results, the duration of the exciting impulse must be large compared to that travel time.

Now the application of a Laplace transform and a two-dimensional Fourier transform to the wave equation for the first-order disturbed fields leads to an integral representation in the Laplace transform space with unknown integration constants. If the function which accounts for the roughness is decomposed into its spectral components the shifting theorem yields explicit expressions for these constants. Using Cagniard's method (CAGNIARD, L., 1939, DE HOOP, A. T., 1959, FELSEN, L. B., 1965) the above-mentioned integral representation can be changed to an explicit Laplace integral if certain restrictions concerning the roughness profile are assumed: the profile must be one-dimensional and band-limited, the maximum spatial frequency component being small compared to an expression implying essentially the reciprocal of the transmitter-receiver distance. Then the solution in the time domain can be read off yielding convolution integrals for arbitrary time varying dipole moment. These integrals have been numerically evaluated by means of the fast Fourier transform, thus yielding first order corrections of the time history of the reflected field if a dielectric surface is allowed to be slightly rough.

2. MATHEMATICAL FORMULATION

The plane earth is described through the half-space $z < 0$ (medium 1) and the atmosphere through the half-space $z > 0$ (medium 2) in a cartesian coordinate system (x, y, z) (Fig. 1). The fields which belong to the two media are marked by corresponding indices; the source of the field is assumed to be a vertical electric dipole at the point $x = y = 0, z = \xi > 0$ whose moment is given by $H(t) \vec{e}_z$, t being the time and \vec{e}_z being a unit-vector in the z -direction. Regarding $H(t)$ we make the causality assumption $H(t) \equiv 0$ for $t < 0$.

The field strengths $\vec{E}_u^{(i)}(x, y, z, t)$, $\vec{H}_u^{(i)}(x, y, z, t)$ ($i = 1, 2$) are those which would result from smooth earth. For the total field strengths in case of a rough surface we postulate a perturbation series of the form

$$\vec{E}_{tot}^{(i)}(x, y, z, t) = \vec{E}_u^{(i)}(x, y, z, t) + \sum_{\nu=1}^{\infty} \delta^{\nu} \vec{E}_{d\nu}^{(i)}(x, y, z, t) \quad (1)$$

$\delta < 1$ being the perturbation parameter of the roughness which we describe through

$$z = \Delta z = \delta f(x, y) \quad (2)$$

The arbitrary function $f(x, y)$ is considered to have continuous derivatives. A formula similar to (1) holds for the magnetic field strength $\vec{H}_{tot}^{(i)}(x, y, z, t)$. These total fields fulfill the wave equation in the two media, for instance

$$\Delta \vec{E}_{tot}^{(i)} - \frac{1}{v_i^2} \frac{\partial^2 \vec{E}_{tot}^{(i)}}{\partial t^2} = \begin{cases} \vec{0} & \text{for } i=1 \\ -\frac{H(t)}{\epsilon_0 \epsilon_2} \text{grad} \left[\frac{\partial}{\partial z} \delta(x, y, z-\xi) \right] + \mu_0 \frac{\partial^2 H(t)}{\partial t^2} \delta(x, y, z-\xi) \vec{e}_z & \text{for } i=2 \end{cases} \quad (3)$$

where $v = (\epsilon_0 \epsilon_i \mu_0 \mu_i)^{-1/2}$ denotes the phase velocity in medium i , ϵ_0, μ_0 being the vacuum permittivity and permeability, respectively; ϵ_i, μ_i are the corresponding relative constants. We assume $\mu_1 = \mu_2 = 1$. In (3) $\delta(x, y, z)$ is the delta-distribution. Once, this equation is solved, $\vec{H}_{tot}^{(i)}(x, y, z, t)$ results from Maxwell's equations. Both total fields must satisfy the transition conditions at $z = \Delta z$

$$\begin{aligned} \vec{n} \times [\vec{E}_{tot}^{(2)} - \vec{E}_{tot}^{(1)}]_{z=\Delta z} &= \vec{0} \\ \vec{n} \times [\vec{H}_{tot}^{(2)} - \vec{H}_{tot}^{(1)}]_{z=\Delta z} &= \vec{0} \end{aligned} \quad (4)$$

with the normal

$$\vec{n} = -\delta \text{grad} f + \vec{e}_z \quad (5)$$

Especially we have

$$\begin{aligned} \vec{e}_z \times [\vec{E}_u^{(2)} - \vec{E}_u^{(1)}]_{z=0} &= \vec{0} \\ \vec{e}_z \times [\vec{H}_u^{(2)} - \vec{H}_u^{(1)}]_{z=0} &= \vec{0} \end{aligned} \quad (6)$$

These conditions and the causality assumption guarantee the uniqueness of the total fields.

3. METHOD OF SOLUTION

Laplace transforming (3) with respect to time yields under consideration of the initial conditions

$$\Delta \vec{e}_{tot}^{(i)} - \frac{s^2}{v_i^2} \vec{e}_{tot}^{(i)} = \begin{cases} \vec{0} & \text{for } i=1 \\ -\frac{h(s)}{\epsilon_0 \epsilon_2} \text{grad} \left[\frac{\partial}{\partial z} \delta(x, y, z-\xi) \right] + \mu_0 s^2 h(s) \delta(x, y, z-\xi) \vec{e}_z & \text{for } i=2 \end{cases} \quad (7)$$

s being the variable in the transform space and $\vec{e}_{tot}^{(i)}(x, y, z, s)$, $h(s)$ denoting the transforms of $\vec{E}_{tot}^{(i)}(x, y, z, t)$ and $H(t)$, respectively.

Further application of a two-dimensional Fourier transform with respect to x and y

$$\vec{\ell}_{tot}^{(i)}(\alpha, \beta, z, s) = \int_{-\infty}^{+\infty} \int_{-\infty}^{+\infty} \vec{e}_{tot}^{(i)}(x, y, z, s) e^{-js\alpha x - js\beta y} dx dy = \mathcal{F}_2 \{ \vec{e}_{tot}^{(i)} \} \quad (8)$$

with the inverse transform

$$\vec{e}_{tot}^{(i)}(x, y, z, s) = \frac{s^2}{4\pi^2} \int_{-\infty}^{+\infty} \int_{-\infty}^{+\infty} \vec{\ell}_{tot}^{(i)}(\alpha, \beta, z, s) e^{js\alpha x + js\beta y} d\alpha d\beta = \frac{s^2}{4\pi^2} \mathcal{F}_2^{-1} \{ \vec{\ell}_{tot}^{(i)} \} \quad (9)$$

yields

$$\frac{\partial^2 \vec{\ell}_{tot}^{(1)}}{\partial z^2} - s^2 \gamma_1^2 \vec{\ell}_{tot}^{(1)} = 0 \quad (9)$$

$$\frac{\partial^2 \ell_{tot,x}^{(2)}}{\partial z^2} - s^2 \gamma_2^2 \ell_{tot,x}^{(2)} = - \frac{js h(s)}{\epsilon_0 \epsilon_2} \alpha \frac{\partial}{\partial z} \delta(z-\xi) \quad (10)$$

$$\frac{\partial^2 \ell_{tot,y}^{(2)}}{\partial z^2} - s^2 \gamma_2^2 \ell_{tot,y}^{(2)} = - \frac{js h(s)}{\epsilon_0 \epsilon_2} \beta \frac{\partial}{\partial z} \delta(z-\xi) \quad (11)$$

$$\frac{\partial^2 \ell_{tot,z}^{(2)}}{\partial z^2} - s^2 \gamma_2^2 \ell_{tot,z}^{(2)} = - \frac{h(s)}{\epsilon_0 \epsilon_2} \frac{\partial^2}{\partial z^2} \delta(z-\xi) + \mu_0 s^2 h(s) \delta(z-\xi) \quad (12)$$

where

$$\gamma_i = (\alpha^2 + \beta^2 + \sigma_i^{-2})^{1/2}, \quad i = 1, 2 \quad (13)$$

Concerning the undisturbed fields, the solution of (7) Regarding (9) - (12) with respect to the Laplace transformed transition conditions (6) is the wellknown Sommerfeld solution

$$e_{u,x}^{(2)}(x, y, z, s) = - \frac{1}{\epsilon_0 \epsilon_2} \frac{js^3 h(s)}{8\pi^2} \mathcal{F}_2^{-1} \left\{ \alpha [\text{sign}(z-\xi) e^{-s\gamma_2|z-\xi|} + c_{12} e^{-s\gamma_2(z+\xi)}] \right\} \quad (14)$$

$$e_{u,y}^{(2)}(x, y, z, s) = - \frac{1}{\epsilon_0 \epsilon_2} \frac{js^3 h(s)}{8\pi^2} \mathcal{F}_2^{-1} \left\{ \beta [\text{sign}(z-\xi) e^{-s\gamma_2|z-\xi|} + c_{12} e^{-s\gamma_2(z+\xi)}] \right\} \quad (15)$$

$$e_{u,z}^{(2)}(x, y, z, s) = \frac{1}{\epsilon_0 \epsilon_2} \frac{s^3 h(s)}{8\pi^2} \mathcal{F}_2^{-1} \left\{ \frac{\alpha^2 + \beta^2}{\gamma_2} [e^{-s\gamma_2|z-\xi|} + c_{12} e^{-s\gamma_2(z+\xi)}] \right\} \quad (16)$$

with

$$C_{12} = \frac{v_1^{-2} \gamma_2 - v_2^{-2} \gamma_1}{v_1^{-2} \gamma_2 + v_2^{-2} \gamma_1} \quad (17)$$

Similar expressions can be derived for $\vec{e}_u^{(4)}$, but they will not be given here, since we restrict our attention to medium 2.

The first term of the integrands in (14) - (16) is the primary field, the second term denotes the diffracted field for plane earth, and C_{12} corresponds to the Fresnel reflection coefficient.

The twice transformed disturbed fields must satisfy homogeneous equations (9) - (12); their solution in the Laplace transform space takes the form

$$\vec{e}_{d_v}^{(2)}(x, y, z, s) = \frac{s^2}{4\pi^2} \mathcal{F}_2^{-1} \left\{ \vec{H}_v^{(2)}(\alpha, \beta, s) e^{-s\gamma_2 z} \right\}, \quad v = 1, 2, 3, \dots \quad (18)$$

with arbitrary integration constants $\vec{H}_v^{(2)}(\alpha, \beta, s)$. To determine these constants the transition conditions (4) are expanded in a Taylor series around $z = 0$; comparing coefficients with respect to powers of δ results in inhomogeneous transition conditions at $z = 0$ for the disturbed fields alone, for instance for the first-order disturbed fields

$$\begin{aligned} \vec{e}_z \times [\vec{E}_{d_1}^{(2)} - \vec{E}_{d_1}^{(4)}]_{z=0} &= \nabla f \times [\vec{E}_u^{(2)} - \vec{E}_u^{(4)}] - \vec{e}_z \times \left[f \frac{\partial}{\partial z} (\vec{E}_u^{(2)} - \vec{E}_u^{(4)}) \right]_{z=0} \\ &= G_x \vec{e}_x + G_y \vec{e}_y \end{aligned} \quad (19)$$

$$\begin{aligned} \vec{e}_z \times [\vec{H}_{d_1}^{(2)} - \vec{H}_{d_1}^{(4)}]_{z=0} &= \nabla f \times [\vec{H}_u^{(2)} - \vec{H}_u^{(4)}] - \vec{e}_z \times \left[f \frac{\partial}{\partial z} (\vec{H}_u^{(2)} - \vec{H}_u^{(4)}) \right]_{z=0} \\ &= L_x \vec{e}_x + L_y \vec{e}_y \end{aligned} \quad (20)$$

The quantities G_x, G_y, L_x, L_y can be interpreted as surface currents, their Laplace transforms result from the Laplace transformed equations (19) and (20) using (14) - (16)

$$\begin{aligned} g_x(x, y, s) &= \frac{v_1^{-2} v_2^{-2}}{4\pi^2 \epsilon_0 \epsilon_2} s^3 h(s) \left[\frac{\partial f}{\partial y} \mathcal{F}_2^{-1} \left\{ \frac{\alpha^2 + \beta^2}{v_1^{-2} \gamma_2 + v_2^{-2} \gamma_1} e^{-s\gamma_2 \delta} \right\} \right. \\ &\quad \left. + j s f \mathcal{F}_2^{-1} \left\{ \frac{\beta(\alpha^2 + \beta^2)}{v_1^{-2} \gamma_2 + v_2^{-2} \gamma_1} e^{-s\gamma_2 \delta} \right\} \right] \end{aligned} \quad (21)$$

$$\begin{aligned} g_y(x, y, s) &= \frac{v_1^{-2} v_2^{-2}}{4\pi^2 \epsilon_0 \epsilon_2} s^3 h(s) \left[\frac{\partial f}{\partial x} \mathcal{F}_2^{-1} \left\{ \frac{\alpha^2 + \beta^2}{v_1^{-2} \gamma_2 + v_2^{-2} \gamma_1} e^{-s\gamma_2 \delta} \right\} \right. \\ &\quad \left. + j s f \mathcal{F}_2^{-1} \left\{ \frac{\alpha(\alpha^2 + \beta^2)}{v_1^{-2} \gamma_2 + v_2^{-2} \gamma_1} e^{-s\gamma_2 \delta} \right\} \right] \end{aligned} \quad (22)$$

$$l_x(x, y, s) = j \frac{v_1^{-2} v_2^{-2}}{4\pi^2} s^4 h(s) f \mathcal{F}_2^{-1} \left\{ \frac{\alpha \gamma_1}{v_1^{-2} \gamma_2 + v_2^{-2} \gamma_1} e^{-s\gamma_2 \delta} \right\} \quad (23)$$

$$l_y(x, y, s) = -j \frac{v_1^{-2} v_2^{-2}}{4\pi^2} s^4 h(s) f \mathcal{F}_2^{-1} \left\{ \frac{\beta \gamma_1}{v_1^{-2} \gamma_2 + v_2^{-2} \gamma_1} e^{-s\gamma_2 \delta} \right\} \quad (24)$$

It is interesting to note that these Laplace transformed first-order surface currents are proportional to the difference of the inverse squared phase velocities, to the amplitude of the deformation function $f(x,y)$ and to the third and forth power of s , respectively. The resulting expressions for the Laplace transformed first-order disturbed fields - their derivation being described below - and hence the second-order surface currents make it obvious that the perturbation series can be truncated after its first term if

$$s(v_1^{-2} - v_2^{-2}) \Delta z_{\max} \cos \vartheta_s < 1 \quad (25)$$

where Δz_{\max} denotes the maximum roughness amplitude and ϑ_s is the polar angle of \vec{R}_s , the vector from the plane earth image source to the point of observation (see Fig. 1). The occurrence of $\cos \vartheta_s$ in (25) is due to the fact that the Laplace transformed disturbed fields decrease with increasing transmitter-receiver distance by $(\cos \vartheta_s)^\nu$, ν being the perturbation order.

If no total reflection is allowed, i.e. $\epsilon_2 < \epsilon_1$, the truncation criterion (25) means in the time domain

$$t - t_s > \frac{\Delta z_{\max}}{v_1} \cos \vartheta_s = \frac{\Delta z_{\max}}{v_2} \sqrt{\frac{\epsilon_1}{\epsilon_2}} \cos \vartheta_s = t_{\Delta z} \quad (26)$$

where t_s is the travel time corresponding to R_s . The physical meaning of (26) is the following: the roughness results in an uncertainty of the situation of the dipole's image given by Δz_{\max} and this distance uncertainty yields a travel time uncertainty $t_{\Delta z}$ to the point of observation. Since the truncation of the perturbation series excludes the early time behavior of the rough surface, it is suggestive to consider only pulse durations T , which are large compared to $t_{\Delta z}$.

The Laplace transformed inhomogeneous transition conditions (19), (20) for the first-order disturbed fields in the Laplace transform space together with (21) - (24) result in a system of integral equations for the components of $\vec{A}_1^{(2)}(\alpha, \beta, s)$ which can be transformed into a system of linear equations by means of the two-dimensional Fourier transform, yielding for the Laplace transformed disturbed field components (the index "1" has been dropped)

$$\begin{aligned} e_{d,x}^{(2)}(x,y,z,s) = & -\frac{s^2}{4\pi^2} \mathcal{F}_2^{-1} \left\{ \left[\frac{(v_1^{-2} - v_2^{-2})\alpha\beta}{(\gamma_1 + \gamma_2)(v_1^{-2}\gamma_2 + v_2^{-2}\gamma_1)} \mathcal{G}_x(\alpha, \beta, s) \right. \right. \\ & - \frac{v_1^{-2}\gamma_2(\gamma_1 + \gamma_2) - \beta^2(v_1^{-2} - v_2^{-2})}{(\gamma_1 + \gamma_2)(v_1^{-2}\gamma_2 + v_2^{-2}\gamma_1)} \mathcal{G}_y(\alpha, \beta, s) \\ & + \mu_0 \frac{v_1^{-2}\gamma_2 + v_2^{-2}\gamma_1 + \alpha^2(\gamma_1 + \gamma_2)}{(\gamma_1 + \gamma_2)(v_1^{-2}\gamma_2 + v_2^{-2}\gamma_1)} \mathcal{L}_x(\alpha, \beta, s) \\ & \left. \left. + \mu_0 \frac{\alpha\beta}{v_1^{-2}\gamma_2 + v_2^{-2}\gamma_1} \mathcal{L}_y(\alpha, \beta, s) \right] e^{-s\gamma_2 z} \right\} \quad (27) \end{aligned}$$

$$\begin{aligned} e_{d,y}^{(2)}(x,y,z,s) = & -\frac{s^2}{4\pi^2} \mathcal{F}_2^{-1} \left\{ \left[\frac{v_1^{-2}\gamma_2(\gamma_1 + \gamma_2) - \alpha^2(v_1^{-2} - v_2^{-2})}{(\gamma_1 + \gamma_2)(v_1^{-2}\gamma_2 + v_2^{-2}\gamma_1)} \mathcal{G}_x(\alpha, \beta, s) \right. \right. \\ & - \frac{(v_1^{-2} - v_2^{-2})\alpha\beta}{(\gamma_1 + \gamma_2)(v_1^{-2}\gamma_2 + v_2^{-2}\gamma_1)} \mathcal{G}_y(\alpha, \beta, s) \\ & + \mu_0 \frac{\alpha\beta}{v_1^{-2}\gamma_2 + v_2^{-2}\gamma_1} \mathcal{L}_x(\alpha, \beta, s) \\ & \left. \left. + \mu_0 \frac{v_1^{-2}\gamma_2 + v_2^{-2}\gamma_1 + \beta^2(\gamma_1 + \gamma_2)}{(\gamma_1 + \gamma_2)(v_1^{-2}\gamma_2 + v_2^{-2}\gamma_1)} \mathcal{L}_y(\alpha, \beta, s) \right] e^{-s\gamma_2 z} \right\} \quad (28) \end{aligned}$$

$$e_{dz}^{(2)}(x, y, z, s) = -j \frac{s^2}{4\pi^2} \mathcal{F}_2^{-1} \left\{ \left[\frac{v_1^{-2} \beta}{v_1^{-2} \gamma_2 + v_2^{-2} \gamma_1} \mathcal{G}_x(\alpha, \beta, s) - \frac{v_1^{-2} \alpha}{v_1^{-2} \gamma_2 + v_2^{-2} \gamma_1} \mathcal{G}_y(\alpha, \beta, s) \right. \right. \\ \left. \left. + \mu_0 \frac{\alpha \gamma_1}{v_1^{-2} \gamma_2 + v_2^{-2} \gamma_1} \mathcal{L}_x(\alpha, \beta, s) + \mu_0 \frac{\beta \gamma_1}{v_1^{-2} \gamma_2 + v_2^{-2} \gamma_1} \mathcal{L}_y(\alpha, \beta, s) \right] e^{-s \gamma_2 z} \right\} \quad (29)$$

where $\mathcal{G}_x, \mathcal{G}_y, \mathcal{L}_x, \mathcal{L}_y$ are the two-dimensional Fourier transforms of g_x, g_y, l_x, l_y . In case of a band-limited one-dimensional roughness profile $f(x)$, whose spectral decomposition is given by

$$f(x) = \frac{1}{2\pi} \int_{-X_{\max}}^{X_{\max}} F(X) e^{jXx} dX \quad (30)$$

the use of the shifting-theorem yields

$$\mathcal{G}_x(\alpha, \beta, s) = j \frac{v_1^{-2} - v_2^{-2}}{2\pi \epsilon_0 \epsilon_2} s^2 h(s) \int_{-X_{\max}}^{X_{\max}} F(X) \frac{\beta [(\alpha - X/s)^2 + \beta^2]}{v_1^{-2} \gamma_2^{(s)} + v_2^{-2} \gamma_1^{(s)}} e^{-s \gamma_2^{(s)} z} dX \quad (31)$$

with

$$\gamma_i^{(s)} = [(\alpha - X/s)^2 + \beta^2 + v_i^{-2}]^{1/2}, \quad i = 1, 2 \quad (32)$$

Similar expressions can be given for $\mathcal{G}_y, \mathcal{L}_x, \mathcal{L}_y$. Hence

$$e_{dx}^{(2)}(x, y, z, s) = -j \frac{v_1^{-2} - v_2^{-2}}{8\pi^3 \epsilon_0 \epsilon_2} s^4 h(s) \int_{-X_{\max}}^{X_{\max}} F(X) i_x(x, y, z, X, s) dX \\ - j \frac{v_1^{-2} - v_2^{-2}}{8\pi^3 \epsilon_0 \epsilon_2} s^3 h(s) \int_{-X_{\max}}^{X_{\max}} X F(X) j_x(x, y, z, X, s) dX \quad (33)$$

where

$$i_x(x, y, z, X, s) = \mathcal{F}_2^{-1} \left\{ \left[\frac{(v_1^{-2} - v_2^{-2}) \alpha \beta^2}{(\gamma_1 + \gamma_2)(v_1^{-2} \gamma_2 + v_2^{-2} \gamma_1)} \cdot \frac{(\alpha - X/s)^2 + \beta^2}{v_1^{-2} \gamma_2^{(s)} + v_2^{-2} \gamma_1^{(s)}} \right. \right. \\ + \frac{v_1^{-2} \gamma_2 (\gamma_1 + \gamma_2) - \beta^2 (v_1^{-2} - v_2^{-2})}{(\gamma_1 + \gamma_2)(v_1^{-2} \gamma_2 + v_2^{-2} \gamma_1)} \cdot \frac{(\alpha - X/s) [(\alpha - X/s)^2 + \beta^2]}{v_1^{-2} \gamma_2^{(s)} + v_2^{-2} \gamma_1^{(s)}} \\ + v_2^{-2} \frac{v_1^{-2} \gamma_2 + v_2^{-2} \gamma_1 + \alpha^2 (\gamma_1 + \gamma_2)}{(\gamma_1 + \gamma_2)(v_1^{-2} \gamma_2 + v_2^{-2} \gamma_1)} \cdot \frac{(\alpha - X/s) \gamma_1^{(s)}}{v_1^{-2} \gamma_2^{(s)} + v_2^{-2} \gamma_1^{(s)}} \\ \left. \left. + v_2^{-2} \frac{\alpha \beta^2}{v_1^{-2} \gamma_2 + v_2^{-2} \gamma_1} \cdot \frac{\gamma_1^{(s)}}{v_1^{-2} \gamma_2^{(s)} + v_2^{-2} \gamma_1^{(s)}} \right] e^{-s \gamma_2^{(s)} z - s \gamma_2 z} \right\} \quad (34)$$

$$j_x(x, y, z, \chi, s) = \mathcal{T}_2^{-1} \left\{ \frac{v_1^{-2} \gamma_2 (\gamma_1 + \gamma_2) - \beta^2 (v_1^{-2} - v_2^{-2})}{(\gamma_1 + \gamma_2) (v_1^{-2} \gamma_2 + v_2^{-2} \gamma_1)} \cdot \frac{(\alpha - \chi/s)^2 + \beta^2}{v_1^{-2} \gamma_2^{(s)} + v_2^{-2} \gamma_1^{(s)}} e^{-s \gamma_2^{(s)} \xi - s \gamma_1 z} \right\} \quad (35)$$

The term with $j_x(x, y, z, \chi, s)$ is due to $\partial f / \partial x$ which occurs in \mathcal{Q}_y .

In the following we want to apply Cagniard's method in the modification of de Hoop in order to get $E_{d,x}^{(2)}(x, y, t, t)$ from the two-dimensional Fourier integral (33).

4. APPLICATION OF CAGNIARD'S METHOD

The essence of this method is to change the integral representation (33) to an explicit Laplace integral (CAGNIARD, L., 1939, DE HOOP, A.T., 1959, FELSEN, L., 1965). In order to apply this idea we must eliminate the s -dependence of the exponential's factor in $i_x(x, y, z, \chi, s)$ and $j_x(x, y, z, \chi, s)$. Therefore we define

$$\begin{aligned} \hat{e}_{d,x}^{(2)}(x, y, z, s) = & -j \frac{v_1^{-2} - v_2^{-2}}{8 \chi^3 \epsilon_0 \epsilon_2} s^4 h(s) \int_{-\chi_{\max}}^{\chi_{\max}} F(\chi) \hat{i}_x(x, y, z, \chi, s) d\chi \\ & - j \frac{v_1^{-2} - v_2^{-2}}{8 \chi^3 \epsilon_0 \epsilon_2} s^3 h(s) \int_{-\chi_{\max}}^{\chi_{\max}} \chi F(\chi) \hat{j}_x(x, y, z, \chi, s) d\chi \end{aligned} \quad (36)$$

where

$$\begin{aligned} \hat{i}_x(x, y, z, \chi, s) &= \int_{-\infty}^{+\infty} d\beta \int_{-\infty}^{+\infty} \hat{I}_x(\alpha, \beta, \chi, s) e^{j s \alpha x + j s \beta y} d\alpha \\ &= \mathcal{T}_2^{-1} \left\{ \hat{I}_x(\alpha, \beta, \chi, s) \right\} \end{aligned} \quad (37)$$

with

$$\hat{I}_x(\alpha, \beta, \chi, s) = \begin{cases} 0 & \text{for } |\operatorname{Re} \alpha| \leq \hat{\alpha} \\ \frac{s^2}{4 \chi^2} \mathcal{T}_2 \left\{ i_x(x, y, z, \chi, s) \right\} & \text{for } |\operatorname{Re} \alpha| > \hat{\alpha} \end{cases} \quad (38)$$

\hat{j}_x is defined analogously.

It will be shown below that the appropriate choice of $\hat{\alpha}$ simply yields $t > t_s + t_{\Delta z}$, an assumption we already postulated to truncate the perturbation series.

Now we restrict the bandlimits of $F(\chi)$ by

$$\left| \frac{\chi_{\max}}{s} \right| \ll \hat{\alpha} \quad (39)$$

then for $|\chi| < \chi_{\max}$ and $|\operatorname{Re} \alpha| > \hat{\alpha}$ we have $(\alpha - \chi/s) \sim \alpha$ and hence from (34) and (38)

$$\hat{I}_x(\alpha, \beta, \chi, s) \sim \hat{I}_x(\alpha, \beta) = \begin{cases} 0 & \text{for } |\operatorname{Re} \alpha| \leq \hat{\alpha} \\ \frac{\alpha \gamma_2 (\gamma_1 \gamma_2 + \alpha^2 + \beta^2)}{(\gamma_1 + \gamma_2) (v_1^{-2} \gamma_2 + v_2^{-2} \gamma_1)} & \text{for } |\operatorname{Re} \alpha| > \hat{\alpha} \end{cases} \quad (40)$$

The above-mentioned s -dependence is thus eliminated resulting in

$$\hat{e}_{d,x}^{(2)}(x,y,z,s) = -j \frac{v_1^{-2} v_2^{-2}}{8 \pi^3 \epsilon_0 \epsilon_2} s^4 h(s) \int_{-x_{\max}}^{x_{\max}} F(x) dx \cdot \int_{-\infty}^{+\infty} d\beta \int_{-\infty}^{+\infty} d\alpha \left\{ \begin{array}{ll} 0 & \text{for } |Re \alpha| \leq \hat{\alpha} \\ \frac{\alpha \gamma_2 (\gamma_1 \gamma_2 + \alpha^2 + \beta^2)}{(\gamma_1 + \gamma_2)(v_1^{-2} \gamma_2 + v_2^{-2} \gamma_1)} & \text{for } |Re \alpha| > \hat{\alpha} \end{array} \right\} \cdot e^{-s \gamma_2 (z+\xi) + j s \alpha x + j s \beta y} d\alpha \quad (41)$$

$$- j \frac{v_1^{-2} v_2^{-2}}{8 \pi^3 \epsilon_0 \epsilon_2} s^3 h(s) \int_{-x_{\max}}^{x_{\max}} x F(x) dx \cdot \int_{-\infty}^{+\infty} d\beta \int_{-\infty}^{+\infty} d\alpha \left\{ \begin{array}{ll} 0 & \text{for } |Re \alpha| \leq \hat{\alpha} \\ \frac{(\alpha^2 + \beta^2) [\alpha v_1^{-2} \gamma_2 (\gamma_1 + \gamma_2) - \beta^2 (v_1^{-2} v_2^{-2})]}{(\gamma_1 + \gamma_2)(v_1^{-2} \gamma_2 + v_2^{-2} \gamma_1)^2} & \text{for } |Re \alpha| > \hat{\alpha} \end{array} \right\} \cdot e^{-s \gamma_2 (z+\xi) + j s \alpha x + j s \beta y} d\alpha$$

The integrand of (41) has no branchpoints and no poles in the complex α -plane for real β . So we can change the integration path from the real α -axis to the hyperbola on which the function $f(\alpha, \beta) = \tau$ is real and positive and

$$f(\alpha, \beta) = \gamma_2 R_s \cos \vartheta_s - j \alpha R_s \sin \vartheta_s \quad (42)$$

where

$$\begin{aligned} z + \xi &= R_s \cos \vartheta_s \\ x &= R_s \sin \vartheta_s \end{aligned} \quad (43)$$

$f(\alpha, \beta)$ is the exponent of the exponential function of (41) for $y = 0$. The hyperbolic path $f(\alpha, \beta) = \tau$ yields (see Fig. 2)

$$\hat{\tau}(\beta) \leq \tau < \infty \quad (44)$$

with

$$\hat{\tau}(\beta) = R_s \left(\beta^2 + v_2^{-2} + 2 \frac{\Delta z}{R_s v_2^2} \sqrt{\epsilon_1/\epsilon_2} \cos \vartheta_s \right)^{1/2} \quad (45)$$

if $\hat{\alpha}$ is chosen to be

$$\hat{\alpha} = \left(2 \frac{\Delta z}{R_s v_2^2} \sqrt{\epsilon_1/\epsilon_2} \cos \vartheta_s \right)^{1/2} \cos \vartheta_s \quad (46)$$

Integrating (41) along the hyperbolic integration path and changing the order of integration yields (DE HOOP, A.T., 1959, LANGENBERG, K.J., 1974):

$$\hat{e}_{d,x}^{(2)}(x,0,z,s) = - \frac{v_1^{-2} v_2^{-2}}{2 \pi^3 \epsilon_0 \epsilon_2 R_s} s^4 h(s) \int_{-x_{\max}}^{x_{\max}} F(x) dx \cdot \int_{\hat{\tau}(0)}^{\infty} [\hat{\beta}(\tau) Re \int_0^{\pi/2} \frac{j \alpha \gamma_2 (\gamma_1 \gamma_2 + \alpha^2 + \beta^2) \cos \psi}{(\gamma_1 + \gamma_2)(v_1^{-2} \gamma_2 + v_2^{-2} \gamma_1)} \cdot \frac{1}{(\tau^2/R_s^2 - \beta^2 - v_2^{-2})^{1/2}} d\psi] e^{-s\tau} d\tau \quad (47)$$

$$- j \frac{v_1^{-2} v_2^{-2}}{2 \pi^3 \epsilon_0 \epsilon_2 R_s} s^3 h(s) \int_{-x_{\max}}^{x_{\max}} x F(x) dx \cdot \int_{\hat{\tau}(0)}^{\infty} [\hat{\beta}(\tau) Re \int_0^{\pi/2} \frac{(\alpha^2 + \beta^2) [\alpha v_1^{-2} \gamma_2 (\gamma_1 + \gamma_2) - \beta^2 (v_1^{-2} v_2^{-2})]}{(\gamma_1 + \gamma_2)(v_1^{-2} \gamma_2 + v_2^{-2} \gamma_1)^2 (\tau^2/R_s^2 - \beta^2 - v_2^{-2})^{1/2}} \cdot \gamma_2 \cos \psi d\psi] e^{-s\tau} d\tau$$

where we have introduced the new variable ψ through

$$\beta = \hat{\beta}(\tau) \sin \psi \quad (48)$$

with

$$\hat{\beta}(\tau) = \left[\frac{\tau^2}{R_s^2} - v_2^{-2} \left(1 + \frac{2 t_{\Delta z}}{t_s} \right) \right]^{1/2} \quad (49)$$

From (45) we have

$$r_{(0)} = \frac{R_s}{v_2} \left(1 + 2 \frac{t_{\Delta z}}{t_s} \right)^{1/2} \sim t_s + t_{\Delta z} \quad (50)$$

if $t_{\Delta z} \ll t_s$. Hence in the time domain

$$\hat{E}_{d,x}^{(2)}(x, 0, z, t) = \hat{E}_{d,x,1}^{(2)}(x, 0, z, t) * \frac{d^4 H}{dt^4} + \hat{E}_{d,x,2}^{(2)}(x, 0, z, t) * \frac{d^3 H}{dt^3} \quad (51)$$

where

$$\hat{E}_{d,x,1}^{(2)}(x, 0, z, t) = \begin{cases} 0 & \text{for } t \leq t_s + t_{\Delta z} \\ -\frac{v_1^{-2} v_2^{-2}}{2 \tilde{x}^3 \epsilon_0 \epsilon_2 R_s} \hat{\beta}(t) \int_{-x_{\max}}^{x_{\max}} F(x) dx \cdot \operatorname{Re} \int_0^{\pi/2} \frac{j \alpha(t, \psi) \gamma_2^2 \cos \psi}{(\gamma_1 + \gamma_2)(v_1^{-2} \gamma_2 + v_2^{-2} \gamma_1)} d\psi \\ \quad \cdot \frac{\gamma_1 \gamma_2 + \alpha^2(t, \psi) + \beta^2}{(t^2/R_s^2 - \beta^2 - v_2^{-2})^{1/2}} d\psi & \text{for } t > t_s + t_{\Delta z} \end{cases} \quad (52)$$

$$\hat{E}_{d,x,2}^{(2)}(x, 0, z, t) = \begin{cases} 0 & \text{for } t \leq t_s + t_{\Delta z} \\ -j \frac{v_1^{-2} v_2^{-2}}{2 \tilde{x}^3 \epsilon_0 \epsilon_2 R_s} \hat{\beta}(t) \int_{-x_{\max}}^{x_{\max}} x F(x) dx \cdot \operatorname{Re} \int_0^{\pi/2} \frac{[\alpha^2(t, \psi) + \beta^2] \gamma_2 \cos \psi}{(\gamma_1 + \gamma_2)(v_1^{-2} \gamma_2 + v_2^{-2} \gamma_1)^2} d\psi \\ \quad \cdot \frac{v_1^{-2} \gamma_2 (\gamma_1 + \gamma_2) - \beta^2 (v_1^{-2} v_2^{-2})}{(t^2/R_s^2 - \beta^2 - v_2^{-2})^{1/2}} d\psi & \text{for } t > t_s + t_{\Delta z} \end{cases} \quad (53)$$

It is understood that the asterisk "*" means the convolution operation. Eq. (51) is valid provided $H(0) = 0$, $dH/dt|_{t=0} = 0$, $d^2 H/dt^2|_{t=0} = 0$, $d^3 H/dt^3|_{t=0} = 0$.

Since our original assumption was $t > t_{\Delta z} + t_s$ we finally get the result

$$\hat{E}_{d,x}^{(2)}(x, 0, z, t) = \hat{E}_{d,x}^{(2)}(x, 0, z, t) \quad \text{for } t > t_s + t_{\Delta z} \quad (54)$$

In a similar way an expression for $\hat{E}_{d,z}^{(2)}(x, 0, z, t)$ can be derived; for $y = 0$ we find that $\hat{E}_{d,y}^{(2)}$ is identically zero.

5. DISCUSSION OF THE RESULTS

The most significant restriction concerning the validity of our theory is equ. (39). Together with (25) and (46) it relates the maximum wavelength $\lambda_{\max} = 2\tilde{x}/x_{\max}$ of the roughness profile and the transmitter-receiver distance through

$$\lambda_{\max} \gg 2\tilde{x} \left(\frac{\Delta z (z + \tilde{g}) \sqrt{\epsilon_1/\epsilon_2}}{2 \cos^2 \theta_s} \right)^{1/2} = 2\tilde{x} R_s \left(\frac{\Delta z \sqrt{\epsilon_1/\epsilon_2}}{2 (z + \tilde{g})} \right)^{1/2} \quad (55)$$

i.e. rapid oscillations of the roughness are not allowed. On the other hand, we are able - at least for large times - to relate directly the roughness spectrum and its transient response by (51), (52) and (53) respectively. For instance, if the roughness profile is an even function, the second term (53) of the transient response vanishes. Once the real parts of the integrals (52) and (53) have been computed, the special influence of the roughness consists merely in a multiplication with its integrated spectrum.

For numerical evaluation we chose the profile

$$f(x) = \cos X_{\max} x \quad (56)$$

which yields

$$\int_{-X_{\max}}^{X_{\max}} F(x) dx = 2\pi \quad (57)$$

and the special initial pulse function

$$H(t) = \left(1 - e^{-t/\tau}\right)^4 \quad (58)$$

which describes a unit-"step"-function with finite rise time T , where $T \gg t_{\Delta t}$. The convolution integral (51) has been evaluated by means of the fast Fourier transform algorithm. Fig. 3 to Fig. 6 show the polar component $E_g^{(1)}(x, 0, z, t)$ of the reflected and disturbed fields as function of the normalized time $t - t_s/t_p$, where t_p is the travel time from the source to the point of observation. The field strengths are normalized to the maximum of the undisturbed field.

The primary far-field of a dipole in free space is proportional to the second derivative of (58); based on the same procedure as described above for the disturbed fields the numerical results show that the earth reflected field is also proportional to the second derivative of $H(t)$, a fact which is shown in Fig. 3 to Fig. 6, whereas the disturbed field is somewhat proportional to the third derivative indicated by the maximum for large times. The relevant time interval of the disturbed fields - that is to say where our theory holds - begins at $t - t_s = t_{\Delta t}$. For smaller times these fields are set to zero. The above-mentioned Figures also show the total fields for times $t - t_s > t_{\Delta t}$ for several transmitter-receiver distances. The greater this distance the smaller the difference between undisturbed and total fields, a fact which has been already stated to truncate the perturbation series.

The most significant change in the received signal due to the earth's roughness is that the trailing edge of the impulse becomes steeper, a fact which is also observed for increasing deformation amplitude (Fig. 7): the rough dielectric surface seems to act like a differentiator or RC-highpass in circuit theory.

6. CONCLUDING REMARKS

The paper presents a first attempt to solve the problem of pulse propagation over irregular terrain. The late time behavior of first-order perturbation fields can be computed if certain assumptions concerning the terrain irregularity are fulfilled: the roughness profile function must be one-dimensional and band-limited, the band-limits being closely connected with the transmitter-receiver distance. Furthermore the duration of the initial transmitted pulse must be large compared to the travel time due to the maximum deformation amplitude, a fact which is physically intuitive, since otherwise the total pulse has already decayed during the early time interval where the time history of the received signal is unknown. On the other hand, even the near-field's time history can be given exactly and the computation of the far-field needs no asymptotic procedure as the time harmonic case does (BECKER, K.-D., et al., 1975)

It will be pointed out that also layered structures can be taken into account (LANGENBERG, K. J., 1974) and since the method works as well for the magnetic dipole one is able to compute polarization effects in the time domain of rough dielectric surfaces and layers.

REFERENCES

- AGARD Conference Proceedings No. 144 on Electromagnetic Wave Propagation Involving Irregular Surfaces and Inhomogeneous Media (1974).
 BECKER, K.-D., DOBMAN, G. and LANGENBERG K.J., 1975, "Space wave field produced by a vertical electric dipole above a rough surface", Appl. Phys., vol. 6, pp. 35-42
 BECKMANN, P. and SPIZZICHINO A., 1963, The Scattering of Electromagnetic Waves from Rough Surfaces. Oxford: Pergamon Press
 CAGNIARD, L., 1939, Réflexion et Réfraction des Ondes Sismiques Progressives. Paris: Gauthier-Villard
 FELSSEN, L.B., 1965, "Transient solutions for a class of diffraction problems", Quart.

Appl. Math., vol. 23, pp. 151-169

HOOP, A.T., 1959, "A modification of Cagniard's method of solving seismic pulse problems", Appl. Sci. Res., vol. B8, pp. 349-356

HUGHES, W.J. and WAIT, J.R., 1975, "Effective wave tilt and surface impedance over a laterally inhomogeneous two-layer earth", Radio Science, vol. 10, pp. 1001-1008

LANGENBERG, K.J., 1974, "The transient response of a dielectric layer", Appl. Phys., vol. 3, pp. 179-188

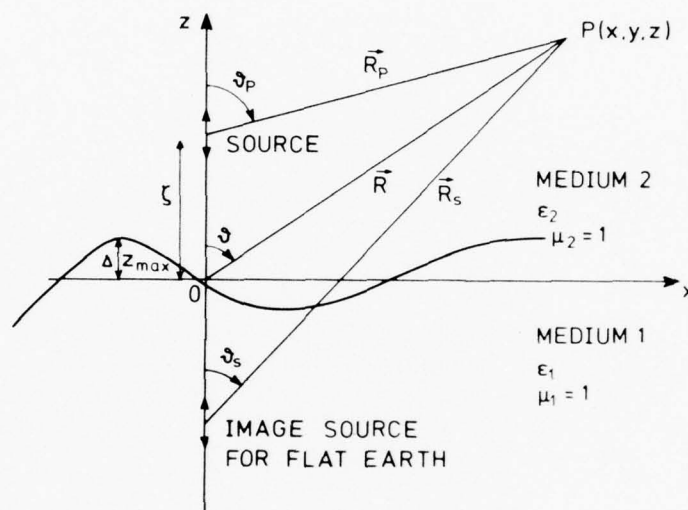


Fig. 1. Geometry of the problem.

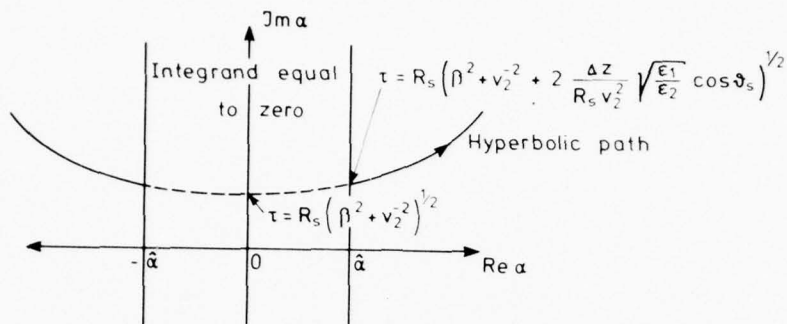


Fig. 2. Integration path in the complex α -plane.

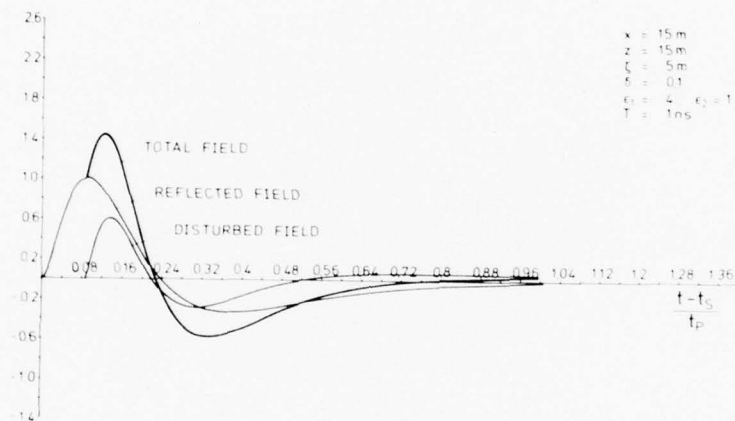


Fig. 3. Time histories of the undisturbed, disturbed and total fields for $x = 15$ m.

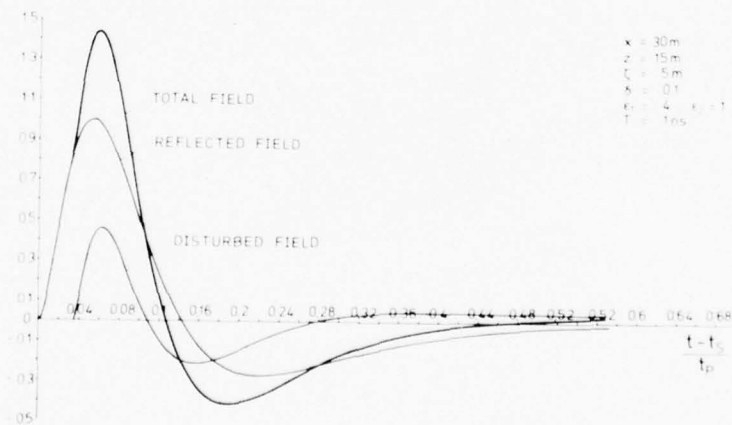


Fig. 4. Time histories of the undisturbed, disturbed and total fields for $x = 30$ m.

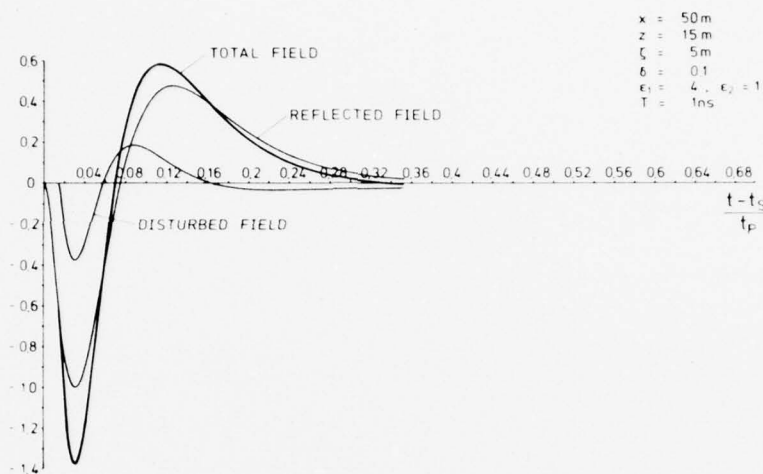


Fig. 5. Time histories of the undisturbed, disturbed and total fields for $x = 50 \text{ m}$.

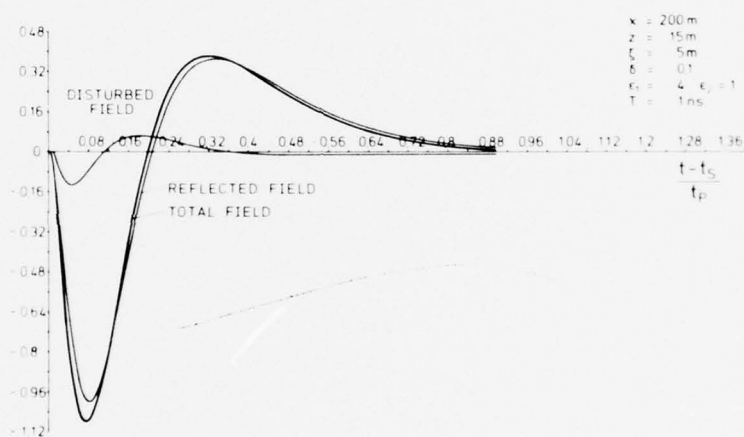


Fig. 6. Time histories of the undisturbed, disturbed and total fields for $x = 200 \text{ m}$.

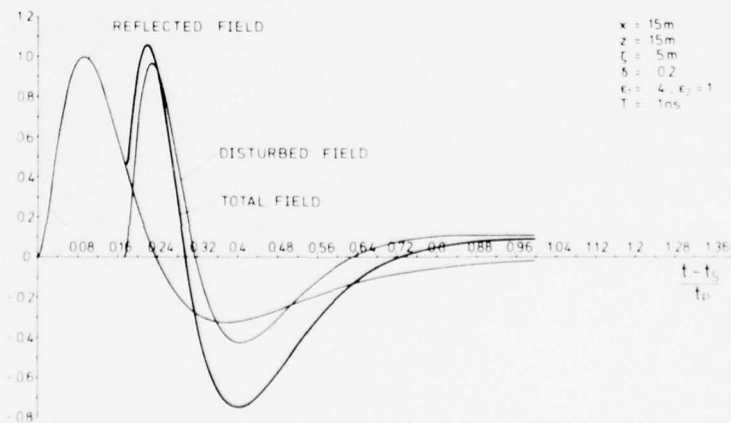


Fig. 7. Time histories of the undisturbed, disturbed and total fields for $\delta = 0.2$.

DISCUSSION

L.B.Felsen: The Cagniard method can be used for closest form inversion only when the integrand (except for the exponential function) is independent of the transform variable, i.e. non-dispersive. Do the restrictions imposed on your rough surface model imply non-dispersivity over the spectral range of your source pulse? It may be possible to include dispersive effects as corrections at low and high frequencies. Have you tried this?

K.J.Langenberg: As a matter of fact, our rough surface model is a non-dispersive one, since the rough surface separates two dielectric half-spaces without any losses. The mentioned S -dependence of the integrand is due to the spectral decomposition of the roughness function, which vanishes if it is chosen to be band-limited and obeying the truncation criterion of the perturbation series. In addition, the pulse width - or its spatial extent, respectively - must be large compared to the maximum roughness amplitude. Hence low-frequency effects are included in the theory; yet high-frequency effects cannot be included in a very similar way. We did not yet try to include them in an extended theory.

EFFECTS OF NOCTURNAL GROUND - BASED TEMPERATURE INVERSION LAYERS ON LINE-OF-SIGHT RADIO LINKS

L. Fehlhaber, H.G. Giloi
Research Institute of
the Deutsche Bundes-
post at the FTZ
6100 Darmstadt, Germany

SUMMARY

In radio relay systems the variations of the transmission loss, caused by propagation effects, are of some importance. These variations occur in the shape of slow fading and fast or multipath fading, mostly at nighttime. With unobstructed line-of-sight propagation they are nearly in all cases due to nocturnal ground based temperature inversions. These inversions cause increased transmission loss by defocussing, that may exceed 15 dB at very long paths. Multipath fading arises, when humidity saturation is reached near the ground. The upper limit of the humid layer, situated some decameters only above ground, is reflecting totally. Besides these effects the inversion causes a shifting of the radio horizon to larger distances and hence to an enlargement of the range of the transmitter. A model of the ground based inversion is presented, that explains the observed effects not only qualitatively but to some extent quantitatively, so that predictions of statistical parameters become possible.

1. INTRODUCTION

Prior investigations in the short-decimeter and centimeter bands have shown that heavy fading on line-of-sight links is found together with ground based temperature inversion layers (Großkopf, J., Fehlhaber, L., 1963 and 1965). In this paper an attempt is made to analyse this correlation and the theoretical results are compared with experimental results. Multipath fading is explained to be caused by temperature inversions. As another effects of this meteorological phenomenon, the radio horizon is shifted to larger distances and the range of transmitters is extended. Furthermore, temperature inversions cause defocussing attenuation which may exceed 15 dB on very long paths. In chapter 2 a model of ground-based inversion layers is given including the slope of the refractive index in these layers. The 3rd chapter comprises the effects on wave propagation and the 4th the experimental results.

2. REFRACTIVE MODULUS AS A FUNCTION OF HEIGHT

The refractive index n of the air as well as the refractivity

$$N = (n-1) 10^6 \quad (1)$$

normally diminishes with height. The radio beam is not a straight line (see Fig. 1a). To simplify the calculations, the spherical earth is transformed into a plane. This is done by means of the refractive index

$$M = N + \frac{h}{r_e} 10^6 = N + .1569 h \quad (2)$$

where h is the height in m above mean sea level and r_e the radius of the earth.

M normally grows with height. When M is a linear function of height, as it is found in a well mixed atmosphere, the radio beam is a parabola (see Fig. 1b).

The refractive modulus may be calculated by Smith's and Weintraub's formula

$$M = \frac{77.6}{T} p + 373\,256 \frac{e}{T^2} + \frac{h}{r_e} 10^6 \quad (3)$$

where p = atmospheric pressure in mb
 T = Kelvin temperature
 e = vapour pressure also in mb

2.1. Situation before the rise of the inversion

On a bright day, the soil is heated by the incoming radiation. The air touching the soil is heated and it rises because of its low density. By this convection the air is well mixed up to a maximum height of 1000 m. In this layer the temperature has the dry adiabatic gradient $\Gamma' = -.01$ K/m, and the specific humidity s is constant, provided that the saturation point is not exceeded. This means the air must be relatively dry.

The vapour pressure may be calculated from the specific humidity by

$$s = \frac{.623}{p - .377 e} \approx .623 \frac{e}{p} \quad (4)$$

In Equation (3) p , e and T are functions of the height. When T_0 is the temperature at the soil ($h = 0$)

$$T = T_0 - .01 h \quad (5)$$

The pressure p is given by the barometric height formula

$$\frac{dp}{p} = - \frac{g}{R_L T} dh \quad (6)$$

$$\begin{aligned} \text{(gravity constant } g &= 9.14 \text{ m s}^{-2} \\ \text{gas constant of the air } R_L &= 287 \text{ m}^2 \text{ s}^{-2} \text{ K}^{-1}) \end{aligned}$$

The vapour pressure is given by Mangnus's formula

$$e = 6.03 U 10^{\frac{7.4475 \mathfrak{A}}{234.67 + \mathfrak{A}}} \quad (7)$$

$$\begin{aligned} \text{(relative humidity } U \text{ (} 0 < U < 1 \text{)} \\ \text{temperature in centigrades } \mathfrak{A} &= T - 273.2) \end{aligned}$$

Equations (3) - (7) yield the refractive modulus as a function of height. It can be approximated very well by a linear function in the height range of interest, which is only a few hundreds of meters. In this range

$$\beta = \frac{dM}{dh} \quad (8)$$

is constant. People, who are used to apply the effective earth radius $k \cdot r_e$ may calculate β from the relation

$$\beta = \frac{10^6}{k r_e} = \frac{0.1569}{k} \quad (9)$$

Table 1 below gives some values of β , when \mathfrak{A} is the temperature, p_0 the atmospheric pressure, and U_0 the relative humidity near the ground.

Table 1
 β , gradient of M
when $T = .01 \text{ K}^{-1}$, $p_0 = 1020 \text{ mb}$

U_0	.4	.6
$\mathfrak{A}/^\circ\text{C}$		
15	.132	.132
25	.133	.132

The calculations of both this chapter and the following ones are performed in (Fehlhaber, L., 1976).

2.2. Inversion before the dew point is reached

During the afternoon, the convection abates and at last stops. The radiation going off exceeds the incoming radiation and the soil is cooling off. The turbulence caused by the wind carries the lower temperature to the air close to the ground. The development of the temperature slope is shown in Fig. 2. At the soil the temperature drops by ΔT . In the ground based layer the temperature grows with height. There is an inversion with a positive temperature gradient Γ_i . The value of Γ_i depends on the turbulence i.e., on the wind velocity. When the wind is slow, Γ_i rises to high values. Above the inversion layer, the temperature gradient is assumed to be the same as during the day. Thus the temperature profile is bilinear. The height of the inversion layer is

$$h_i = \frac{\Delta T}{\Gamma_i - \Gamma} = \frac{\Delta T}{\Gamma_i + .01} \quad (10)$$

This profile is a simplification. In fact, there is an isothermic intermediate layer (Ahrens, D., 1975), but it is unimportant in most wave propagation problems. While the air cools off, the specific humidity does not change, as long as the saturation is not reached.

The bilinear temperature profile produces an M-profile which is also bilinear. The gradient of M in the inversion layer

$$\beta_i = \frac{dM}{dh} \quad (11)$$

is a function of Γ_i (Fig. 3). It is smaller than β (see Table 1)

$$v = \frac{\beta_i}{\beta} < 1 \quad (12)$$

If Γ_i is very great, M may become negative.

2.3. Ground based vapour saturated layer

When the temperature drops below the dew point, the vapour begins to condense. A foggy layer of the height h_f forms near the ground. Rather than the soil, now this layer cools off by radiation causing an unstable temperature slope. This will change soon to a stable slope and a discontinuity occurs at the surface as it is seen in Fig. 4a. In the foggy layer, the specific humidity is no longer constant. Here, the relative humidity $U = 1$. As the vapour pressure e is a function of the temperature (equation (7)), a discontinuity in temperature causes also a discontinuity in e , as it is seen in Fig. 4b. These temperature and vapour pressure slopes produce a refractive modulus slope an example of which is evident from Fig. 4c. Above the height h_i the M-gradient is $\beta = .13 \text{ m}^{-1}$. Below h_i the M-gradient decreases to $.054 \text{ m}^{-1}$ because of the temperature inversion. At the height h_f , there is a discontinuity $\Delta M = 3.3$.

As can be seen from chapter 4, inversions rarely produce moist saturated layers above dry soil. Most of them are found in autumn. On wet soil the evaporation continues when the inversion begins to form. The vapour is carried upward by turbulence, but not higher than the inversion layer. Thus, a moist saturated layer is much more likely to form. The above mentioned effects are found more often above river basins and fens.

2.4. Layered atmosphere in the dry part of the inversion

The discontinuity of M at the surface of the moist saturated layer is not the only one in an inversion layer. The temperature growing with height prevents the vertical motions. A volume of air, which was going up during the convection period, now stops and spreads out horizontally. So a layered structure forms with more discontinuities of M. But their values are much lower than ΔM at the surface of the moist saturated layer.

2.5. Decomposition of the inversion

The radiation beginning again in the morning decomposes the inversion layer beginning at the moist saturated layer. First the discontinuity of M vanishes. Later on, when the convection has entirely formed again, the break in the M-curve at the surface of the inversion layer vanishes, too.

3. WAVE PROPAGATION EFFECTS OF INVERSION LAYERS ON LINE-OF-SIGHT LINKS

Both the variation of the M-gradient at the surface of the inversion layer as the discontinuity of M at the surface of the moist saturated layer have effects on the wave propagation of cm and short dm waves.

3.1. Rays and field strength in a linear and a bilinear M-profile

The problems caused by the break of the M-curve at the surface of the inversion layer can be solved by optical ray calculations. The M-gradients are not great and according to equation (11) the condition $\beta_i/\beta < 2$ is satisfied i.e., there are no focussing effects. The optical rays can be calculated from the equation

$$\frac{d^2 h}{d x^2} = \frac{dM}{dh} = \beta \quad (3.1)$$

where h is the height in m and x the distance in km.

When the M-profile is linear, β is constant and the ray is a parabola

$$h = \frac{1}{2} \beta x^2 + \alpha_s x + h_s \quad (3.2)$$

At $x = 0$, the transmitter is situated at the height h_s and α_s is approximately the angle of the ray in mrad.

When there is an inversion layer, the M-profile is bilinear, at least in the upper part (see Fig. 4c). There are two gradients β and β_i , and the ray consists of parts of parabolas (see Fig. 5):

$$\begin{aligned} \text{Zone I} \quad 0 \leq x \leq x_1 \\ h = \frac{1}{2} \beta x^2 + \alpha_s x + h_s \end{aligned} \quad (3.3)$$

$$\begin{aligned} \text{zone II} \quad x_1 \leq x \leq x_2 \\ h = \frac{1}{2} \beta_i (x - x_1)^2 + \alpha_i (x - x_1) + h_i \end{aligned} \quad (3.4)$$

$$\begin{aligned} \text{zone III} \quad x \geq x_2 \\ h = \frac{1}{2} \beta (x - x_2)^2 - \alpha_i (x - x_2) + h_i \end{aligned} \quad (3.5)$$

The quantities x_1 , x_2 , and α_i are calculated under the conditions that h and dh/dx are steady at x_1 and x_2 .

The attenuation relative to the free space may be calculated as

$$A = 10 \lg \left| \frac{1}{x} \frac{h}{\alpha_s} \right| \quad (3.6)$$

(Großkopf, J., Fehlhaber, L., 1965).

If the profile is linear

$$A = 0$$

ensues from equation (3.2).

The same result is found in zone I of the bilinear profile (3.3). In the zones II and III defocussing attenuation occurs (see chapter 3.3).

3.2. Shift of the radio horizon

The radio horizon is defined by the ray touching the ground, the horizon-ray. It is derived from equations (3.2) - (3.5) calculating α_s on the condition:

$$\begin{aligned} \text{at } x = x_0 \\ h = 0 \quad \text{and} \quad \frac{dh}{dx} = 0. \end{aligned}$$

When an inversion occurs, the radio horizon is shifted to a greater distance. The distance x_0 grows from

$$\sqrt{\frac{2h_s}{\beta}} \quad \text{to a maximum of} \quad \sqrt{\frac{2h_s}{\beta_i}}$$

and from there onwards the horizon-ray runs at lower heights. Fig. 6 shows an example. The transmitter is situated at a height of 250 m. In Fig. 6a the gradient of M is almost normal. A receiver belonging to the hatched area is in the shadow. When there is an inversion with $\beta_i = \beta/2 = .059 \text{ m}^{-1}$ and a height of more than 250 m (Fig. 6b), the shadow is considerably reduced. Fig. 6c shows the radio horizon when the inversion layer is only 50 m high. Nevertheless the range of sight is evidently extended.

This may cause interference when the service radius of a transmitter spreads out into the primary coverage area of another transmitter at the same frequency.

A radio horizon exists only when $\beta_i > 0$. According to Fig. 3, β becomes negative when the temperature gradient has very great values. Then a wave guide occurs in the troposphere and a horizon cannot be defined.

3.3. Attenuation by defocussing

According to chapter 3.1, no attenuation is caused by a simply linear M-profile. Now there are two layers and in the lower one β_i is greater than zero. Then the

defocussing effects cause an attenuation in the zones II and III in Fig. 5. This defocussing loss is calculated by means of equations (3.4) - (3.6). Fig. 7 shows this loss in the case of the example in Fig. 6c. Below the ray touching the surface of the inversion layer, an attenuation $A > 0$ relative to free space is found. It grows with distance. At 75 km A has a maximum amount of 3 dB. The diffraction loss near the horizon is neglected for it is of no use in understanding the above mentioned effects.

When β_i is reduced, the loss observed at a fixed point increases. The value of β_i is low, when the temperature gradient in the inversion layer is great. This happens, when the wind-velocity is low. Thus, great defocussing loss is found when the wind is slow.

As may be seen from Fig. 7, the loss as a function of height has a maximum at a fixed distance. While the inversion layer develops, it increases in height and so does the maximum of A . At any time the maximum will move over the aerial of a receiver and more or less heavy fading occurs.

When $\beta_i \leq 0$ is valid, an area should exist where waves cannot enter. But this is due to the simplification of the bilinear M-profile. In reality there is a smooth transition in M and in the mentioned area the attenuation is finite.

Multipath fading.

In Fig. 4c a discontinuity ΔM is found at the height of the vapour saturated layer. In the atmosphere, an actual discontinuity cannot exist but for a small difference in height, the refractive modulus diminishes to such an extent, that the discontinuity is a good approximation for calculating refraction problems.

When the height of the vapour saturated layer is lower than transmitter and receiver stations as it is seen in Fig. 8, a direct wave and a wave reflected at the surface of the layer are travelling to the receiver. Their phase interference causes fading. The fading is heavy when both waves have nearly the same field strength, that means when the second wave is reflected totally. Total reflection occurs when the reflecting medium has the lower refractive modulus and the grazing angle α_f is less than the critical angle of total reflection α_G . This angle is a function of M (Großkopf, J., Fehlhaber, L., 1963)

$$\alpha_G = \sqrt{2\Delta M}$$

(α_G in mrad).

Calculating the direct and the reflected ray, the M gradients of the inversion layer and of the atmosphere above it are to be considered. Here only two path rather than multipath propagation is described. There is a third wave caused by the reflection process (Fehlhaber, L., 1970) and some more waves reflected by the discontinuities of M in the dry part of the inversion (see chapter 2.4). These waves usually do not cause heavy fading since either their field strength is too low or their phase difference with respect to the direct wave is too small. Movements of the reflecting layer change the phase difference. Furthermore, the surface of the layer is not homogeneous in ΔM nor, as a consequence, in α_G . Areas, in which α_G is greater than α_f , and those, where it is lower than α_f , are drifted by the wind over the place of reflection. So the reflection coefficient varies with time.

Both effects cause great and fast variations of the receiver level as they are seen in the strip chart recording of Fig. 9a.

4. MEASUREMENTS OF METEOROLOGICAL AND WAVE PROPAGATION EFFECTS

In the previous chapters it was attempted to investigate quantitatively how ground based temperature inversion layers influence the wave propagation in line-of-sight radio links. Here the frequency of inversion layers will be given. The coincidence of temperature inversion layers and wave propagation effects is investigated.

4.1 Frequency of inversion layers

Daily records of inversion layers are given by the balloon ascents of the meteorological services. As there are ascents only at 1.00 and 13.00 o'clock central European time, they cannot show the development of an inversion layer. Furthermore, the time constants of the measuring instruments are very high. Hence the temperature and humidity gradients obtained by the balloon ascents are falsified to such an extent, that they cannot be used for calculating wave propagation problems. But the records show the ground based inversion layer qualitatively. In this way statistics of the occurrence of inversions were established. Fig. 10 shows the numbers of nights when layers were found at the radio-sonde-stations of Stuttgart and Hannover in 1962 or 1965 respectively. Stuttgart is situated in a hilly region at a height of 300 m whereas Hannover lies at a height of 50 m and may represent the conditions on the plains of Northern Germany. The nights, when moist saturation was found at 1 o'clock are marked by hatching. As in many nights moist saturation may occur after this time, these numbers should not be used to evaluate the frequency of fading. But it is seen that at both stations most nights with moist saturation are found in autumn.

4.2 Coincidence of inversion and multipath fading

Good conditions for testing the coincidence of inversion periods with fading periods existed on an experimental radio link of 69 km from Hambach to Darmstadt (Fig.

11). Near this link, a 64 m tower was built and instruments were installed to measure the temperature and humidity pattern. A time is called an inversion time when the temperature at the top of the tower is higher by .1 K than near the ground (4 m). An hour, during which the received level varies by more than 10 dB, is called a fading hour. A night is called a fading night when it includes at least one fading hour. To compare fading nights with inversion nights, measurements made in June 1966 were chosen. Simultaneous recordings of the attenuation at 6.7 GHz and of the meteorological data exist for twenty days of this month. Inversion layers were found in 14 nights and fading in 13 nights. In six nights there were neither inversion layers nor fading. This is a very good correlation.

On the other hand, fading does not occur in all hours, where inversion layers exist. From June to October 1966, there were 912 measuring times of the meteorological tower. At 255 of these an inversion was found, that means in 28% of the whole period. In the same period, fading was found in only 15% of the hours recorded. This means that fading was caused by only half of the recorded inversions. Statistics of the occurrence of ground based inversion layers in various districts may be established by tolerable expenditure of work using the balloon ascents of the meteorological services. A relation of such statistics with adequate fading statistics would be very useful. Such a relation does in fact exist. The number of inversion nights per month in Stuttgart (see chapter 4.1) and the number of fading nights at the aforementioned link between Hambach and Darmstadt (Fig. 11) were compared. This was done in some periods of the years 1964 - 1967. Overall measurements of twenty months were evaluated. The correlogram is shown in Fig. 12. The correlation coefficient is $r = .872$. When Z_i is the number of inversion nights and Z_s the number of fading nights, the linear regression function is given by

$$Z_s = 1.1 Z_i - 1 \quad (4.1)$$

The numbers of fading nights and inversion nights are almost identical. These are rather good results for Stuttgart is about 100 km off the center of the radio link.

4.3 Shift of the radio horizon

The effect of the radio horizon shifted by temperature inversions can be well observed on a link, where the ray from the transmitter to the receiver, calculated at the median value $\beta = .118$ ($k = 4/3$ in equation (9)) just touches the ground or an obstacle. This condition is found on the 125 km Merkur-Darmstadt link. The profile is shown in Fig. 13. The frequency is 6.8 GHz. Two examples of the diurnal attenuation pattern are given in Fig. 14.

During the day the attenuation relative to free space is about 20 dB. Some times in the evening and during the night, when inversion layers are found, the attenuation is much lower. When β grows to values, where both the direct ray is free and the first Fresnel zone, multipath fading may occur as evident from Fig. 14b.

4.4 Defocussing effects

On links up to 70 km in length defocussing causes only a small decrease in the field strength as may be seen in chapter 3.3. On long links, however, the effect is well observable. Defocussing attenuation is mostly found in the evening before sunset. Fig. 9b shows one of the examples found on a line-of-sight link. The link from Hornisgründe to Feldberg/Taunus has a length of 180 km, the frequency is 6 GHz. The defocussing effect is clearly different from the multipath fading in Fig. 9a and at the end of Fig. 9b. At 18 o'clock the attenuation reaches a maximum of about 15 dB.

5. CONCLUSIONS

As the comparisons with measurements have shown, the presented model of temperature inversion layers can be used to explain wave propagation effects not only qualitatively but to some extent quantitatively as well. Simplifications of this model are the break in the refractive modulus slope at the surface of the inversion layer and the omission of the isothermic part. The break prevents the calculation of some defocussing effects. The isothermic part of the temperature slope should be taken into account for more detailed fading statistics.

In spite of this lack, the model provides the possibility of forecasting fading statistics (Fehlhaber, L., 1, 1976) and of estimating the influence of line-geometry on these statistics (Fehlhaber, L., 2, 1976).

6. REFERENCES

1. Großkopf, J., Fehlhaber, L.: Feldstärke- und Schwundbeobachtungen auf Landstrecken mit optischer Sicht im dm- und cm-Wellenbereich, Techn. Ber. des FTZ Nr. 5577 vom 15. 8. 1963.
2. Großkopf, J., Fehlhaber, L.: Zur Deutung der Schwunderscheinungen auf Sichtstrecken im dm- und cm-Wellenbereich, Techn. Ber. des FTZ Nr. 5578 vom 1. 4. 1965.

3. Fehlhaber, L., 1: Einfluß nächtlicher Strahlungsinversionen auf die Ausbreitung von Mikrowellen auf Sichtstrecken, Techn. Ber. des Forschungsinstituts der DBP beim FTZ, 455 TBr 58 vom Februar 1976.
4. Ahrens, D.: Feuchte- und Temperatursondierungen in der bodennahen Atmosphäre über Mannheim, Meteorol. R. 28 (1975), 129 - 138.
5. Fehlhaber, L., : Zweiwegeausbreitung im Richtfunk auf Funkfeldern mit direkter Sicht und freier erster Fresnelzone, Techn. Ber. des FTZ, A 455 TBr 27 vom Juni 1970.
6. Fehlhaber, L., 2: Einfluß der Streckengeometrie auf den Schwund auf Richtfunkfeldern mit Sichtverbindung, Techn. Ber. des Forschungsinstituts der DBP beim FTZ, 455 TBr 59 vom Februar 1976.

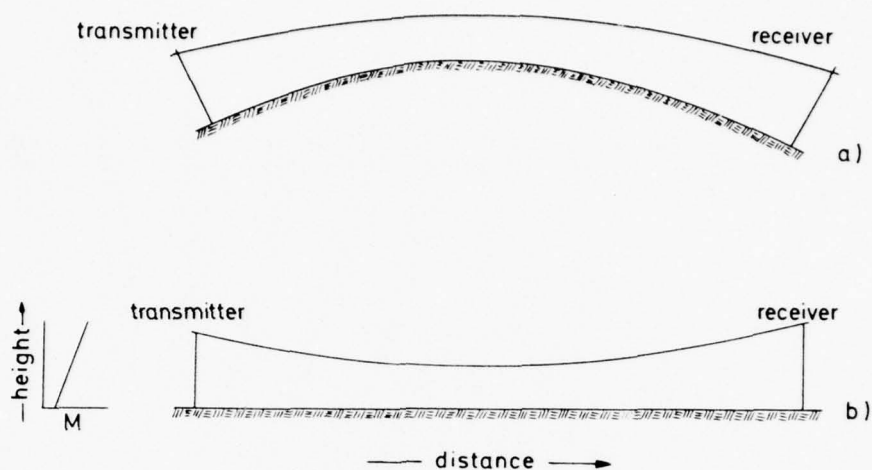


Fig. 1 Radio beam of a line-of-sight link
 a) above the spherical earth
 b) when the earth is transformed into a plane

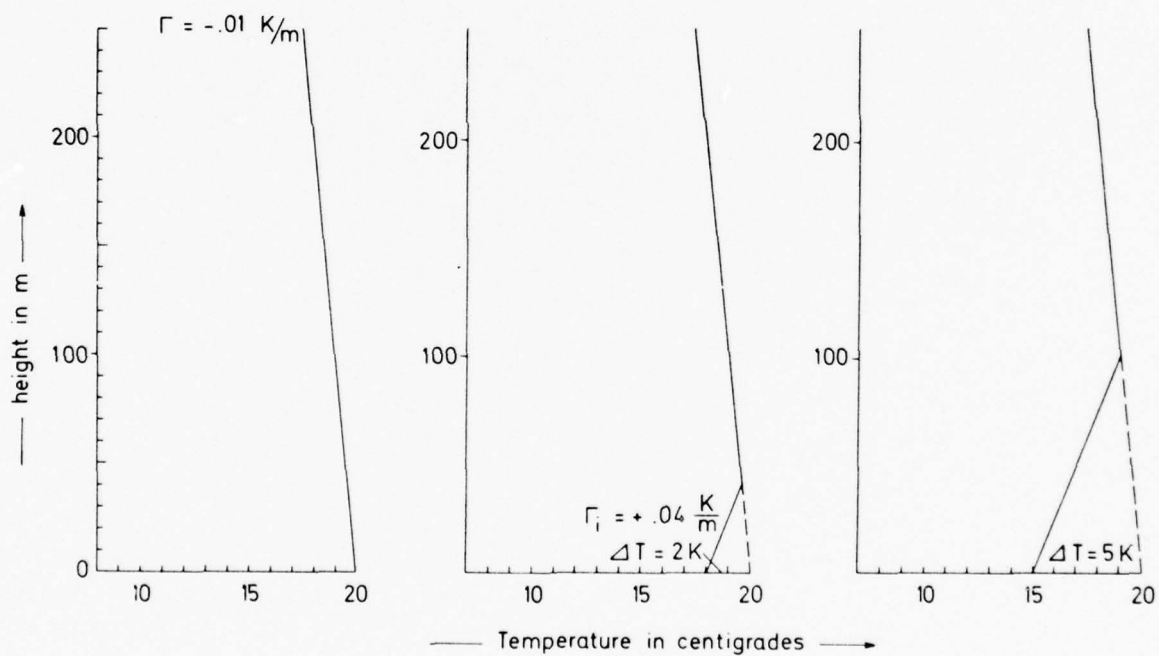
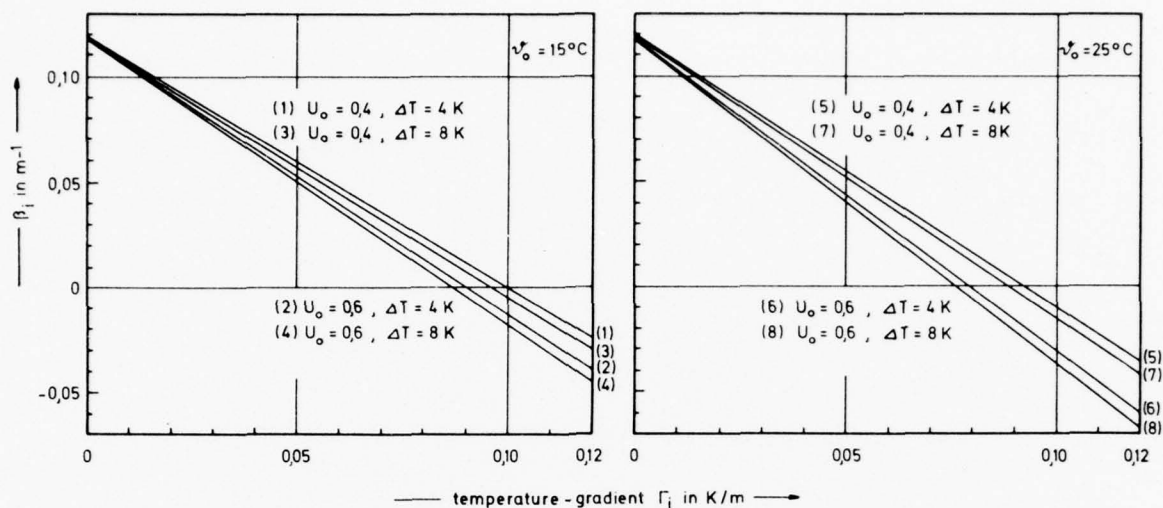
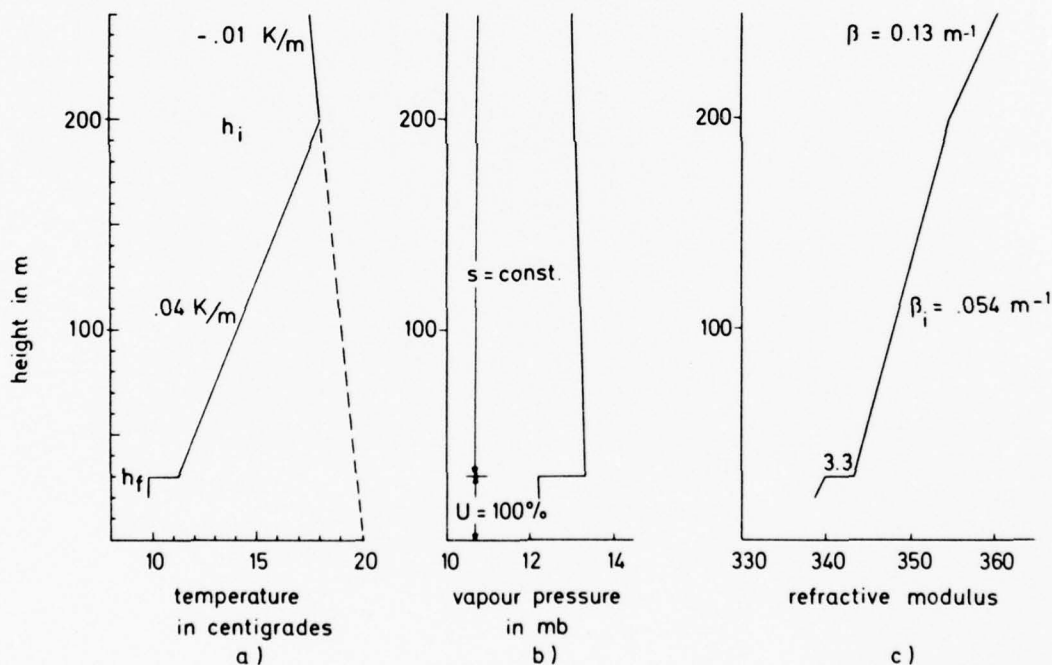


Fig. 2 Development of the inversion layer as long as the saturation point is not exceeded

Fig. 3 M-gradient β in the inversion layerFig. 4 Temperature, vapour pressure and refractive modulus in the inversion-layer (h_i) and the saturated layer (h_f)

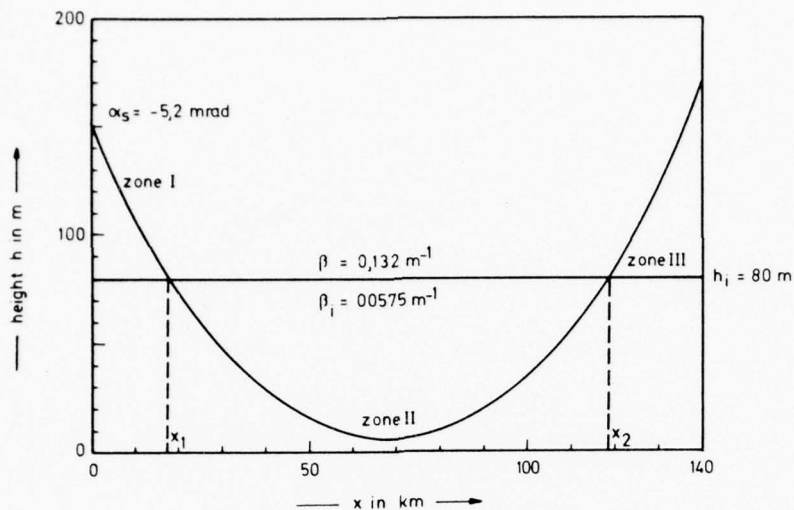


Fig. 5 A ray passing two layers with different M-gradients

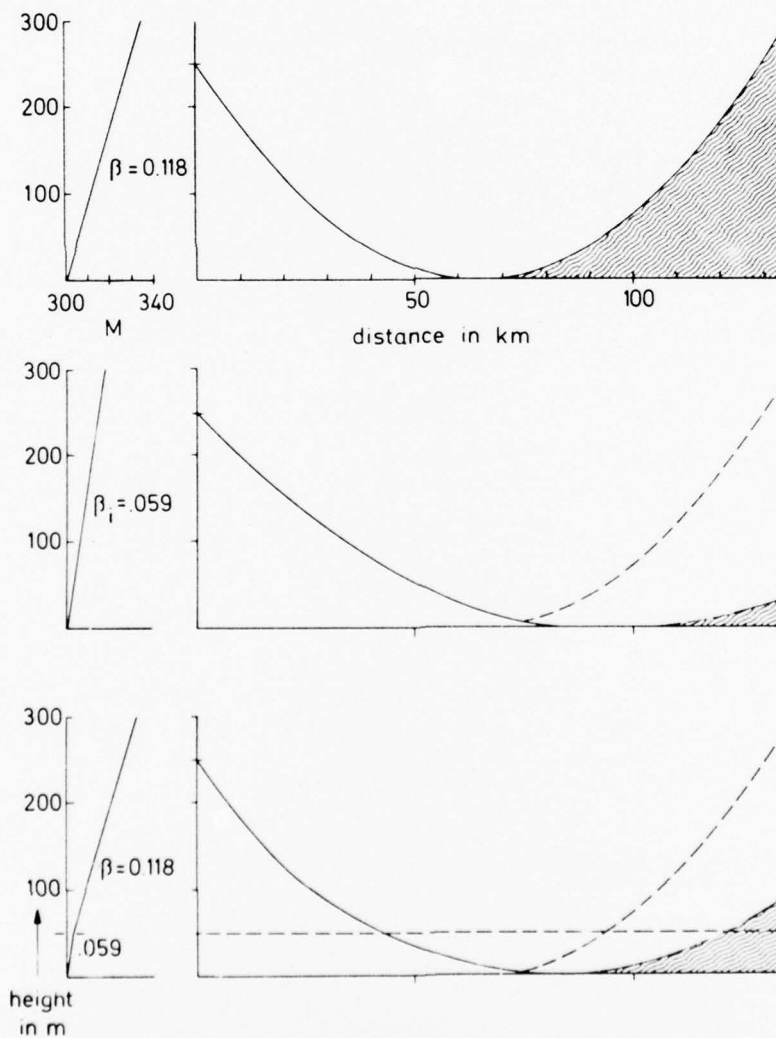


Fig. 6 Shift of the radio horizon when the inversion layer is higher than the transmitter station and when it is much lower

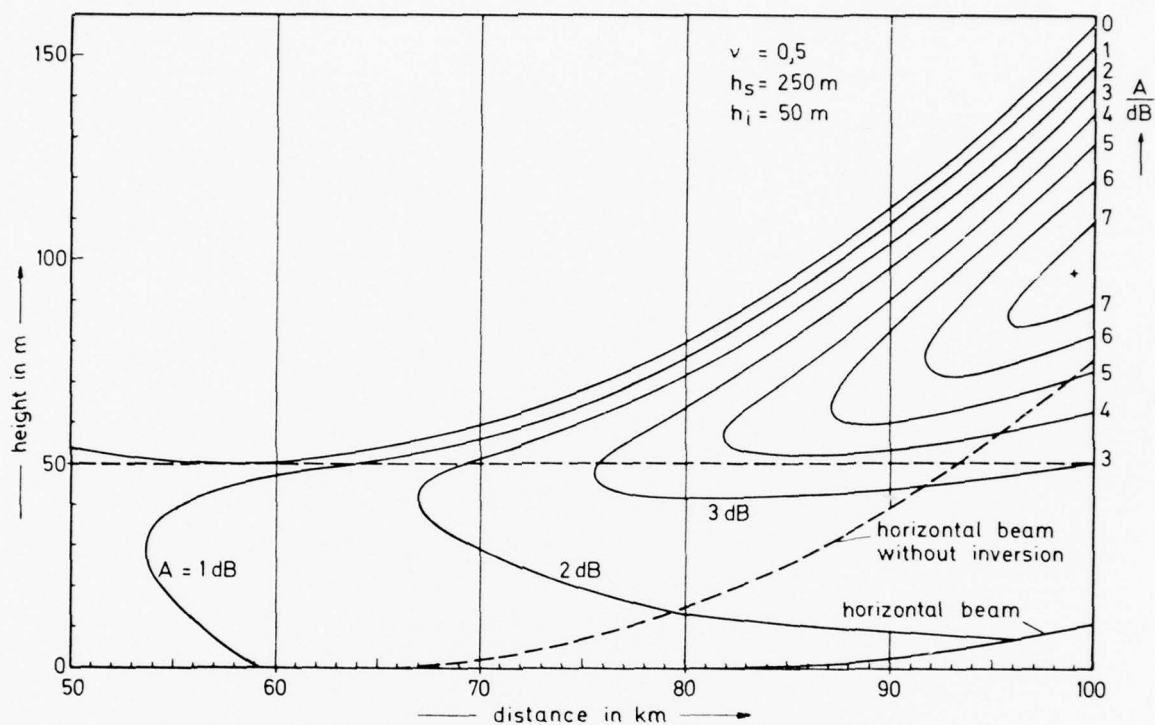


Fig. 7 Defocussing effect of an inversion layer lower than the transmitter station

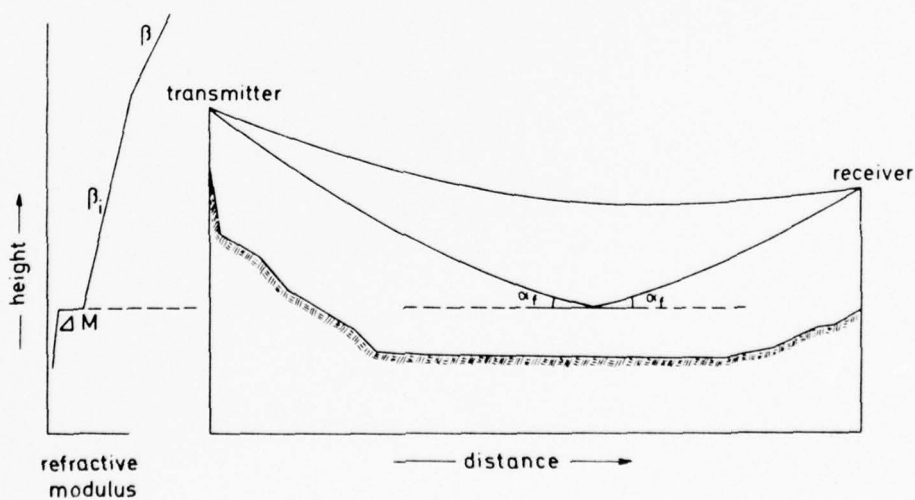


Fig. 8 Two path propagation in an atmosphere with a discontinuity in the M-slope

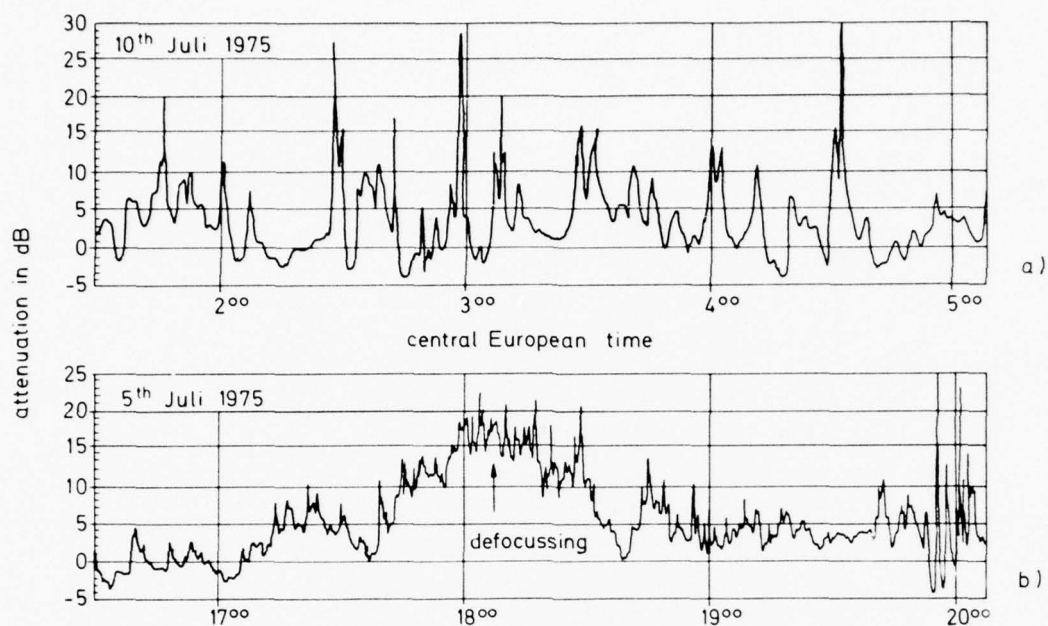


Fig. 9 Strip chart recordings of the attenuation at the 181 km line-of-sight link Hornisgrinde - Feldberg, $f = 6$ GHz

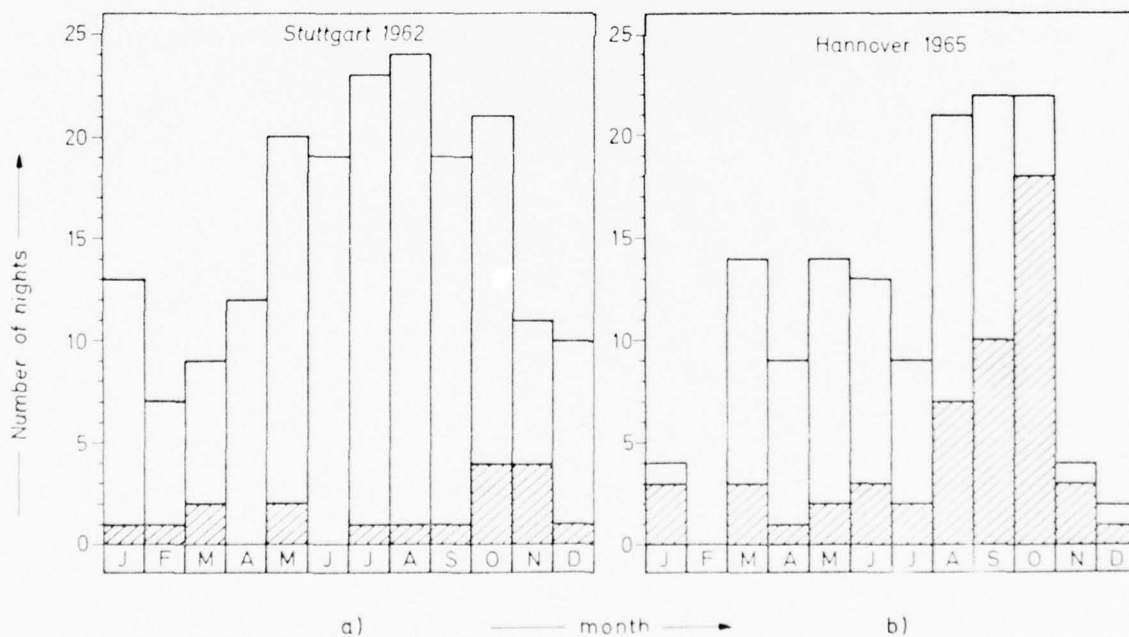


Fig. 10 Number of nights per month when a ground based inversion layer (white) or a moist saturated layer respectively (hatched) was found during balloon ascents at 1.00 o'clock central European time in Stuttgart and Hannover

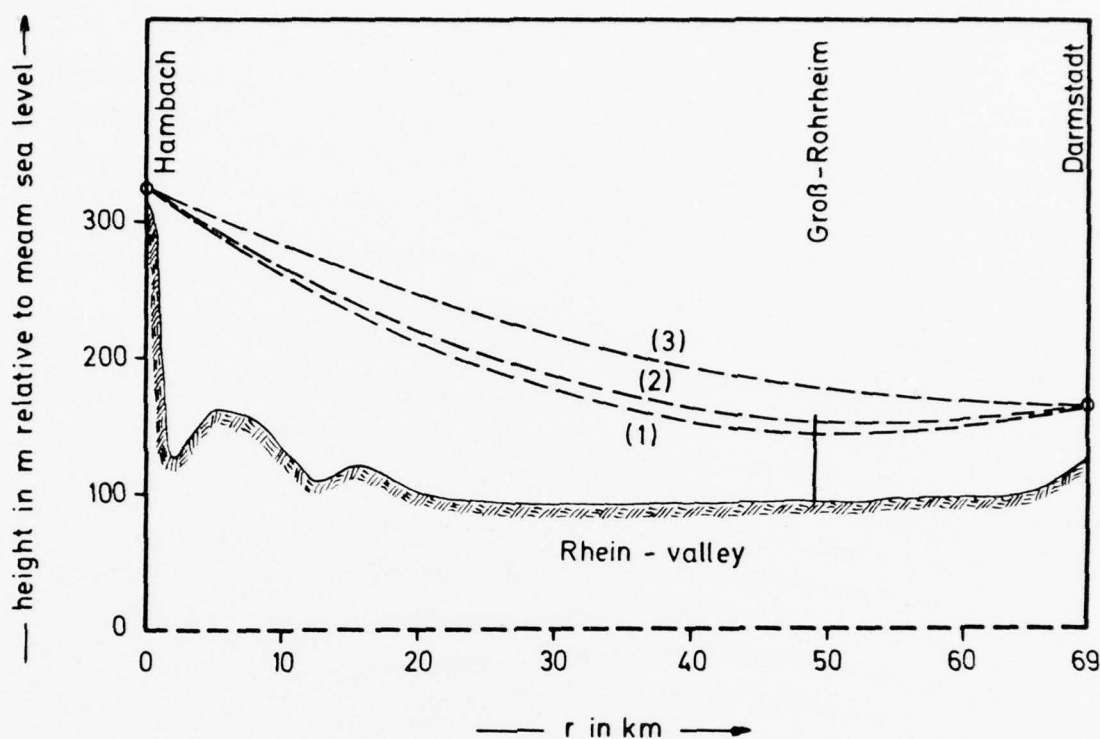


Fig. 11 Profile of the Hambach-Darmstadt link, direct ray at (1) $\beta = .132 \text{ m}^{-1}$
 (2) $\beta = .118 \text{ m}^{-1}$ (3) $\beta = .066 \text{ m}^{-1}$

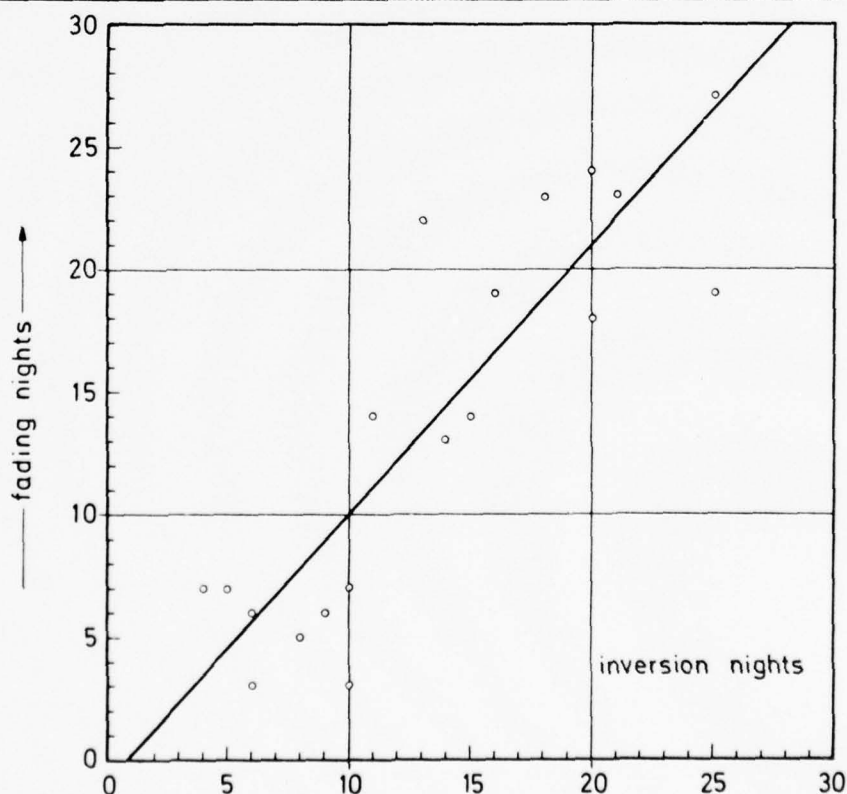


Fig. 12 Correlogram of the inversion nights in Stuttgart and the fading nights at the Hambach - Darmstadt link

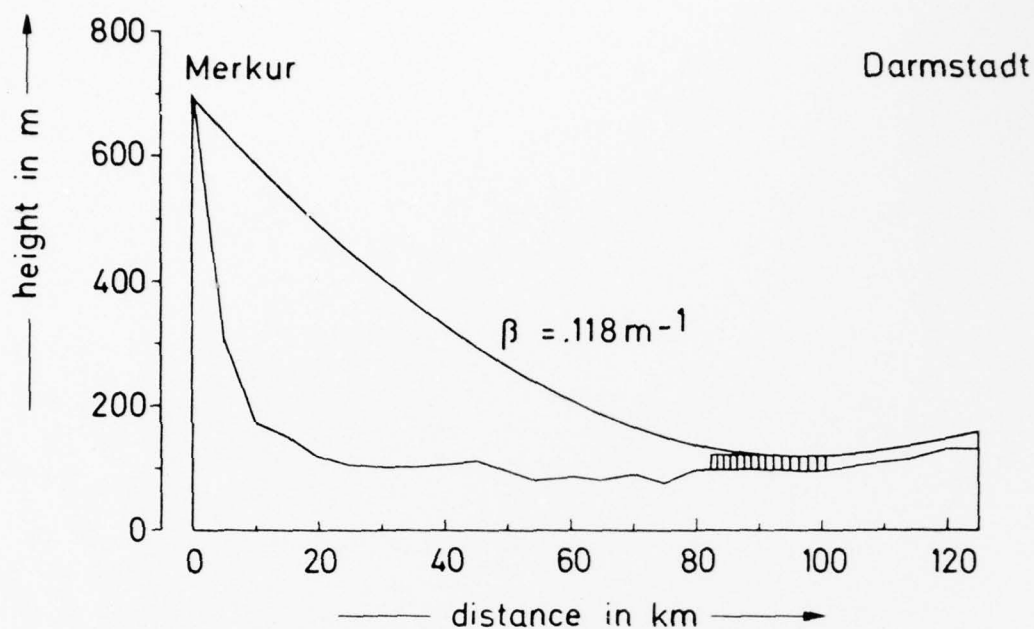


Fig. 13 Profile of the Merkur - Darmstadt link, $f = 6.8 \text{ GHz}$

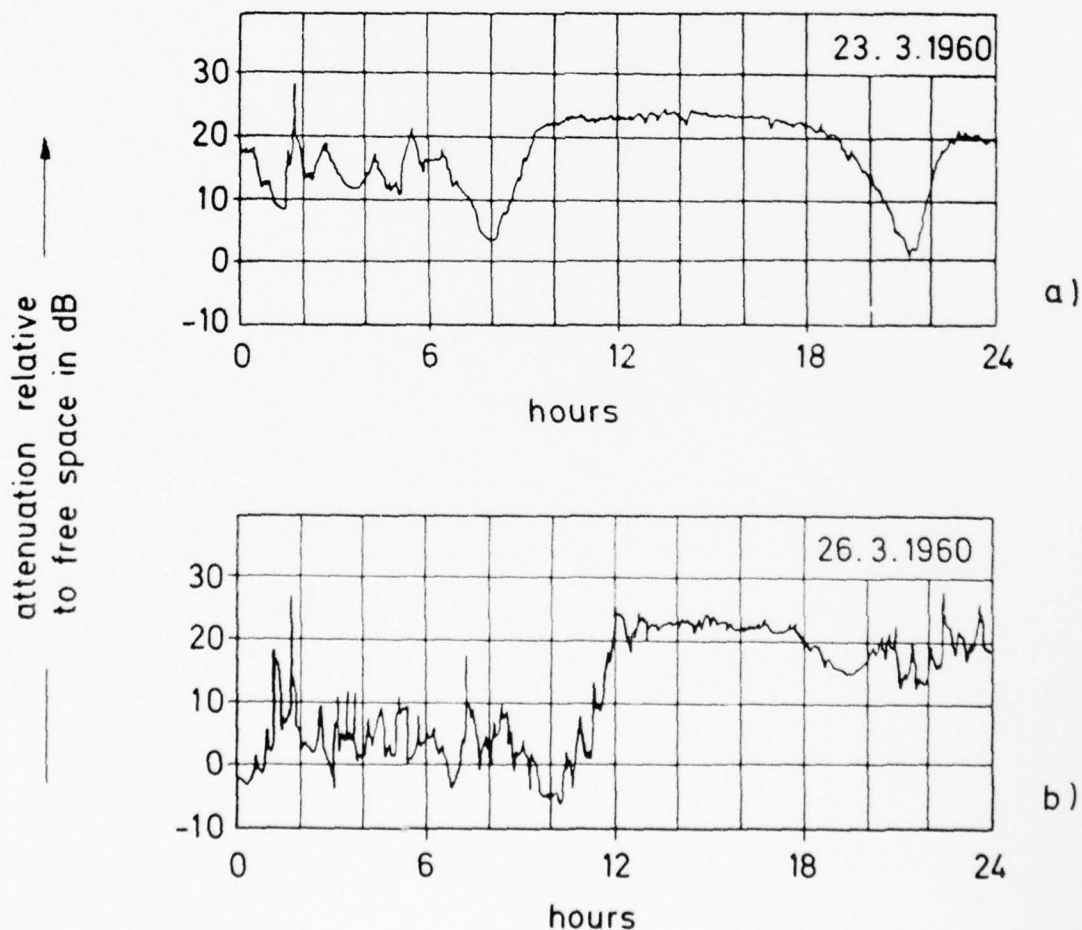


Fig. 14 Diurnal attenuation patterns of the Merkur - Darmstadt link with effects of shifted radio horizon

DISCUSSION

J.S.Belrose: In your pictorial sketch illustrating propagation employing elevated transmitters and receivers you show the direct path concave down rather than the actual path which is concave up. Why do you employ this representation for the ray path?

Further, you interpret the signal fading to result from an interference between the direct path and a path reflected from an inversion layer. How do you differentiate between this latter path and the more usual ground-reflected path which you do not seem to have taken into account? Is the ground so rough at SHE that it is not a good reflector?

H.G.Giloi: A concave ray path above the spherical earth is not easy to handle. Normally we use a straight ray above an earth with a radius $k r_e$. This is a good way when dm/dh is constant. But here dm/dh is a function of height. I should use different values of $k r_e$ to have straight ray paths in the different layers. So this is the best way of transforming the spherical earth into a plane and the concave down path into a concave up path. In all figures the distance in height between ray and ground is the same at appropriate points.

Most objects on the ground are larger if compared to the wavelength of about 5 cm in our experiments so the ground is indeed too rough to be a good reflector. Low echoes from houses, rocks, etc. do not cause remarkable phase interference. But when their time delay is very great (more than 10 ns), they may cause intermodulation noise. This noise can be measured when no fading occurs.

H.J.Albrecht: In referring to the variation of the so-called "k-factor", H.G.Giloi described the behaviour of this calculation aid (based on dn/dh) with a disturbed and an undisturbed tropospheric propagation medium.

H.G.Giloi: The k-factor has a median value of 1.34. According to the lower values of dn/dh in an inversion layer, the values are much higher, k may become infinite, also negative values are possible.

V.Böhm: The data given by the author were derived from 6 GHz-links. How do data from links at other frequencies (e.g., 2,4, or 8 GHz) compare with these?

H.G.Giloi: Measurements were also performed at 4,8,9, and 12 GHz. Up to 10 GHz multipath propagation is the only reason for deep fading in line-of-sight links. In the mentioned range of frequencies the distribution of fading does not vary. At higher frequencies rain attenuation becomes also important.

EXPERIMENTAL RESULTS CONCERNING THE INFLUENCE OF WAVE PROPAGATION ON TELEMETRY DATA TRANSMISSIONS AT 230 MHz COMPARED

WITH 2,3 GHz

G. V. Mayer
DFVLR-GSOC
8031 Oberpfaffenhofen
West Germany

ABSTRACT

The data transmission in the VHF- and UHF band from surface vehicles to a fixed receiving station is studied by experiments in different kinds of terrain.

In broadband systems, as used for telemetry, it is necessary to compare not only the received Signal Power but also to add another criteria for the transmission quality, e.g. the bit error rate in digital systems.

Thus a digital pulse code modulated data stream is simultaneously transmitted in both bands. The signal strength and the missed frame synchronization words of both data links are recorded on paper tapes for a quicklook analysis. A magnetic type is produced for a computer comparison of each piece of information (bit) with the known transmitted bitpattern. The bit error rate per data frame of both systems may be then correlated.

1. INTRODUCTION

Data transmission from space and surface vehicles to fixed receiving station have switched within the last few year from the P-Band range of frequencies (210 - 260 MHz) up to the S-Band (2200 - 2300 MHz).

The reason was the increase of data rate, requiring greater transmission bandwidth and the rising problems with interference with other users, e.g. military UHF-services.

Thus the range commanders council controlling the range services as defined in the IRIG (Inter Range Instrumentation Group) standard deleted the further operation in P-Band.

The change in frequency raised no real problems for space operations as normally free space propagation on the link calculation was applicable.

Table 1 gives an estimate on the received signal power and the noise performance on both bands.

Tab.1: Free Space Propagation

Received Signal Power

$$P_R = \bar{p} \cdot A = \frac{E^2}{120\pi} \cdot A = \frac{P_T \cdot G_T}{4\pi R^2} \cdot \frac{\lambda \cdot G_R}{4\pi}$$

P_T ...transmitted power

R ...distance from transmitting to receiving site

\bar{p} ...power density at the receiving antenna

A ...effective aerea of the receiving antenna

G_T, G_R ...gain of the transmitting resp. receiving antenna

λ, f ...wavelength resp. frequency of operation

P_R ...power at the receiving antenna

P-Band	47,23 dB	20 dB
	$P_R = 32,45 - 20 \log R_{km} - 20 \log f_{MHz} + P_T + G_T + G_R$	dBm
S-Band	67,23 dB	34 dB
	effective antenna aperture lower	rec. antenna gain higher

System Noise

$$N = B \cdot N_0 = K \cdot T \cdot B$$

K ...Boltzmanns constant

B ...bandwidth

N_0 ...power density

T ...noise temperature

P-Band	$1000^\circ K = 30 \text{ dB}$
	$N = -198,6 + 10 \log B_{Hz} + 10 \log T_{OK}$
S-Band	$300^\circ K = 24 \text{ dB} - \text{solar and galactic noise lower}$

In S-Band the loss in effective antenna aperture is partly compensated by the higher gain achievable with an antenna of similar dimensions and partly by the lower temperature of solar and galactic noise at the higher frequency.

Unfortunately with data transmissions from surface vehicles this was not the case; the influence of the topography, buildings or even vegetation, or nearby ships in sea operations, required a new approach to make allowance for these environmental factors.

2. Surface Propagation

Wave propagation along earth surface is mainly influenced by
 quality of soil (conductivity and dielectric constant)
 topography
 vegetation

When the antennas of the transmission line are positioned in a certain height above ground, secondary effects like

reflection
 defraction
 depolarization
 scattering

may be predominant, especially at higher frequencies.

Tab. 2 shows a possible theoretical way of estimating the field strength of surface transmission at any quality of ground and low angles of radiation.

Tab.2: Surface propagation, theoretical approach

Field strength E_0 of a
 Short dipole over ground with infinite conductivity *

$$E_0 \left(\frac{\text{mV}}{\text{m}} \right) = \frac{300 \sqrt{P} (\text{KW})}{d (\text{km})}$$

Reflection coefficient R at elevated transmitting and receiving antenna and low angle of incidence φ of the irregular ray and $|\epsilon_R| \gg 1$

$$\underline{R} = \frac{\sin \varphi - \sqrt{\epsilon_R}}{\sin \varphi + \sqrt{\epsilon_R}}$$

$$\frac{C_V}{\epsilon_R} \approx \frac{1}{\epsilon_R} \quad \text{for vertical polarization}$$

$$\frac{C_H}{\epsilon_R} \approx \epsilon_R \quad \text{for horizontal polarization}$$

$$\epsilon_R = \epsilon_R - j60 \times \lambda \quad \text{komplex dielectric constant of ground}$$

At any quality of ground and low angle of radiation

$$E = E_0 \cdot \frac{\lambda}{\pi d C} \left(1 - j \frac{2\pi h_t}{\lambda} \cdot \sqrt{\epsilon_R} \right) \left(1 - \frac{2\pi h_e}{\lambda} \cdot \sqrt{\epsilon_R} \right)$$

Sommerfeld height factors
attenuation

d ... distance between transmitting and receiving antenna

h_t ... height of transmitting antenna

h_e ... height of receiving antenna

The influence of the ground profile and the vegetation (predominating at high frequencies) could be included into the ground conductivity $\kappa(1)$.

The basic equation of a vertical short dipole over a flat surface with infinitive conductance is multiplied by an attenuation factor and height factors of each antenna, both a function of the complex dielectric constant.

This allows a calculation of the field strength with respect to the quality of soil and the reflected wave superposed to the direct wave.

At frequencies in the UHF range the influence of the ground profile (roughness) and the vegetation is predominant.

Attempts have been made to include both factors into the effective conductance, but in the end an estimate of the received power or field strength may not be adaptable to the expected data quality of the transmission.

In both, analog and digital data streams reflections may introduce a significant amount of distortion.

As indicated in Tab. 2 the reflection coefficient R is frequency dependent. Therefore at wideband transmissions such as in telemetry applications the superposition of the direct wave with the sum of the reflected energy at the receiving antenna may cause a significant spectral distortion of the signal, even when the sum of received power is reasonably high.

It was thought better to compare the performance of data transmission within both bands by experiment.

The idea to do this came from colleagues who had been given the task to make tests with tracked vehicles using S-Band equipment while driving through forested areas in order to study propagation on S-Band.

3. Mobile Surface Telemetry

Data transmission via telemetry from moving surface vehicles like

- trains
- automobiles
- tracked vehicles
- boats
- buoys
- sounds
- probes

also from human beings and animals is gaining more interest in the fields

- evaluation of vehicle performances
- environmental research
- biomedical engineering.

Optimisation of the transmission link is normally limited by the small height of the vehicle antenna over ground with the result that the transmission path follows a low angle of elevation. Furthermore the type of antenna, the antenna construction and the possible maximum transmitting power are a function of the vehicle dimensions and the duration of the mission itself.

The quality of the transmission is estimated by the received signal power to noise power ratio and the performance of transmitted data.

The data quality may be easily determined by computer, when a digital kind of transmission e.g. Pulse Code Modulation (PCM) is applied. PCM is the most attractive kind for telemetry applications, giving high accuracy and an extensive immunity to noise and interference.

The criteria for transmission quality is the bit error rate. For a test of a PCM system a simulated frame pattern including synchronization and data words is used to modulate the transmitter. After passage through the propagation path and the receiving station each detected binary information (bit) is compared to the originally generated message. The errors per time unit may be counted and registered (2,3).

4. Experiments

The influence of the surface propagation on the signal stream is studied by a simultaneous telemetry transmission in P- and S-Band. Fig. 1 shows the block diagram of the experimental set up.

In the vehicles board system a binary PCM test pattern of known sequence is generated, which modulates both, a P- and a S-Band transmitter. The signals cross the propagation path to the receiving station. After reception and demodulation the (distorted) PCM data stream is regenerated by a bit synchronizer and then decoded by the decommutator. The bit synchronizer has to decide whether the momentary status of the binary signal is high or low. These limits are specified for a certain range of signal distortion, e.g. caused by the propagation path. Above these limits the bit error rate will rise significantly.

For a quicklook the number of missed frame synchronization words per time unit is counted and recorded, together with the automatic gain control (AGC) of the receiver, which is a measure for the strength of the received power. The PCM data and the AGC are recorded on an analogue tape for a later computer processing, where each bit of information is analyzed. Attenuators in front of the receivers are used to calibrate both signal levels before starting the experiment. The spectrum analyzer is used to set an equal modulation index on both transmitters. Tab.3 notes the most important system parameters.

Tab.3: Experimental System

- Frequencies $f_1 = 230 \text{ MHz}$ $f_2/f_1 \approx 10$
 $f_2 = 2250 \text{ MHz}$

- Vehicle Transmitting Antennas

$\lambda/2$ - Dipole (vertical, horizontal)
1,5m over ground

- Antennas of fixed Receiving Station (Medium Gain), 7m over ground

- Yagi (p-Band)

- Horn (S-Band)

- Data Coding and Transmission

PCM
240 KB/s
34 words/frame
12 bit/word
2 words/sync.pattern
Biphase
Premod. Filter
Modulation Index $m = 1,8$

Main points of the experimental program were:

propagation in flat, undisturbed terrain (optical sight)
deflection due to a large obstacle
influence of vegetation (forrest)
propagation over water surface
influence of polarization.

5. First results

Some typical examples are selected from a number of actual recordings. Fig. 2 demonstrates the passing of a vehicle at a constant distance behind a large hangar. Note the total signal drop out of the higher frequency (S-Band) signal and a modest attenuation on the P-Band signal. The basic attenuation on S-Band at a distance of 2 km is more than 20dB higher than at the lower frequency.

In the figures shown α represents the signal-to noise ratio (S/N) of the receiver used.

In Fig.3 shows field strength as a function of distance through a pine-wood (tall trees, ca 15 m). The P-Band signal drops continuously with distance, but the S-Band signal drops quite suddenly in step form within the first 100 meters and remaining with a marginal signal strength after 1 km. The influence of polarization is not noticeable. The height of the receiving antennas was half that of the top of the trees forrest and there was no possibility to study the influence of the lateral wave which skins on top of the forest and penetrates by refraction (4).

Fig. 4 shows part of a transmission over a water surface (lake). The S-Band signal although more attenuated than the P-Band signal shows a lower number of frame sync. losses, registered by the event markers of the recorder. The same effect has been found with propagation over a flat, undisturbed terrain (e.g. grassland).

This somewhat surprising result may be easily interpreted, when one considers that the influence of the surface profile (roughness) is dominant at higher frequencies over the electrical parameters of the soil, ie. conductivity and dielectric constant.

Beckmann and Spizzichino (5) studied the nature of the scattered energy on a model of a sine wave surface profile.

Fig. 5 shows the energy distribution of the scattering products as a function of the roughness, standardized to the wavelength of transmission λ . The wavelength Λ of the sinewave surface is 10λ , the angle of incidence $\gamma = 10^\circ$.

As long as the roughness d/λ is low, the main energy is reflected below an angle equivalent with the angle of incidence. With increasing d/λ the main part of energy is scattered away toward higher angles of elevation, so having no chance to interfere with the direct wave at the receiving antenna. Note, that d/λ is 10 times higher on S-Band, so it is understandable, that the influence of surface on the data is lower at these higher frequencies.

Tab.4 gives a survey over the first results of the experiments.

A computer comparison of each piece of information is not yet completed.

Fig. 6 to 8 illustrate the measurement equipment on the vehicles and the receiving station.

Tab.4: First ResultsIn flat terrain (optical sight)

S-Band: Signal attenuation higher.
Data quality higher than P-Band transmission, no noticeable function of polarization.

P-Band: Horizontal polarization gives better performance than vertical

Defraction due to obstacles (buidings)

S-Band: very poor, total signal drop out
P-Band: signal attenuated, but no drop out

Propagation in Forest

S-Band: signal attenuation higher than P-Band ($\propto f^3$), independent of polarization.
Statistical data evaluation not yet completed.

Propagation over Water Surface

S-Band: Data quality higher at vertical polarization compared with S-Band horizontal and P-Band.

P-Band: higher quality at horizontal polarization compared with P-Band vertical, signal attenuation less than S-Band, independent of polarization.

5. Conclusions

As long as optical sight is guaranteed, the data stream transmitted under a low angle of elevation in S-Band is more immune to interferences by reflections although the signal attenuation is higher than in P-Band.

As the effect of land surface roughness is ten times higher in S-Band than in P-Band the most part of reflected energy is scattered away towards higher angles of elevation.

Thus the direct ray is not so much effected by reflections.

The use of S-Band in forest and open country with larger buildings is very restricted to small distances.

Further experiments are planned with circular polarization and different digital codes of transmission.

References:

- (1) Großkopf, 1970, Wellenausbreitung, BI Hochschultaschenbücher, Band 141
- (2) IRIG, 1975, Test Methods for Telemetry Systems and Subsystems, Document 118-75, Range Commanders Council WSMR.
- (3) Mayer, 1975, Fundamentals of Radio Telemetry, Lecture of AGARD/Cranfield Flight Test Instrumentation Course, AGARDograph No. 160, suppl.
- (4) Tamir, 1974, Mixed Path Considerations for Radio Waves in Forest Environments, AGARD Conference Proceedings Nr. 144.
- (5) Beckmann, Spizzichino, 1963, The Scattering of Electromagnetic Waves from Rough Surfaces, Pergamon Press.

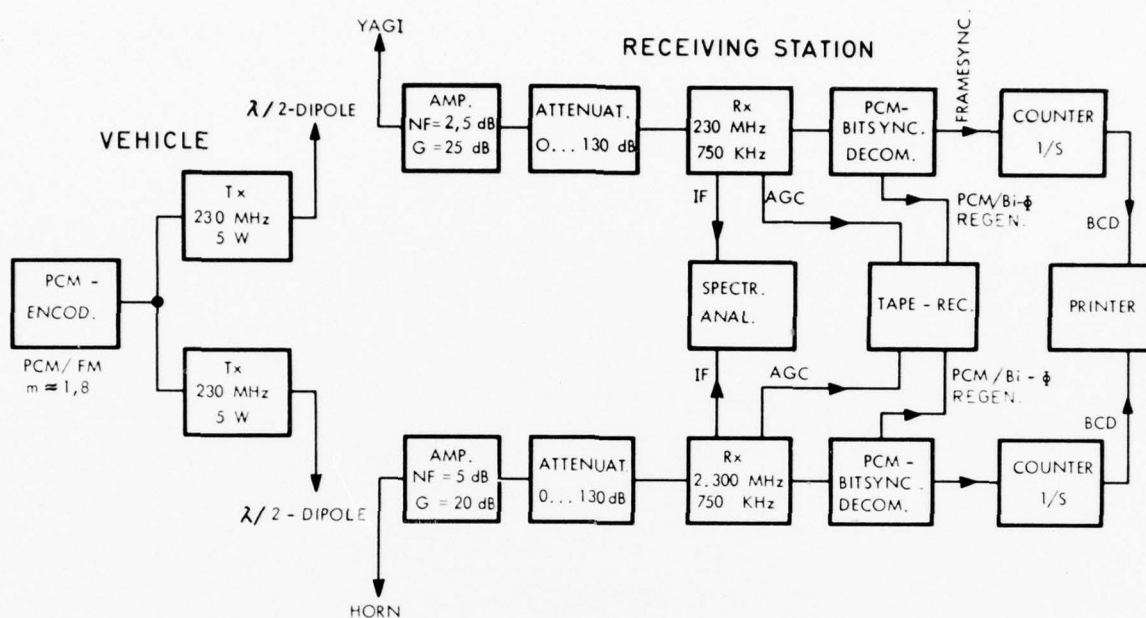


Fig. 1 Experimental set up for surfaces telemetry transmissions

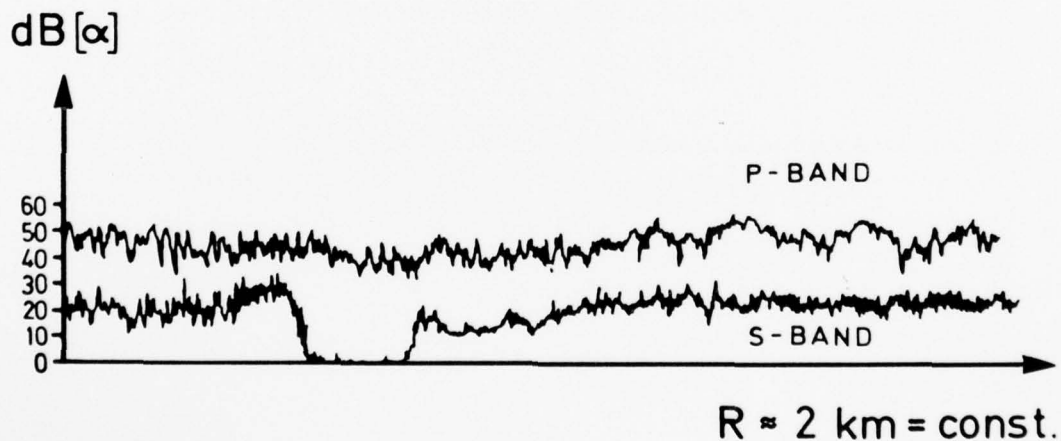


Fig. 2 Telemetry transmission behind a large obstacle

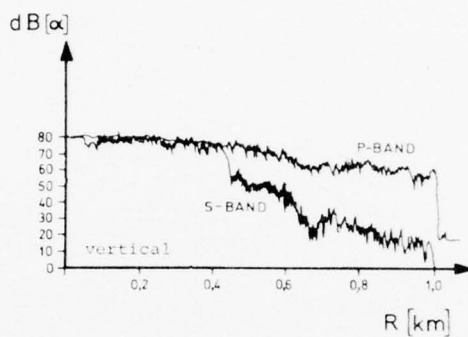
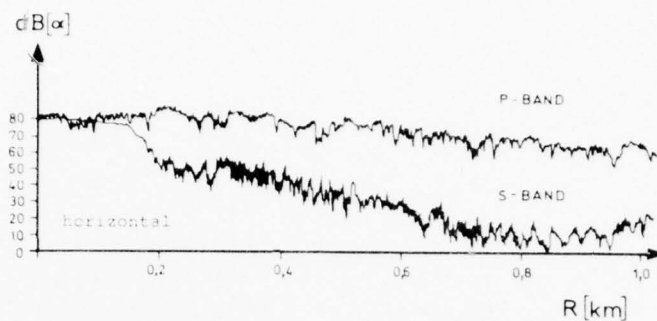


Fig. 3 Telemetry transmission in forest

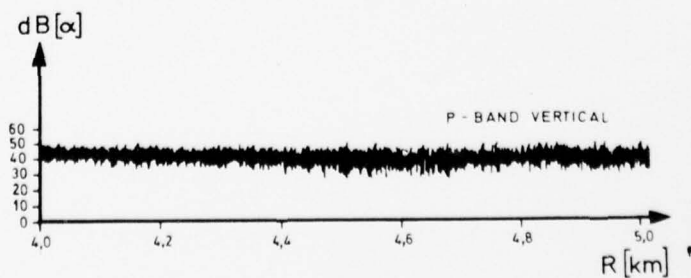
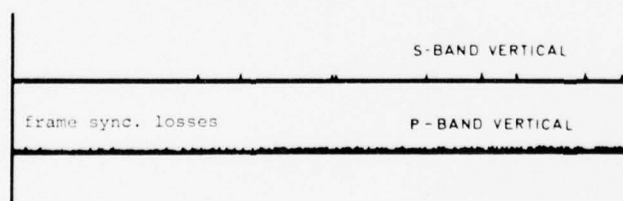
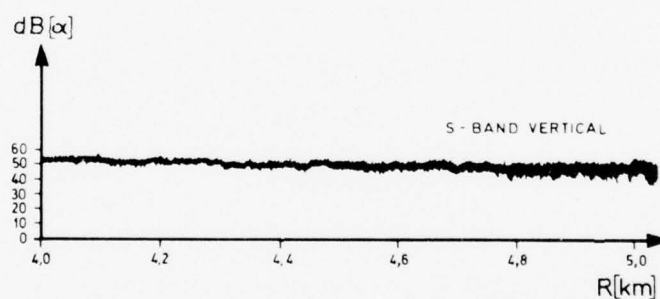


Fig. 4 Telemetry transmission over water surface

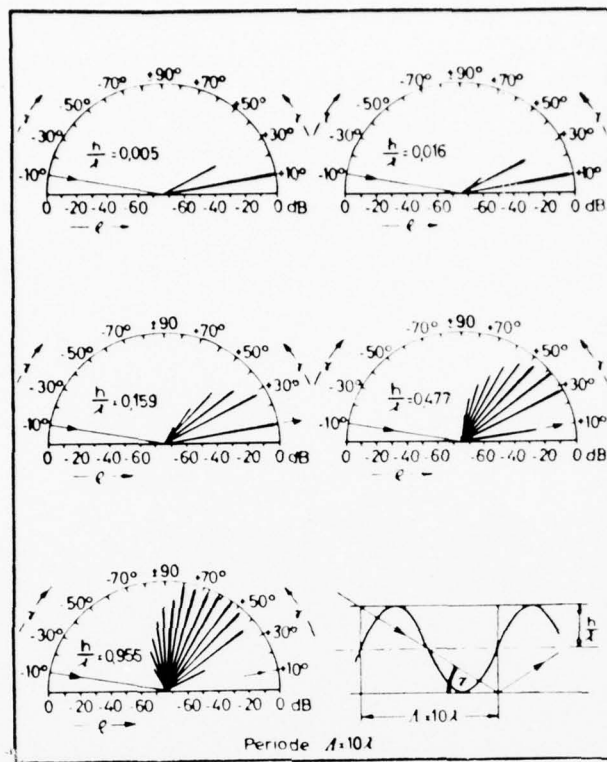


Fig. 5 Scattering on sinewave surface



Fig. 6 Vehicle transmission unit with horizontal polarized antennas on top of a car



Fig. 7 Vehicle transmission unit with vertical polarized antennas on a motor-boat.



Fig. 8 Fixed station vehicle with medium gain receiving antennas.

DISCUSSION

H. Sepp: You told us in your introduction that the reflection factor is an important point if the influence of wave propagation is concerned. Can you give us some figure about the maximum reflection factor which is to be expected over sea and ground without and with vegetation?

G.V. Mayer: Reflection coefficients under a low angle of elevation are almost independent of the quality of soil. For plain surface $R = -1$; this means that the amplitude of the reflected wave is not attenuated, the phase, however, is shifted by 180 degrees. Introducing roughness on the surface, the amplitude is attenuated depending on the relative height h/λ of the roughness profile. In S-band ($\lambda = 13$ cm), for example, the attenuation on a sine wave profile for h/λ approximately equal to 0.5, is more than 20 dB.

It is not easy to measure R by experiment, as at a receiving site with simple methods only the integral effect (reflection from an unknown number of reflection points) may be determined.

H.J. Albrecht: Considering the three main categories of possible terrain, viz., plane, hilly, and mountainous terrain, would your measurements be adequate in quantity to be representative of any one category?

G.V. Mayer: We concentrated our activities to get information about propagation over sea and over flat terrain with vegetation to support future military and civil research and evaluation programs which employ S-band telemetry from boats, buoys and tracked vehicles. Measurements in hilly and mountainous terrain will possibly follow in case there is a future application in such terrain.

L.B. Felsen: You mentioned that some of your data involve propagation from undisturbed terrain into a forest environment. Did you carry out an interpretation of the data, and if so, did you find it necessary to take into account the lateral wave which skims on top of the forest and penetrates by refraction?

G.V. Mayer: Interpretation of the data is not yet completed due to a computer exchange in our research center which was a factor of delays. It is hoped to include the results into the AGARD publication of the meeting.

We know of an earlier AGARD paper which describes the lateral wave propagation on top of the forest and we hope to get experimental data about it, when our hardware is prepared to do this.

SPECULATIONS ON MEDIA INTERFACES WITH INTERESTING
ELF COMMUNICATIONS

Giorgio Tacconi*
MARIPERMAN, LA SPEZIA
and
UNIVERSITY OF GENOVA
ITALY

SUMMARY

Ionosphere, atmosphere, oceans, earth's crust, etc., represent, in the main, a set of layers with different electrical properties. In this paper the influences of structures and behaviours of different layers on ELF communications will be examined and some theoretical approaches to propagation will be reviewed, taking into account certain methodologies assessed for a particular transmission channel, i.e. the acoustic channel.

1. INTRODUCTION

Surfaces, interfaces, layers — these very general expressions are interpreted as follows: the surface is an abstract geometrical concept; the interface is a surface of separation between two propagating media; the layer is a region delimited by two interfaces. From a physical point of view and, in particular, for telecommunications when a boundary is considered, it has to be regarded as being in one of the three physical aspects mentioned above, which respectively imply a variety of parametric considerations that cannot be ignored and that depend, of course, on the required definition. In the concept of propagation, the transference of "something" from one point in a space to another is implicit; "something" may be matter, or energy, or information, or all three together.

The basic formal mathematical approach for electromagnetic propagation and for acoustic (elastic waves) propagation is the same, and in both cases the behaviour and the structure of interfaces affect the propagation or, more precisely, the signal that has to be transmitted and received. In principle, it is impossible to disregard telecommunication problems from any physical measurement, since any type of measurement can be considered as a sort of non- or quasi-semantic communication, or a unidirectional communication; passive detection is also the same type of communication. In a physical measurement the information at the receiver is somehow produced by making a comparison between the received signal and the originating physical phenomenon, whereas in telecommunications the comparison is made between the received signal and the transmitted one. In both cases however, a certain a priori knowledge of the expected signal is required. Many authors have treated the problem of electromagnetic ELF communications (BANOS, 1966; IEEE Trans., 1974; BERNSTEIN et al, 1974; NATO ASI, 1974; TACCONI, 1974; WAIT, 1970; WAIT, 1974). It is well known that electromagnetic perturbations in the ELF range propagate in that particular wave guide which is the earth-ionosphere gap even at circumterrestrial distances. The mathematical approach is identical for any frequency range and the well known formula for the skin depth underlines the physical meaning of the approach:

$$\delta = \sqrt{\frac{2}{\omega \mu \sigma}}$$

where μ is the relative permeability of the medium; in the case of air-sea interface, the medium is the sea water.

ω is the angular frequency.

σ is the electrical conductivity of the sea water.

Electromagnetic ELF propagation presents, with respect to the boundaries, a property of high penetration power (skin depth) which, from the point of view of communication through dispersive media, represents a remarkable advantage. Ionosphere, earth's crust, and the oceans are examples of such media.

* The author who is Professor of Electroacoustics at the University of Genoa is grateful to MARIPERMAN (Italian Navy), La Spezia for its precious cooperation in developing a research programme partially financed by the Italian National Research Council (CNR Rome) Contract No. CT 75.00707.07. The study of this paper was done in the ambit of the above contract.

2. THE ELF TRANSMISSION CHANNEL

The general theory of telecommunications can be used also in the case of electromagnetic ELF links. In general, a transmission channel can be considered as in Fig. 1. The medium is represented in this figure by a block, in the more common cases such a block is considered as a linear filter, in reality the linear-filter analogy represents a drastic and unrealistic simplification. However, the associated filter can take into account the various significative parameters of the medium whatever it is. A very general model of a signal propagating in a medium delimited by two interfaces (Fig. 2) can represent an electromagnetic as well as an acoustic scenario. In this simple model the three effects of surface scattering $S(s)$, bottom scattering $S(b)$, and volume scattering $S(v)$ are combined and, as a consequence of this multiple combination, the signal detected by the receiver is deformed. The deformation of the signal can be summarized in terms of time spreading and of frequency smear and, although this is still a simplification of the problem, it represents a very useful tool for investigating the characteristics of the transmission channel. In the case of electromagnetic propagation between the ionosphere and the earth's surface, the volume scattering of the atmosphere is not taken into consideration, whereas that of the ionosphere and of the earth's surface (the boundaries) must be carefully considered.

Propagation phenomena can be studied in a general way from a purely physical point of view with very little consideration being given to the practical aspects. On the contrary, with telecommunications certain practical parameters such as wave length, range, skin depth values and others, must be carefully considered. In particular, at ELF ranges and with particular sizes of layers, the ray tracing approach, namely the solution of the eikonal equation, is not sufficient to satisfactorily describe the propagation phenomena, an approach in terms of normal modes is required for such a case. In the ELF ranges, the scattering strength of interfaces is not due only to the geometrical structure and fluctuations of boundaries but also, and mainly, to the distribution of some of the physical parameters of the medium on the other side of the boundaries and where the perturbation penetrates, namely the thickness of the skin. The most important of those parameters for electromagnetic propagation is the conductivity σ .

3. SOME ASPECT OF TELECOMMUNICATIONS IN RANDOM MEDIA

As outlined in Fig. 1 the block denominated MEDIUM must include also the effects of the boundaries. Making some assumptions on the properties of the physical parameters, it is possible to assess a model that enables the MEDIUM to be considered as a filter with a certain response. In order to take into account, in the most realistic way, the behaviour of a medium — randomly variant in time and in space — using the filter analogy, it is convenient to summarize starting with the most simple situation. Tables 1, 2, 3, 4 and 5 summarize the formal filter-analogy expression of various aspects of a transmission channel. In Tables 1, 2 and 3 the space characterization is in parenthesis, because the effect of space is not explicitly considered, whereas in Table 4 and 5 space is considered but not time.

TABLE 1

TIME (& SPACE) INVARIANT CHANNEL

$$H(f) = \text{Transfer function}$$

$$h(\tau) = \text{Impulse response} = \mathcal{F}[H(f)]$$

$$\mathcal{F} \text{ is the symbol of Fourier transformation}$$

TABLE 2

TIME VARIANT (& SPACE INVARIANT) CHANNEL

$$H(f, t) : \text{Transfer function}$$

$$h(\tau, t) : \text{Impulse response}$$

$$B(f, \phi) : \text{Bifrequential function} = \mathcal{F}[H(f, t)]$$

$$S(\tau, \phi) : \text{Diffusion function} = \mathcal{F}[h(\tau, t)]$$

The channel described in Table 3 can be represented by means of one of the four functions connected to each other by Fourier transformation and antitransformation (SØSTRAND, 1968; LAVAL, 1972), for instance, the $R_H(f, f', t, t')$ is a function defined in a four dimensional representative space, where \underline{f}' is independent from \underline{f} , and \underline{t}' is independent from \underline{t} .

TABLE 3

TIME RANDOMLY VARIANT (& SPACE INVARIANT) CHANNEL	
$R_H(f, f', t, t')$	$= \overline{H(f, t) H^*(f', t')}$
$R_h(\tau, \tau', t, t')$	$= \overline{H(\tau, t) h^*(\tau', t')}$
$R_B(f, f', \phi, \phi')$	$= \overline{B(f, \phi) B^*(f', \phi')}$
$R_S(\tau, \tau', \phi, \phi')$	$= \overline{S(\tau, \phi) S^*(\tau', \phi')}$
WSSUS	
	$R_H(\Delta f, \Delta t)$
Wide Sense Stationary	$R_h(\tau, \Delta t)$
Uncorrelated Scattering	$R_B(\Delta f, \phi)$
	$R_S(\tau, \phi)$

The function $R_S(\tau, \phi)$ is the scattering function, assuming valid the WSSUS conditions. The convolution of $R_S(\tau, \phi)$ with the ambiguity function of the signal produces a combined ambiguity function of the signal and the medium (GRANDVAUX, 1971).

In the three models represented in Tables 1, 2 and 3, the medium is practically considered uniform and isotropic. Vice versa, assuming the medium time-invariant, and considering only space variations (disuniformities, anisotropies, etc.), the transmission channel can be represented as in Table 4.

TABLE 4

SPACE VARIANT (& TIME INVARIANT) CHANNEL	
$H(f, \bar{x})$	Space Transfer Function
$h(\tau, \bar{x})$	Space Impulse Response
$B(f, U)$	$= \mathcal{F}[H(f, \bar{x})]$ = Space Bifrequential Function
$S(\tau, U)$	$= \mathcal{F}[h(\tau, \bar{x})]$ = Space Diffusion Function
WSSUS Hypothesis
$R_S(\tau', U')$	where $\tau' = \Delta\tau$ and $U' = \Delta U$

Adding time dependance, the model in Table 5 is obtained.

TABLE 5

TIME VARIANT & SPACE VARIANT CHANNEL	
$H(f, t, \bar{x})$	Space-Time Transfer Function
$h(\tau, t, \bar{x})$	Space-Time Impulse Response
$B(f, \phi, \bar{x})$	$= \mathcal{F}_t[H(f, t, \bar{x})]$
$C(\tau, t, U)$	$= \mathcal{F}_{\bar{x}}[h(\tau, t, \bar{x})]$
..... Assuming the WSSUS hypothesis in both time and space, and reducing the spatial variation to two coordinates components \underline{a} , \underline{b} , it will be possible to define a scattering function in four variables: $R_S(\tau, \phi, \underline{a}, \underline{b})$ (WASILJEFF, 1976)	

AD-A044 800

ADVISORY GROUP FOR AEROSPACE RESEARCH AND DEVELOPMENT--ETC F/G 20/14
EM PROPAGATION CHARACTERISTICS OF SURFACE MATERIALS AND INTERFA--ETC(U)
JUN 77 H J ALBRECHT
AGARD-CP-208

UNCLASSIFIED

3 OF 3
ADA
044800

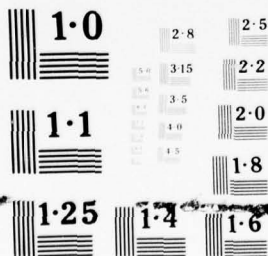
NL

END
DATE
FILMED

10-77

DOC

3 OF 3
ADA
044800



NATIONAL BUREAU OF STANDARDS
MICROCOPY RESOLUTION TEST CHART

The scattering function limited to the case of Table 3 has been computed and used in underwater acoustics, and to some extent it could be used with advantage also for electromagnetic communications in a layered media. The statistical evaluation of the physical processes that generate alteration in the transmitted signal is quite important for approaching the analytical characterization of the channel.

From the preceding considerations it is evident that in the proposed mathematical models, the statistical evaluation of the noise and the signal is of determinant importance in making generally operative the application of similar algorithm.

4. THE BOUNDARIES IN ELF RANGES

Due to the wave lengths, the distances involved in ELF communications range from the order of a kilometre to thousands of kilometres. The interfaces of interest are then, in the main, those represented in Fig. 3. The main boundaries involved are as consequence the Upper boundary, which is the ionosphere, and the Lower Boundary, which is the earth's surface.

4.1 The Upper Boundary

The upper boundary, namely the ionosphere, is a region of the upper atmosphere between 50 and 300 km above the earth's surface. The ionosphere conductivity varies between 1 mhos/m and 20 mhos/m. The skin depth of an electromagnetic wave in a medium of such conductivity has been calculated and reported by KRAICHMAN, 1970, and can be of the order of many hundreds of metres. A signal propagating through the ionosphere to reach the earth's surface is evidently influenced by the behaviour in time and the space distribution of the conductivity. The model of a layered medium in regular layers with a well known conductivity is, in this case, quite far from the reality. The conductivity behaviour in the ionosphere is summarized in the following formulas (EGELAND et al, 1973):

$$\underline{g} = \begin{bmatrix} \sigma_P & \sigma_H & 0 \\ -\sigma_H & \sigma_P & 0 \\ 0 & 0 & \sigma_{//} \end{bmatrix}$$

Current Density:

$$\underline{j} = \underline{g} \cdot (\underline{E} + \underline{v} \times \underline{B})$$

$$\sigma_P = \left[\frac{\nu_{en} \omega_{ce}}{\nu_{en}^2 + \omega_{ce}^2} + \frac{\nu_{in} \omega_{ci}}{\nu_{in}^2 + \omega_{ci}^2} \right] \frac{e N e}{B}$$

PEDERSEN CONDUCTIVITY

$$\sigma_H = \left[\frac{\omega_{ce}^2}{\nu_{en}^2 + \omega_{ce}^2} - \frac{\omega_{ci}^2}{\nu_{in}^2 + \omega_{ci}^2} \right] \frac{e N e}{B}$$

HALL CONDUCTIVITY

$$\sigma_{//} = \left[\frac{1}{m_e \nu_{en}} + \frac{1}{m_i \nu_{in}} \right] e N e$$

PARALLEL CONDUCTIVITY

$$\sigma_C = \sigma_P + \frac{\sigma_H^2}{\sigma_P}$$

COWLING CONDUCTIVITY

ν_i = collision frequency

ω_e = gyro frequency

i = ion

e = electron

From which it is deduced that conductivity is a tensor depending from time and related with the physics of plasma and hydrodynamics.

If ionosphere is considered a transmission medium, and since the most important parameter of such a medium is the conductivity as a consequence of the previous consideration upon transmission (i.e., WSSUS hypothesis), a statistical evaluation of the fluctuations in time must be done. In the ELF range some evaluation of the background noise and of its distribution has been carried out by BERNSTEIN ET AL 1974, and Fig. 4 gives an example of the typical distribution of the ELF noise compared with the assumed Gaussian noise. More specifically, in hydrodynamic turbulent velocity fields, it is not adequate to assume a certain process as random but, more rigorously, as statistically determined; TATARSKII, 1971, underlines that assumptions of randomness in many cases are no more adequate.

The plasma physics and the ionosphere hydrodynamics can supply the needed information on the fluctuations and on the space distributions of the conductivity, which will be useful in correlating the non-Gaussian distribution of the noise with a physical predictable phenomenon. Telecommunication theories and techniques can supply useful diagnostic tools (DAVIS and MEYERS, 1974). Figure 5 represents an ELF signal propagating in the earth-ionosphere gap and received at a distance of about 5 nanometres. The ripples represent anomalies related to magnetospheric phenomena. In this case the ELF transmission can be used as a diagnostic tool.

4.2 The Lower Boundary

The lower boundary of such a particular wave guide (earth-ionosphere gap) is the earth's surface. This consist of 71% of oceans and seas and the remainder of land. For the oceans similar considerations made for the ionosphere can be applied. In this case, the behaviour of the conductivity is more simple and easily correlated to other physical parameters of the sea water (i.e. salinity, temperature, pressure). The conductivity of sea water ranges from 2.5 to 5 mhos/m and the skin depth can reach several hundredes of metres. In Table 6 a synthesis is shown of the implications of interfaces at ELF ranges. The field components, represented in the Table by points, are different to each other and depend not only on the conditions of the boundaries, but also on the type of dipole (vertical electric, vertical magnetic, horizontal electric, horizontal magnetic), and also on the range that implies the frequency (wave-length). For practical applications in ELF telecommunications, the particular cases summarized in Table 6 must be taken into account carefully. The calculation of the values for various field components are reported by KRAICHMAN, 1970.

TABLE 6

INTERFACE IMPLICATIONS AT ELF RANGES									
Range	Propagation	Dipole Type	Field Components						
FAR FIELD $\rho \gg \lambda_0$	Subsurface - Free Space	VED	E_ρ	E_ϕ	E_z	H_ρ	H_ϕ	H_z	
		VMD	
		HED	
		HMD	
	Subsurface - Subsurface	VED	
		VMD	
		HED	
		HMD	
	(U.O.A.D. propagation)		HMD	
	NEAR FIELD $\rho \approx \lambda_0$	Subsurface - Free Space $h \leq 0^+ \quad z \geq 0^-$	VED
			VMD
			HED
HMD			
Free Space - Subsurface $h \geq 0^+ \quad z \leq 0^+$		VED	
		VMD	
		HED	
		HMD	
Subsurface - Subsurface $h \leq 0^- \quad z \leq 0^-$		VED	
		VMD	
		HED	
		HMD	
QUASI-STATIC FIELD $\rho \ll \lambda_0$		Surface - Surface (i) General $ \gamma_0 \rho \ll 1$	VED
			VMD
			HED
			HMD
	(ii) Quasi-near range $ \gamma_0 \rho \ll 1 \ll \gamma_1 \rho $	VED	
		VMD	
		HED	
		HMD	

TABLE 6 (Cont.)

Range	Propagation	Dipole Type	Field Components						
QUASI-STATIC FIELD	(iii) $ \gamma_0 \rho \ll 1; \gamma \rho \ll 1$	VED	$E_\rho, E_\phi, E_z, H_\rho, H_\phi, H_z$						
		VMD
		HED
		HMD
	Free Space - Subsurface (i) $ \gamma_0 R' \ll 1$	VED
		VMD
		HED
		HMD
	(ii) $ \gamma_1 R' \gg 1$	VED
		VMD
		HED
		HMD
	(iii) $R' \gg z $	VED
		VMD
		HED
		HMD
	Subsurface - Free Space (i) $ \gamma_0 R \ll 1$	VED
		VMD
		HED
		HMD
	(ii) $ \gamma_1 R \gg 1$	VED
		VMD
		HED
		HMD
	(iii) $R \gg h $	VED
		VMD
		HED
		HMD
	Subsurface - Subsurface	VED
		VMD
		HED
		HMD

5. CONCLUSIONS

The matter presented above may appear farraginous, because each argument is only briefly mentioned. More precise details are contained in the references. In telecommunications, in general, the behaviour of the medium (including boundaries) must be considered and objectively evaluated. But how? From the communication theory it appears necessary to approach any problem related to transmission media in a statistical way. Enormous amounts of data have been gathered already by many scientists working in magnetosphere research and in ocean research, and their problems can be approached with similar methodologies, at least, for telecommunication purposes.

REFERENCES

- BANOS, A., 1966, "Dipole Radiation in the Presence of a Conducting Half Space", Pergamon Press.
- BERNSTEIN, S. et al, 1974, "Long Range Communications at Extremely Low Frequencies" Proc. of the IEEE, Vol. 62.
- DAVIS, R.J. and MEYERS, W.D., 1974, "Solar-Geophysical Effects on Northern and on Mid-latitude ELF Propagation", NRL Rep 7771.
- EGELAND, A., et al, 1973, "Cosmical Geophysics", Universitetsforlaget, Oslo.
- GRANDVAUX, B., 1971, "Le Canal de Transmission Acoustique Sous-Marin Considere comme un Filtre Lineaire Non Homogene", Proc. GRETSI, Nice.
- IEEE Trans, 1974, "On Communications", (Special Issue - April).
- KRAICHMAN, M.B., 1970, "Handbook of Electro Magnetic Propagation in Conducting Media", NAVMAT P.2302.
- LAVAL, R., 1972, "Sound Propagation Effects on Signal Processing", NATO ASI on Signal Processing, Loughborough, U.K.
- NATO ADVANCED STUDY INSTITUTE "ELF - VLF Radio Wave Propagation", Ed. J. Holtet, Publ. D. Reidel, Netherland, held in Spatind, Norway, April 1974.
- SØSTRAND, K.A., 1968, "Mathematics of the Time-Varying Channel, NATO ASI on Signal Processing with Emphasis on Underwater Acoustics held in Enschede, The Netherlands.
- TACCONI, G., 1974, "On the Evaluation of Man-Made Electromagnetic Noise Interfering with Communications in the ELF Range", AGARD Meeting on Electromagnetic Noise, Interference and Compatibility, Paris, France.
- TATARSKII, V.I., 1971, "The Effects of the Turbulent Atmosphere on Wave Propagation", Jerusalem IPST.
- WAIT, J.R., 1970, "Electromagnetic Propagation in an Idealized Earth's Crust Waveguide, Electromagnetic Wave in Stratified Media", Pergamon Press.
- WAIT, J.R., 1974, "Theories of Electromagnetic Waves in the Earth's Crust and the Ocean", International Symposium on Radio Propagation in Natural Media, Florence, Italy.
- WASILJEFF, A., 1976, "The Influence of Time and Space Variant Random Filters on Signal Processing", NATO ASI on Signal Processing with Emphasis on Underwater Acoustics, La Spezia, Italy.

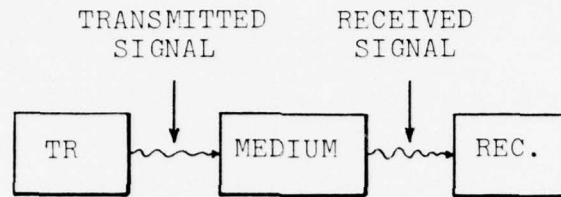
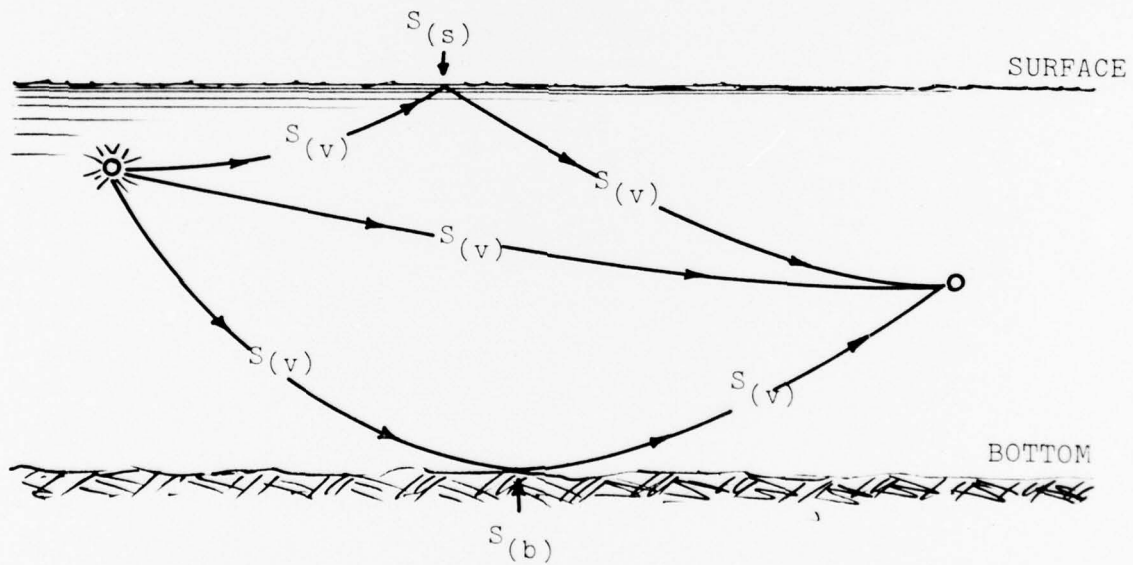


FIG. 1 GENERAL TRANSMISSION CHANNEL



$S(v)$ = VOLUME SCATTERING
 $S(s)$ = SURFACE SCATTERING
 $S(b)$ = BOTTOM SCATTERING

FIG. 2 TRANSMISSION CHANNEL BETWEEN TWO INTERFACES

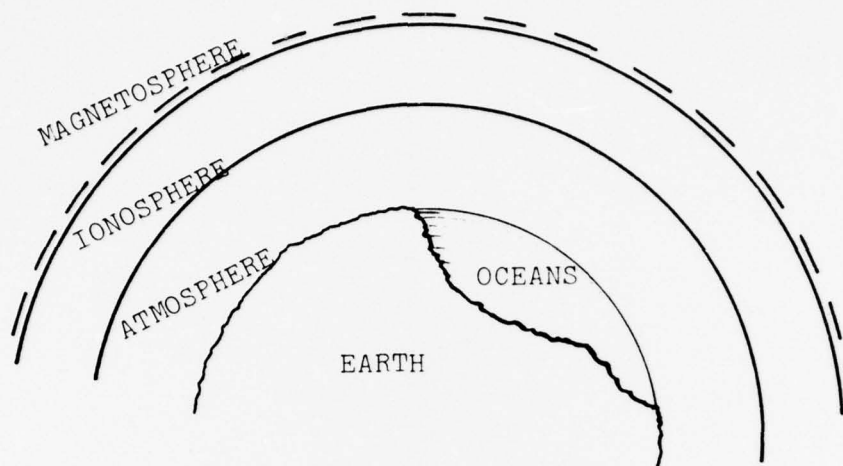


FIG. 3 INTERFACES INTERESTED IN ELF PROPAGATION

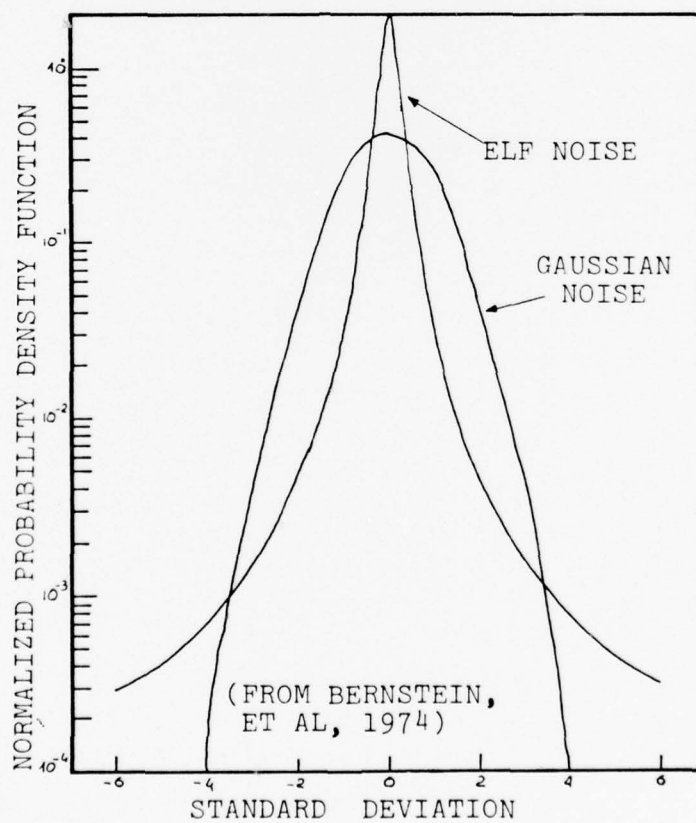


FIG. 4 STATISTICAL DISTRIBUTION OF ELF NOISE COMPARED WITH GAUSSIAN NOISE (From BERNSTEIN, 1974)

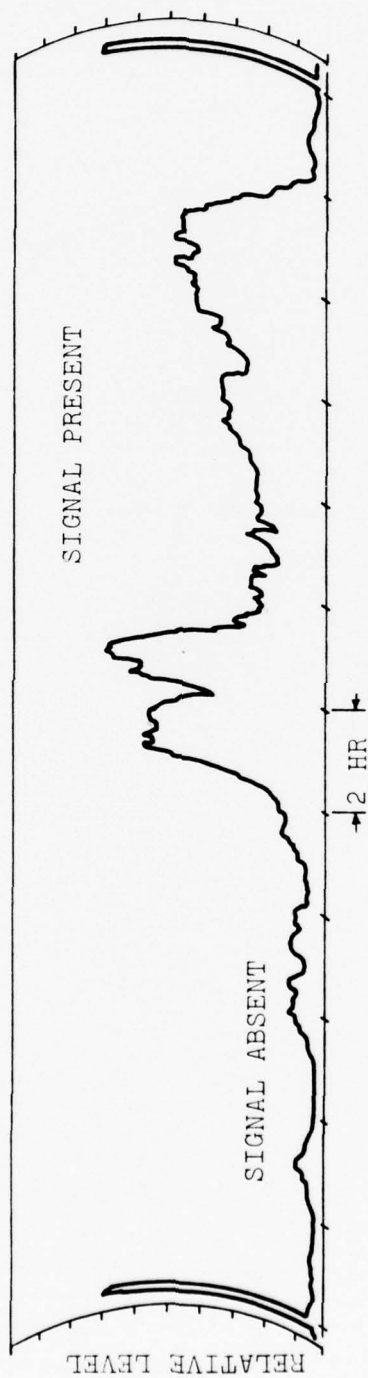


FIG. 5 EXPERIMENTAL DETECTION OF ELF SIGNAL AFFECTED BY IONOSPHERIC FLUCTUATIONS

SATELLITE - BORNE MONITORING OF ATMOSPHERIC
AND SURFACE CHARACTERISTICS AFFECTING THE
PROPAGATION OF MICROWAVES IN THE TROPOSPHERE

E. Raschke
Institut für Geophysik und Meteorologie
Universität zu Köln
D - 5 Köln 41
Germany

SUMMARY

In this paper are considered some possibilities to observe and monitor on a global scale such atmospheric and surface properties which affect the propagation of microwaves in the troposphere. These are the fields of atmospheric temperature, moisture, pressure and also of precipitating clouds, further the sea state, ice and snow cover and the soil moisture.

A manifold of satellite techniques has been developed in the last years, primarily for meteorological applications. They may provide useful informations for the purposes to estimate the atmospheric transfer properties for the microwave region. However the existence of the ducting inversion layers near the ground might be only indirectly deducable from them.

1. INTRODUCTION

The propagation of electromagnetic waves of the microwave region within layers of the troposphere depends on the magnitude and spatial gradients of the refractive index and on the presence of damping materials, such as various gases (in particular water vapor and oxygen) and of clouds within the atmosphere. Furthermore the conductivity of the subsurface soil layers and the roughness of the oceans and sea-ice-cover play an important role in this respect.

Also spatial and temporal variations of the refractive index are strongly linked to those of the atmospheric pressure and temperature fields and the water vapor content (see e.g. KRUSPE, 1965). Fluctuations of the moisture are also responsible for changes of the wave damping, where, of course, clouds - in particular precipitating clouds - play a dominating role.

A global climatology of the refractive index and damping for electromagnetic waves can therefore traced back within the accuracy of a variable formula to the climatology of temperature, moisture, pressure and cloud fields in the troposphere. BEAN and DUTTON (1966) published average maps computed from climatological averages of these relevant quantities. The expression "climatology" is used here in the sense of a detailed statistics of the mentioned field parameters in various time and space scales. These maps refer to a mean state of the atmosphere.

While such a climatology might be important for the planning and installation of communication links, the present state of the atmosphere needs also to be known in many cases for very immediate decisions. This refers in particular to the formation and presence of "ducting" inversions near the ground, at the top of the planetary boundary layer and in the troposphere above, and of precipitating clouds and thunder cells with large amounts of liquid and frozen water.

Informations on these atmospheric properties may be obtained in some detail from the observational material of the conventional meteorological network, which is gathering every day data for analysis and forecast purposes. In this network meteorological satellites play now an important role to fill with their continuous measurements over the entire globe (ICSU - WMO 1975) gaps in the conventional ground-based network. Satellite techniques have also been used for global observations of continents for many resources problems and also of the oceans. Therefore, it has been found worthwhile to consider the usefulness of these informations for the purposes of prediction and analyses of microwave propagations.

2. ATMOSPHERIC PROPERTIES

2.1 Principle of Satellite Soundings

The recent advances of technology for remote soundings of meteorological parameters

from satellite platforms have been reviewed extensively during the 10. COSPAR - Meeting in Philadelphia (BANDEEN and RUTTENBERG, 1976). In principle passive radiometry uses solar and terrestrial or also stellar radiation as source of information. In active soundings the informations need to be deduced from backscattered or transmitted signals, where the radiating source, a laser or a radar, is carried in a satellite.

The latter category has been proven to be useful during many aircraft flights and in a few research satellites, but is still under development for operational use in satellites.

Passive soundings in the solar spectral range and in the infrared are now in operational use. Vertical measurements enable global observations of temperature and cloud fields in the troposphere and lower stratosphere. Limb scanning techniques are in use - not yet operational - to obtain informations on upper strato- and mesospheric state parameters. Passive microwave measurements have also been used in various research satellites for both purposes, imaging ground properties and sounding the atmosphere.

2.2 Temperature and Moisture Fields

From vertical multispectral soundings in the infrared the vertical temperature profile in the troposphere can be obtained with $\pm 1.5^{\circ}\text{C}$ RMS-error, if compared with nearly simultaneous radiosonde measurements over the same area (FRITZ et al., 1972). But, the vertical resolution is basically limited to the order of 2 - 4 km. Thus the in their vertical extent much smaller, but very effective, inversion layers cannot be discovered and monitored. Since clouds contaminate all soundings in the infrared, there have been methods developed for simultaneous measurements in the infrared and microwave region. These promise an improvement of the accuracy for the mean temperature, profiles in the lower troposphere but not their vertical resolution.

Vertical soundings of tropospheric gaseous water vapor content and profiles may only yield to accuracies of 15 - 20% of the observed specific humidity and to vertical profiles resolving informations of 4-6 km apart. Again the discontinuities in vertical moisture profiles, which are associated with inversions cannot be located.

Limb scanning and occultation (stars, sun) techniques yield to higher vertical resolutions. But they cannot be applied to the lower troposphere due to cloud effects.

Thus, these multispectral satellite soundings may improve our present knowledge on the spatial large - scale climatology of temperature and moisture fields. But, the finer and in this aspect much more important details in their vertical structure, such as ground inversions etc., remain largely undiscovered.

Their presence might be deduced from other indicators which can still be observed from satellites. These are mainly cloud fields associated to frontal systems, trade wind systems and strongly developed planetary boundary layers. The latter are usually capped with an inversion. Also over snow and icefields an inversion layer forms consistently.

The temporal resolution of such measurements may range from once or twice to about 40 times a day, where even gravity waves travelling along inversion might be tracked, if they visible in the cloud field structures. There have been many examples of gravity waves studied with time lapse movies, which can be obtained conveniently from images taken in rather short time steps (20 - 30 min) from geostationary satellites.

2.3 Atmospheric Pressure

Remote sensing of the atmospheric pressure at any defined level from satellites requires in principle measurements of the total air mass between that level and the satellite. Such techniques can use in principle multispectral microwave radars to avoid cloud and aerosol effects. They are under development and may be useful for the interpolation between surface data - in particular over oceans - measured otherwise at well calibrated land stations. It has not yet been proven, that they will accomplish accuracies of the order of 1 hPa, the common radiosonde error. Also the feasibility of spectral measurements over the ocean has been studied.

Other possibilities to obtain the pressure at some reference level have been explored within activities for the World Weather Watch. Ballons floating nearly at constant pressure levels can easily carry pressure gauges and radioaltimeters. The latter enable altitude controls within less than 10 m. However their use might be restricted only to the Southern Hemisphere due to air traffic safety regulations and also political reservations.

Definitely, crude estimates of pressure fields over the oceans are also possible from cloud patterns in cyclones and anticyclones.

2.4 Cloud Fields

The feasibility to monitor cloud fields has been demonstrated since more than 15 years with imaging methods in the visible and infrared. With these data, only cloud phenomenology may be a useful method to estimate the liquid water content of non-precipitating clouds. However, no such "climatology" has been reported in the literature.

Recent progress in the microwave techniques yielded to routine measurements of thermal emission in the microwave region from several US satellites near 19 GHz and 37 GHz. These measurements enabled over oceans clear distinctions between precipitating clouds of various rainfall rates. Even an annual "climatology" of precipitation over oceans could be accomplished from Nimbus 5 data (RAO, ABBOTT, THEON, 1976).

Measurements of the thermal emission in the 37 GHz region enable even over the higher emitting land surfaces the location of raining clouds associated to frontal and convective systems (SAVAGE and WEINMAN, 1975).

Thus, if such imaging measurements in the microwave region are used on the next generation of geostationary satellites, the attenuation due to mainly precipitating clouds can be estimated and forecasted on a reasonable short time and space scale.

So far, on the present generation of geostationary satellites only instruments are being flown which image the globe with their measurements in the visible and infrared.

The system of 4 - 5 geostationary satellites, which will be established for the purposes of FGGE (First GARP Global Experiment) in 1978 and 1979, may already help to accomplish hourly forecasts for fast developing convective system. This requires, however, a properly developed data management system.

3. GROUND STATE PARAMETERS

3.1 Sea State

The roughness of ocean surfaces may effect the microwave propagation due to multiple reflections between various wave-crests, and it is known to enhance the formation of the evaporation duct. Recent efforts to obtain the wind field near the sea surface have led to the development of techniques to determine the sea state or roughness from satellite altitudes (ALISHOUSE, 1975). For this purpose active nano-second radar altimeters and multiple (2-3) frequency radar interferometer might be proper tools (ALPERS, HASSELMANN, SCHIELER, 1965). Also passive imaging methods allowing accuracies of better than 1°C have been found useful to estimate the sea state and even the foam or white-cap coverage. Perhaps also use of the polarisation characteristics of emitted radiation can be made.

These latter measurements enable clear and convenient distinctions between ice-free and ice-covered ocean and lake areas. Their continuous application on several Nimbus satellites led to a much clearer picture on the ice coverage and dynamics over both polar regions.

The water temperature underneath the surface and the salinity which affect to some degree the penetration depth cannot be monitored from satellites. Only the surface temperature can be obtained from measurements in the infrared and in the microwave region within 1 - 1.5°C RMS-error. The salinity affects considerably the emission of microwaves at frequencies of less than 4 GHz (ALISHOUSE, 1975).

3.2 Properties of Land Surfaces

The dielectric properties of continents depend not only on the type of soil or of rocks, but also on their stratifications. Thus, their spatial variations might be over many areas very strong, which is a useful tool to explore with airborne radar geological structures covered with vegetation. Extensive use has already been made of the side-looking-airborne-radar.

The soil moisture, which controls to some extent the penetration depth has not yet been measured from satellites. There have been discussed proposals to use polarisation techniques in the visible, and also several passive and active microwave techniques, which still need further development. Since the soil moisture controls largely the exchange of heat between continents and the air aloft, the amount and temporal changes of it are also required for numerical forecasts of weather - and perhaps also of weather statistics (climate).

The continental snow cover can be monitored on images in the visible. Microwave techniques led to reasonable estimates of the snow thickness (perhaps 3 scales) and wetness (due to drastic changes of emissivity). These latter techniques have not yet been flown in satellites.

4. CONCLUSIONS

In this paper are shortly reviewed possibilities to monitor several atmospheric and ground parameters, which affect the propagation of microwaves in the lower troposphere. The in this respect perhaps most important temperature inversions in the atmosphere, which are also associated with discontinuities in moisture profiles, cannot be inferred directly from vertical soundings. There are ample opportunities to observe cloud fields - also precipitating cloud systems, and many surface characteristics.

In order to judge more thoroughly, than done in this paper, the importance of various remote sensing techniques to monitor the transfer properties of the atmosphere and of the ground for microwaves in communication links, a preparatory study of the accuracy requirements for all these parameters mentioned above needs to be done.

5. REFERENCES

- ALISHOUSE, J.C., 1975: A Summary of the Radiometric Technology Model of the Ocean Surface in the Microwave Region.
NOAA Techn. Memorandum NESS 66, Washington D.C.
- ALPERS, W., HASSELMANN, K., SCHIELER, M., 1975: Fernerkundung der Meeresoberfläche von Satelliten aus.
RAUMFORSCHUNG, 1, 8-14
- BANDEEN, W.R. and RUTTENBERG, S., ed., 1976: Proceedings of the "Symposium on Meteorological Observations from Space", held during the 19. COSPAR Meeting, available through COSPAR Secretariat, 75016 Paris
- BEAN, B.R. and DUTTON, E.J., 1966: Radio Meteorology, National Bureau of Standards Monograph 92, U.S. Government Printing Office, Washington D.C.
- FRITZ, S., WARK, D.Q., FLEMING, H.L., SMITH, W.L., JACOBOWITZ, H., HILLEARY, D.T., ALISHOUSE, J.C., 1972: Temperature Sounding from Satellites,
NOAA Technical Report NESS 59, Washington D.C.
- ICSU - WMO, 1975 : The Physical Basis of Climate and Climate Modelling,
GAFF Publ. Series N° 16, World Meteorological Organisation
Genève
- KRUSPE, G., 1965 : Der atmosphärische Brechungsindex und seine Messung mit
Mikrowellen - Refraktometern
Meteorologisches Institut, Universität Hamburg
- RAO, M.S.V. ABBOTT, W., THEON, J.S., 1976: Satellite Derived Global Oceanic Rainfall Maps, in BANDEEN and RUTTENBERG, ed., 1976, p 121 - 123
- SAVAGE, R.C. and WEINMAN, J.A., 1975: Preliminary Calculations of the Uperwelling Radiance from Rainclouds at 37.0 and 19.35 GHz
Bull. Am. Meteorol. Soc., 56, 1272 - 1274

DISTRIBUTION OF ELECTRICAL RESISTIVITY ON CONTINENTAL AREAS

V. Haak, M. Beblo, A. Berktold

Institut für Allgemeine und Angewandte Geophysik der

Ludwig-Maximilians-Universität München

Theresienstr. 41/4

D-8000 München 2

Germany

SUMMARY

The electrical resistivity of the earth has been investigated by several geophysical methods. The resistivity-distribution in the uppermost kilometers on continental areas as inferred from such measurements turned out to be rather inhomogeneous. Generally a correlation between the distribution of resistivity and the distribution of the geological units as displayed on geological maps exists. A few exceptions are known and will be discussed in the text.

1. Introduction

The electrical resistivity is one of the parameters whereof structures and constitution of the interior of the earth may be inferred. In particular the d.c.-resistivity of the rocks between the upper surface of the earth and about 1000 km depth is a quantity measurable at the earth's surface. On a global scale one can distinguish 3 stories at different depths of different resistivity. In the deepest storey below 700 km the resistivity is less than 1 ohm·m (this storey is called the conductosphere); the storey above is called the resistosphere where the resistivity may reach values as high as several thousand ohm·m; the uppermost storey consists of low resistive sediments, weathered rocks and the oceans. Its thickness is laterally varying between some 100 m to several kilometers. The resistivity depends on the amount of the pore-fluid and the concentration of ions in the pore-fluid. The following discussion will deal with the distribution of the resistivity in the upper 10 km, thus partly with the resistivity in the uppermost storey and partly with the uppermost resistivity-distribution in the middle storey, the resistosphere, in particular considering the resistivity on continental areas.

2. From numerous investigations all over the world we may conclude that such maps of the lateral distribution of the electrical resistivity can readily be constructed by means of geological maps. A geological map displays by different colours different types of rocks, and since different types of rocks have different resistivities one may indeed transform a geological map into a map of the resistivity-distribution. For example, red colours - representing metamorphic rocks - display regions of rather high resistivity (more than 1000 ohm·m); blue and brownish colours - representing mesozoic rocks like limestone and sandstone - display regions of medium resistivity (around some hundreds ohm·m); a yellow colour - representing young tertiary sediments - displays a region of rather low resistivity (tens of ohm·m and even less). The numerical values of the resistivity of the different rock-types can be taken from some handbooks (given in the references at the end). But one must be careful about how such listed values have been obtained. Only resistivities measured in the field-site at some typical outcrops of the rocks are actually representative for the construction of such resistivity-maps but no laboratory measurements at rock samples.

Such maps of the distribution of the resistivity based on the geological map have been constructed. For example in the U.S. the resistivity has been measured at some radiostations and roughly classified as high or medium or low resistivity. These classifications obtained from a few selected sites were extrapolated by means of a geological map for the whole area of the U.S. (see figure 1). But since the colours of the geological maps refer to the outcropping rocks at the surface of the earth only it is open to question how deep these rocks reach, i.e. whether such maps of extrapolated resistivities are valid. This question can be answered by geophysical methods measuring the electrical resistivity as function of depth. It is informative to compare resistivity-distributions as inferred from geological maps with resistivity-distributions as obtained by two geophysical methods. These methods are called the "magnetotelluric method" and the "geomagnetic depth-sounding method". The comparison will yield examples of good correlation and examples of no correlation. But before going to discuss that topic it is necessary to roughly outline both methods.

3. Both methods, the magneto-telluric and the geomagnetic depth-sounding methods, are based on the induction of time-varying electric and magnetic fields in the earth. The origin of the inducing magnetic fields are time-varying electrical currents in the ionosphere and magnetosphere produced by the interaction of the solar wind with the main magnetic dipole-field of the earth. The frequencies of the observed time-variations reach from 1 to 0.0001 cps. The electric field of the earth is recorded by two non-polarizable electrodes which are inserted into the soil. The electrode-spacing may differ from some tens of meter to some hundreds of meter. The horizontal components only are recorded, usually in EW and NS direction. The magnetic field is recorded at the surface of the earth by magnetometers in its three components, i.e. the vertical and both horizontal components.

Theoretically the induction-process is governed by Maxwell's equations. Because of the low frequencies of the electromagnetic fields concerned and the actually low resistivities of the rocks the term regarding the displacement currents may be dropped within an accuracy of some orders of magnitude. This implies that the induction process inside the earth is to be described by a diffusion process rather than by a wave propagation process. The fundamental equations are therefore the "diffusion-equations":

$$\nabla^2 \vec{E} = i \omega \mu_0 \sigma \vec{E} \quad \text{and} \quad \nabla^2 \vec{B} = i \omega \mu_0 \sigma \vec{B}$$

with \vec{E} electric field ($V \cdot m^{-1}$)
 \vec{B} magnetic field (Tesla)
 μ_0 magnetic permeability ($4 \pi \cdot 10^{-7} \text{ ohm} \cdot s \cdot m^{-1}$)
 ω angular frequency (s^{-1})
 σ electrical conductivity ($ohm^{-1} \cdot m^{-1}$) = resistivity $^{-1}$

The electrical conductivity σ in both equations is a real value, not dependent on frequency, solely dependent on the properties of the rocks.

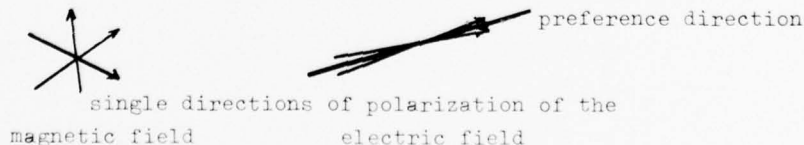
Both methods, the magneto-telluric and the geomagnetic depth-sounding method, are based on the same physical process, they just differ by the choice of field-components they take into account. In the magneto-telluric method only the horizontal components of the electric and magnetic field are considered, in the geomagnetic depth-sounding the three components of the magnetic field are considered.

In the magneto-telluric method one fundamental quantity is the apparent resistivity:

$$\varrho_a(\omega) = \frac{\mu_0}{\omega} \left| \frac{E_x(\omega)}{B_y(\omega)} \right|^2$$

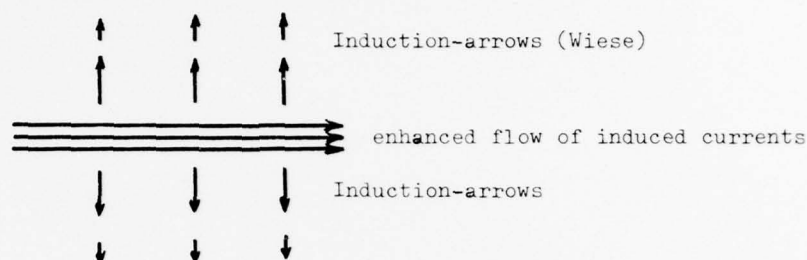
where x and y designate orthogonal, horizontal field-components. The apparent resistivity is a function of frequency. This frequency-dependence is not caused by the actually negligible displacement currents but caused by the frequency dependent depth of penetration (skin-effect) of the induced fields. The depth of penetration increases with decreasing frequency. The apparent resistivity may roughly be understood as a mean resistivity from the surface of the earth till the depth of penetration. There exist methods to transform the measured apparent resistivity as function of frequency into the true resistivity as function of depth.

Another fundamental quantity in the magneto-telluric method is the preference direction of the electric field. Usually the inducing magnetic field is elliptically polarized with arbitrary directions of polarization. The corresponding directions of polarization of the electric field should be perpendicular to the directions of polarization of the magnetic field. But this is only true in lateral uniform distributions of resistivity. In lateral non-uniform resistivity-distributions the directions of polarization of the electric field are confined to a more or less narrow angle.



The mean value of that angle is called the preference direction of the electric field. Some authors prefer to call this quantity the "direction of the major axis of the anisotropic apparent resistivity". In case of a long, but narrow trough filled with low resistive sediments in higher resistive surrounding the preference directions of the electric field are parallel to the strike direction of the trough inside the trough, whilst they are perpendicular to the strike-direction outside the trough.

A fundamental quantity of the geomagnetic depth-sounding method is the induction arrow. The length of the induction arrow is just simply the ratio of the amplitudes of the vertical and horizontal component of the magnetic field and is proportional to the contrast between the resistivity inside and outside of an anomaly. If we consider straight line-currents then the magnetic field lines form elliptical loops around it. The direction of the induction arrow is always parallel to the plane of these loops.



In case of the long, narrow trough filled with low resistive sediments - as considered above - the induction arrows would be perpendicular to the strike direction of the trough.

These three most important quantities are commonly used to display the first and even further results of field-operations. They are true anyway because they are calculated directly from the observed electric and magnetic fields where the hereof inferred distribution of the true resistivity may be biased by some incompleteness of the used interpretation-theory.

4. How do the resistivity-distributions obtained by these methods correlate with the resistivity-distributions as inferred from the geological map? There exist regions where the correlation is perfect. In figure 2 a close-up view of a part of the Eastern Alps displays the geology and the observed preference directions of the electric field. After transforming the geology into the distribution of resistivity the preference directions of the electric field were calculated theoretically. If one compares, the agreement of such calculated and the observed preference directions is rather obvious. In figure 3 the geological map of Southern Germany and adjacent countries was transformed into a resistivity map, just using the three classifications: high or medium or low resistivity. By comparing the preference directions of the electric field with the resistivity-distribution at the Rhinegraben and in the region of the molasse-basin we again observe the high degree of agreement: The preference directions of the electric field are parallel to the strike direction inside the low resistive region, perpendicular to the strike direction outside the low resistive region. In figure 4 the preference directions of the electric field in the region of the Baikal Rift shows the same good agreement with the geology.

It seems to be rather general that the distribution of the preference directions of the electric field behaves very sensitive to the near surface resistivity distribution and therefore agrees quite perfectly with the resistivity distribution as inferred from geological maps. However the induction arrow of the magnetic field is also rather sensitive to deeper buried inhomogeneities of the resistivity.

In figure 5 the geology of Central Europe is represented, again by a classification with three resistivities. In the right part of the figure some of the induction arrows known for that area are shown. They are such called Wiese-arrows pointing by definition towards the highly resistive regions. The flow of enhanced currents deduced from the distribution of the induction arrows is represented by the thick curves. They coincide with the low resistive zones of the crust. In the Rhinegraben area we observe the correlation between the resistivity-distribution inferred from the geological map and the low resistive zone deduced from the induction arrows. Another example of correlation is to be seen in the North-German/ Polish sedimentary basin, where the induction arrows point away from the low resistive zone.

5. The induction arrows at the coast of the Baltic Sea in figure 5 are pointing towards the Sea. It seems to be rather astonishingly since one would expect the sea-water to be the better conductor than the sediments of the continent. One would indeed

expect the induction arrows to point away from the Sea towards the continent. From these observations shown we can infer that the sediments of that area must be much less resistive than the seawater. Indeed, very low resistivities of the sediments of the North German sedimentary basin, as low as 1 ohm-m, have been reported very recently (LOSECKE and WAGENITZ, 1976). Such case could be classified as a case of "over-correlation": One would indeed infer from a geological map a low resistivity but never as low as has been actually observed. Also for the coastal plain of the Gulf of Mexico in the U.S. such low resistivities have been reported (VOZOFF, 1972). We should therefore observe the "coast-effect", i.e. the transition from the very low to the very high resistivity, on the electromagnetic field somewhere inside the land, not as usually at the coast itself.

The other possibility of over-correlation would exist if the actually observed apparent resistivities are higher than the predicted one. Such unexpected intensification may be met in areas of high resistivities as for example in the Bohemian Massif. In figure 6 the left part shows the apparent resistivities as function of period in the German part of the Bohemian Massif, the right part shows the apparent resistivities in the Czechoslovakian part. The values are very high for all periods (i.e. all depths of penetration). Such intensification may be explained theoretically by the near-surface lateral inhomogeneities of the resistivity.

6. The third possible state of correlation would exist if there is no correlation between the resistivity distribution as inferred from geological maps and the resistivity distribution as deduced from the observed electromagnetic fields. Indeed, there exist anomalies of the resistivity which do not reach the earth's surface and hence are not indicated in a geological map. If we consider for example the resistivity of the pre-cambrian shield in Wisconsin in the U.S., we would infer from the existence of metamorphic rocks a high resistivity. Such a high resistivity is true for the upper few kilometers. The apparent resistivity we would expect is given by the thick solid curve in figure 7. The observed apparent resistivities, however, are decreasing with increasing depth of penetration. The inferred resistivities as functions of depth are shown in the lower part of the figure (DOWLING, 1970). A rather similar resistivity-distribution has been published by CANER (1970) for the region west of the Rocky Mountain Trench in Canada, represented in figure 8. The British Isles seem to be underlain by two low resistive slabs (BAILEY and EDWARDS, 1976): This conclusion has been drawn from the distribution of the induction arrows in figure 9 (they are such-called Parkinson-arrows which point by definition towards the low resistive regions). The cross-section of the resistivity-distribution shows two low resistive slabs striking about SW-NE. In figure 10 the distribution of the induction arrows (they are Wiese-arrows) in the area of Kirovograd in the Ukraine (U.S.S.R) is shown. The low-resistivity anomaly is proposed to be an elongated body with an elliptically shaped cross-section. Such crustal anomalies exist on all continents. Also in the South of Australia anomalously low resistivities below 1 ohm-m have been measured (in figure 11) and in South Africa a rather long low resistive zone has been deduced from the distribution of the induction arrows (figure 12).

This list of crustal anomalies will be concluded with two examples which are very similar to each other. The one area concerned is Ethiopia, the other area is Iceland: Both areas are covered, respectively, entirely built up by basalts such that one would expect high resistivities somewhere around 1000 ohm-m. But the actually observed resistivities at numerous sites in the basaltic area of Ethiopia are as low as 50 ohm-m or less (figure 13). Quite similar are the resistivities reported from Iceland (HERMANCE and GRILLOT, 1974). But considering the origin and the generation of basalt such low resistivities may be reasonable: The basaltic material upwelling from the Upper Mantle is hot and probably partially molten. Since the resistivity of basalts decrease with increasing temperature such low resistivities may be met in all tectonically active regions.

7. We may conclude that the transformation of a geological map into a map of the distribution of resistivity is a good approach to the real resistivity-distribution. of the upper few kilometers. Below that depth there may exist crustal anomalies of lower resistivities than expected considering the surface rocks only. A possible indication for such crustal anomalies could be the existence of tectonic activity.

REFERENCES

- ADAM, A. (editor), 1976, "Geoelectric and Geothermal Studies (East-Central Europe, Soviet-Asia)", KAPG Geophysical Monograph, Akadémiai Kiadó, Budapest.
- ADAM, A., F. HORVATH and L. STEGENA, 1970, "Investigation of Plate Tectonics by Magnetotelluric Anisotropy", *Annales Universitatis Budapestinensis de Rolando Eötvös nominatae, Sectio Geologica*, Tomus XIV, pp. 209.
- BAILEY, R.C. & R.N. EDWARDS, 1976, "The effect of source field polarization on geomagnetic variation anomalies in the British Isles", *Geophys. J. R. astr. Soc.*, **45**, pp. 97 - 104.
- BEBLO, M., 1976, "Electrical conductivity in the geothermal anomaly of the Urach volcanic area, SW-Germany", abstract in: Third workshop on electromagnetic induction in the earth, Sopron, Hungary.
- DE BEER, J.H., J.S.V. VAN ZIJL, R.M.J. HUYSEN, P.L.V. HUGO, S.J. JOUBERT and R. MEYER, 1976, "A magnetometer array study in South-West Africa, Botswana and Rhodesia", *Geophys. J. R. astr. Soc.*, **45**, pp. 1 - 17.

- BERKTOLD, A., M. BEBLO and K. KEMMERLE, 1976, "On the distribution of the electrical conductivity below the Eastern Alps", *Geolog. Rundschau*, 65, 2, pp. 715 - 735.
- BERKTOLD, A., V. HAAK and G. ANGENHEISTER, 1975, "Magneto-telluric measurements in the Afar area", in: Afar Depression of Ethiopia, Inter-Union Commission on Geodynamics, Scientific Report No. 14, vol.1, E. Schweizerbart'sche Verlagsbuchhandlung, Stuttgart, pp. 66 - 79.
- CANER, B., 1970, "Electrical conductivity structure in Western Canada and petrological interpretation", *J. Geomagn. Geoelectr.*, 22, No. 1 - 2, pp. 113 - 129.
- CANER, B., P.A. CAMFIELD, F. ANDERSEN and E.R. NIBLETT, 1969, "A large scale magnetotelluric survey in Western Canada", *Can. J. Earth Sc.*, vol.6, no. 5, pp. 1245 - 1261.
- DOWLING, F.L., 1970, "Magnetotelluric measurements across the Wisconsin Arch", *J. Geophys. Res.*, vol. 75, pp. 2683 - 2698.
- EDWARDS, R.N., 1976, "Electromagnetic methods for the mapping of regional crustal conductivity anomalies", review paper in: Third workshop on Electromagnetic induction in the earth, Sopron, Hungary.
- HERMANCE, J.F. and L.R. GRILLOT, 1974, "Constraints on temperatures beneath Iceland from magnetotelluric data", *Phys. Earth Plan. Int.*, 8, pp. 1 - 12.
- KELLER, G.V., 1966, in: Handbook of physical constants, publ. by The Geological Society of America, Inc., Memoir 97, pp. 553.
- KELLER, G.V., 1967, "Properties of rocks and minerals", in: Electrical properties of rocks, by E.I. Parkhomenko, Plenum Press, New York.
- KIESSLING, W., 1970, "Untersuchung der Variationen des erdelektrischen und erdmagnetischen Feldes im Oberpfälzer Wald zur Bestimmung der elektrischen Leitfähigkeit in größeren Tiefen mit der Methode der Magnetotellurik", Diplom-Arbeit Inst. Angew. Geophysik Universität München.
- LANDOLT-BÖRNSTEIN, 1952, "Zahlenwerte und Funktionen aus Physik, Chemie, Astronomie, Geophysik, Technik", 3. Band, 6. Auflage, pp. 349.
- LILLEY, F.E.M. and H.Y. TAMMEMAGI, 1972, "Magnetotelluric and geomagnetic depthsounding methods compared", *Nat. Phys. Science*, 240, no. 104, pp. 184 - 187.
- LOSECKE, W. and V. WAGENITZ, 1976, "First results of magnetotelluric measurements in North-West Germany", abstract in: Third workshop on electromagnetic induction in the earth, Sopron, Hungary.
- PARKHOMENKO, E.I., 1967, "Electrical properties of rocks", Plenum Press, New York.
- PORATH, H. and A. DZIEWONSKI, 1971, "Crustal Resistivity Anomalies from Geomagnetic Deep-Sounding Studies", *Rev. Geophys. Space Phys.*, vol.9, no. 4, pp.891 - 915.
- PORSTENDORFER, G., W. GÖTHE, K. LENGNING, CH. OELSNER, R. TANZER and E. RITTER, 1976, "Nature and possible causes of the anomalous behaviour of electric conductivity in the North of the GDR, Poland and the FRG", in: Geoelectric and Geothermal Studies, KAPG Geophysical Monograph, Akadémiai Kiado, Budapest, pp. 487 - 500.
- PRAUS, O., 1971, "Electric Conductivity of the Earth in Czechoslovakia studied by Magnetotelluric and Geomagnetic Methods", in: Upper Mantle Project Programme in Czechoslovakia 1962 - 1970, Geophysics, Final Report, pp. 162 - 186.
- ROKITYANSKY, I.I., S.N. KULIK, I.M. LOGVINOV and V.M. SHUMAN, 1976, "Deep magnetovariation studies in Ukraine", in: Geoelectric and Geothermal Studies, KAPG Geophysical Monograph, Akadémiai Kiado, Budapest, pp. 634 - 639.
- VOLARIVICH, M.P., E.I. PARKHOMENKO, 1976, "Electrical Properties of Rocks at High Temperatures and Pressures", in: Geoelectric and Geothermal Studies, KAPG Geophysical Monograph, Akadémiai Kiado, Budapest, pp. 321 - 369.
- VOZOFF, K., 1972, "The magnetotelluric method in the exploration of sedimentary basins", *Geophysics*, vol. 37, no. 1, pp. 98 - 141.

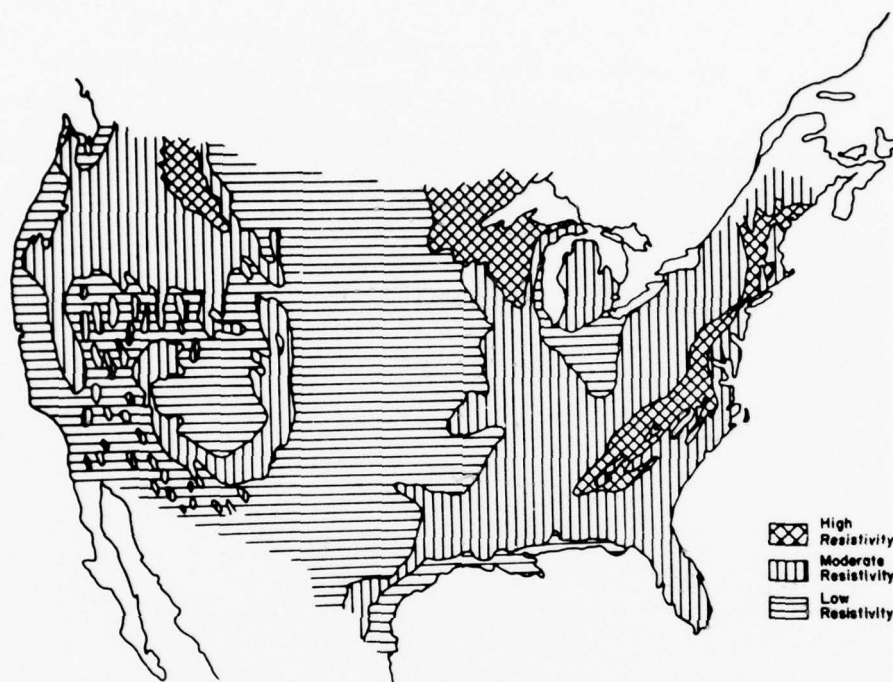


Fig. 1. The distribution of electrical resistivity in the U.S.A. The resistivities were measured at some radiostations at radio-frequency and then extrapolated to the whole area of the U.S. by means of a geological map using a rough classification into high - medium - low resistivity (KELLER, G.V., 1967)

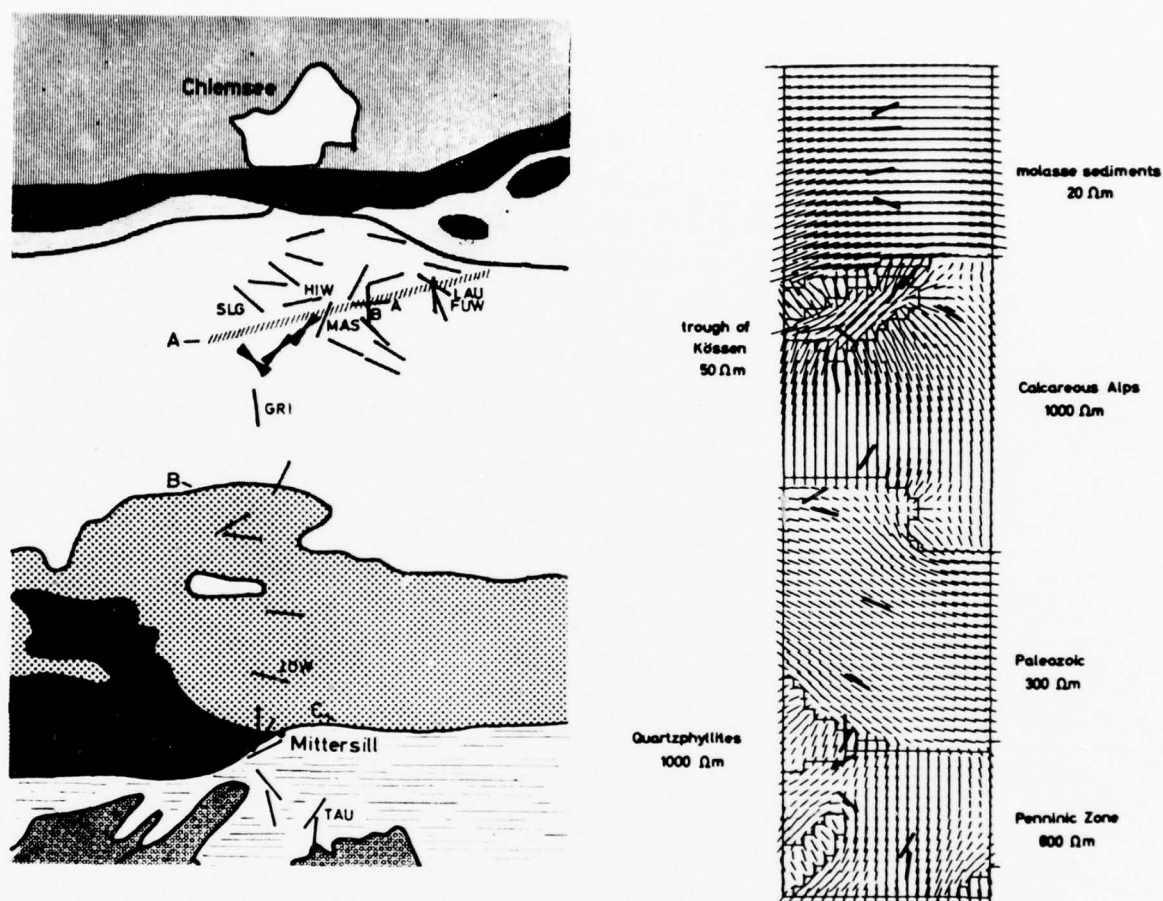


Fig. 2. Demonstration for a nearly perfect correlation between geological structures and the distribution of resistivity. The left part is a geological map of a part of the Eastern Alps (extension about 80 km x 20 km). Inserted are the measured preference directions of the electric field for periods of about 100 sec. The resistivities of the different geological units were measured in situ at some outcrops and extrapolated to the whole area by means of a geological map. For this resistivity-distribution the preference directions of the electric field have been calculated theoretically. They are represented in the right part of the figure by the thin bars at each square km. The thick bars are the observed preference directions. There is a near perfect agreement between the observed and the calculated preference directions, thus demonstrating the validity of the resistivity distribution. (BERKTOLD, A., M. BEBLO and K. KEMMERLE, 1976)

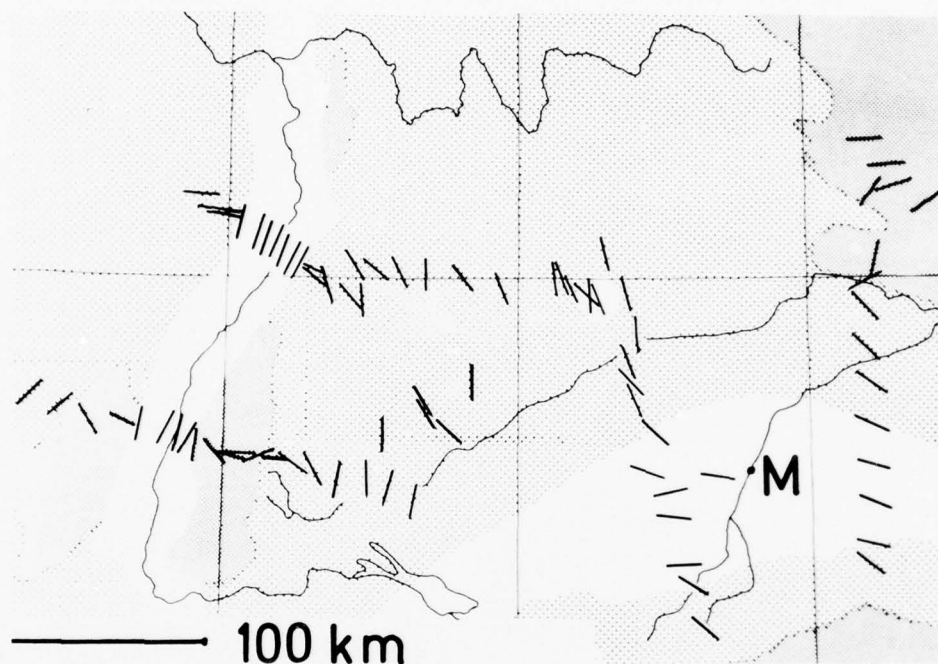


Fig. 3. The resistivity distribution of Southern Germany and the adjacent countries as inferred from the geological map. A rough classification was used: Crystalline and metamorphic rocks = High resistivity (dark shaded area); Mesozoic rocks = medium resistivity (light shaded area); tertiary and quaternary sediments = low resistivity (white area). Inserted are the observed preference directions of the electric field for periods greater than 100 sec. The preference directions are parallel to the geological borders within the low resistive sediments, but perpendicular to the borders outside (see the two profiles crossing the Rhine-graben at the left and the two profiles crossing the molasse basin at the lower right part). The NS-preference directions in the central, light shaded area are possibly caused by subsurface structures of the crystalline basement.

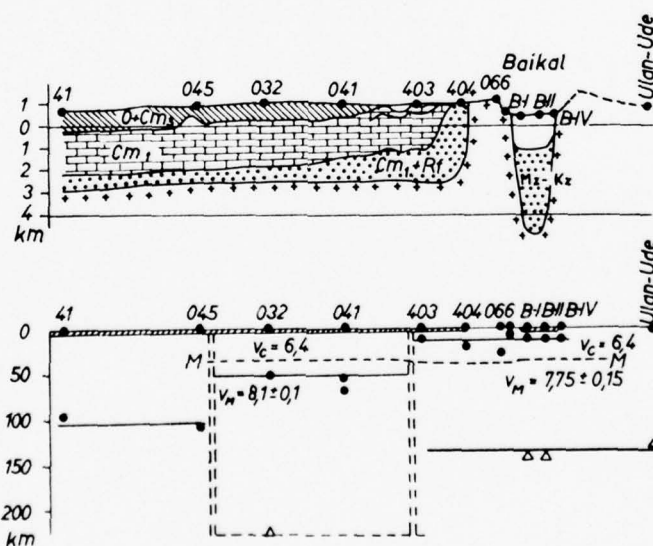
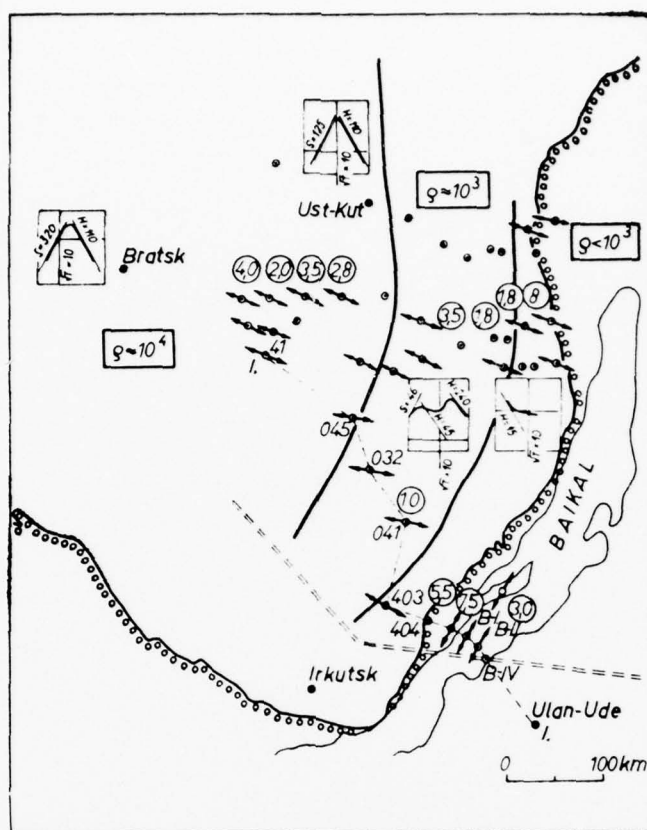


Fig. 4. The preference directions of the electric field in the area of the Baikal Rift, U.S.S.R.: They are perpendicular to the strike direction of the rift in the more resistive area, and parallel to the rift in the lower resistive area of the rift proper. (ADAM, A., F. HORVATH, L. STEGENA, 1970)

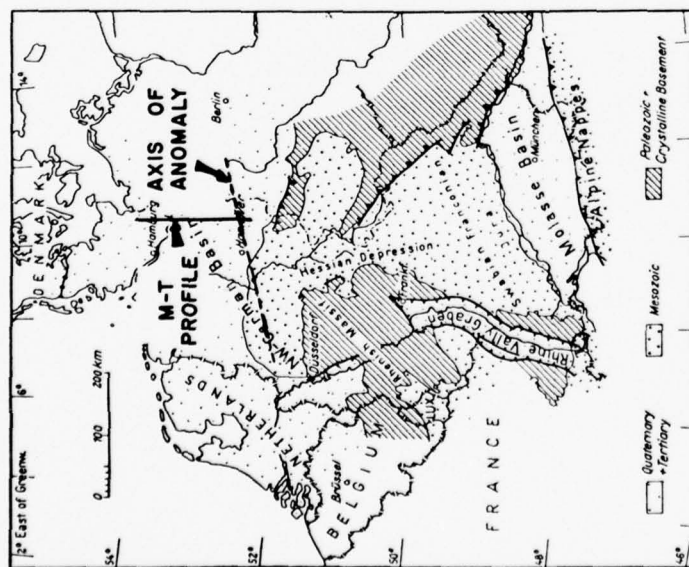
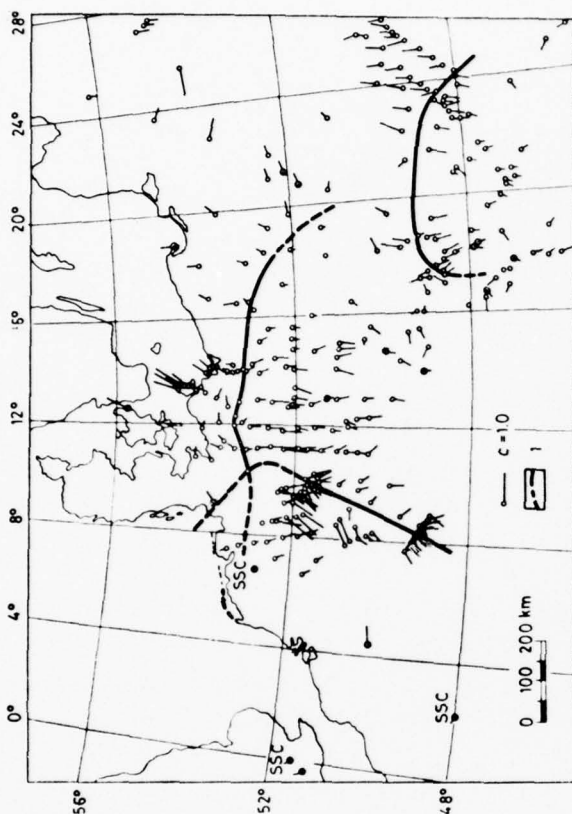


Fig. 5. At the left a simplified geological map of Germany which may readily be transformed into the distribution of resistivity: Quaternary + Tertiary = low resistivity; mesozoic = medium resistivity; paleozoic + crystalline basement = high resistivity. (PORATH, H. and A. DZIEWONSKI, 1971). At the right side the distribution of the induction arrows of the magnetic field (PORSTENDORFER, G., W. GÖTHE, K. LEMMING, CH. GELSNER, R. TANZER, E. RITTER, 1976). The heavy curves indicate the direction of the enhanced flow of induced currents within the earth. They indicate the zones of low resistivity. Such low resistive zones may partly be inferred from the geological map at the left: The Rhinegraben at the lower left part and the North German - Polish sedimentary basin in the central upper part. But there are also low resistive zones not displayed by the geological map: The northern continuation from the Rhinegraben through the Rhenish Massif and the low resistive zone beneath the Carpathian Arch partly shown at the lower right side. Not expected are also the length and the direction of the induction arrows at the shore of the Baltic Sea because they indicate the North German sedimentary basin to be lower resistive than the Baltic Sea.

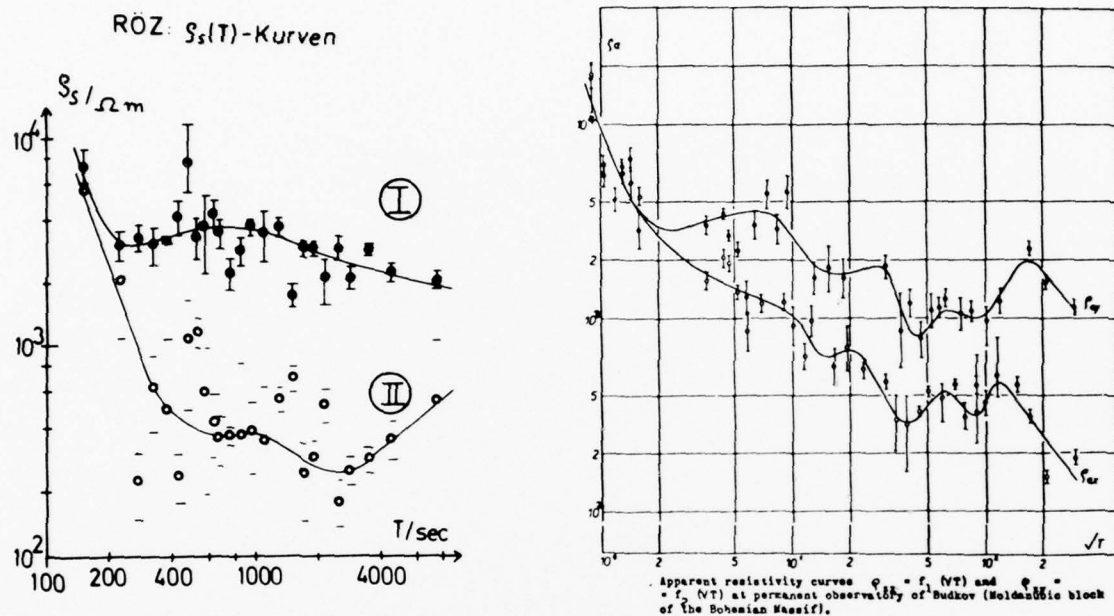


Fig.6. Apparent resistivities at site in the Bohemian Massif (Left: KLESSLING, W. 1970, right: PRAUS, O., 1971). They indicate higher resistivities than one would expect (granite and gneisses). This enhancement and the anisotropy (different resistivities in different directions) are caused probably by near surface inhomogeneities of the resistivity.

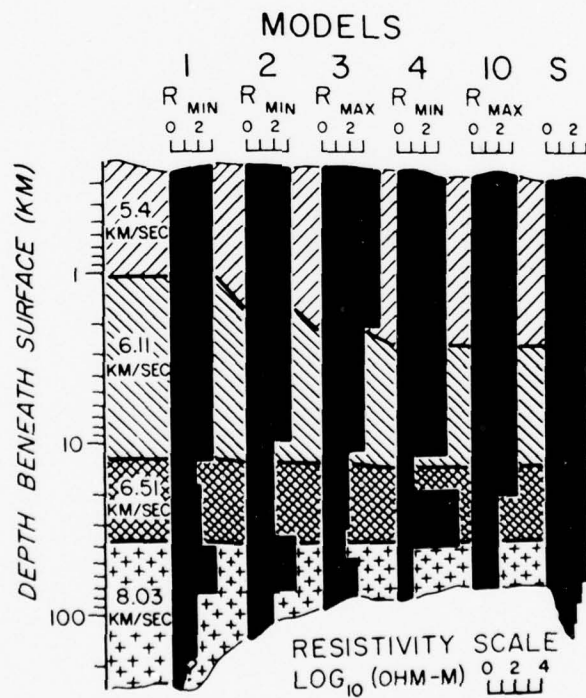
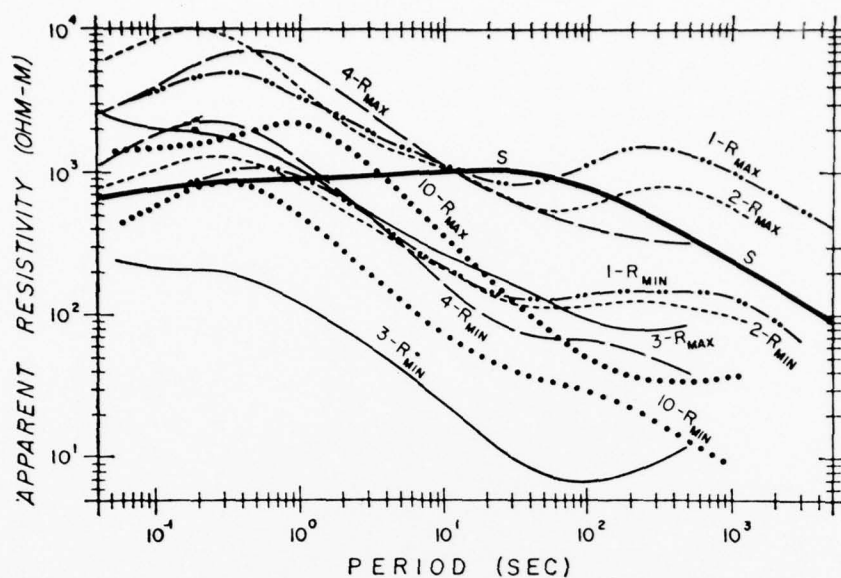


Fig. 7. Apparent resistivities (upper part) and the inferred resistivity - depth distribution (lower part) in the precambrian crust in Wisconsin, U.S.. One would expect an apparent resistivity for that type of rock as indicated by the heavy solid curve. The observed apparent resistivities, however, are decreasing with increasing period, i.e. increasing depth of penetration, thus revealing a low resistive zone in the lower crust. (DOWLING, F.L., 1970).

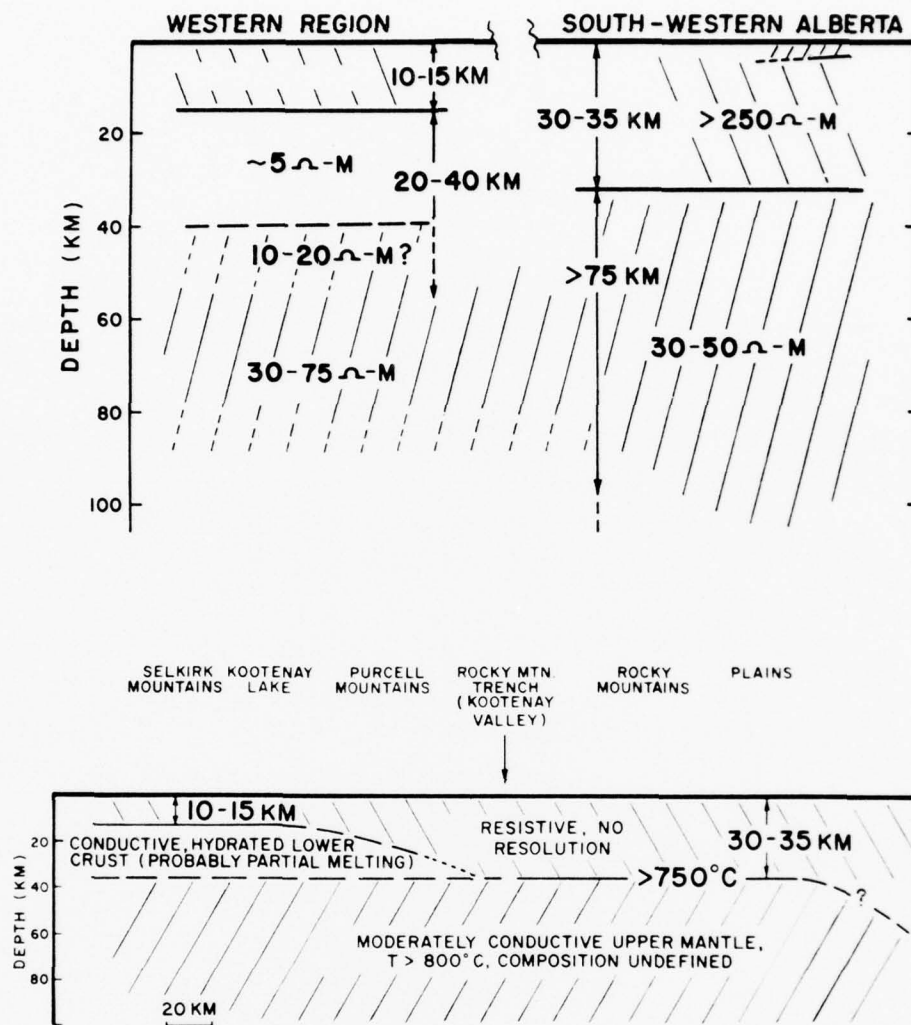


Fig. 8. The resistivity-models for the region around the Rocky Mountain Trench in Canada as inferred from magnetotelluric measurements. (CANER, B., 1970)

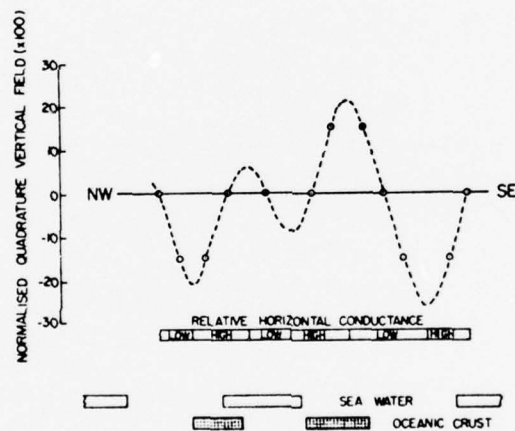
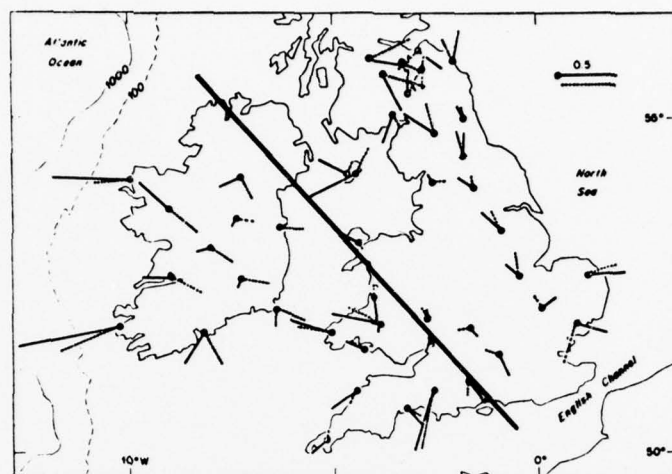


Fig. 9. The distribution of induction arrows (Parkinson-arrows, cf. the text) in the British Isles. The cross-section below of the resistivity-distribution refers to the profile indicated by the straight line above. The distribution of the induction arrows can be explained if two slabs of low resistive rocks within the crust are taken into account. (BAILEY, R.C. and R.N. EDWARDS, 1976).

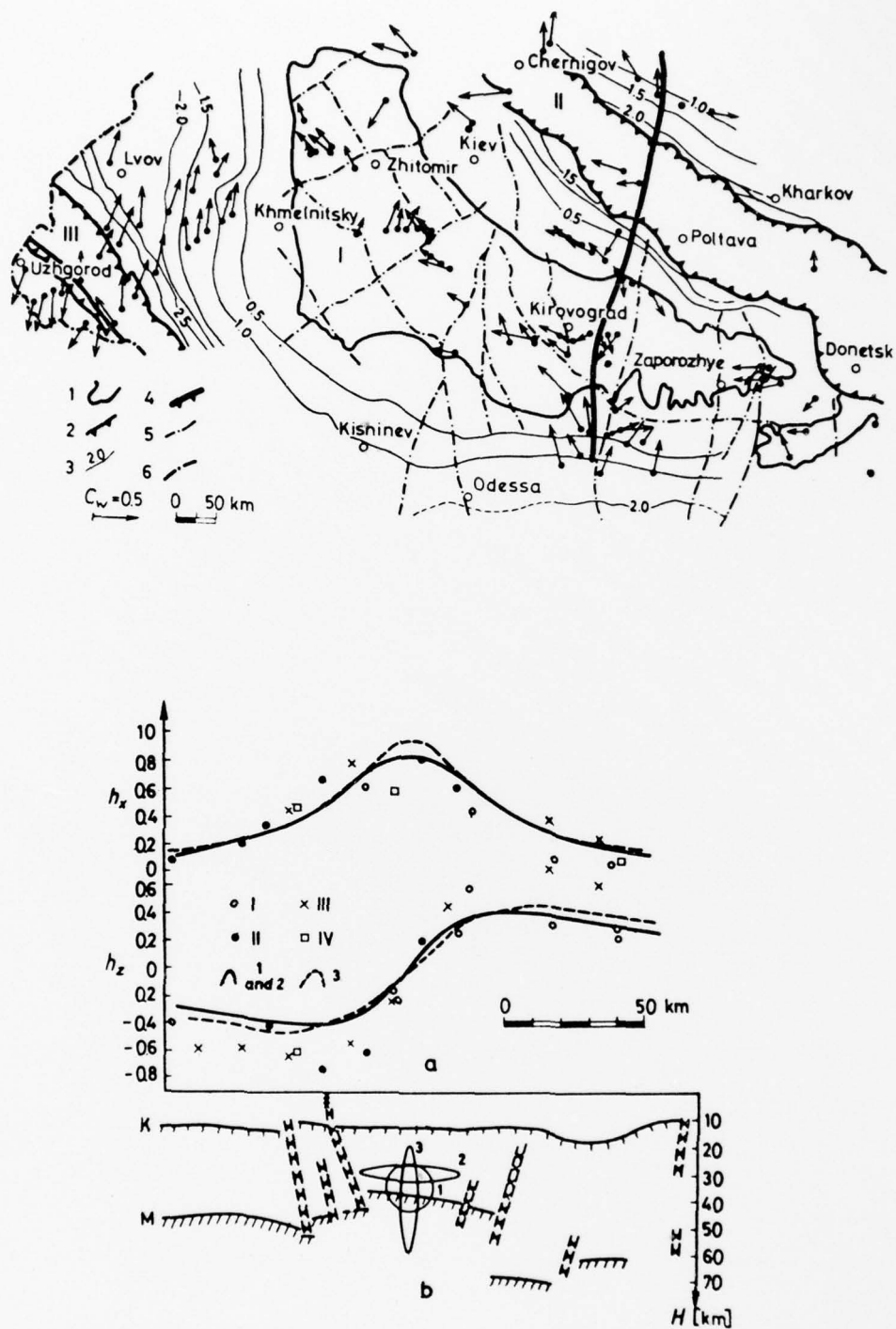


Fig. 10. The distribution of induction arrows in the area of Kirovograd, U.S.S.R.. The solid curve indicates the inferred zone of low resistivity in the lower crust. In the lower part of the figure possible shapes of a cross-section are given for a profile perpendicular to the strike direction of the resistivity anomaly. In the central part of the figure the agreement of observed and calculated values are demonstrated. (ROKITYANSKY, I.I., S.N.KULIK, I.M. LOGVINOV and V.N. SHUMAN, 1976)

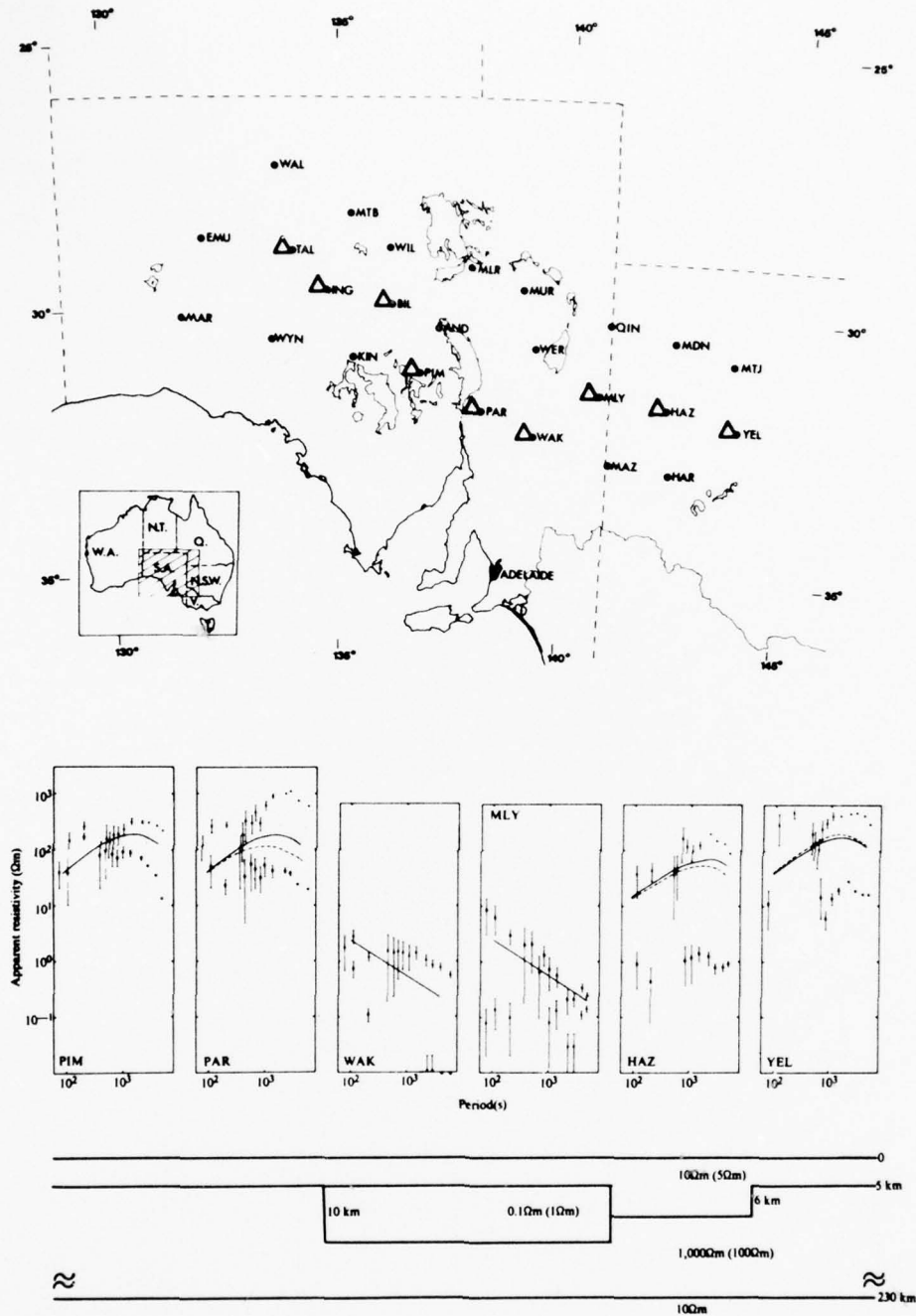


Fig. 11. The resistivity distribution along a profile across the Adelaide geosyncline in southern Australia, as inferred from magnetotelluric and geomagnetic measurements. A remarkable feature of the resistivity distribution proposed is the extreme low resistive body of only 0.1 ohm-m, a value comparable to the resistivity of seawater (0.25 ohm-m). (LILLEY, F.E.M. and H.Y. TAMMEMAGI, 1972).

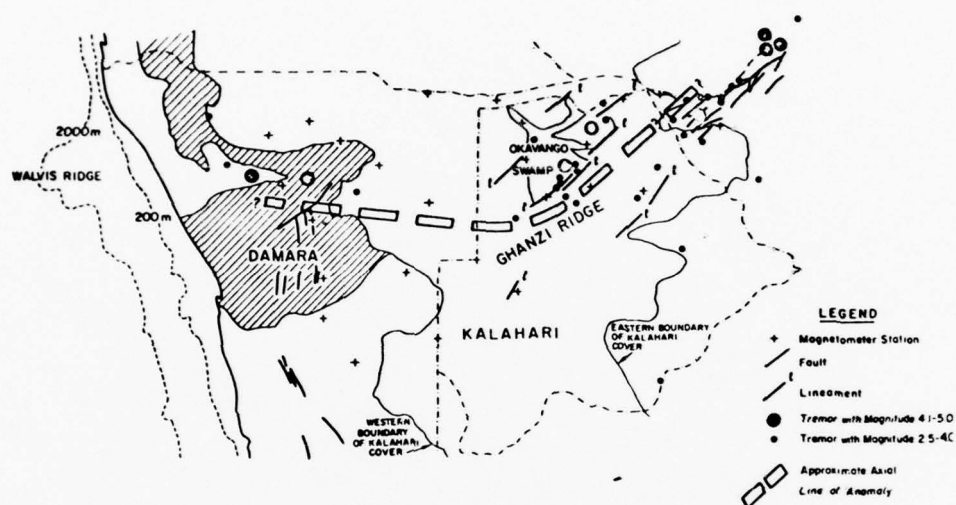


Fig. 12. A low resistive zone within the crust in South-West Africa, Botswana and Rhodesia, indicated by the dashed line. This result has been inferred from geomagnetic depth-soundings and does not correspond to any known surface-structures. (DE BEER, J.H., J.S.V. VAN ZIJL, R.M.J. HUYSEN, P.L.V. HUGO, S. J. JOUBERT, R. MEYER, 1976)

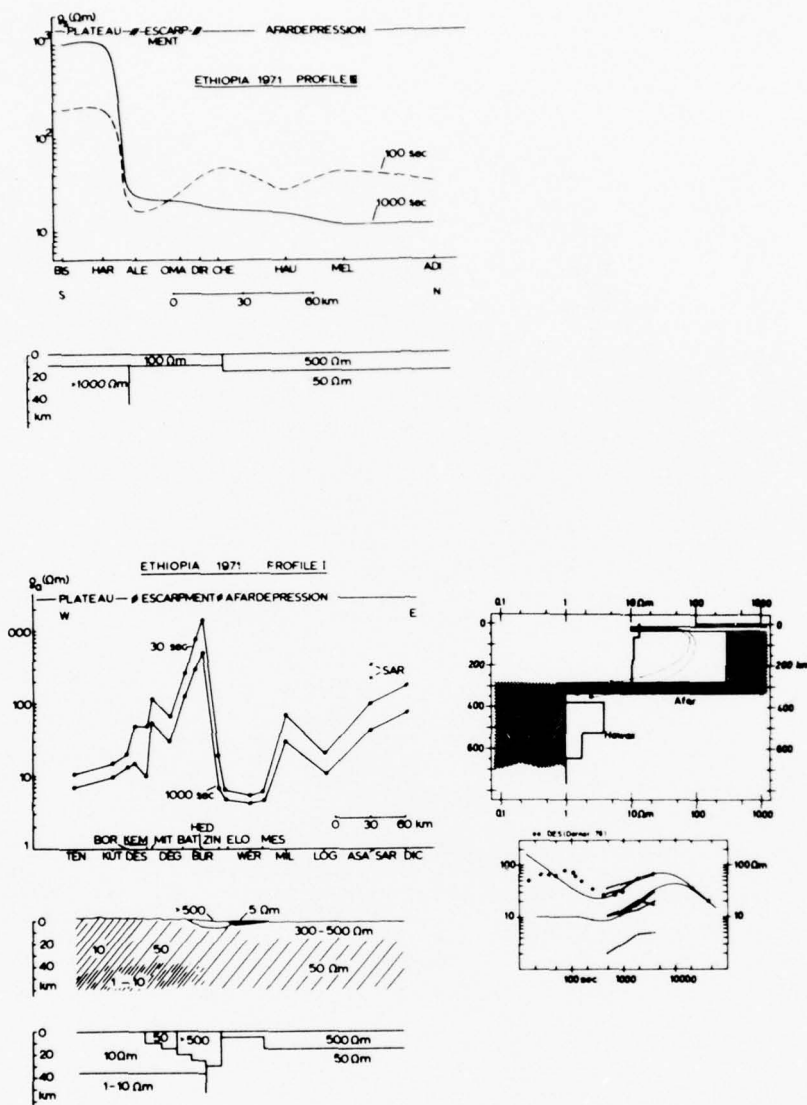


Fig. 13 The resistivity distribution along two profiles through the Afar-area, Ethiopia, inferred from magnetotelluric measurements. The Afar area and the adjacent highlands are covered by mighty layers of basalt. The resistivity, however, is as low as 10 - 50 Ohm-m. The whole area concerned is several hundreds kilometers in diameter. The low resistivities may be explained by anomalously high temperatures at shallow depths, probably caused by upwelling, overheated material of the Upper Mantle. (BERKTOLD, A., V. HAAK, G. ANGENHEISTER, 1975)

CONSEQUENCES DE LA DIFFUSION ET DE LA DEPOLARISATION DES ONDES ELECTROMAGNETIQUES PAR LE SOL DANS LES PROBLEMES DE RETRODIFFUSION

par

C.Goutelard et J.L.Coatanhay
LETTI - Université Paris - Sud
9, avenue de la Division Leclerc
94230 Cachan - France

RESUME

La diffusion des ondes électromagnétiques par la surface terrestre est un phénomène dont les difficultés d'étude sont bien connues.

Son importance est due aux applications nombreuses qui découlent et sa difficulté est due, d'une part aux ordres de grandeurs semblables des longueurs d'ondes et des aspérités, d'autre part à la complexité que posent les mesures expérimentales.

Le présent exposé traite, à partir de modèles théoriques dont la validité a été vérifiée expérimentalement, des conséquences qu'entraînent dans les problèmes de rétrodiffusion, les phénomènes de dépolarisation et de diffusion des ondes électromagnétiques par la surface terrestre. Une théorie de la formation des échos de rétrodiffusion est reprise et vérifiée par la confrontation des mesures effectuées simultanément par un sondeur zénithal et un sondeur par rétrodiffusion.

A partir de la simulation du profil d'ionisation par une couche parabolique, et de ses variations, une étude quantitative des spectres des échos de rétrodiffusion a été menée. Les profils d'ionisation ont été mesurés à partir d'une station de sondage zénithal et les spectres calculés à partir de ces mesures. Ils ont été ensuite comparés aux spectres des échos obtenus à partir d'une station de sondage par rétrodiffusion. La bonne corrélation entre ces résultats montre l'influence de la diffusion des ondes électromagnétiques par le sol ainsi que celle des mouvements des couches ionosphériques.

1. INTRODUCTION

Les problèmes de diffusion des ondes électromagnétiques par la surface terrestre prennent un aspect particulier lorsque leur longueur d'onde est de l'ordre de grandeur des dimensions des aspérités: c'est le cas de la diffusion par le sol des ondes courtes dont les longueurs d'onde dans le vide sont comprises entre 10 et 100 m.

Cette gamme est celle des propagations ionosphériques transhorizon.

Ces problèmes ont été abordés par de nombreux auteurs. Outre les études théoriques fondamentales de P.Beckmann et A.Spizzichino¹, M.A.Isakovitch², L.M.Brekovskikh³ des auteurs ont plus spécialement étudié l'effet de la diffusion des OEM dans le domaine des ondes courtes: L.H.Tventen⁴, et D.E.Barrick, J.M.Headrick, R.W.Bogle et D.D.Crombie⁵, qui se sont plus spécialement intéressés au problème de la rétrodiffusion des ondes par la mer.

Le contenu de cet exposé porte spécifiquement sur ce problème.

Deux cas ont été envisagés:

- Le cas où la diffusion se fait sur le sol. Dans ce cas la surface peut-être définie par un modèle théorique à caractéristiques aléatoires.
- Le cas où la diffusion se fait sur la mer: dans ce cas la surface peut-être définie à partir d'un modèle ayant des caractéristiques périodiques représentant la houle et d'un modèle ayant des caractéristiques aléatoires représentant le clapotis.

Le sujet traité dans cet article porte sur l'étude, à partir de modélisations simples de la surface terrestre, des phénomènes de diffusion qui apparaissent, des moyens expérimentaux de vérification et enfin des applications que l'on peut développer.

2. MODELISATION DE LA SURFACE TERRESTRE

Les modèles utilisés pour représenter la surface de la terre sont établis par la superposition de deux surfaces caractérisées par des propriétés statistiques définies dans un précédent article⁶. Ces modèles sont applicables aux cas où la surface éclairée S est très grande devant le carré de la longueur d'onde λ .

2.1 Cas de la réflexion sur le sol

Dans ce cas il faut tenir compte des aspérités du sol et des inhomogénéités du sous sol, la profondeur de pénétration des ondes, pour cette gamme étant de plusieurs mètres.

Le calcul a été effectué à partir de la théorie de Beckmann où les aspérités sont supposées normalement distribuées et caractérisées par:

leur écart type σ

leur distance de corrélation T

Il est nécessaire de faire apparaître pour ce modèle:

- Les aspérités à grande échelle représentant les vallonnements du terrain et caractérisées par T_1 et σ_1
- Les aspérités à petite échelle représentant les petits accidents dus à la végétation, aux constructions, aux inhomogénéités du sous sol... et caractérisées par T_2 et σ_2

Les résultats obtenus sont illustrés par le graphique de la figure 1 qui représente le coefficient de diffusion:

$$\rho = \left| \frac{E_2}{E_{20}} \right|^2$$

où E_2 = champ électrique de l'onde diffusée.

E_{20} = champ électrique qui serait diffusé dans la direction de réflexion spéculaire si la surface S était parfaitement plane, dans le cas où l'angle d'incidence est égale à 60° et pour différentes valeurs des paramètres σ_1 , T_1 , σ_2 , T_2 définissant la surface.

Il apparaît que:

- Dans les directions voisines de la direction de réflexion spéculaire l'affaiblissement peut devenir très important si le sol est très accidenté, tel le cas des montagnes, ce qui s'explique facilement par la plus grande diffusion de l'énergie incidente.
- Dans les autres directions, la diffusion est due uniquement aux aspérités à petite échelle. Le coefficient de diffusion demeure alors voisin de -100 dB quelque soit la direction considérée.

2.2 Pour la Mer

Il est nécessaire de tenir compte, ajouté à la structure périodique de la houle, du clapotis qui s'y superpose. Dans le cas le plus simple, la houle peut-être assimilée à une variation sinusoïdale et le clapotis a un modèle aléatoire superposé⁶.

La houle est définie par sa longueur d'onde Λ son amplitude h , et le clapotis par sa distance de corrélation T_2 et son écart type σ_2 .

La figure 2 illustre les résultats obtenus dans le plan d'incidence en donnant la valeur du coefficient de diffusion ρ dans le cas où $\Lambda = 5\lambda$ et pour différentes valeurs de $H = 2\pi \frac{h}{\lambda}$, le clapotis étant défini par σ_2 , T_2 .

Il apparaît que:

- Dans la direction de réflexion spéculaire l'affaiblissement n'est jamais très grand, même pour une mer agitée ($H = 2$).
- Dans les autres directions du plan d'incidence le clapotis est la principale cause de la diffusion. Le coefficient de diffusion est de l'ordre de -100 dB quelque soit la direction d'incidence.

Enfin, il est à noter que cette étude permet de mettre en évidence des lobes de diffusion situés en dehors du plan d'incidence lorsque la houle a une direction de propagation non située dans ce plan⁶.

2.3 Conclusion

De cette étude il ressort:

- Que dans les directions voisines de la direction d'incidence, le coefficient de diffusion est voisin de -100 dB
- Que ce phénomène étant causé par les aspérités à petite échelle leurs caractéristiques aléatoires entraînent une dépolarisation de l'onde diffusée.
- Qu'enfin, la transmission dans la direction de réflexion spéculaire est en général moins bonne lorsque la réflexion a lieu sur le sol plutôt que sur la mer.

3. CONSEQUENCES DE LA DIFFUSION ET DE LA DEPOLARISATION DES OEM DANS LES PROBLEMES DE RETRODIFFUSION.

Le principe des sondeurs à rétrodiffusion est bien connu: une onde électromagnétique émise du sol est réfractée par l'ionosphère et revient au sol à une distance de plusieurs centaines de kilomètres du point d'émission. La rétrodiffusion par le sol donne naissance à une onde qui revient vers le point d'émission où elle peut-être captée.

Le mécanisme de la formation des échos de rétrodiffusion peut-être analysé facilement à partir du diagramme de la figure 3 donnant les variations du temps de propagation t en fonction de la fréquence d'émission f .

A un instant donné la formation de l'écho est due (fig.3):

- à un rayon dit bas (1) ayant atteint la distance D_1 , le mode de propagation étant le même à l'aller qu'au retour.
- à un rayon dit haut (4) ayant atteint la distance D_3 , le mode de propagation étant le même à l'aller qu'au retour.
- à un mode de propagation mixte constitué par deux rayons atteignant une distance D_2 dû à une trajectoire aller de type haut (ou bas) et à une trajectoire retour de type bas (ou haut) causée par l'effet de diffusion quasi isotrope de la surface terrestre au voisinage de la direction d'incidence.

En résumé l'effet de diffusion des ondes par le sol fait apparaître trois modes de propagation: haut, bas, mixte.

L'influence du champ magnétique terrestre et l'effet de dépolarisation dû au sol complique la propagation puisque chaque mode incident donne naissance à un mode de propagation ordinaire et extraordinaire, et que l'effet de dépolarisation du sol introduit à son tour un dédoublement des modes de propagation pour les trajectoires de retour. Ainsi chacun des 4 modes de propagation pour les trajectoires aller induit 4 modes de propagation pour les trajectoires retour, comme l'illustre le tableau de la figure 4(a).

Les mouvements des couches ionosphériques introduisent pour chaque mode de propagation des variations de chemin optique qui se traduisent par l'effet doppler bien connu. Compte tenu du fait que, pour les fréquences utilisables dans les sondages par rétrodiffusion, les chemins des modes ordinaires et extraordinaires sont très voisins, on obtient finalement un spectre constitué par 3 quadruplets correspondant au mode de propagation haut, bas et mixte.

Les écarts de fréquence entre chacune des raies et la fréquence d'émission traduit l'effet Doppler, et l'apparition des quadruplets l'effet Faraday. Le fading affectant les signaux reçus résulte de l'interférence entre ces différentes composantes spectrales.

Le calcul des spectres des signaux de rétrodiffusion a été effectué à partir d'une modèle parabolique de l'ionosphère défini par sa fréquence critique F_c , la hauteur du maximum d'ionisation H_m , et sa demi épaisseur Y_m .

L'amplitude de chaque composante a été calculée à partir de l'équation classique du radar dont l'application au cas des propagations ionosphériques donne pour la puissance reçue dP_r :

$$dP_r = P_0 A^2 G_e G_r \left(\frac{d_a}{4\pi} \right)^2 \rho^2 \sin i_1 \sin i_2 \left(\frac{di_2}{dD} \right) \left(\frac{di_1}{dD} \right) (\delta D)^2$$

Expression dans laquelle: (fig.5)

- P_0 : puissance émise
- A : coefficient d'absorption déviative et non déviative dans l'ionosphère
- G_e : gain d'antenne à l'émission
- G_r : gain d'antenne à la réception
- d_a : ouverture azimutale du lobe d'antenne supposée identique à l'émission et à la réception.
- ρ : carré du module du coefficient de diffusion du sol
- i_1 et i_2 : angles d'incidence, respectivement pour la trajectoire aller et pour la trajectoire retour.
- D : distance atteinte

Les déplacements en fréquence ont été calculés par l'intermédiaire du chemin optique de chacun des rayons. La variation de phase ϕ le long d'un trajet pouvant se mettre sous la forme:

$$\phi = \phi_1 + \phi_2,$$

avec

$$\phi_1 = \frac{2R\omega \sin \theta}{c \sin i_0}$$

et

$$\phi_2 = \frac{2\omega}{c} \int_{H_0}^{H_s} \frac{n^2(R+H)}{[n^2(R+H)^2 - (R+H_0)^2 \sin^2 i_0]^{1/2}} dH$$

où (fig.5)

- R : rayon terrestre
- ω : pulsation de l'onde émise
- H_0 : hauteur du bas de la couche
- H_s : hauteur de réflexion
- θ : angle géocentrique de la trajectoire
- i_0 : angle d'incidence de l'onde à la hauteur h
- n : indice du milieu à la hauteur h
- c : vitesse de la lumière dans le vide.

Les résultats obtenus sont illustrés par les figures 6 et 7 qui montrent que:

- Les trois modes de propagation ont des amplitudes comparables au voisinage de la focalisation et que seul subsiste le rayon bas loin de la focalisation.
- Les courbes de phase ϕ versus D/c font apparaître des variations rapides de la phase en fonction de la distance pour le rayon haut.

Ces courbes ont été calculées pour un ensemble de 63 figurations des couches permettant une représentation de tous les états standards de l'ionosphère.

Il a été possible ainsi de calculer la fréquence Doppler f_d dont est affecté chacun des modes. Le résultat des calculs menés par ordinateur a permis d'exprimer l'effet Doppler par la relation:

$$F_d = -F_e \left[\frac{\partial \phi}{\partial H_m} (Y_m, K) \frac{dH_m}{dt} + \frac{\partial \phi}{\partial Y_m} (H_m, K) \frac{dY_m}{dt} + \frac{\partial \phi}{\partial K} (H_m, Y_m) \frac{dK}{dt} \right]$$

où

- F_e : fréquence d'émission
- K : F_e/F_c

$$\frac{\partial \phi}{\partial H_m} (Y_m, K); \frac{\partial \phi}{\partial Y_m} (H_m, K); \frac{\partial \phi}{\partial K} (H_m, Y_m);$$

dérivées partielles de la variation de phase dont les valeurs sont données sur les planches des figures 8, 9, 10.

Ces résultats font ressortir que:

- la fréquence Doppler du rayon mixte est la moyenne arithmétique des fréquence Doppler des rayons bas et haut.
- le rayon bas est peu affecté par les variations de la fréquence critique alors que le rayon haut y est très sensible.
- les variations de hauteur du maximum d'ionisation et de la demi épaisseur affectent de façon semblable tous les rayons.

Ces calculs permettent de montrer que l'effet Faraday se traduit par la création des quadruplets précédemment cités, mais dont l'observation paraît actuellement peu probable, le dédoublement des raies initiales n'étant que de quelques millièmes de hertz.

4. VERIFICATIONS EXPERIMENTALES

Les vérifications expérimentales ont été faites à partir d'un sondeur ionosphérique à rétrodiffusion installé à Rennes (France). Les essais ont été effectués avec une direction de tir située dans le sud de façon à avoir une rétrodiffusion sur le sol et non sur la mer. Les mesures ont été confrontées avec les calculs théoriques effectués à partir de sondage zénithaux obtenus à la station de Lannion (France).

Les résultats présentés ici correspondant à une série de mesures effectuées durant le mois de Septembre 1975.

Durant cette période les moyennes mensuelles des paramètres F_c , H_m , $H_o = H_m - Y_m$ des couches ont été représentées sur la figure 11(a). Il est alors possible d'en déduire pour chacun des rayons: haut, bas, mixte, les fréquences doppler (fig. 11(b)).

Il apparaît que le matin les fréquences Doppler calculées sont positives et le soir négatives.

Les résultats expérimentaux ont été obtenus par l'utilisation d'un système d'analyse spectrale dont la résolution maximale est de 0,01 Hertz.

La figure 12 montre, en exemple, 3 enregistrements types effectués le matin, en milieu de journée et le soir. On peut observer la présence de trois raies dont les fréquences doppler sont positives le matin et négatives le soir. En milieu de journée les trois raies sont confondues, les variations des paramètres ionosphériques étant très faibles à ces heures.

La confrontation des résultats des mesures directes et des calculs menés à partir de sondages zénithaux a été effectuée en reportant l'ensemble des points des mesures directes sur le graphique de la figure 13 et en déterminant la droite de régression. Cette droite de régression comparée à celle obtenue par le calcul montre le bon accord des résultats expérimentaux et théoriques.

Une corrélation établie à partir des résultats obtenus sur le journée du 18 Septembre 1975 montre encore le bon accord entre les résultats théoriques et expérimentaux.

CONCLUSION

Les effets de diffusion des ondes électromagnétiques par le sol sont causes de l'apparition de trois raies principales dans les spectres d'échos de rétrodiffusion.

Ces trois raies sont observées dans les relevés expérimentaux. Il apparaît que les positions de ces raies sont corrélées avec les variations des paramètres ionosphériques.

Une modélisation parabolique de l'ionosphère permet de relier de façon quantitative la fréquence Doppler de chaque mode aux vitesses de variation de la fréquence critique, de la demi épaisseur et de la hauteur du maximum d'ionisation des couches.

Dés lors, il paraît envisageable d'utiliser ces résultats pour affiner des méthodes de prévisions ionosphériques à très court terme.

REFERENCES

1. Beckmann, P.
Spizzikino, A. *The Scattering of Electromagnetic Waves From Rough Surfaces.* Pergamon Press London, 1963.
2. Isakovitch, M.A. *The Scattering of Waves From a Statistically Rough Surface.* Zh.Eksp. Théor, Vol 23, pp 305-314, 1952.
3. Brekovskikh, L.M. *The Diffraction of Waves by Rough Surface.* Zh.Eksp. Théor, Vol 23, pp 275-289, 1952.
4. Tventen, L.H. *Ionospheric Propagated Sea Scatter.* Science, Vol 157, p 1302-1304, 1969.
5. Barrick, D.E.
Headrick, J.M.
Bogle, R.W.
Crombie, D.D. *Sea Back Scatter at HF: Interpretation and Utilisation of The Echo.*
6. Goutelard, C. *La Reflexion des Ondes Décamétriques par la Surface Terrestre en Emission Impulsionnelle et Son Role Dans l'Interprétation des Spectres de Fréquence des Echos Obtenus dans les Sondages par Rétrodiffusion.* AGARD Conference Proceedings 37, XIVth Symposium on Electromagnetic Wave Propagation, August 1968.

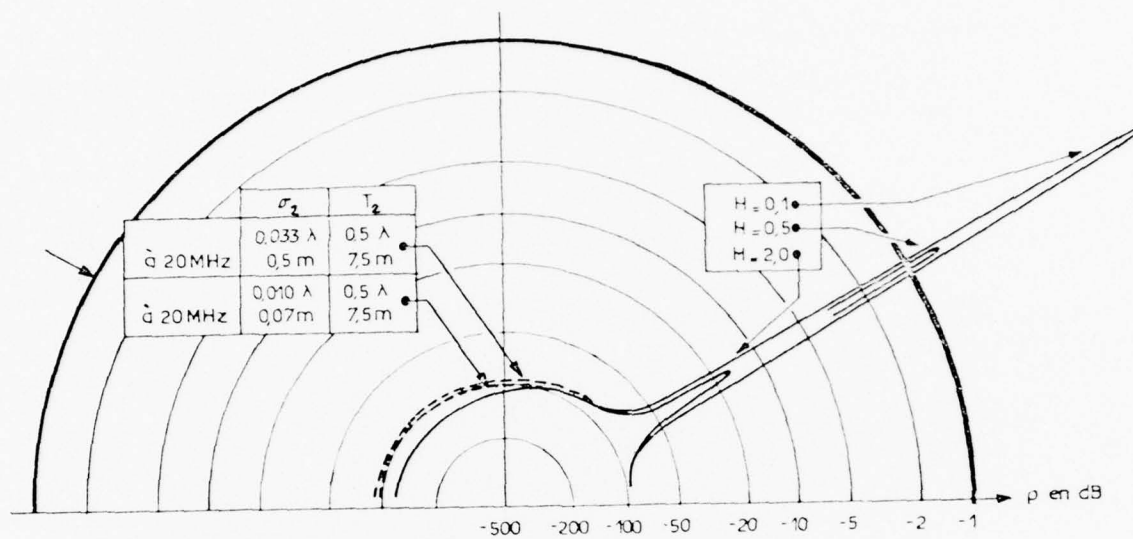


Fig.1 Coefficient de diffusion obtenu sur la mer

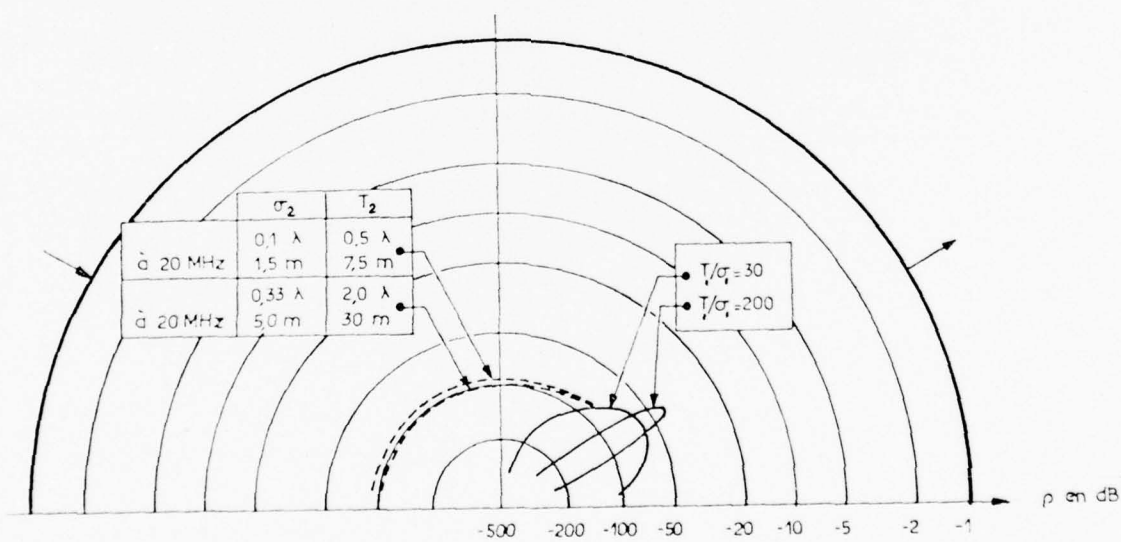


Fig.2 Coefficient de diffusion obtenu sur le sol terrestre

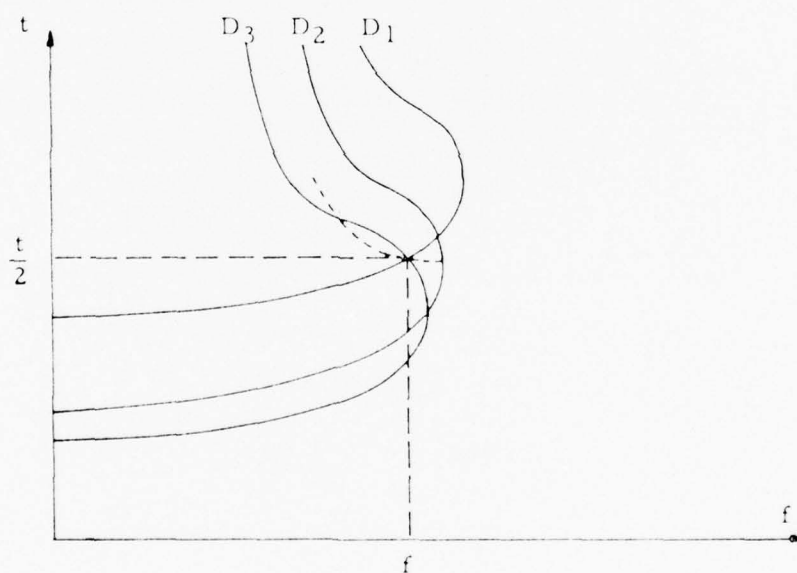
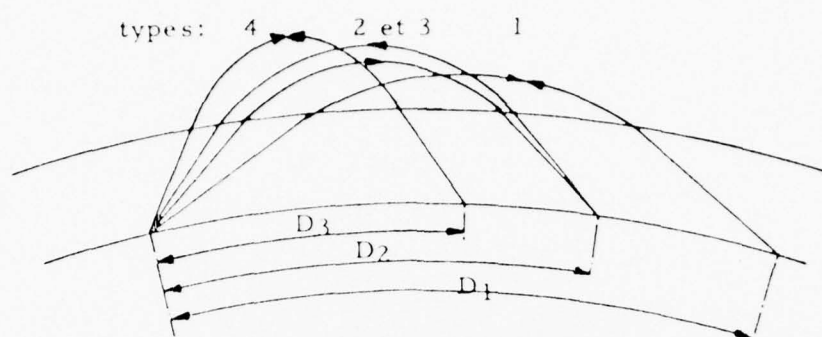


Fig.3 Mécanisme de formation des échos de rétrodiffusion

	Bas		Haut	
	Ordinaire	Extraordin.	Ordinaire	Extraordin.
Trajet aller	↓	↓	↓	↓
Effet du sol	Diffusion - Dépolarisation			
Trajet retour	↑	↑	↑	↑
	↑	↑	↑	↑
	↑	↑	↑	↑
	↑	↑	↑	↑

Fig.4(a) Résumé des modes de propagation possibles

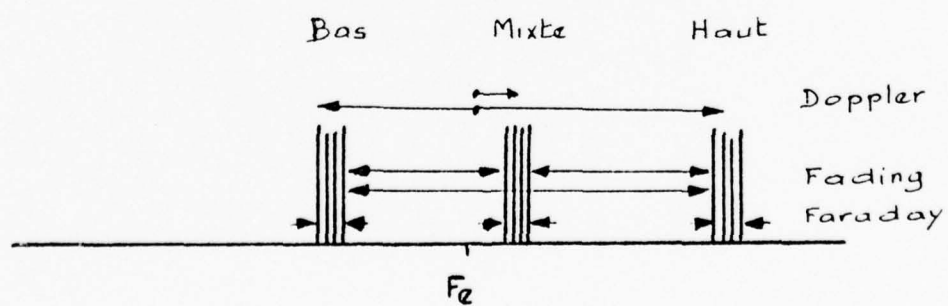


Fig.4(b) Allure générale des spectres obtenus en rétrodiffusion

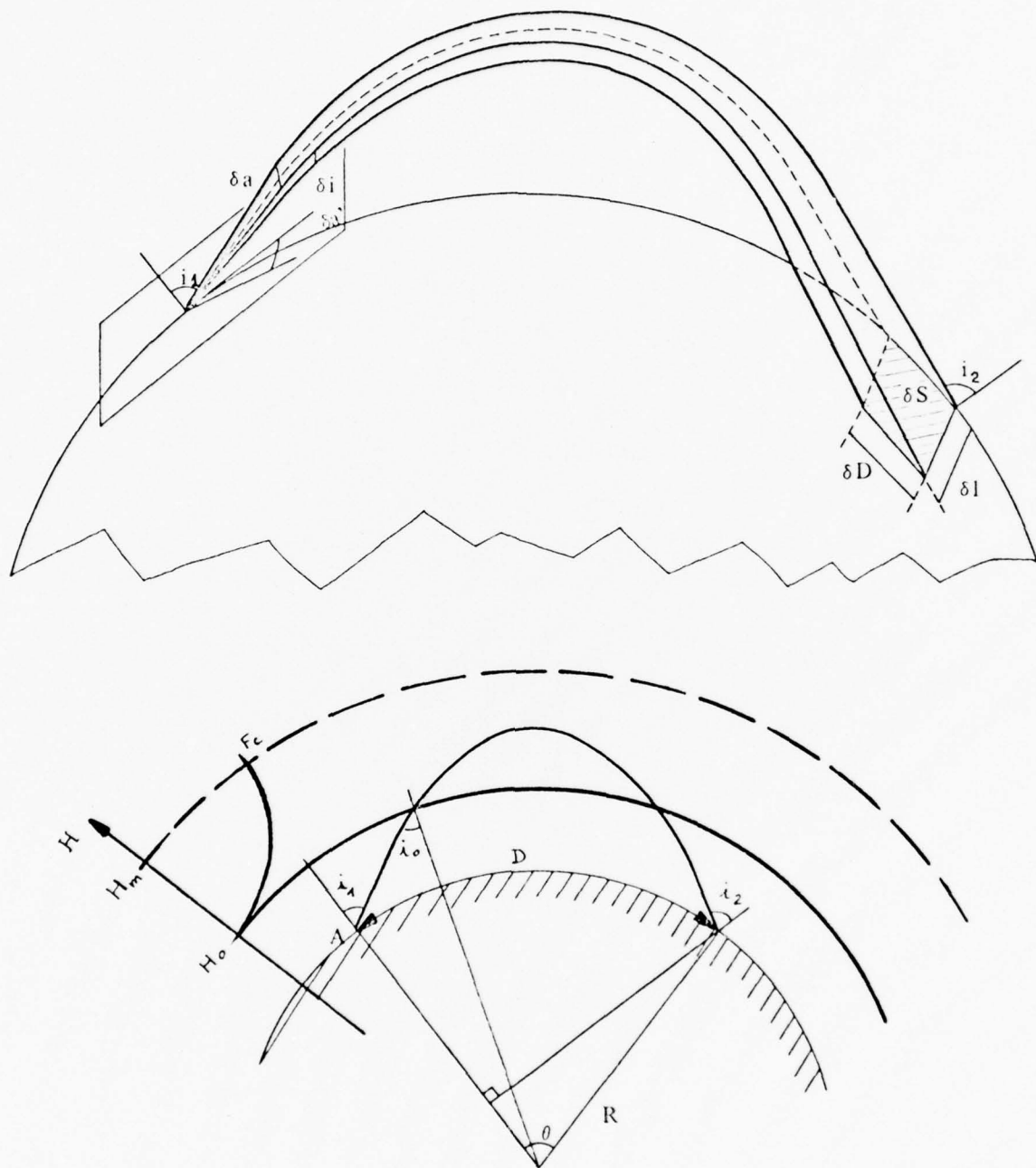


Fig.5 Géométrie et notation relatives aux modes de propagation

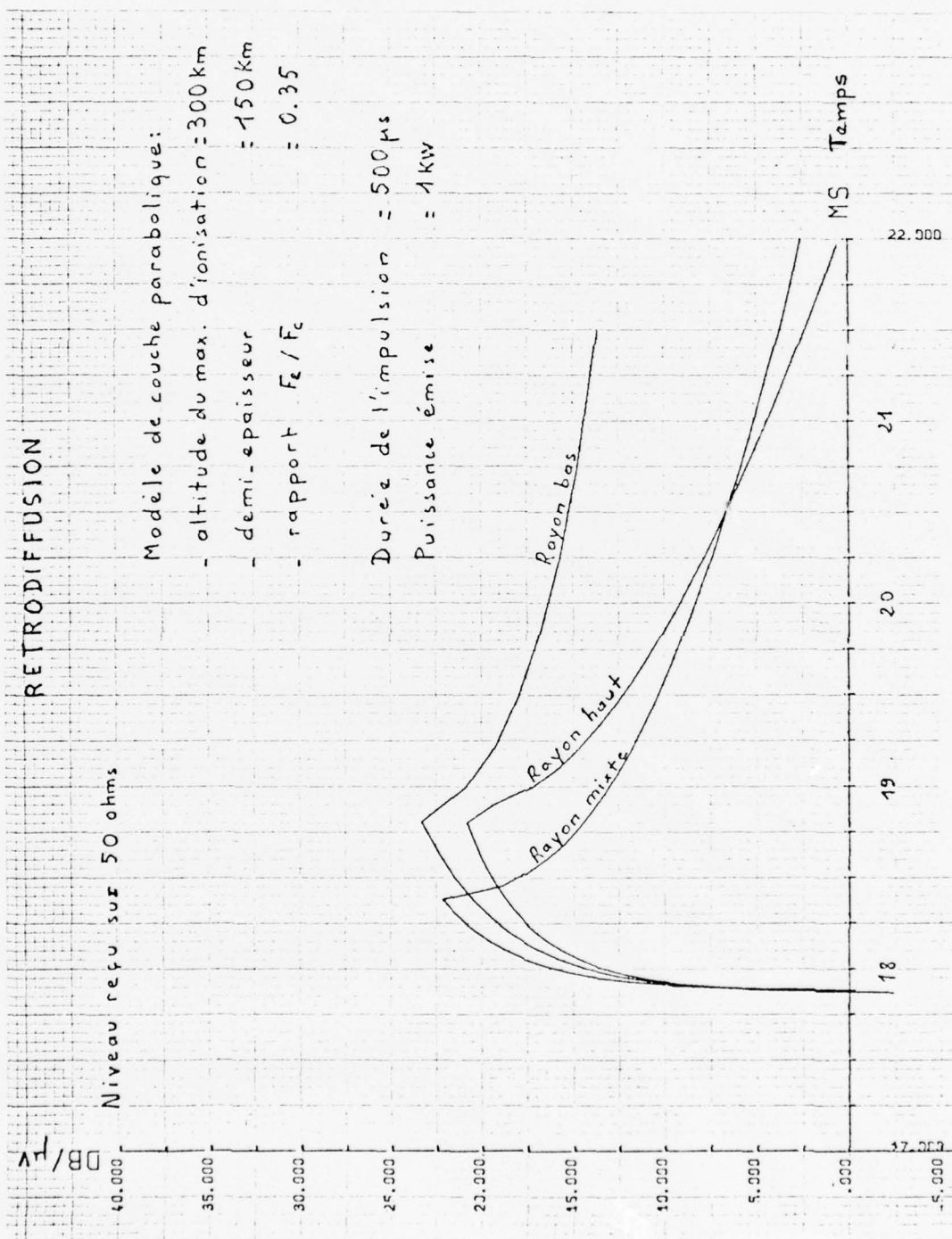


Fig.6 Amplitude des 3 modes de propagation

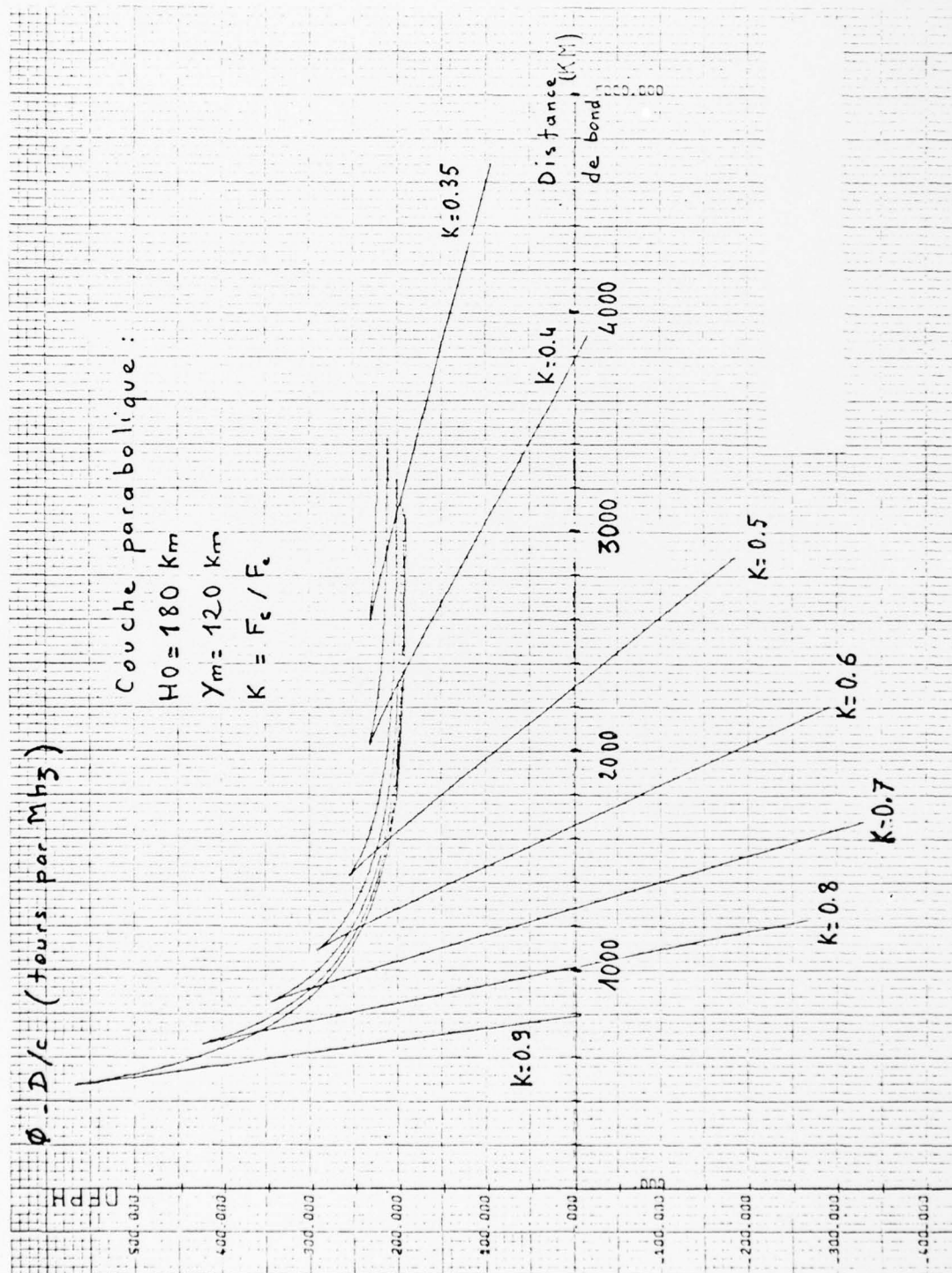
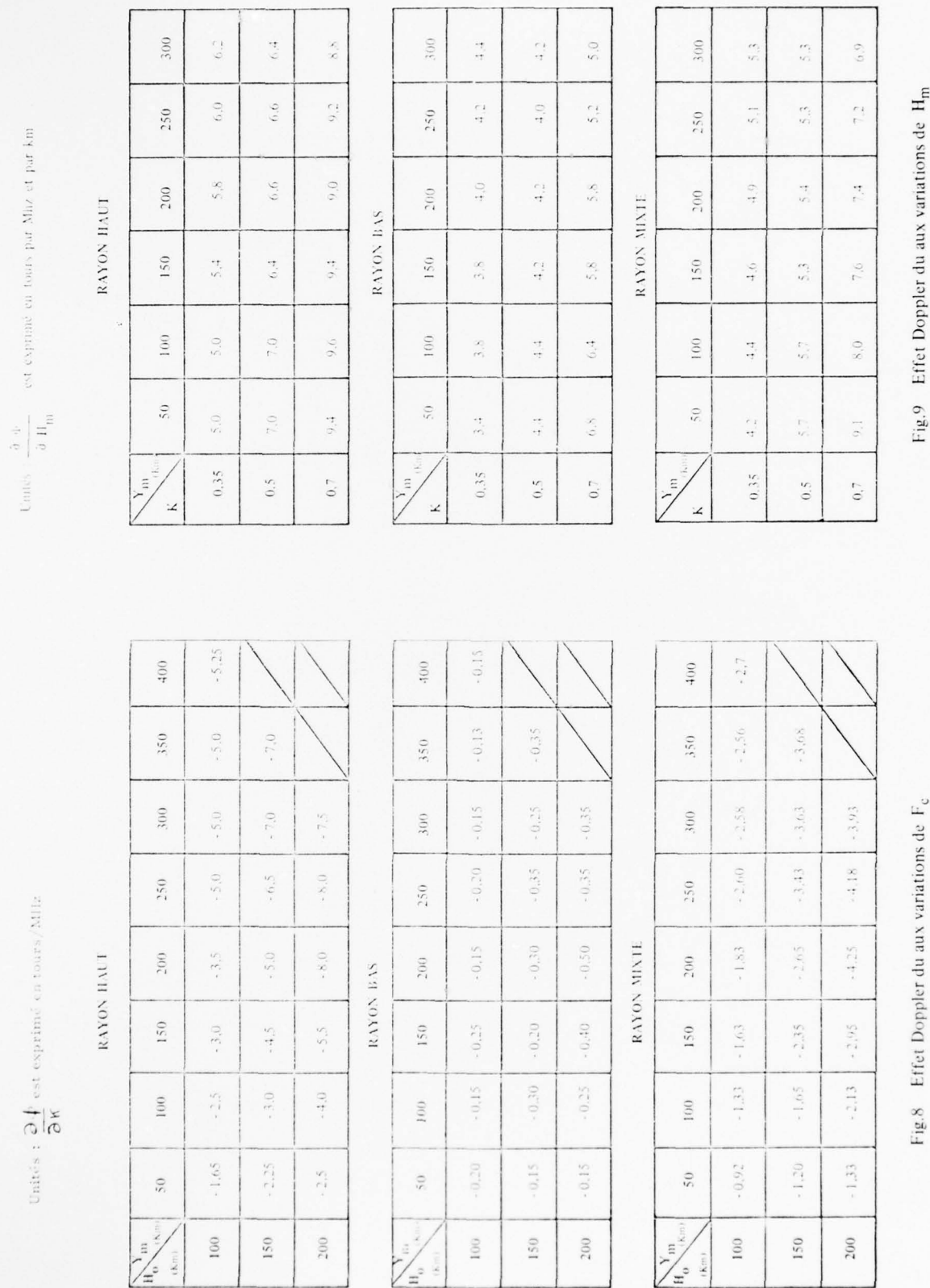


Fig.7 Phase des 3 modes de propagation

Fig.8 Effet Doppler du aux variations de F_c Fig.9 Effet Doppler du aux variations de H_m

Unités : $\frac{\partial \omega}{\partial Y_m}$ est exprimé en tours par Mhz/km

RAYON HAUT

$\frac{H_m}{K}$ K	200	250	300	350	400	450	500
0.35	- 3,0	- 3,0	- 3,2	- 3,6	- 3,9	- 4,0	
0.5	- 4,0	- 4,4	- 4,2	- 4,4	- 4,6	- 4,6	- 4,6
0.7	- 5,2	- 5,5	- 5,5	- 5,7	- 5,8	- 5,8	- 6,0

RAYON BAS

$\frac{H_m}{K}$ K	200	250	300	350	400	450	500
0.35	- 3,0	- 3,0	- 3,2	- 3,3	- 3,6		
0.5	- 4,0	- 4,0	- 4,0	- 3,8	- 3,8	- 3,8	- 3,8
0.7	- 5,4	- 5,3	- 5,3	- 5,0	- 4,8	- 4,6	- 4,6

RAYON MIXTE

$\frac{H_m}{K}$ K	200	250	300	350	400	450	500
0.35	- 3,0	- 3,0	- 3,2	- 3,4	- 3,8		
0.5	- 4,0	- 4,2	- 4,1	- 4,1	- 4,2	- 4,2	- 4,2
0.7	- 5,3	- 5,4	- 5,4	- 5,4	- 5,3	- 5,2	- 5,3

Fig.10 Effet Doppler du aux variations de Y_m

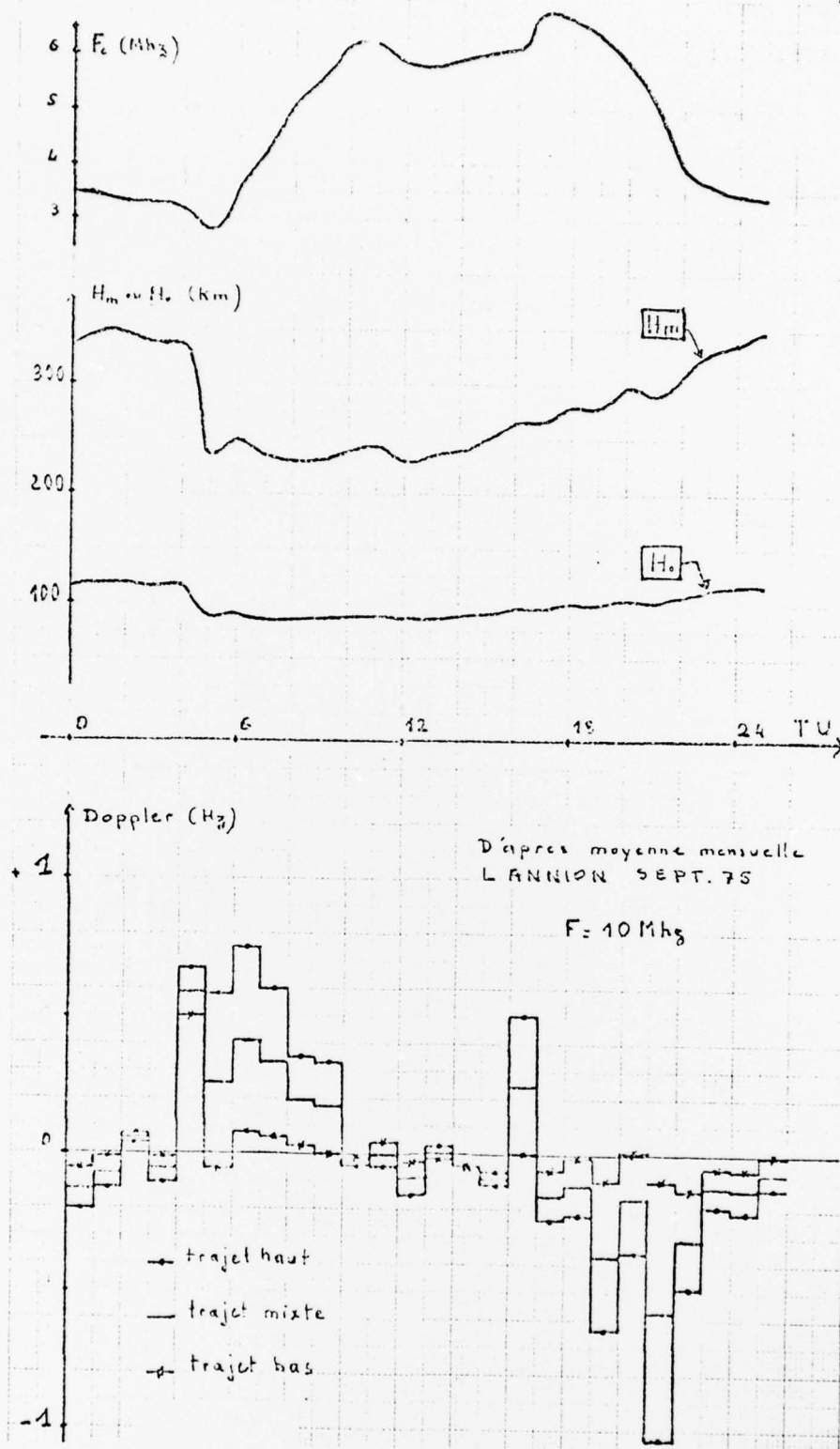
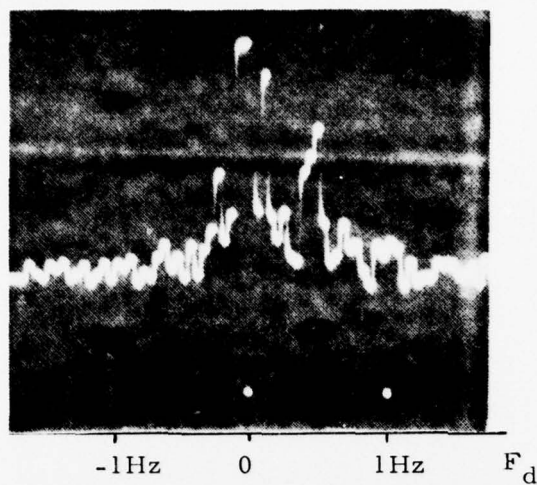
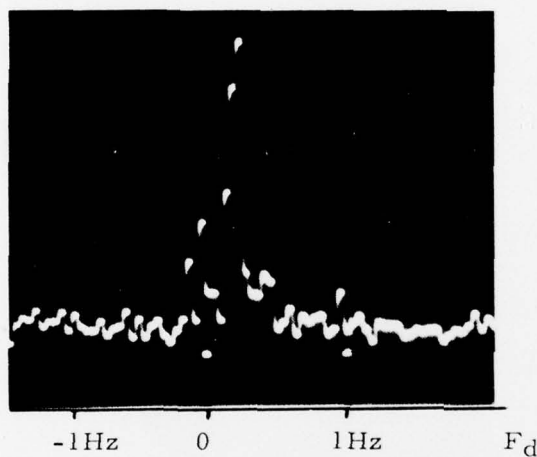


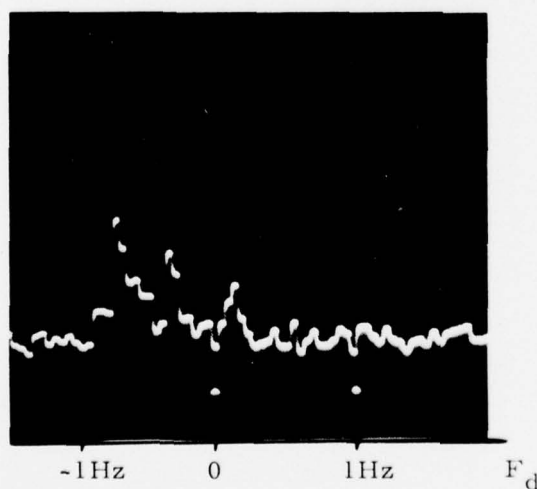
Fig.11 Effet Doppler affectant chaque mode et calculé à partir des résultats de sondages zénithaux effectués à la station du CNET de LANNION



Spectre obtenu à 07 h 25 TU
 $F_e = 16,5$ MHz
 Distance : 2100 km



Spectre obtenu à 13 h 30 TU
 $F_e = 16,0$ MHz
 Distance : 2025 km



Spectre obtenu à 16 h 45 TU
 $F_e = 18,5$ MHz
 Distance : 2100 km

Fig.12 Exemples de spectres relevés expérimentalement à la station de Rennes le 12 Septembre 1975 dans la direction de tir 235

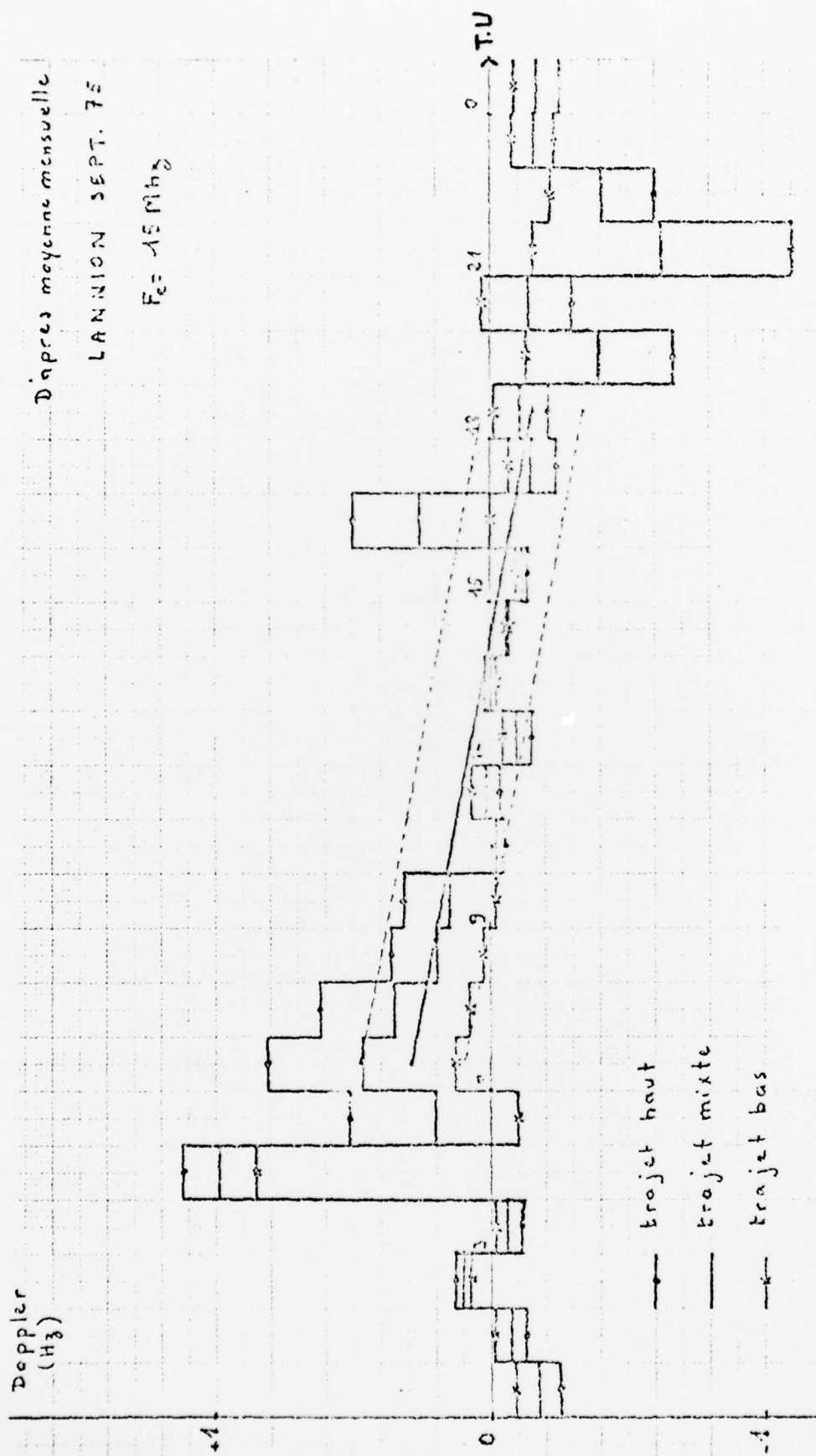


Fig.13(a) Résultats obtenus à partir de la station de sondage zénithale de Lannion pour le mois de Septembre 1975 et droite de régression pour la période 6h - 18 h TU

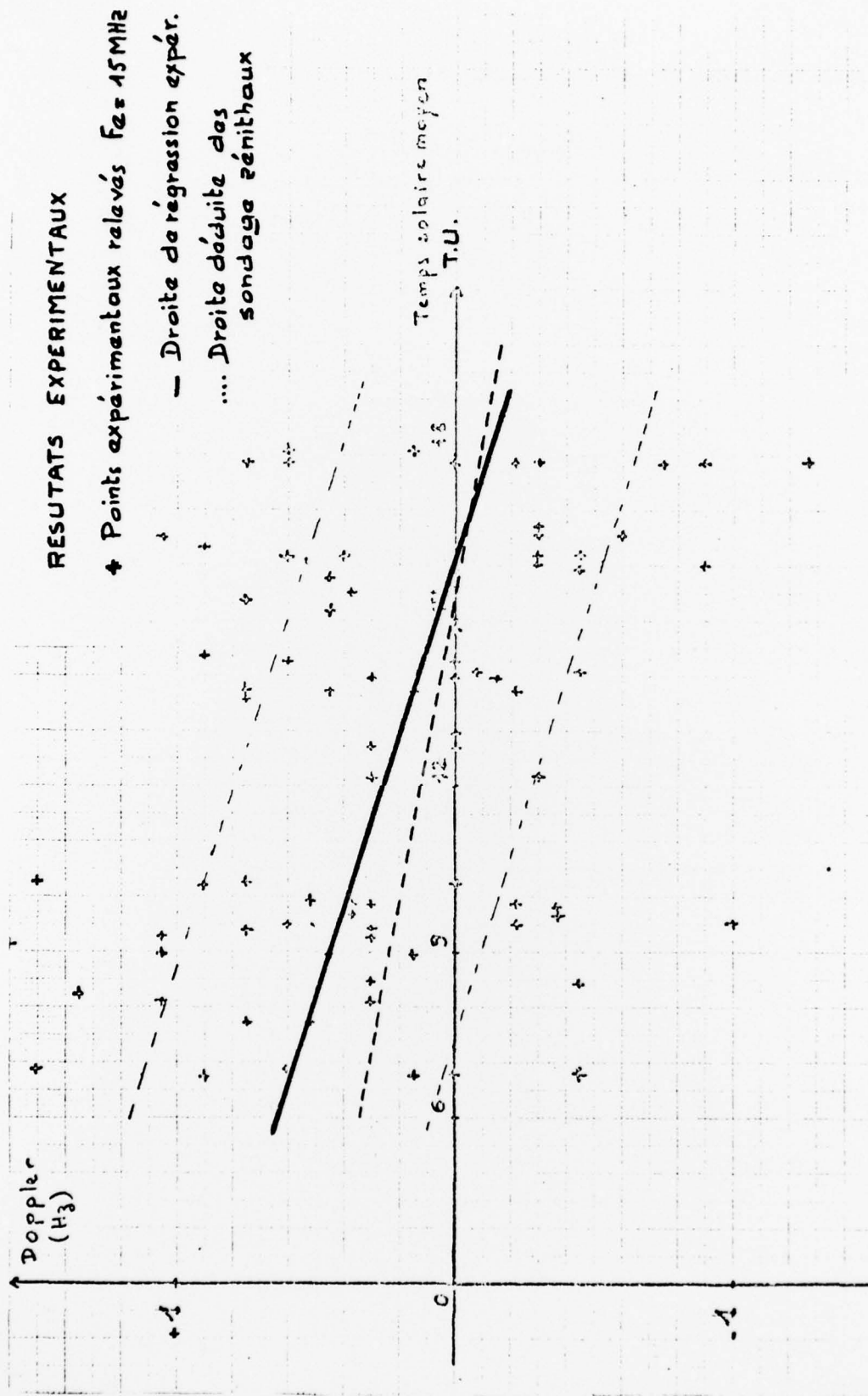


Fig.13(b) Résultats expérimentaux et comparaison avec ceux déduits des sondages zénithaux

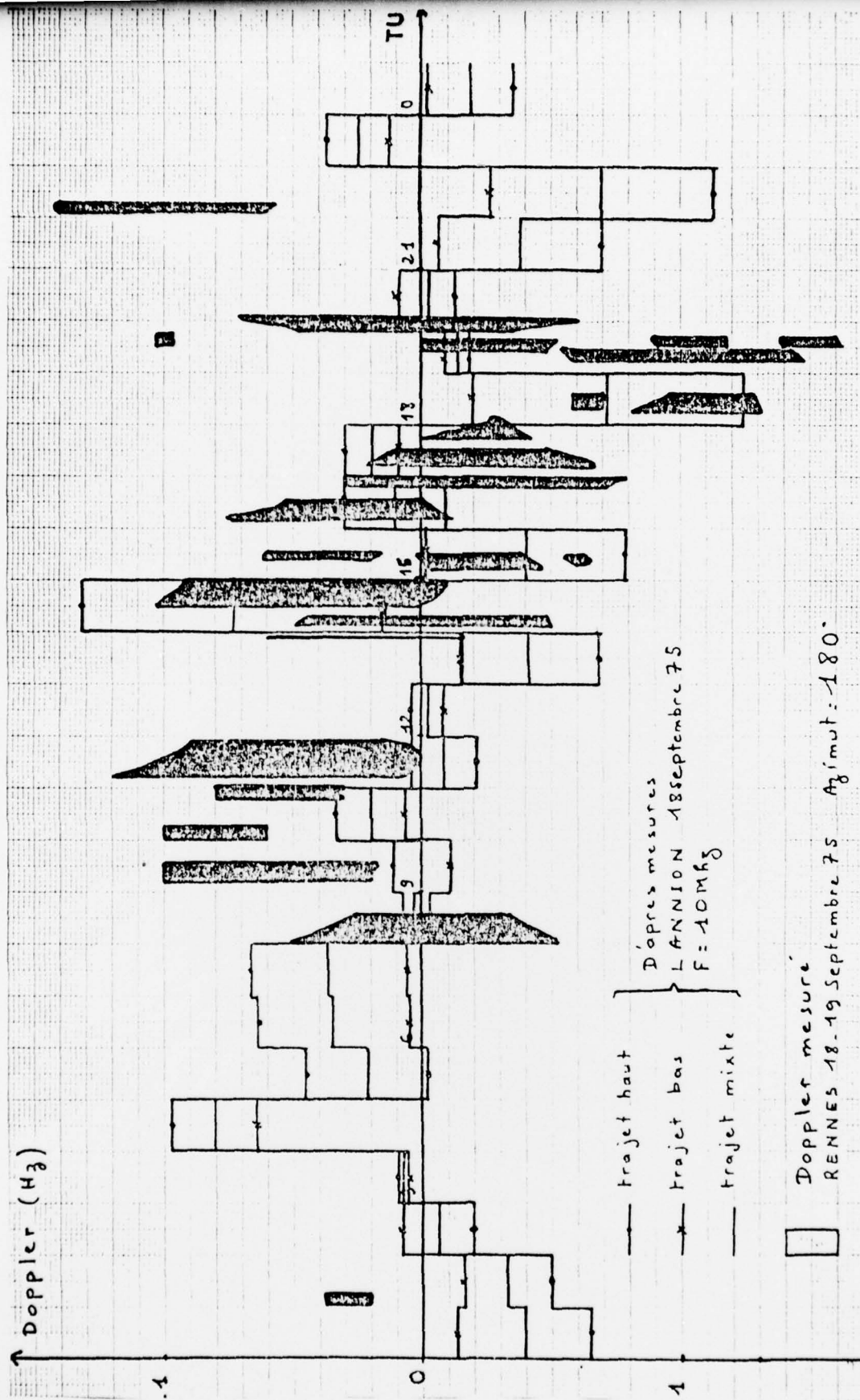


Fig.14 Comparaison des résultats obtenus la journée du 18 Septembre 1975

ROUND-TABLE DISCUSSION
ON
EM PROPAGATION CHARACTERISTICS OF SURFACE MATERIALS AND INTERFACE ASPECTS

Participants at Round Table: H.J. Albrecht (Chairman)
J.S. Belrose
A.W. Riggs
L.B. Felsen
E. Raschke

In his initial comments, H.J. Albrecht emphasized the suitability of round-table discussions as a method of summarizing results of a scientific meeting, with particular regard to the state of the art, engineering aspects, and promising areas of research. He then introduced the participants at the round table and invited the audience to contribute to the discussion.

Referring to a previous meeting held 1967 in Turkey (in Ankara, Conference Proceedings No. 33, edited by K. Davis, issued 1970), J.S. Belrose enquired on progress achieved in work then reported and relevant to the subject of this meeting. Particular reference was made to studies on propagation over ice-covered sea, displaying real discontinuities in conductivity and lesser forms of this phenomenon over rather stratified media in ground-wave propagation.

A.W. Riggs commented on this subject and described experiments conducted in Alaska and Greenland over a deeper ice area with the objective of finding evidence for surface-wave propagation. However, signal enhancements observed were apparently due to the recovery effect as a consequence of a ground wave travelling without too much attenuation over sea water and then touching an area of considerably different refractive index. H.J. Albrecht added that he contributed himself to the appropriate session of the Ankara meeting as an author and co-author, one of the papers referring to a propagation path using buried antennae, one on a very low frequency and one around one GHz, the latter one enclosed in a radome to make sure that the lossy medium would not be in the direct surroundings of the antenna. He added that the objectives of this particular work had been reached some time ago, and that it had not been continued.

Turning to another subject, H.J. Albrecht drew the attention of the audience to propagation in interface media as one of the possibly promising areas of research, and particularly mentioned the variable effect of ground-inversion layers upon propagation paths, as indicated in the paper contributed by L. Fehlbauer and H.G. Giloi. His comments further referred to consequent changes in multipath fading characteristics of any particular link suffering from the sum of the direct ray plus the reflected ray, due to changes in the altitude and in the refraction characteristics of the inversion layer. This leads to variations in the modes that may appear in the duct, and is directly connected to more meteorological questions. Confirming these comments from a meteorological point of view, E. Raschke stated that appropriate measurements would have to be done in each case, at heights up to about 250 meters, because relevant inversion layers may demonstrate appropriate intensity up to that order of altitude. Considering weather situation, cloud cover, as well as the total influxes of moisture and heat going from ground into the air, and the radiation budget, a theoretical model may possibly be established for calculation and prediction of propagation effects.

Referring to the subject under discussion, B. van Dijl addressed the question of a possible relation between inversion layers and the type of soil, not only in the case of valleys but generally. H.J. Albrecht mentioned a recent paper with some connection to this problem (G. Zdunkowski, J. Paegle, J.P. Reilly, The effects of soil moisture upon the atmospheric and soil temperature near the air-soil interface, Arch. Met. Geoph. Bio., A-24, pp. 245-268, 1975). In his reply, E. Raschke emphasized the effect of heat conductivity and moisture of the soil and mentioned as an example that, with enough moisture available to be evaporated, an inversion may not be as intense as in the case of a very dry surface with low heat conductivity. This conductivity here refers to heat flow from the ground into the air because the inversion should always be considered as some type of steady state of equilibrium between vertical heat flux, radiation, and heat penetrating into the ground, and vice versa from the ground into the air. There is thus a pronounced relationship between some soil type and the intensity of an inversion. Summarizing the discussion so far, H.J. Albrecht then referred to the importance of theoretical aspects in interface problems.

In addressing the subject of ground-wave and ducted propagation theory, L.B. Felsen pointed out that interface properties can be represented in terms of surface impedance. Work has been done on propagation over ground that can have variable surface impedance and discontinuities in surface impedance; the techniques developed are primarily integral equation techniques and mode-matching techniques. He added that the surface-impedance concept is not always applicable. If it is necessary to look beneath the surface, one cannot just close the surface off by means of a surface impedance. With stratification under the ground and, in particular, with possible discontinuities in stratification where layers terminate abruptly and then join onto some other layers, one must employ a more detailed analysis of propagation and junction problems. This is also true for a forest environment, with propagation taking place over smooth ground and a junction discontinuity being represented by the forest boundary. Thus the general problem of discon-

tinuities, essentially of abruptly terminated slab regions, requires attention and can be approached by different techniques. Most customary is the mode-matching procedure whereby the field on either side of the discontinuity is represented in terms of the characteristic modes that can propagate there, and then these fields are matched across the interface to satisfy required continuity conditions. This leads to an infinite system of equations or to an integral equation, either of which has been treated by numerical methods. L.B.Felsen then continued that while numerical methods have been employed very extensively and are in principle capable of generating highly accurate answers, it is necessary to look much more closely at the errors inherent in a numerical procedure before a numerical solution can be accepted with blind faith. Thus, the quality control of numerical solutions requires attention. Also, numerical solutions of integral equations are not very efficient for problems involving "high" frequencies whereby a ground inhomogeneity or a junction effect appears large compared to the wavelength. This is so because the discretization of the integral has to be such that each wavelength contains several segments, thereby making the number of segments unacceptably large. To deal with this difficulty one attempts to extract the predominant high frequency behaviour of a particular scattering problem by analytical means, and the computer is then more efficiently applied to the residual low frequency content. This area representing a mixture of analytical and numerical methods requires urgent attention.

L.B.Felsen continued that, in connection with ducts or layers, one should not limit himself immediately either to a study in terms of the guided modes of the layer or a study in terms of the ray-optical model of the layer. Both methods have their areas of applicability; recent techniques have been developed which allow one to change from a ray-optical description to a guided-mode description. Thus, it is not necessary to adhere to the ray-optical description of ducted propagation once a study has so commenced: ray-optical descriptions may be used in the vicinity of the source where they are more efficient while further along the duct, they may be converted to a mode description.

Continuing, L.B.Felsen indicated the steady need for statistical approaches. Many propagation paths have statistical content. The statistical aspects of the propagation mechanism have to be explored more vigorously. While the influence of statistical surface properties on ground waves has been taken into account quite frequently in connection with reflection and scatter phenomena, the effects (reflection, transmission and guiding) of two penetrable media separated by a randomly varying interface have been given little consideration. In this context, L.B.Felsen supported the approach of one of the papers presented during the meeting. He then suggested to the theoreticians to keep in touch with the practitioners as much as possible for the purpose of choosing models for their theoretical analysis. A theoretical model which can be solved is not necessarily optimum if it has to be applied to a practical situation. On the other hand, a warning has to be given to the practitioner as well. Taking measurements first and then asking the theoretician for an analysis is not an optimum approach; usually such data material is so complicated that significant features cannot be extracted. L.B.Felsen emphasized the importance of scientific meetings like the present one, to establish a continuing dialogue between practitioners and theoreticians so that they can learn to appreciate each other's problems. H.J.Albrecht supplemented these comments by remarks on the task of AGARD as a scientific advisory institution, which is scientific research as well as valid engineering advice to all the entities requiring such assistance within NATO. Interface aspects between theory and practice are addressed very frequently in AGARD activities.

Referring to L.B.Felsen's comments on the surface-impedance concept, K.D.Becker asked when this concept should be used and when it should not be used under any circumstances. In reply, L.B.Felsen supported the impedance concept as a very good one if the medium is highly lossy and if the source is removed sufficiently far from the interface so that no interaction can occur between source and interface via the storage fields. This implies that the interface is in the radiation zone (i.e., out of the near field zone) of the source. In that fashion, the concept was originally formulated by Leontovitch in the 1940s. It is also possible to use the surface-impedance concept rigorously as long as only propagation within a single mode is considered. With a single mode, even over a stratified medium, one can look into the medium vertically and obtain an input impedance to it, which then becomes an effective surface impedance for that mode. But a different mode generally sees a different effective surface impedance. Under certain conditions -- i.e., with certain combinations of medium constants and propagation characteristics, and with a limited spectral range of the mode -- it is possible to make variations in these modal impedances fairly small. One can then use a surface impedance for several modes, even though the medium is somewhat transparent. But this may depend sensitively on the arrangement of the dielectric constants. The safe way to proceed is to set up the problem rigorously (for example, in a multi-layered medium) and ascertain the circumstances under which simplifications leading to a valid surface impedance can be recognized. In summary, the surface-impedance concept is a useful but limited one; it should be approached with great care and caution.

Commenting on L.B.Felsen's remarks on the relation between theory and experiment, J.S.Belrose reported on projects at the Communication Research Centre at Ottawa, in particular on the propagation over actual earth and on a computer programme dealing with such propagation for the purposes of engineering or spectral management of communication circuits. At frequencies of VHF and UHF, a computer programme had been developed based on empirical and semi-empirical methods, not rigorous ones, to calculate field-strengths. The programme includes a complete topographical map of the area of concern. It is simple for the user who only has to enter the geographical coordinates of transmitter and receiver, heights of antennae, and power of the transmitter. Experiments are being con-

ducted to test the accuracy of the computer programme with respect to reality. Referring to L.B.Felsen's paper and his description of the physical picture of ground-wave propagation in the presence of smooth hills and depressions, J.S.Belrose commented on smoothness criteria, and mentioned that some multi-reflection hopping modes or whispering gallery modes imply a surface smoothness rarely found in nature. He emphasized the practical importance of propagation over hills and depressions, and, as an example, the extent of the shadowing effect of a depression for VHF and UHF signals. H.J.Albrecht commented briefly on the topographic map of an area of concern being stored in a computer programme, which is also referred to as digital mapping of communication links, and also on the resolution being limited with regard to path profile and undisturbed tropospheric conditions. With any sort of ground-inversion layer, and other disturbances, this approach is not very suitable. There have been some attempts in Europe in this direction, as, for instance, by the German PTT, but this and similar concepts are in line with work done in the United States some years ago, by the US Army Topographic Command. He also referred to an appropriate contribution of this entity to an AGARD-Symposium sponsored by this Panel, and held in Colorado in 1971, on "Propagation Limitations in Remote Sensing" (Conference Proceedings No. 90).

In reply to J.S.Belrose's question, L.B.Felsen mentioned that, as a theoretician, one tries to understand the physical mechanism of propagation that can be supported by a particular surface. Here emphasis is placed upon concave surfaces which, unlike convex surfaces, have not been adequately investigated before. Under certain circumstances, as noted above, the surface-impedance concept is applicable. Presently, attempts are being made to understand how the wave types dealt with in the paper are affected by surface impedance. It is quite likely that the whispering gallery modes that propagate closest to the ground are attenuated if the surface impedance is sufficiently lossy, so that the ray-optical fields then become the prime contributors. If, on the other hand, the soil has very little dissipation associated with it, and if the propagation takes place over smooth profiles (for example, sand dunes in the desert) the model in the paper and the corresponding mechanism may really be operative. Thus each environment has to be looked at in its own right. In the case of vegetation, the model and the kind of analysis indicated may have to be generalized.

H.J.Albrecht added that with vegetation as an example, a model may become considerably more complicated, and if ad hoc models are visualized, it might even be relatively easy to include the meteorological characteristics of the surroundings, more or less in line with E.Raschke's comments at the beginning of the round-table discussion. He then suggested to use the remaining few minutes of the discussion period to touch upon the subject of the possibility of remote sensing methods for the prediction of propagation behaviour or, in other words, the use of global remote sensing or at least remote sensing over wide areas to monitor characteristics mainly of the interface between ground and tropospheric propagation medium, and perhaps even of the surface-ground characteristics. He referred to E.Raschke's paper and, in particular, to the discussion of the usefulness of present remote sensing methods in analyzing data for propagation work, as well as to the catalogue presented in the paper on the present status of knowledge.

Enlarging upon the catalogue just mentioned, E.Raschke emphasized that only a few characteristics may be observed from space or airplane. The most effective one in propagation work, the refractive index distribution in the lower troposphere, cannot be observed from space or airplane because the exact structure of the planetary boundary layer is not known and cannot be derived with remote sensing methods. In this case, some indirect indications may have to be used, as the planetary boundary-layer stratus, or dust layers, etc. With regard to the surface, the most promising parameter to be monitored from space seems to be moisture. This is also of interest from the meteorological point of view, because the moisture-evaporation flux is a huge heat flux. Almost 50% of the heat exchange between air and ground is due to evaporation. This quantity may be observed with an accuracy approximating only 50%.

Some preliminary results obtained in a current project were reported upon by A.W.Biggs. During the early summer of 1976 and thereafter attention was paid to the areal distribution and ice-thickness distributions over the Great Lakes in the United States and also with the arctic sea-ice north of Point Barrow in the vicinity of Labrador. The use of a side-looking airborne-radar system resulted in a very broad coverage of the ice distribution. Measurements were conducted during day and night. Ice-types could be identified very well, in terms of old ice, new ice, etc. Following an ice-radar picture over the areal coverage image a short pulse radar was employed; this is basically a vertical incidence radar based on specular reflection and not back-scatter. In the Great Lakes, ice was detected up to several feet in thickness, while in sea-ice depths were twelve inches. The purpose of these investigations is connected to the period of navigability which now extends throughout the entire year instead of ending in December and commencing again in April. This has increased the tonnage by almost 20% and thus represents an economic factor. The motivation of the survey of ice north of Point Barrow is again economic, i.e. oil barges are moved, but only regions with thin ice can be used. To a degree this concerns propagation problems, inasmuch as anomalies of propagation over the surface are considered.

Concluding this round-table discussion, H.J.Albrecht again referred to its main objective, namely the discussion of state of the art, engineering aspects, and promising areas of research. He emphasized the importance of the last item and expressed hope that an adequate number of ideas and suggestions had been discussed. He summarized the discussion and stated that all the objectives were dealt with as much as possible in the limited period available. Finally, he thanked round-table participants and the audience.

REPORT DOCUMENTATION PAGE												
1. Recipient's Reference	2. Originator's Reference AGARD-CP-208	3. Further Reference ISBN 92-835-0196-9	4. Security Classification of Document UNCLASSIFIED									
5. Originator	Advisory Group for Aerospace Research and Development North Atlantic Treaty Organization 7 rue Ancelle, 92200 Neuilly sur Seine, France											
6. Title	EM PROPAGATION CHARACTERISTICS OF SURFACE MATERIALS AND INTERFACE ASPECTS											
7. Presented at	the Electromagnetic Wave Propagation Panel Specialists' Meeting held in Istanbul, 18-19 October 1976.											
8. Author(s) Various			9. Date June 1977									
10. Author's Address Various			11. Pages 246									
12. Distribution Statement	This document is distributed in accordance with AGARD policies and regulations, which are outlined on the Outside Back Covers of all AGARD publications.											
13. Keywords/Descriptors	<table border="0"> <tr> <td>Electromagnetic wave transmission</td> <td>Earth surface</td> <td>Electromagnetic properties</td> </tr> <tr> <td>Surface properties</td> <td>Remote sensing</td> <td>Reflectivity</td> </tr> <tr> <td>Boundary layer</td> <td>Target recognition</td> <td>Scattering</td> </tr> </table>			Electromagnetic wave transmission	Earth surface	Electromagnetic properties	Surface properties	Remote sensing	Reflectivity	Boundary layer	Target recognition	Scattering
Electromagnetic wave transmission	Earth surface	Electromagnetic properties										
Surface properties	Remote sensing	Reflectivity										
Boundary layer	Target recognition	Scattering										
14. Abstract	<p>In the field of electromagnetic wave propagation, essential limiting conditions may be represented by characteristics and behaviour of boundaries of the propagation environment. The performance of propagation paths may depend significantly upon variations in such surface properties.</p> <p>A Specialists' Meeting was particularly concerned with surface characteristics and accounted for the increasing importance of appropriate parameters for a number of modern fields of research and engineering applications, such as remote sensing and surveillance, target recognition, sub-surface propagation, etc. Sessions dealt with EM surface characteristics, propagation in interface media, and global distribution of EM surface characteristics. Material presented and discussed was supplemented by a round-table discussion.</p> <p>The meeting provided a review of the state of the art in this field of research, discussed theoretical and engineering aspects, and indicated promising areas of research.</p> <p>Papers and discussion material in this publication were presented at the Specialists' Meeting of the AGARD Electromagnetic Wave Propagation Panel on EM Propagation Characteristics of Surface Materials and Interface Aspects held in Istanbul, Turkey, on 18th and 19th October 1976.</p>											

ABSTRACT

ducted to test the accuracy of the computer programme with respect to reality. Referring to L.B.Felsen's paper and his description of the physical picture of ground-wave propagation in the presence of smooth hills and depressions, J.S.Belrose commented on smoothness criteria, and mentioned that some multi-reflection hopping modes or whispering gallery modes imply a surface smoothness rarely found in nature. He emphasized the practical importance of propagation over hills and depressions, and, as an example, the extent of the shadowing effect of a depression for VHF and UHF signals. H.J.Albrecht commented briefly on the topographic map of an area of concern being stored in a computer programme, which is also referred to as digital mapping of communication links, and also on the resolution being limited with regard to path profile and undisturbed tropospheric conditions. With any sort of ground-inversion layer, and other disturbances, this approach is not very suitable. There have been some attempts in Europe in this direction, as, for instance, by the German PTT, but this and similar concepts are in line with work done in the United States some years ago, by the US Army Topographic Command. He also referred to an appropriate contribution of this entity to an AGARD-Symposium sponsored by this Panel, and held in Colorado in 1971, on "Propagation Limitations in Remote Sensing" (Conference Proceedings No. 90).

In reply to J.S.Belrose's question, L.B.Felsen mentioned that, as a theoretician, one tries to understand the physical mechanism of propagation that can be supported by a particular surface. Here emphasis is placed upon concave surfaces which, unlike convex surfaces, have not been adequately investigated before. Under certain circumstances, as noted above, the surface-impedance concept is applicable. Presently, attempts are being made to understand how the wave types dealt with in the paper are affected by surface impedance. It is quite likely that the whispering gallery modes that propagate closest to the ground are attenuated if the surface impedance is sufficiently lossy, so that the ray-optical fields then become the prime contributors. If, on the other hand, the soil has very little dissipation associated with it, and if the propagation takes place over smooth profiles (for example, sand dunes in the desert) the model in the paper and the corresponding mechanism may really be operative. Thus each environment has to be looked at in its own right. In the case of vegetation, the model and the kind of analysis indicated may have to be generalized.

H.J.Albrecht added that with vegetation as an example, a model may become considerably more complicated, and if ad hoc models are visualized, it might even be relatively easy to include the meteorological characteristics of the surroundings, more or less in line with E.Raschke's comments at the beginning of the round-table discussion. He then suggested to use the remaining few minutes of the discussion period to touch upon the subject of the possibility of remote sensing methods for the prediction of propagation behaviour or, in other words, the use of global remote sensing or at least remote sensing over wide areas to monitor characteristics mainly of the interface between ground and tropospheric propagation medium, and perhaps even of the surface-ground characteristics. He referred to E.Raschke's paper and, in particular, to the discussion of the usefulness of present remote sensing methods in analyzing data for propagation work, as well as to the catalogue presented in the paper on the present status of knowledge.

Enlarging upon the catalogue just mentioned, E.Raschke emphasized that only a few characteristics may be observed from space or airplane. The most effective one in propagation work, the refractive index distribution in the lower troposphere, cannot be observed from space or airplane because the exact structure of the planetary boundary layer is not known and cannot be derived with remote sensing methods. In this case, some indirect indications may have to be used, as the planetary boundary-layer stratus, or dust layers, etc. With regard to the surface, the most promising parameter to be monitored from space seems to be moisture. This is also of interest from the meteorological point of view, because the moisture-evaporation flux is a huge heat flux. Almost 50% of the heat exchange between air and ground is due to evaporation. This quantity may be observed with an accuracy approximating only 50%.

Some preliminary results obtained in a current project were reported upon by A.W.Biggs. During the early summer of 1976 and thereafter attention was paid to the areal distribution and ice-thickness distributions over the Great Lakes in the United States and also with the arctic sea-ice north of Point Barrow in the vicinity of Labrador. The use of a side-looking airborne-radar system resulted in a very broad coverage of the ice distribution. Measurements were conducted during day and night. Ice-types could be identified very well, in terms of old ice, new ice, etc. Following an ice-radar picture over the areal coverage image a short pulse radar was employed; this is basically a vertical incidence radar based on specular reflection and not back-scatter. In the Great Lakes, ice was detected up to several feet in thickness, while in sea-ice depths were twelve inches. The purpose of these investigations is connected to the period of navigability which now extends throughout the entire year instead of ending in December and commencing again in April. This has increased the tonnage by almost 20% and thus represents an economic factor. The motivation of the survey of ice north of Point Barrow is again economic, i.e. oil barges are moved, but only regions with thin ice can be used. To a degree this concerns propagation problems, inasmuch as anomalies of propagation over the surface are considered.

Concluding this round-table discussion, H.J.Albrecht again referred to its main objective, namely the discussion of state of the art, engineering aspects, and promising areas of research. He emphasized the importance of the last item and expressed hope that an adequate number of ideas and suggestions had been discussed. He summarized the discussion and stated that all the objectives were dealt with as much as possible in the limited period available. Finally, he thanked round-table participants and the audience.

REPORT DOCUMENTATION PAGE			
1. Recipient's Reference	2. Originator's Reference AGARD-CP-208	3. Further Reference ISBN 92-835-0196-9	4. Security Classification of Document UNCLASSIFIED
5. Originator	Advisory Group for Aerospace Research and Development North Atlantic Treaty Organization 7 rue Ancelle, 92200 Neuilly sur Seine, France		
6. Title	EM PROPAGATION CHARACTERISTICS OF SURFACE MATERIALS AND INTERFACE ASPECTS		
7. Presented at	the Electromagnetic Wave Propagation Panel Specialists' Meeting held in Istanbul, 18-19 October 1976.		
8. Author(s) Various			9. Date June 1977
10. Author's Address Various			11. Pages 246
12. Distribution Statement	This document is distributed in accordance with AGARD policies and regulations, which are outlined on the Outside Back Covers of all AGARD publications.		
13. Keywords/Descriptors	Electromagnetic wave transmission Surface properties Boundary layer	Earth surface Remote sensing Target recognition	Electromagnetic properties Reflectivity Scattering
14. Abstract			
<p>In the field of electromagnetic wave propagation, essential limiting conditions may be represented by characteristics and behaviour of boundaries of the propagation environment. The performance of propagation paths may depend significantly upon variations in such surface properties.</p> <p>A Specialists' Meeting was particularly concerned with surface characteristics and accounted for the increasing importance of appropriate parameters for a number of modern fields of research and engineering applications, such as remote sensing and surveillance, target recognition, sub-surface propagation, etc. Sessions dealt with EM surface characteristics, propagation in interface media, and global distribution of EM surface characteristics. Material presented and discussed was supplemented by a round-table discussion.</p> <p>The meeting provided a review of the state of the art in this field of research, discussed theoretical and engineering aspects, and indicated promising areas of research.</p> <p>Papers and discussion material in this publication were presented at the Specialists' Meeting of the AGARD Electromagnetic Wave Propagation Panel on "EM Propagation Characteristics of Surface Materials and Interface Aspects" held in Istanbul, Turkey, on 18th and 19th October 1976.</p>			

<p>AGARD Conference Proceedings No. 208 Advisory Group for Aerospace Research and Development, NATO EM PROPAGATION CHARACTERISTICS OF SURFACE MATERIALS AND INTERFACE ASPECTS Edited by H.J. Albrecht Published June 1977 246 pages</p> <p>In the field of electromagnetic wave propagation, essential limiting conditions may be represented by characteristics and behaviour of boundaries of the propagation environment. The performance of propagation paths may depend significantly upon variations in such surface properties.</p> <p>P.T.O.</p>	<p>AGARD-CP-208</p> <p>Electromagnetic wave transmission Surface properties Boundary layer Earth surface Remote sensing Target recognition Electromagnetic properties Reflectivity Scattering</p>	<p>AGARD Conference Proceedings No. 208 Advisory Group for Aerospace Research and Development, NATO EM PROPAGATION CHARACTERISTICS OF SURFACE MATERIALS AND INTERFACE ASPECTS Edited by H.J. Albrecht Published June 1977 246 pages</p> <p>In the field of electromagnetic wave propagation, essential limiting conditions may be represented by characteristics and behaviour of boundaries of the propagation environment. The performance of propagation paths may depend significantly upon variations in such surface properties.</p> <p>P.T.O.</p>	<p>AGARD-CP-208</p> <p>Electromagnetic wave transmission Surface properties Boundary layer Earth surface Remote sensing Target recognition Electromagnetic properties Reflectivity Scattering</p>
<p>AGARD Conference Proceedings No. 208 Advisory Group for Aerospace Research and Development, NATO EM PROPAGATION CHARACTERISTICS OF SURFACE MATERIALS AND INTERFACE ASPECTS Edited by H.J. Albrecht Published June 1977 246 pages</p> <p>In the field of electromagnetic wave propagation, essential limiting conditions may be represented by characteristics and behaviour of boundaries of the propagation environment. The performance of propagation paths may depend significantly upon variations in such surface properties.</p> <p>P.T.O.</p>	<p>AGARD-CP-208</p> <p>Electromagnetic wave transmission Surface properties Boundary layer Earth surface Remote sensing Target recognition Electromagnetic properties Reflectivity Scattering</p>	<p>AGARD Conference Proceedings No. 208 Advisory Group for Aerospace Research and Development, NATO EM PROPAGATION CHARACTERISTICS OF SURFACE MATERIALS AND INTERFACE ASPECTS Edited by H.J. Albrecht Published June 1977 246 pages</p> <p>In the field of electromagnetic wave propagation, essential limiting conditions may be represented by characteristics and behaviour of boundaries of the propagation environment. The performance of propagation paths may depend significantly upon variations in such surface properties.</p> <p>P.T.O.</p>	<p>AGARD-CP-208</p> <p>Electromagnetic wave transmission Surface properties Boundary layer Earth surface Remote sensing Target recognition Electromagnetic properties Reflectivity Scattering</p>

<p>A Specialists' Meeting was particularly concerned with surface characteristics and accounted for the increasing importance of appropriate parameters for a number of modern fields of research and engineering applications, such as remote sensing and surveillance, target recognition, sub-surface propagation, etc. Sessions dealt with EM surface characteristics, propagation in interface media, and global distribution of EM surface characteristics. Material presented and discussed was supplemented by a round-table discussion.</p> <p>The meeting provided a review of the state of the art in this field of research, discussed theoretical and engineering aspects, and indicated promising areas of research.</p> <p>Papers and discussion material in this publication were presented at the Specialists' Meeting of the AGARD Electromagnetic Wave Propagation Panel on "EM Propagation Characteristics of Surface Materials and Interface Aspects" held in Istanbul, Turkey, on 18th and 19th October 1976.</p> <p>ISBN 92-835-0196-9</p>	<p>A Specialists' Meeting was particularly concerned with surface characteristics and accounted for the increasing importance of appropriate parameters for a number of modern fields of research and engineering applications, such as remote sensing and surveillance, target recognition, sub-surface propagation, etc. Sessions dealt with EM surface characteristics, propagation in interface media, and global distribution of EM surface characteristics. Material presented and discussed was supplemented by a round-table discussion.</p> <p>The meeting provided a review of the state of the art in this field of research, discussed theoretical and engineering aspects, and indicated promising areas of research.</p> <p>Papers and discussion material in this publication were presented at the Specialists' Meeting of the AGARD Electromagnetic Wave Propagation Panel on "EM Propagation Characteristics of Surface Materials and Interface Aspects" held in Istanbul, Turkey, on 18th and 19th October 1976.</p> <p>ISBN 92-835-0196-9</p>
<p>A Specialists' Meeting was particularly concerned with surface characteristics and accounted for the increasing importance of appropriate parameters for a number of modern fields of research and engineering applications, such as remote sensing and surveillance, target recognition, sub-surface propagation, etc. Sessions dealt with EM surface characteristics, propagation in interface media, and global distribution of EM surface characteristics. Material presented and discussed was supplemented by a round-table discussion.</p> <p>The meeting provided a review of the state of the art in this field of research, discussed theoretical and engineering aspects, and indicated promising areas of research.</p> <p>Papers and discussion material in this publication were presented at the Specialists' Meeting of the AGARD Electromagnetic Wave Propagation Panel on "EM Propagation Characteristics of Surface Materials and Interface Aspects" held in Istanbul, Turkey, on 18th and 19th October 1976.</p> <p>ISBN 92-835-0196-9</p>	<p>A Specialists' Meeting was particularly concerned with surface characteristics and accounted for the increasing importance of appropriate parameters for a number of modern fields of research and engineering applications, such as remote sensing and surveillance, target recognition, sub-surface propagation, etc. Sessions dealt with EM surface characteristics, propagation in interface media, and global distribution of EM surface characteristics. Material presented and discussed was supplemented by a round-table discussion.</p> <p>The meeting provided a review of the state of the art in this field of research, discussed theoretical and engineering aspects, and indicated promising areas of research.</p> <p>Papers and discussion material in this publication were presented at the Specialists' Meeting of the AGARD Electromagnetic Wave Propagation Panel on "EM Propagation Characteristics of Surface Materials and Interface Aspects" held in Istanbul, Turkey, on 18th and 19th October 1976.</p> <p>ISBN 92-835-0196-9</p>

AGARD

NATO  OTAN

7 RUE ANCELLE · 92200 NEUILLY-SUR-SEINE
FRANCE

Telephone 745.08.10 · Telex 610176

**DISTRIBUTION OF UNCLASSIFIED
AGARD PUBLICATIONS**

AGARD does NOT hold stocks of AGARD publications at the above address for general distribution. Initial distribution of AGARD publications is made to AGARD Member Nations through the following National Distribution Centres. Further copies are sometimes available from these Centres, but if not may be purchased in Microfiche or Photocopy form from the Purchase Agencies listed below.

NATIONAL DISTRIBUTION CENTRES

BELGIUM

Coordonnateur AGARD — VSL
Etat-Major de la Force Aérienne
Caserne Prince Baudouin
Place Dailly, 1030 Bruxelles

CANADA

Defence Scientific Information Service
Department of National Defence
Ottawa, Ontario K1A 0Z2

DENMARK

Danish Defence Research Board
Østerbrogades Kaserne
Copenhagen Ø

FRANCE

O.N.E.R.A. (Direction)
29 Avenue de la Division Leclerc
92 Chatillon sous Bagneux

GERMANY

Zentralstelle für Luft- und Raumfahrt-
dokumentation und -information
Postfach 860880
D-8 München 86

GREECE

Hellenic Armed Forces Command
D Branch, Athens

ICELAND

Director of Aviation
c/o Flugrad
Reykjavik

ITALY

Aeronautica Militare
Ufficio del Delegato Nazionale all'AGARD
3, Piazzale Adenauer
Roma/EUR

LUXEMBOURG

See Belgium

NETHERLANDS

Netherlands Delegation to AGARD
National Aerospace Laboratory, NLR
P.O. Box 126
Delft

NORWAY

Norwegian Defence Research Establishment
Main Library
P.O. Box 25
N-2007 Kjeller

PORTUGAL

Direcção do Serviço de Material
da Força Aérea
Rua de Escola Politécnica 42
Lisboa
Attn: AGARD National Delegate

TURKEY

Department of Research and Development (ARGE)
Ministry of National Defence, Ankara

UNITED KINGDOM

Defence Research Information Centre
Station Square House
St. Mary Cray
Orpington, Kent BR5 3RE

UNITED STATES

National Aeronautics and Space Administration (NASA),
Langley Field, Virginia 23365
Attn: Report Distribution and Storage Unit

THE UNITED STATES NATIONAL DISTRIBUTION CENTRE (NASA) DOES NOT HOLD
STOCKS OF AGARD PUBLICATIONS, AND APPLICATIONS FOR COPIES SHOULD BE MADE
DIRECT TO THE NATIONAL TECHNICAL INFORMATION SERVICE (NTIS) AT THE ADDRESS BELOW.

PURCHASE AGENCIES

Microfiche or Photocopy

National Technical
Information Service (NTIS)
5285 Port Royal Road
Springfield
Virginia 22151, USA

Microfiche

Space Documentation Service
European Space Agency
10, rue Mario Nikis
75015 Paris, France

Microfiche

Technology Reports
Centre (DTI)
Station Square House
St. Mary Cray
Orpington, Kent BR5 3RF
England

Requests for microfiche or photocopies of AGARD documents should include the AGARD serial number, title, author or editor, and publication date. Requests to NTIS should include the NASA accession report number. Full bibliographical references and abstracts of AGARD publications are given in the following journals:

Scientific and Technical Aerospace Reports (STAR),
published by NASA Scientific and Technical
Information Facility
Post Office Box 8757
Baltimore/Washington International Airport
Maryland 21240, USA

Government Reports Announcements (GRA),
published by the National Technical
Information Services, Springfield
Virginia 22151, USA



Printed by Technical Editing and Reproduction Ltd
Harford House, 7-9 Charlotte St, London W1P 1HD

ISBN 92-835-0196-9